

Defect-rich Titanium (IV) Oxide and
Zirconium (IV) Oxide Nanostructures for
Ultra-efficient Photocatalyst and High-Tc
Dilute Ferromagnetic Semiconductor
Applications

by

Md Anisur Rahman

A thesis
presented to the University of Waterloo
in fulfillment of the
thesis requirement for the degree of
Doctor of Philosophy
in
Chemistry

Waterloo, Ontario, Canada, 2016

© Md Anisur Rahman 2016

AUTHOR'S DECLARATION

I hereby declare that I am the sole author of this thesis. This is a true copy of the thesis, including any required final revisions, as accepted by my examiners.

I understand that my thesis may be made electronically available to the public.

Abstract

In transparent conductive oxide nanostructures, oxygen vacancy defects (neutral, singly charged, and doubly charged defects) are found to be one of the most important and prevalent defects due to the enhancement of light absorption and charge transport properties, improved performance in photoelectrochemical water splitting reaction driven by visible light, and the introduction of ferromagnetism. However, the traditional methods of creating of oxygen vacancies, including hydrogen thermal treatment, high energy particle bombardment, and thermal annealing under oxygen depletion condition, generate oxygen vacancies mostly at the surface of the nanostructures. The performance of these nanostructures is therefore limited to surface oxygen vacancies. More importantly, the surface oxygen vacancies are found to be highly susceptible to oxidation upon long-term exposure to air. In addition, the dependence of optical, photoelectrochemical, and magnetic properties on the surface morphology and oxygen vacancy defect composition of the one-dimensional transparent conductive oxide nanostructures are not well understood. For these reasons, there is a great interest in the development of a novel method to create oxygen vacancies both at the surface and in the bulk of transparent conductive oxide nanostructures.

As two of the most important functional transparent conductive oxides, TiO_2 and ZrO_2 are specially preferred catalysts for photoelectrochemical water splitting reaction because of their suitable band edge positions for hydrogen evolution and exceptional stability against photocorrosion upon optical excitation. In the present work, highly oxygen-deficient TiO_2 and ZrO_2 nanostructures including nanobricks, nanopopcorns, nanowires and nanosheets are prepared on Si substrates by a one-step catalyst-assisted pulsed laser deposition method. The use of a high vacuum system and Ar flow, and precise control of the gold-nanoisland catalyst size, interfacial SiO_2 layer thickness, and growth temperature have enabled us to produce oxygen-deficient single-crystalline nanostructured films with different morphologies and different composition of oxygen vacancy defects.

The oxygen-deficient TiO_2 nanostructures have been chosen as the starting point of the present study. For TiO_2 nanowires reported to date, the oxygen vacancies have been found to form just within a few tens of nanometers at the outer surface of these nanowires, and the photocurrent density is significantly reduced by two to three orders of magnitude when ultraviolet light (<430 nm) is filtered out from the AM 1.5G simulated sunlight. Here, we demonstrate, for the first time, that by manipulating the thickness of the SiO_2 buffer layer, together with appropriately optimized growth

temperature and growth environment, it is possible to synthesize TiO₂ nanobelts, and corrugated nanowires, straight nanowires, and tapered TiO₂ nanowires decorated with TiO₂-nanocrystallites using a one-step catalyst-assisted pulsed laser deposition method. We further show that the amount of oxygen vacancy defects depends on the growth temperature, while our electrochemical impedance measurement confirms the lower charge transfer resistances at the depletion layer of the decorated nanowires. Photoelectrochemical measurement under simulated sunlight (100 mW/cm²) shows that the photocurrent density measured at 0.5 V (vs Ag/AgCl) for the decorated nanowires (1.5 mA/cm²) is found to be significantly higher than those of nanobelts (0.18 mA/cm²), nanobricks (0.25 mA/cm²), straight nanowires (0.6 mA/cm²), and corrugated nanowires (0.94 mA/cm²). More importantly, the photocurrent density of defect-rich decorated nanowires is reduced only slightly from 1.5 mA/cm² to 1.4 mA/cm² when the ultraviolet light (<430 nm) is filtered out, which represents 87% of the overall photocurrent. The high activity in the visible region can be attributed to a larger amount of oxygen vacancy defects in decorated nanowires, and to the enhanced charge transfer from the nanocrystallites to the cores of the decorated nanowires.

To extend the aforementioned method to other transparent conductive oxides, ZrO₂ nanowires with different morphologies and compositions of oxygen vacancy defects have been prepared by tuning the gold-nanoisland catalyst size and growth temperature. The as-grown hierarchical ZrO₂ nanowires (12.1 mA/cm²), consisting of individual ZrO₂ nanowires decorated with ZrO₂ nanoplates, have shown 1.9 times more photocurrent density than that of as-grown regular nanowires (6.4 mA/cm²). The photoelectrochemical performance of as-grown nanostructures has been further improved by partial delamination or flaking of the as-grown nanostructured film by a simple hydrofluoric acid treatment. The photocurrent density of the partially delaminated hierarchical nanowires, obtained after the HF treatment, is found to increase remarkably to 42.4 mA/cm², i.e. nearly 3.5 times that of the as-grown hierarchical nanowires due to improvement of the composition of oxygen vacancy defects, charge carrier transport resistance, and specific surface area of the as-grown single-crystalline hierarchical nanowires. More importantly, the HF-treated partially delaminated hierarchical nanowire film electrode provides the highest cathodic photocurrent of 32.2 mA/cm² (at -0.8 V vs reversible hydrogen electrode) in the visible light (>400 nm) region reported to date.

The variation of the pulsed deposition growth temperature also produces ZrO₂ nanostructures with different specific surface areas and amounts of oxygen vacancy defects, including nanobricks,

nanopopcorns, nanospikes, and nanowires. The presence of different types of oxygen vacancies (neutral, singly charged, and doubly charged defects) and their correlation to the Zr^{x+} oxidation states ($4 > x > 1$) are found to affect the exchange interactions and the ferromagnetic properties of these nanostructures. The saturation magnetization measured at 2000 Oe for the nanowires (5.9 emu/g) is found to be significantly greater than those of nanospikes (2.9 emu/g), nanopopcorns (1.2 emu/g), and nanobricks (0.6 emu/g), while the coercivity for the nanowires (99 Oe) is approximately twice that of the nanobricks (50 Oe). More importantly, a Curie temperature (T_c) considerably above room temperature has also been observed for these ZrO_2 nanostructures, including nanowires (700 K), nanospikes (650 K), nanopopcorns (550 K), and nanobricks (400 K). We also provide the first experimental evidence that it is the amount of defects in and not the phase of ZrO_2 that controls the ferromagnetic order in undoped ZrO_2 nanostructures. The present work therefore provides, for the first time, a direct correlation between the surface morphology and the composition of oxygen vacancy defects with the photoelectrochemical and ferromagnetic properties of the TiO_2 and ZrO_2 nanostructures.

Acknowledgements

First, I would like to express my sincere appreciation to my advisor, Prof. Kam Tong Leung, for his guidance, encouragement, and patience over the last five years. He gave me the opportunity to be a part of the Waterloo Advanced Technology Laboratory (WATLab). I have learned a lot from Prof. Leung regarding work ethics, the design and maintenance of high quality instruments and experiments, and inspiration to become a better scientist, and for that I am thankful. I would also like to thank my advisory committee members, Dr. William Wong, Dr. Shirley Tang, Dr. Paul Rowntree, and Dr. Jonathan Baugh for their invaluable suggestions and feedback on the work.

I was also fortunate to have the opportunity to interact with a number of talented and friendly people in WATLab. I would like to thank all WATLab members, especially Dr. Nina Heinig, Dr. Lei Zhang, Dr. Liyan Zhao, Dr. Joseph Palathinkal Thomas, Dr. Samad Bazargan, Dr. Xiongyao Wang, Dr. Debabrata Pradhan, Dr. Shantinarayan Rout, Dr. Avisek Chatterjee, Dr. Yan Wang-Duffort, Saurabh Srivastava, Donald McGillivray, Marwa Abd-Ellah, Jung-Soo Kang, Bahareh Rahsepar, Hannieh Farkhondeh, Nafiseh Moghimi, and Mahdi Beedel. I will always be proud for being a part of this significant family. I gratefully acknowledge all members of the University of Waterloo Chemistry Department, the Waterloo Institute for Nanotechnology, and the Natural Sciences and Engineering Research Council of Canada for their generous funding of my research in Canada.

Finally, I would like to express my deepest appreciation to my family, my parents, and my sibling whose love, encouragement, and unfailing support made it possible to complete my graduate school. I would not have been able to accomplish what I have today without their unconditional support.

Dedication (if included)

To my supportive loving parents Waliullah and Monowara, I dedicated this thesis.

Table of Contents

| | |
|---|------|
| AUTHOR'S DECLARATION | ii |
| Abstract | iii |
| Acknowledgements | vi |
| Dedication (if included)..... | vii |
| Table of Contents | viii |
| List of Figures | x |
| List of Tables..... | xx |
| Chapter 1 Introduction..... | 1 |
| 1.1 Transparent Conducting Oxides | 1 |
| 1.2 Visible-light Driven Photoelectrochemical Water Oxidation..... | 3 |
| 1.2.1 TiO ₂ as the photocatalyst for photoelectrochemical water splitting | 3 |
| 1.2.2 ZrO ₂ as a photocatalyst for photoelectrochemical water oxidation..... | 17 |
| 1.3 Transparent dilute ferromagnetic semiconductor oxides..... | 23 |
| 1.3.1 Prospects and challenges in the development of transparent dilute ferromagnetic semiconductor oxides | 23 |
| 1.3.2 Existing models of ferromagnetism in TDFSOs | 27 |
| 1.4 Motivations and Scope of the Thesis..... | 31 |
| Chapter 2 Experimental Techniques | 34 |
| 2.1 Pulsed Laser Deposition..... | 34 |
| 2.2 Characterization of Physical Properties..... | 37 |
| 2.2.1 Scanning electron microscopy..... | 37 |
| 2.2.2 Helium ion microscopy | 38 |
| 2.2.3 Transmission electron microscopy | 40 |
| 2.2.4 X-ray diffraction crystallography | 41 |
| 2.3 Chemical-state Composition Analysis | 43 |
| 2.4 Characterization of Electrical, Optical and Magnetic Properties | 44 |
| 2.4.1 Electrochemical techniques for analysis..... | 44 |
| 2.4.2 Electrochemical impedance spectroscopy | 46 |
| 2.4.3 Hall effect measurements | 49 |
| 2.4.4 Ultra-Violet/Visible (UV/Vis) spectroscopy | 51 |
| 2.4.5 Measurement of magnetic properties | 52 |

| | |
|---|-----|
| Chapter 3 Defect-rich Decorated TiO ₂ Nanowires for Super-efficient Photoelectrochemical Water Splitting Driven by Visible Light | 53 |
| 3.1 Introduction | 53 |
| 3.2 Materials and Methods | 54 |
| 3.3 Results and Discussions | 56 |
| 3.3.1 Growth of defect-rich 1D Nanostructures | 56 |
| 3.3.2 Photoelectrochemical properties..... | 69 |
| 3.4 Summary | 76 |
| Chapter 4 Defect-rich Delaminated p-type ZrO ₂ Hierarchical Nanowires for Super-efficient Photoelectrochemical Water Reduction under Visible Light | 79 |
| 4.1 Introduction | 79 |
| 4.2 Experimental details | 81 |
| 4.3 Results and Discussions | 83 |
| 4.3.1 Growth and Characterization of ZrO ₂ Hierarchical Nanowires..... | 83 |
| 4.3.2 Photoelectrochemical properties..... | 98 |
| 4.3.3 Conclusion..... | 106 |
| Chapter 5 High-T _C Ferromagnetism in Defect-rich Dopant-free ZrO ₂ Nanostructures | 108 |
| 5.1 Introduction | 108 |
| 5.2 Materials and Methods | 111 |
| 5.3 Results and Discussion | 112 |
| 5.4 Conclusion..... | 139 |
| Chapter 6 Concluding Remarks and Future Work | 141 |
| 6.1 Summary of Contributions | 141 |
| 6.2 Suggestions for Future Work..... | 145 |
| Appendix A Permissions | 148 |
| Bibliography | 162 |

List of Figures

| | |
|---|----|
| Figure 1.1 Crystal structures of TiO ₂ : (a) rutile, (b) anatase and (c) brookite. Ti and O atoms are represented by big blue and small red spheres, respectively. ¹⁷ | 4 |
| Figure 1.2 Phase diagram of Ti-O system. The alloys of titanium can be classified into three main groups: alpha (α), alpha-beta (α + β), and beta (β). α-alloys are not heat treatable and they have low to medium strength. β-alloys are readily heat treatable and they offer high strength. (α + β) alloys are metastable and they generally include properties of both α-alloys and β-alloys. The region Ti ₂ O ₃ -TiO ₂ contains Ti ₂ O ₃ , Ti ₃ O ₅ , seven discrete phases of the homologous series Ti _n O _{2n-1} (Magneli phases), and TiO ₂ . ¹⁸ | 5 |
| Figure 1.3 Representative thermodynamically (a) suitable and (b) unsuitable materials for water splitting reactions, with their bandgaps and band-edge positions in relation to the redox potentials for water splitting shown with respect to normal hydrogen electrode (NHE) and vacuum (Vac). ²³ | 6 |
| Figure 1.4 Schematic diagram of the mechanism of a photoelectrochemical water splitting reaction. An expanded view of a TiO ₂ nanocluster (NC, red sphere), consisting of Ti (green spheres), O (pink spheres), and H atoms (brown spheres), is shown as the bottom inset. The top inset shows the electron-hole pair generation in TiO ₂ upon UV-Vis light illumination, which supplies holes (h ⁺) for the oxidation of OH ⁻ leading to O ₂ evolution at the photoanode and electrons (e ⁻), upon traveling to the counter electrode through an external circuit, for reduction leading to H ₂ generation. ²² | 7 |
| Figure 1.5 Schematic diagram of band gap engineering and mechanism of photocatalysis reactions for pure, transition-metal (TM) doped, non-metal (NM) doped, and oxygen vacancy defect-rich TiO ₂ | 9 |
| Figure 1.6 (a) SEM image and (b) TEM image of 1D TiO ₂ nanostructure prepared by a typical wet-chemistry method. TEM image shows that the as-grown nanowires are composed of nanoparticles of TiO ₂ . ⁶⁰ | 13 |
| Figure 1.7 Schematic representation of the growth of Si nanowhiskers by the vapor-liquid-solid growth mechanism. (a) Initial droplet formation at the catalyst site. (b) Growth of nanowires with metallic alloy at the tip. ⁶³ | 14 |
| Figure 1.8 (a) Photocurrent densities and (b) IPCE spectra for the pristine TiO ₂ nanowires, and TiO ₂ nanowires after annealing in H ₂ at 350, 400, and 450 °C, as a function of applied potential vs. Ag/AgCl, along with their photographs (insets). ¹² | 16 |

| | | |
|-------------|---|----|
| Figure 1.9 | Cubic, tetragonal and monoclinic ZrO_2 lattice structures (lower panel). In the upper panel, the individual polymorph cells are space-expanded to provide a better view of the three different phases. In the lower panel, the cubic cell is taken as reference to show the deformation of the oxygen sublattice for tetragonal and monoclinic ZrO_2 (dashed lines and arrows). Large dark red spheres and small light grey spheres represent O and Zr atoms, respectively. ⁷⁶ | 18 |
| Figure 1.10 | Zr-O phase diagram. At room temperature, zirconium exhibits a hexagonally close packed crystal structure, α -Zr, which changes to β -Zr, a body-centered cubic crystal structure, at 1163 K. Zirconium exists in the β -phase until the melting point. The phase transitions between the monoclinic and tetragonal phases and between the tetragonal and cubic phases are observed at 1478 K and 2650 K, respectively. ¹⁸ | 19 |
| Figure 1.11 | Calculated band-edge positions of pure ZrO_2 , $ZrO_2:Fe_s$, and $ZrO_2:Fe_i$. $ZrO_2:Fe_s$ and $ZrO_2:Fe_i$ represent ZrO_2 doped with Fe atoms in substitutional and interstitial positions, respectively. ⁸⁷ | 20 |
| Figure 1.12 | (A) Schematic drawing of the fabrication procedure of zirconia nanowire arrays on glass substrates by a tailored two-step anodization process. (B) Scanning electron micrograph of a fractured cross-section of a highly ordered anodic zirconia nanowire array partially embedded in a porous alumina film. ¹⁰¹ | 22 |
| Figure 1.13 | Saturated magnetization (at 300 K) for transition metal-doped TiO_2 thin films grown on a $LaAlO_3$ substrate at 923 K. The inset shows the magnetization curve taken at 300 K for a V-doped TiO_2 film (with the magnetic field applied parallel to the surface of the film). ¹²² | 25 |
| Figure 1.14 | Magnetization vs magnetic field curves for ZrO_2 thin films with different crystal phases: S218 – completely tetragonal ZrO_2 , S317 – mixture of monoclinic and tetragonal ZrO_2 , and S416 – completely monoclinic ZrO_2 . Inset shows the enlarged hysteresis loop of S218. ⁵ | 27 |
| Figure 1.15 | Interaction of two magnetic polarons. The polarons are shown as grey circles, while the small and large arrows represent impurity and holes spins, respectively. ¹⁴¹ | 29 |
| Figure 1.16 | Schematic representation of the proposed charge-transfer ferromagnetism model for TDFSOs containing mixed-valence transition metal dopants such as manganese. This mechanism involves electron transfer from Mn^{2+} to the local density of states ($N_s(E)$) associated with the interfacial structural defects, raising the Fermi level to a peak in $N_s(E)$ and causing Stoner splitting (an exchange interaction that splits the energy of states with different spins and states near the Fermi level are polarized) of the defect band (indicated with red and blue colors). ¹⁴³ | 30 |

| | |
|---|----|
| Figure 2.1 Photographs of (top) the pulsed laser deposition system, consisting of the KrF excimer laser, the alignment, focusing and rastering optics, and the vacuum deposition chamber, along with the electronic control rack and gas box; (bottom left) the multi-target carousel and substrate mount assembly inside the chamber; and (bottom right) the ablation laser plume of the target during deposition. | 36 |
| Figure 2.2 Photograph of the Zeiss Merlin field-emission scanning electron microscope, equipped with both in-lens and out-of-lens secondary electron detectors, an energy-selective (EsB) and an angle-selective (AsB) backscattered detectors, and an EDAX energy-dispersive X-ray analysis system. | 38 |
| Figure 2.3 Photograph of a Zeiss Orion Plus helium ion microscope. | 39 |
| Figure 2.4 Photograph of a Zeiss Libra 200 MC transmission electron microscope. | 41 |
| Figure 2.5 Photograph of the Panalytical X'pert Pro MRD X-ray diffractometer used for crystal structure characterization of the as-prepared supported nanostructures. The instrument is set up in the parallel beam geometry employing an X-ray mirror as the incident beam optics and a parallel plate collimator as the diffracted beam optics. | 42 |
| Figure 2.6 Photograph of the Thermo-VG Scientific ESCALab 250 X-ray Photoelectron Microprobe used for chemical-state quantification of nanostructured materials. | 44 |
| Figure 2.7 Photograph of an electrochemical station (CHI 660E) connected to a three-electrode electrochemical cell in typical photoelectrochemical water splitting reaction setup. The nanostructured sample is used as the working electrode, in the presence of a Pt wire counter electrode and an Ag/AgCl reference electrode. A 300 W solar simulator (Newport-Oriel Instruments, Model 68811) was used to provide the AM 1.5G solar light. The light intensity of the solar simulator was calibrated to 1 sun (100 mW cm^{-2}) using a power meter (Molelectron, EPM 1000e). | 45 |
| Figure 2.8 Photograph of the SRS-UGA gas analyzer with a two-stage pressure reduction scheme. | 46 |
| Figure 2.9 (a) Typical Nyquist plot for a TiO_2 nanowire film under illumination of simulated sunlight (100 mW/cm^2). The experimental data (solid circles) are collected in a frequency range between 0.01 Hz and 100 Hz with an AC voltage amplitude of 10 mV and a DC bias of -0.5 V , and they are fitted with (b) an equivalent circuit model (solid line). The equivalent circuit consists of a series resistance (R_s), an RC circuit with a resistance (R_D) and a chemical capacitance element (CPE_D) for the semiconductor depletion layer, along with a second RC circuit containing the charge transfer resistance for the Helmholtz layer (R_H) and the Warburg diffusion impedance | |

| | |
|--|----|
| (Z_w), and the capacitance for the electrochemical double layer (CPE_H) in a second RC circuit connected in series. ⁷¹ | 49 |
| Figure 2.10 (a) Photograph of the Ecopia HMS-5300 Hall effect measurement system, (b) sample mounting fixture with upper cooling reservoir..... | 50 |
| Figure 2.11 Photograph of the Perkin-Elmer Lambda 1050 UV/Vis/NIR spectrophotometer. | 51 |
| Figure 2.12 Photograph of the Quantum Design MPMS SQUID VSM system with Evercool technology. | 52 |
| Figure 3.1 SEM images of (a1, b1, c1) typical TiO ₂ nanobricks deposited in 200 mTorr Ar at 700 °C and (a2, b2, c2) typical gold nanoislands (GNIs), with the corresponding near-Gaussian size distributions (insets), formed on H-Si (top row), RCA-Si (middle row) and Ox-Si (bottom row). SEM images of the TiO ₂ nanostructures grown in 200 mTorr of Ar at 700 °C on GNI/H-Si (top row), GNI/RCA-Si (middle row), and GNI/Ox-Si templates (bottom row) taken as (a3, b3, c3) top view and (a4, b4, c4) cross-sectional view. Insets in (a3, b3, c3) schematically show the respective nanostructures. Insets in (a4, b4, c4) show the corresponding cross-sectional backscattered electron images. | 58 |
| Figure 3.2 SEM images of TiO ₂ nanostructures grown in 20 mTorr Ar at (a1, b1, c1) 675 °C, (a2, b2, c2) 700 °C, (a3, b3, c3) 720 °C, and (a4, b4, c4) 750 °C on GNI/H-Si (top row), GNI/RCA-Si (middle row) and GNI/Ox-Si templates (bottom row). The corresponding lower left insets show schematic models of the respective as-grown nanostructures, with the magnified SEM images of selected nanostructures shown in the upper right insets. | 60 |
| Figure 3.3 Schematic models of TiO ₂ nanostructures grown on gold nanoisland (GNI) modified Si(100) templates at 675, 700 and 720 °C. | 60 |
| Figure 3.4 TEM images of a typical (a) TiO ₂ nanobelt, (b) corrugated nanowire (NW), (c) straight nanowire, and (d) decorated nanowire. Lower-right insets show the corresponding high-resolution TEM images, while the upper-right inset in (d) depicts the high-resolution TEM image of a nanocrystallite..... | 62 |
| Figure 3.5 Glancing-incidence XRD patterns of different rutile TiO ₂ nanostructures obtained at an incidence angle of 0.4°. The PDF2 reference patterns of the FCC phase of Au (#00-041-0784) and of rutile TiO ₂ (#00-021-1276) are shown as top and bottom bar graphs, respectively. The features marked by asterisks (*) correspond to the modified Si substrate..... | 62 |

| | |
|--|----|
| Figure 3.6 (a) Photographs and (b) XPS spectra of O 1s, Ti 2p _{3/2} , and Si 2p regions of TiO ₂ nanostructured films consisting of nanobelts, corrugated nanowires (NWs), straight NWs, and decorated NWs. | 65 |
| Figure 3.7 XPS spectra of the Ti 2p region, relatively normalized at the Ti 2p _{3/2} peak maxima, for TiO ₂ nanobelts, corrugated nanowires (NWs), straight NWs, and decorated NWs. The arrows indicate the full widths at half maxima of 2p _{3/2} and 2p _{1/2} peaks of the decorated NWs..... | 66 |
| Figure 3.8 UV-Vis reflectance spectra of TiO ₂ nanobelts, corrugated nanowires (NWs), straight NWs, and decorated NWs. | 66 |
| Figure 3.9 Tauc plots for PLD-grown 1D TiO ₂ nanostructured films..... | 67 |
| Figure 3.10 Nyquist plots of predominant TiO ₂ nanostructured films (a) under illumination of simulated sunlight (100 mW/cm ²). The experimental data (symbols) are collected in a frequency range between 0.01 Hz and 100 Hz with an ac voltage amplitude of 10 mV and a dc bias of -0.5 V, and they are fitted with (b) an equivalent circuit model (solid lines). | 68 |
| Figure 3.11 Quantification of gas evolution for photoelectrochemical water splitting reaction with decorated TiO ₂ nanowires as the photoanode with light on and light off..... | 70 |
| Figure 3.12 (a) Current density and (b) the corresponding photoconversion efficiency measured as a function of applied potential from different TiO ₂ nanostructured photoanodes and from pristine RCA-Si, and RCA-Si/GNI templates (used as the control). The measurements are performed in a 1M KOH solution with a scan rate of 10 mV/s under 100 mW/cm ² simulated sunlight illumination with a AM 1.5G filter. (c) Photocurrent density of decorated nanowires for repeated on/off cycles of simulated sunlight illumination. (d) Linear sweep voltammograms of decorated TiO ₂ nanowire photoanode from an AM 1.5 G light (100 mW/cm ²) and with long-pass (>430 nm) and short-pass (<400 nm) filters. | 73 |
| Figure 3.13 Photocurrent density of decorated TiO ₂ nanowire at -0.2 V versus Ag/AgCl in 1 M KOH solution under simulated sunlight..... | 74 |
| Figure 3.14 Current density measured as a function of applied potential for (a) decorated and (b) straight nanowires in 1M KOH and 1M KOH-0.5M Na ₂ SO ₃ under simulated solar light illumination..... | 74 |
| Figure 3.15 Schematic diagram for the charge separation and migration process in TiO ₂ decorated nanowires in a photoelectrochemical water splitting reaction driven by visible light irradiation. | 76 |
| Figure 4.1 SEM images of (a) typical gold nanoislands (GNIs), with its corresponding near-Gaussian size distribution (inset), formed on the Ox-Si substrate, (b) PLD-grown ZrO ₂ hierarchical | |

nanowires on the GNI/Ox-Si template at 770 °C in 200 mTorr of Ar for 90 min, and (c1 – c4) ZrO₂ hierarchical nanowires scrapped-off from the GNI/Ox-Si template, taken after dispersing onto holey carbon TEM copper grids. TEM images of (d) a typical ZrO₂ hierarchical nanowire. (e) SEM image of ZrO₂ nanobricks PLD-grown in the absence of GNIs on bare Ox-Si substrate in 200 mTorr of Ar at 770 °C for 90 min. In (d) and (e), the lower-left insets show schematic representations of the respective PLD-grown nanostructures, while the upper-right insets show high-resolution TEM images of selected areas of the respective nanostructures. 85

Figure 4.2 SEM images of (a1, b1, c1) typical gold nanoislands (GNIs), with the corresponding near-Gaussian size distributions (insets), formed on Ox-Si templates by magnetron sputtering a gold target for (a1) 3 s, (b1) 6 s, and (c1) 15 s followed by annealing in air at 600 °C for 1 h. SEM images of (a2) regular nanowires, (b2) hierarchical nanowires, and (c2) octopus-like nanowires PLD-grown in 200 mTorr Ar at 770 °C for 90 min on the respective GNI/Ox-Si templates shown in (a1, b1, c1). The corresponding lower-left insets show schematic models of the as-grown nanostructures, while the upper-right insets in (a2, b2) and in (c2), respectively, depict the magnified TEM images and SEM image of the respective as-grown nanostructures. 87

Figure 4.3 TEM image of as-grown regular ZrO₂ nanowires, with a high-resolution TEM image of a selected area of an individual nanowire shown in inset..... 88

Figure 4.4 Schematic diagram of proposed catalyst-assisted vapour-liquid-solid growth mechanism for typical ZrO₂ hierarchical nanowires..... 89

Figure 4.5 Glancing-incidence XRD patterns of ZrO₂ hierarchical nanowire and nanobrick films obtained at an incidence angle of 0.3°. The PDF2 reference patterns of the FCC phase of Au (#03-065-8601), and of the monoclinic phase (#01-083-0940) and tetragonal phase (#01-080-0784) of ZrO₂ are shown as top, and bottom bar graphs, respectively..... 90

Figure 4.6 SEM images of (a) as-grown and (b) HF-treated ZrO₂ hierarchical nanowire films, with magnified views of selected areas in insets. Schematic models of the hierarchical nanowire film (c) before and (d) after the HF treatment. Nyquist plots of (e) as-grown and (f) HF-treated hierarchical nanowire samples under illumination of simulated sunlight (100 mW/cm²). The experimental data (solid circles) are collected in a frequency range between 0.01 Hz and 100 Hz with an AC voltage amplitude of 10 mV and a DC bias of -0.9 V, and they are fitted with (g) an equivalent circuit model (solid lines). 92

Figure 4.7 XPS spectra of Zr 3d and O 1s regions of (a) as-deposited, and (b) HF-treated ZrO₂ nanobrick (top row), regular nanowire (middle row) and hierarchical nanowire films (bottom

| | |
|--|-----|
| row). In addition to the ZrO_2 and SiO_x ($2 > x > 1.5$) features, two sets of oxygen vacancy defect features corresponding to ZrO_{x1} ($2 > x1 > 1.5$) and ZrO_{x2} ($1.5 \geq x2 > 1$) are used to fit the residual intensities. Photographs of the as-grown and HF-treated nanostructured samples are shown as insets in (a) and (b), respectively. | 95 |
| Figure 4.8 UV-Visible reflectance spectra of as-grown and HF-treated ZrO_2 nanostructured films. . | 96 |
| Figure 4.9 Current density measured by linear sweep voltammetry as a function of applied potential for (a) as-grown and (b) HF-treated ZrO_2 nanostructured film photocathodes, and for HF-treated hierarchical nanowire film photocathodes obtained with (c) short-pass and long-pass filters and (d) band-pass filters at 400, 500, 600, 700, and 800 nm. The measurements are performed in a (0.1 M H_2SO_4 + 0.01 M K_2SO_4) solution with a scan rate of 10 mV/s under 100 mW/cm ² simulated sunlight illumination with repeated light-on/light-off cycles. The inset in (d) shows the relative photocurrent density vs wavelength profiles of hierarchical nanowire (HNW), regular nanowire (RNW), and nanobrick (NB) films with respect to the natural sunlight spectrum. The HNW profile is point-normalized to the maximum of the natural sunlight spectrum. | 100 |
| Figure 4.10 Quantification of gas evolution for photoelectrochemical water splitting reaction with HF-treated hierarchical ZrO_2 nanowire (NW) film as the photocathode. A Stanford Research Systems Universal Gas Analyzer system is used to analyze the gas sample at atmospheric pressure via a specially designed, 1.8 m-long capillary tube (175 μ m ID). The measurement is performed with a three-electrode electrochemical cell in a sealed quartz beaker, with the capillary inserted to collect the gases generated by the reaction. The partial pressures for H_2 , O_2 , N_2 , H_2O and CO_2 before and during the water-splitting reaction are monitored. Evidently, only the partial pressures of H_2 and O_2 are found to increase as the reaction commences, while those of the other gases remain flat and unchanged. It should be noted that the amount of time for the evolved gases to reach saturation depends on the amount of catalysts on the sample and the efficiency of gas production (both of which affect the amounts of H_2 and O_2 produced by the water-splitting reaction), as well as the volume of space above the liquid solution in the beaker. Evidently, it only takes ~20 minutes for the produced gases to displace the air in the volume above the solution. | 101 |
| Figure 4.11 Photocurrent density of HF-treated hierarchical ZrO_2 nanowire film at -0.6 V vs RHE in 0.1 M H_2SO_4 + 0.01 M K_2SO_4 solution under simulated sunlight. Virtually no degradation in the photocurrent density is observed over the experiment period of 2 h. | 103 |

| | |
|--|-----|
| Figure 4.12 Schematic diagram for the charge separation and transfer process in the nanoplates of the HF-treated ZrO ₂ hierarchical nanowires in a photoelectrochemical water splitting reaction driven by visible light irradiation. Similar process involving their corresponding defect states [located between the valence band minimum (VB) and conduction band maximum (CB)] is expected to occur also in the trunks of these nanowires..... | 105 |
| Figure 5.1 SEM images of (a) typical gold nanoislands (GNIs), with the corresponding near-Gaussian size distribution (inset), deposited on an Ox-Si template, (b) ZrO ₂ nanobrick film PLD-grown on pristine Ox-Si template (without any GNI) at 770 °C, ZrO ₂ nanopopcorns, nanospikes and nanowires PLD-grown on the GNI/Ox-Si templates in 200 mTorr Ar for 90 min at, respectively, (c1, c2) 550 °C, (d1, d2) 650 °C, and (e1, e2) 770 °C. The corresponding lower left insets show schematic models of the respective as-grown nanostructures, with the backscattered electron images (upper right insets) depicting a gold nanoparticle (c2) at the core and (d2, e2) at the tips of the respective nanostructures. The SEM image in the upper right inset of (c1) illustrates the shape of the ZrO ₂ nanopopcorns..... | 114 |
| Figure 5.2 Schematic models of ZrO ₂ nanostructures grown on Ox-Si templates without and with gold nanoislands (GNIs) in 200 mTorr Ar for 90 min at 550 °C, 650 °C, and 770 °C. | 116 |
| Figure 5.3 Glancing-incidence XRD patterns of different PLD-grown ZrO ₂ nanostructures obtained at an incidence angle of 0.3°. The PDF2 reference patterns of the FCC phase of Au (#03-065-8601), and of the monoclinic phase (#01-083-0940) and tetragonal phase (#01-080-0784) of ZrO ₂ are shown as top, and bottom bar graphs, respectively..... | 117 |
| Figure 5.4 TEM images of typical (a1, a2) ZrO ₂ nanopopcorns, (b1, b2) nanospikes, and (c1, c2) nanowires, with the corresponding high-resolution images of selected areas of individual nanostructures shown in insets. (d) Magnetization (<i>M</i>) vs magnetic field (<i>H</i>) curves of as-grown ZrO ₂ nanostructures, with the enlarged view of the hysteresis loops for ZrO ₂ nanobricks and nanowires given in inset. (e) <i>M-H</i> curves for as-grown and annealed ZrO ₂ nanowires under different post-treatment conditions of annealing temperature and atmosphere, with the enlarged view of the respective hysteresis loops given in inset. | 120 |
| Figure 5.5 TEM image of ZrO ₂ nanobricks located in the gap among the ZrO ₂ nanowires. The corresponding insets showing the magnified images of individual nanobricks, with interplanar spacings of 2.9 Å and 2.5 Å, corresponding to the (101) and (110) planes of tetragonal ZrO ₂ , respectively..... | 121 |

- Figure 5.6 XPS survey spectrum for ZrO₂ nanowires. The corresponding inset shows the enlarged range from 600 eV to 800 eV, confirming the absence of any magnetic impurity..... 124
- Figure 5.7 (a) XPS spectra of Zr 3d, and O 1s regions of (a) as-deposited ZrO₂ nanostructures, and (b) ZrO₂ nanowires as-deposited and post-annealed under different conditions. In addition to the ZrO₂ features, two sets of defect features corresponding to ZrO_{x1} ($2 > x1 > 1.5$) and ZrO_{x2} ($1.5 \geq x2 > 1$) are used to fit the residual intensities. The minor changes in the peak positions (and widths) of these defect features from the marked positions correspond to the changes in the defect distributions within the considered x1 and x2 ranges. Photographs of the as-grown nanostructured samples are shown as insets in (a). (c1-c4) Schematic representations of three plausible types of oxygen vacancies in ZrO₂. The Zr⁴⁺ ions are marked by open white circles, and only the Zr³⁺ and Zr²⁺ ions [i.e. with relocation of electrons (with spin up and spin down as represented by up and down arrows, respectively) from the oxygen-vacancy defect sites] are shown as solid circles. In the interest of clarity, oxygen atoms are not shown, and the oxygen vacancy sites are marked as open squares. 125
- Figure 5.8 Comparison of UV-Vis-NIR reflectance spectra of as-deposited ZrO₂ nanostructured films, along with that of the pristine Ox-Si template..... 127
- Figure 5.9 (a) *M-H* curves for ZrO₂ nanowires measured at 3000 Oe for temperature (T) = 5, 77, 200, 300, and 400 K. The insets show the magnified hysteresis loops near the origin at 5 K and 400 K. (b) Magnetization as a function of temperature following field-cooled and zero-field-cooled measurements at *H* = 100 Oe..... 131
- Figure 5.10 (a) Arrott plot for ZrO₂ nanowires measured at 3000 Oe for temperature (T) = 5, 77, 200, 300, and 400 K. (b) Normalized saturation magnetization (*M_S/M₀*) as a function of temperature, where *M₀* is the saturation magnetization at 0 K. According to the Ginzburg-Landau mean field theory for ferromagnetism, the free energy of a ferromagnetic material close to the phase transition gives a relation for the magnetization order parameter: $M^2 = (1/b)(H/M) - (a/b)\epsilon$, where the magnetization *M* is the order parameter, *H* is the applied magnetic field, *a* and *b* are arbitrary constants, $\epsilon = (T-T_c)/T_c$, and *T_c* is the Curie temperature. In a plot of *M²* vs *H/M* (the Arrott plot) for various temperatures, the line without an intercept corresponds to the dependence at the Curie temperature. As shown in Figure 5.10a, the intercept is not zero even at 400 K, which means that *T_c* has yet to be reached. By using the instantaneous slope obtained at 400 K, a parallel dash line could be used to extrapolate to the origin, which indicates that *T_c* is above 400

K. Moreover, the temperature dependence of the saturation magnetization (Figure 5.10b) enables estimation of T_c using a power-law equation from the critical behavior model: 132

Figure 5.11 Normalized saturation magnetization (M_s/M_0) for ZrO_2 (a) nanospike, (b) nanopopcorn, and (c) nanobrick films as functions of temperature. 133

Figure 5.12 (a) Formation of bound magnetic polarons (marked by light green circles) by singly-charged and doubly-charged oxygen vacancies. The Zr^{4+} ions are marked by open white circles, while the Zr^{3+} ions are shown as solid white circles. In the interest of clarity, oxygen atoms are not shown, and the oxygen vacancy sites are marked by open white squares. The neutral oxygen vacancy site is highlighted by open dashed circle. The arrows indicate the direction of the spins. (b) Schematic representations of the proposed defect-induced bound polaron model for ferromagnetism in undoped ZrO_2 nanostructures containing oxygen vacancies and mixed-valence of Zr ions. This mechanism involves formation of an impurity band and its overlapping with Zr 4d states leading to ferromagnetic exchange coupling. 138

List of Tables

| | |
|--|-----|
| Table 3.1 Parameters extracted from fitted results of electrochemical impedance spectra for TiO ₂ nanostructured films under simulated sunlight..... | 69 |
| Table 4.1 Comparison of the relative percentages of the Zr 3d and O 1s peak intensities for oxygen vacancy defect features: ZrO _{x1} ($2 > x1 > 1.5$) and ZrO _{x2} ($1.5 \geq x2 > 1$), [#] for the as-grown and HF-treated ZrO ₂ nanostructured films. | 96 |
| Table 4.2 Parameters extracted from fitted results of electrochemical impedance spectra for as-grown and HF-treated ZrO ₂ nanostructured films under AM 1.5 G light..... | 98 |
| Table 5.1 Comparison of the estimated specific surface area, percentages of the monoclinic and tetragonal phases, percentages of the Zr 3d and O 1s peak intensities for defect-related features (ZrO _{x1} , ZrO _{x2} , and their sums), ^{&} and the saturated magnetization (<i>Ms</i>), remanence (<i>Mr</i>) and coercivity (<i>Hc</i>) measured at room temperature for the ZrO ₂ nanostructured films as-deposited at the specified temperature and for ZrO ₂ nanowires upon various post-treatments. | 126 |
| Table 5.2 Calculations for specific surface areas of ZrO ₂ nanostructures..... | 127 |

Chapter 1

Introduction

The present work focusses on the development of defect-rich, one-dimensional transparent conductive oxide (TCO) nanomaterials, particularly that of TiO_2 and ZrO_2 , and their applications as ultra-efficient photocatalysts for photoelectrochemical water splitting reaction (for hydrogen generation) and as high- T_C dilute ferromagnetic semiconductors for spin-based technologies. This Chapter will briefly describe the general properties of TCO nanostructured materials, the significance of TiO_2 and ZrO_2 over other TCOs, and the advantage of non-stoichiometric nanostructures over stoichiometric TiO_2 and ZrO_2 nanostructures. This will be followed by an overview of the strategies used to improve the visible-light photoelectrochemical water splitting performance of TiO_2 and ZrO_2 nanostructures, and the basic concepts in the development of dilute ferromagnetic semiconductor oxides. The last section will discuss the scope and structure of the thesis.

1.1 Transparent Conducting Oxides

Transparent conductive oxides (TCOs) are conductive metal oxides with a wide band gap (greater than 3 eV) that enables the transmittance of light up to the ultra-violet (UV) region and are often found to be n-type.¹ Over the past four decades, TCO nanostructured materials have received considerable attention due to their availability, biocompatibility, versatile morphologies, and enhanced performance in catalytic photoelectrochemical water splitting for hydrogen generation, photodegradation of organic pollutants, and dye-sensitized solar cells.² In general, TCOs have two unique structural features: switchable and/or mixed cation vacancies, and adjustable oxygen deficiency,³ which are the bases for the development of smart functional materials with unique electronic, optical, and chemical properties. A number of theoretical calculations and experimental studies have also suggested that doping,⁴ phase structure,⁵ and intrinsic point defects⁶ could contribute to the ferromagnetic behaviour of these oxides.

Among the various TCOs, TiO_2 and ZrO_2 are two of the most important functional oxides, and are especially popular for photoelectrochemical reaction because of their exceptional stability against photocorrosion upon optical excitation. Like other TCOs, TiO_2 and ZrO_2 are mainly synthesized in nanoparticle or thin film forms, partly because of the natural increase in the specific surface area in the nanoscale and the potential opportunity in manipulating their nanoscale properties, both of which are of great interest to catalysis, sensing and other nanotechnology applications. Recently, synthesis of one-dimensional (1D) TiO_2 and ZrO_2 nanostructures has attracted much attention due to their many unique physical and chemical properties, including low dimensionality,

single crystallinity, high length-to-width aspect ratio, and the quantum confinement effect. Together with their excellent mechanical strength, chemical stability, and outstanding optical property, the wire geometry also provides a 1D confinement channel for charge transport.⁷

As the stoichiometric nanostructure has a similarly large band gap as that of the bulk material ($\geq 3\text{eV}$), they only absorb photons with wavelength in ultraviolet region ($\lambda < 400\text{ nm}$), which represents only 5–8% of the solar spectrum at sea level. This poor light absorption, especially in the visible region, limits the efficiency and leads to the requirement of artificial UV illumination of the catalysts in order to achieve better performance. To improve the photocatalytic activity in the visible region ($\lambda > 400\text{ nm}$), various efforts have been made to tune the band gaps of TCOs, and these include doping with metals and nonmetals, and creation of oxygen vacancies by thermal annealing in hydrogen or oxygen depletion condition. The current problem with doped catalysts is that they have almost no activity in the visible light region,⁸ and in some cases they actually exhibit lower activity in the ultraviolet region than the undoped TCOs⁹ because of the high charge carrier recombination in dopant-induced defects. The major challenge with the oxygen-deficient TCOs is that the post-treatment creates oxygen vacancies only at the surface of the nanostructures, and the photoactivity performance of these TCOs remains limited by the surface oxygen vacancies of the nanostructures.⁸

The relative composition of the oxygen vacancy defects (neutral, singly-charged, and doubly-charged oxygen vacancies) has been found to be the origin of some of the most fascinating properties in these oxides, including increased conductivity,¹⁰ enhanced visible-light absorption,¹¹ greatly improved photoelectrochemical water splitting reactivity,¹² and room-temperature ferromagnetic property.¹³ For 1D nanostructures of TCOs, engineering the types and composition of defects, including oxygen vacancies, are crucial to controlling the physical and chemical properties of these oxides. The dependence of optical, photoelectrochemical, and magnetic properties on the surface morphology and on the composition of oxygen vacancy defects of 1D TCO nanostructures are, however, not well understood. The present work will therefore focus on defect-rich TiO_2 and ZrO_2 1D nanostructures.

1.2 Visible-light Driven Photoelectrochemical Water Oxidation

1.2.1 TiO₂ as the photocatalyst for photoelectrochemical water splitting

1.2.1.1 Properties of stoichiometric TiO₂ nanostructures

TiO₂ occurs in nature in three mineral forms: rutile ($a = b = 4.584 \text{ \AA}$, $c = 2.953 \text{ \AA}$), anatase ($a = b = 3.753 \text{ \AA}$, $c = 9.372 \text{ \AA}$), and brookite ($a = b = 3.753 \text{ \AA}$, $c = 9.372 \text{ \AA}$).¹⁴ While rutile is the most common form in nature and the most stable polymorph among the three forms, anatase and brookite can both be converted to rutile by annealing. The crystal structures of these polymorphs are shown in Figure 1.1. Both the anatase and rutile belong to the tetragonal crystal system, while the brookite has the orthorhombic crystal system. In all these polymorphs, a titanium atom is surrounded by six oxygen atoms in a somewhat distorted octahedral configuration. In rutile, the octahedron shows a slight orthorhombic distortion, while the octahedron of anatase is significantly distorted so that its symmetry is lower than orthorhombic. These differences in the lattice structures lead to different volume densities and electronic structures as well as other chemical and physical properties. The band gaps of rutile, anatase and brookite TiO₂ are estimated to be 3.0, 3.4, and 3.3 eV, respectively.¹⁵ In addition, TiO₂ can be easily reduced, and the titanium–oxygen phase diagram¹⁶ is very rich with multiple stable phases containing a variety of crystal structures (Figure 1.2). The reduced rutile TiO₂ is the focus of the present study, and TiO₂ here refers to rutile TiO₂ unless stated otherwise.

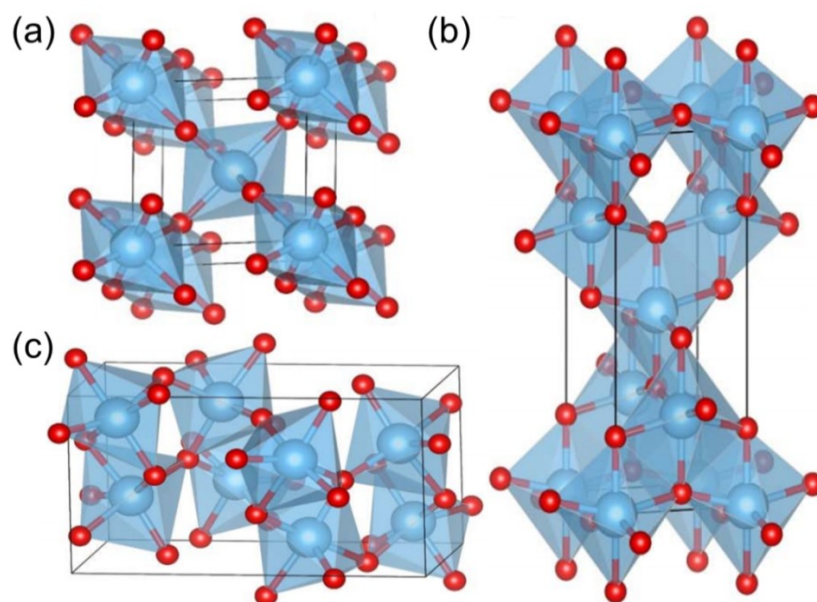


Figure 1.1 Crystal structures of TiO_2 : (a) rutile, (b) anatase and (c) brookite. Ti and O atoms are represented by big blue and small red spheres, respectively.^{17*}

* Reproduced with the permission from: Zhu, T.; Gao, S. *J. Phys. Chem. C* **2014**, *118*, 11385–11396. Copyright (2014) by the American Chemical Society.

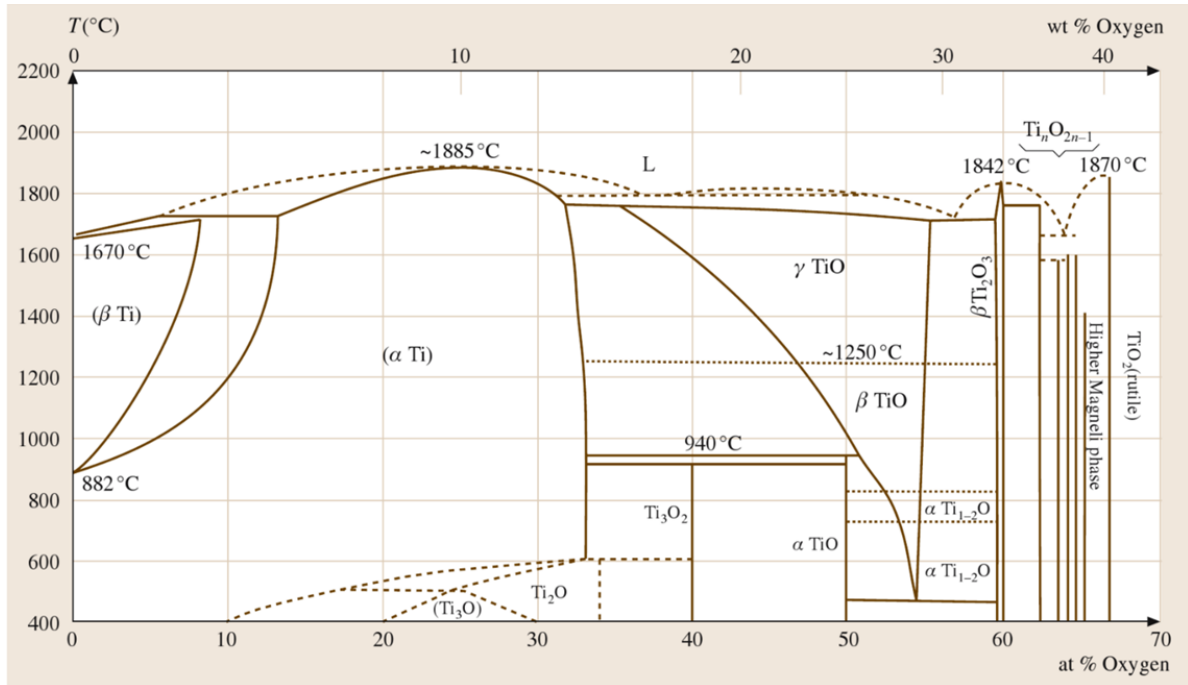


Figure 1.2 Phase diagram of Ti-O system. The alloys of titanium can be classified into three main groups: alpha (α), alpha-beta ($\alpha + \beta$), and beta (β). α -alloys are not heat treatable and they have low to medium strength. β -alloys are readily heat treatable and they offer high strength. ($\alpha + \beta$) alloys are metastable and they generally include properties of both α -alloys and β -alloys. The region Ti_2O_3 - TiO_2 contains Ti_2O_3 , Ti_3O_5 , seven discrete phases of the homologous series $\text{Ti}_n\text{O}_{2n-1}$ (Magneli phases), and TiO_2 .^{18†}

The high chemical stability, non-toxic environmental acceptability, long lifetime of photogenerated carriers, suitable band gaps and band-edge positions in relation to the redox potentials for water splitting (Figure 1.3), low cost and general availability have made TiO_2 one of the most promising photocatalysts for hydrogen production through photoelectrochemical water splitting reaction and for the other applications including water or air purification and dye-sensitized solar cells.^{19–21} Figure 1.4 shows the operation principle of a photoelectrochemical water splitting cell using an n-type TiO_2 nanocluster as the photoanode, a Ag/AgCl reference electrode, and a Pt wire counter electrode.²² Upon absorption of a photon with energy equal or higher than the band gap

[†] Reproduced with the permission from: Warlimont, H.; Martienssen, W. (Eds.). Springer Handbook of Condensed Matter and Materials Data; Springer: Berlin, 2005. Copyright (2005) by the Springer Berlin Heidelberg.

energy, an electron is promoted from the valence band into the conduction band of the semiconductor, leaving a positive charge (the hole) in the valence band. The photogenerated electrons and holes are then separated by an electric field close to the interface between the semiconductor and the electrolyte. This electric field is developed due to the formation of a Schottky-type contact between the semiconductor and the electrolyte. The photogenerated electrons travel to the Si substrate and are then transported to the counter electrode where they reduce H^+ ions and generating the hydrogen gas. The positive holes migrate to the interface, where they oxidize OH^- ions to produce the oxygen gas.

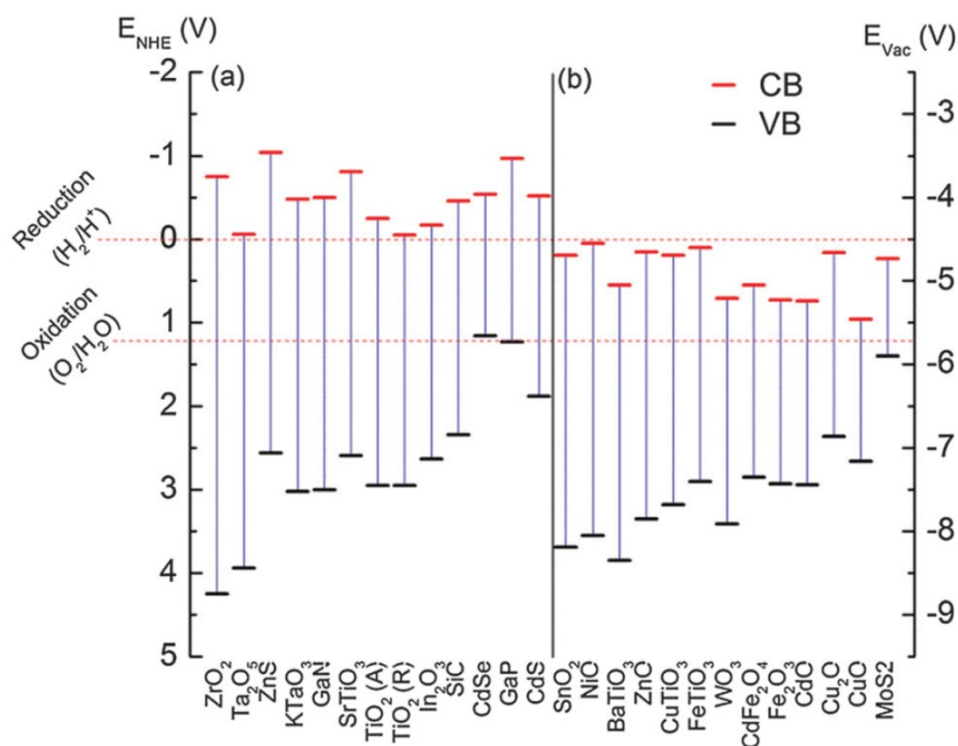


Figure 1.3 Representative thermodynamically (a) suitable and (b) unsuitable materials for water splitting reactions, with their bandgaps and band-edge positions in relation to the redox potentials for water splitting shown with respect to normal hydrogen electrode (NHE) and vacuum (Vac).^{23‡}

[‡] Reproduced with the permission from: Babu, V. J.; Vempati, S.; Uyar, T.; Ramakrishna, S. *Phys. Chem. Chem. Phys.* **2015**, *17*, 2960–2986. Copyright (2016) by the Royal Society of Chemistry.

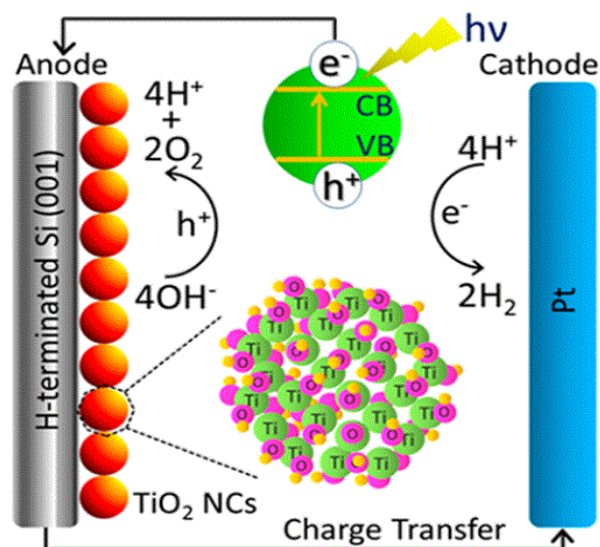


Figure 1.4 Schematic diagram of the mechanism of a photoelectrochemical water splitting reaction. An expanded view of a TiO₂ nanocluster (NC, red sphere), consisting of Ti (green spheres), O (pink spheres), and H atoms (brown spheres), is shown as the bottom inset. The top inset shows the electron–hole pair generation in TiO₂ upon UV–Vis light illumination, which supplies holes (h⁺) for the oxidation of OH⁻ leading to O₂ evolution at the photoanode and electrons (e⁻), upon traveling to the counter electrode through an external circuit, for reduction leading to H₂ generation.^{22§}

1.2.1.2 Modification of TiO₂ nanostructure to improve the performance in visible-light

Given that stoichiometric TiO₂ has a band gap of 3.0 eV,²⁴ it can absorb only UV light, making it an inherently poor sunlight-driven photocatalyst because ultraviolet light ($\lambda < 400$ nm) represents only 5–8% of the solar spectrum at sea level. In order to achieve significant improvement in catalytic activity by using the visible light component (representing 43% of the solar spectrum), precise control of the stoichiometry, shape and specific surface area of the nanostructures, as well as the types and concentrations of dopants is necessary.

(a) Doping

Doping is the introduction of foreign elements into the host oxide without giving rise to new crystallographic forms, phases or structures.^{25–29} The strategy to alter the band gap of TiO₂ by doping is an important approach as this could determine the portion of the solar spectrum that the catalyst

[§] Reproduced with the permission from: Srivastava, S.; Thomas, J. P.; Rahman, A.; Abd-ellah, M.; Mohapatra, M.; Pradhan, D.; Heinig, N. F.; Leung, K. T. *ACS Nano* **2014**, *8*, 11891–11898. Copyright (2014) by the American Chemical Society.

absorbs and, consequently, the amount of energy that can potentially be converted to reactive species. Several approaches for TiO₂ band gap modification have been proposed: metal-ion implantation of TiO₂ with metal ions of transition metals (Cu, Co, Ni, Cr, Mn, Mo, Nb, V, Fe, Ru, Au, Ag, Pt),^{25,26} and doping TiO₂ with nonmetals (N, S, P).²⁷⁻²⁹ Composites of TiO₂ with semiconductors with a lower band gap energy (e.g., sensitization using CdS nanoparticles, heterostructures of Cu₂O/ZnO/TiO₂)^{30,31} have been prepared to further extend the region of light absorption.

Modifying pure photocatalyst materials with metal ions, especially d-block transition metal ions such as Fe³⁺ and Cr³⁺, causes the insertion of impurity energy levels between the parent conduction band and valence band (Figure 1.5). The inserted energy levels provide sub-band gaps inside the original band gap, and cause electron excitation at a lower energy than those required by pure TiO₂.²⁶ The resulting excitation could originate from the dopant d-band to the host conduction band or from the host valence band to the dopant d-band (Figure 1.5). As a result, photocatalytic reactions can be initiated by the absorption of photons with energy equal to or less than the band gap of the TiO₂. The electrons and holes for the excited state can recombine and dissipate the input energy as heat, get trapped in metastable surface states, or react with respective electron acceptors and electron donors adsorbed on the semiconductor surface or within the surrounding electrical double layer of the charged particles. The electrons and holes could therefore participate in redox reactions with water, hydroxide ion (OH⁻), organic pollutants or oxygen, leading to mineralization of the pollutants (e.g., CO₂ and H₂O), as the valence-band hole is strongly oxidizing while the conduction-band electron is strongly reducing. There are two routes through which OH⁻ radicals can be formed, i.e. by the reaction of the valence-band holes with either adsorbed H₂O or the surface OH groups on the TiO₂ particle. Depending upon the exact conditions, the holes, OH⁻ radicals, O₂⁻, H₂O₂ and O₂ itself can play important roles in the photocatalytic reaction mechanism.

However, several studies have indicated that doping could create structural defects that could become the sources of charge recombination, which creates a potentially negative effect.^{32,33} In some studies, co-doping with a conjugate metal cation pair is found to be more useful than single atom doping, because co-doping with a conjugate metal cation pair such as Rh³⁺/Sb⁵⁺ can preserve charge equality of the doped photocatalysts and result in improved and extended photocatalytic ability.³⁴ However, this may not necessarily prevent structural defects arising from the differences in cationic radii between the dopants and the host photocatalyst.

Doping with nonmetals such as N, C and S in TiO₂ could introduce impurity energy levels above the host valence band (Figure 1.5). Similar to metal doping strategies, anionic co-doping, e.g., involving N/F-TiO₂ or N/F- and C/N-ZnWO₄,³⁵ has been used to lower the charge defects, but the quantum efficiencies in many cases remain inferior when compared with the excited photocatalysts, because of the pronounced charge recombination at the dopant-induced defect sites.³⁶

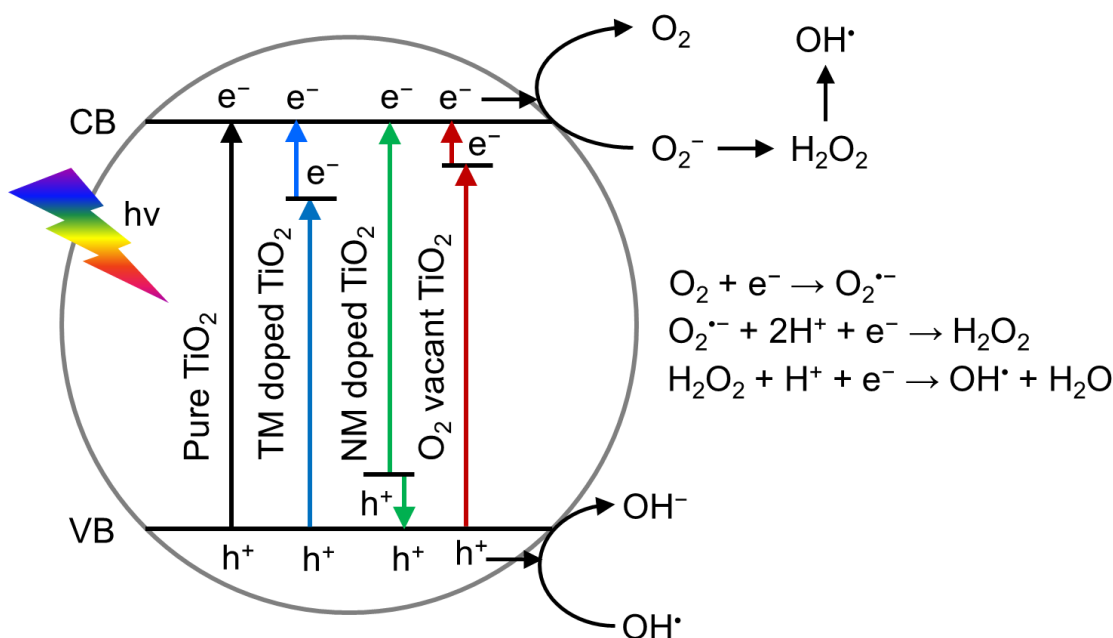


Figure 1.5 Schematic diagram of band gap engineering and mechanism of photocatalysis reactions for pure, transition-metal (TM) doped, non-metal (NM) doped, and oxygen vacancy defect-rich TiO₂.

Doping with transition metal and nonmetal ions therefore red-shifts the TiO₂ absorption from the UV to the visible region, but there are a number of challenges associated with the use of metal and nonmetal doping to improve the efficiency of the photocatalytic processes. Although the presence of metal and nonmetal dopants has been found to enhance charge separation in some cases and interfacial charge transfer in many other cases, the dopants could actually cause rapid charge recombination through their switchable redox states and/or by introduction of defects. For example, the reaction $\text{Fe}^{3+} + \text{e}^- \rightleftharpoons \text{Fe}^{2+}$ could reduce the photogenerated electron diffusion length and lifetime.³⁷ In recent studies, it has been found that extended photo-response may actually originate from the

color centers (a type of crystallographic defects in which an anionic vacancy in the crystal is filled by one or more unpaired electrons) and oxygen vacancies that arise from doping.³⁸

(b) Oxygen vacancy defects

Oxygen vacancies in TiO₂ can behave as both important adsorption and active sites for heterogeneous catalysis, which ultimately affect the reactivity of TiO₂.³⁹ Moreover, it has been found that the electronic structure,⁴⁰ charge transport,⁴¹ and surface properties of TiO₂ are closely related to the amount of oxygen vacancies.⁴² For example, the formation of oxygen vacancies in TiO₂ could lead to the creation of unpaired electrons or Ti³⁺ centers, which produce donor levels in the electronic structure of TiO₂ (Figure 1.5).⁴³ Both theoretical and experimental results suggest that the excess electrons located on the oxygen vacancy states could affect surface adsorption and the reactivity of key adsorbates such as O₂ or H₂O on TiO₂.⁴⁴ In addition, oxygen vacancies have been found to reduce the electron-hole recombination and increase the conductivity of TiO₂.⁴⁵

There are a number of methods to create oxygen vacancies in TiO₂ and other TCOs, including:

- thermal annealing in a hydrogen environment;
- high-energy particle bombardment;
- doping with metal and nonmetal ions; and
- thermal annealing under oxygen depleted conditions (i.e., in an inert environment).

Thermal annealing in a hydrogen environment. The interactions between H₂ and TiO₂ are different depending on the elevated temperature.⁴⁶ Below 300 °C, H₂ interacts physically with the adsorbed oxygen, which has been confirmed by the disappearance of the electron spin resonance signals of adsorbed oxygen. Above 300 °C, electrons from the hydrogen atoms are transferred to the oxygen atoms, and the oxygen atom from the surface of TiO₂ leaves with the H atom via the formation of H₂O. When the temperature is raised to 450 °C, the reaction between H₂ and TiO₂ proceeds more dramatically, by which the electrons of the H atoms are transferred to Ti⁴⁺ of TiO₂, creating Ti³⁺ defects. At 560 °C, the electrons located in the oxygen vacancy states are driven away and transferred to Ti⁴⁺, decreasing the amount of oxygen vacancies while increasing the amount of Ti³⁺. In addition, Ti interstitials are also found in the reduced TiO₂ matrix during annealing in hydrogen.⁴⁷ Ti interstitials do not affect the chemical and physical properties as much as oxygen vacancies.⁴⁸

High-energy particle bombardment. High-energy electron and ion impact can generate oxygen vacancies on the TiO₂ surface by preferentially removing oxygen ions and neutral atoms from

the surface.^{49,50} Electrons with energy greater than 34 eV can desorb surface oxygen atoms through an interatomic Auger recombination process.^{50,51} Similar to electron bombardment, ion sputtering (such as argon ion, Ar⁺) and plasma treatment (involving high-energy species such as electrons, ions, atoms and radicals) could also create oxygen vacancies on the surface of TiO₂.^{52,53} The disadvantage of these techniques is that oxygen vacancies are created exclusively in the surface region and can be easily healed by exposure to molecular oxygen even at low temperature.⁵³

Doping with metal and nonmetal ions. Doping of TiO₂ with metal or nonmetal ions also creates oxygen vacancies in TiO₂. For example, the substitution of Fe³⁺ for Ti⁴⁺ ions in the lattice can result in formation of oxygen vacancies in TiO₂.⁵⁴ However, it is generally difficult to control substitutional doping, and in most cases atoms are often found on the interstitial sites of the host lattice. These interstitial dopant atoms can act as recombination centres for photogenerated electrons and holes, which would become counterproductive to the performance.

Thermal annealing under oxygen depleted condition. Oxygen vacancies can also be created in pure TiO₂ by annealing at elevated temperature (generally >400 °C) in an inert environment, such as a pure He, N₂ or Ar atmosphere or in vacuum.^{52,55} The reduction of O₂ partial pressure generally increases the concentration of oxygen vacancies. However, the oxygen vacancies so produced are created mostly at the surface region, and they slowly disappear upon exposure to air, even at room temperature.

As all the aforementioned methods create oxygen vacancies mostly in the surface region, the performance of photoactivity of TiO₂ (and other TCOs) remains largely restricted to the surface oxygen vacancies of the nanostructures. While the development of a new method that will create oxygen vacancies in both the bulk and the surface region of the TCO nanostructures remains a big challenge, it is fundamentally important to nanoscience and is of great interest to nanotechnology applications.

(c) Developing defect-rich, single-crystalline TiO₂ nanostructures with high specific surface areas

For all catalyst materials, a high specific surface area is an essential physical attribute because this generally increases the number of active sites per unit area and therefore the reactivity. The smaller the particle size, the larger is the surface area with respect to the volume (i.e., the specific surface area), and therefore the higher is the activity for the same amount of material.⁵⁶ The 1D nanostructures, including nanowires, nanorods, nanobelts and nanofibers, have been extensively studied, because of their specific morphology and novel properties. In comparison with nanoparticles,

1D nanostructures not only inherit almost all of the typical features of nanoparticles, but also display new properties and improved performances in some specific areas,⁵⁷ when the diameter (along the radial dimension) of a 1D nanostructure is comparable to such important physical parameters as the exciton Bohr radius, the wavelength of incident light, and the phonon mean free path. In addition, the single crystallinity of a 1D nanostructure provides a highway for charge carrier transport along the axial direction.⁵⁸ In the present thesis, we will mainly focus on oxygen vacancy defect-rich, single-crystalline 1D TiO₂ nanostructures.

A variety of 1D TiO₂ nanostructures have been synthesized by both wet-chemistry and dry deposition techniques.⁵⁹ The wet-chemistry methods, including hydrothermal, sol-gel, anodization, and electrospinning, are efficient for mass production and they are capable of providing highly uniform products. However, these types of processes often require very precise control of the parameters of the solutions involved (e.g. concentrations of precursors and growth solutions, pH, viscosity, and growth temperature). As the precipitate precursors could contain unwanted contaminant species, additional removal and purification steps are required once the growth is complete. Additionally, post treatments such as cleaning, compaction, and sintering are often necessary to integrate these nanostructures into the final material product or a device, thus adding both cost and complexity to the process. The major disadvantage of the wet-chemistry synthesis is that the 1D nanostructures so obtained are invariably polycrystalline in nature (Figure 1.6).⁶⁰ The high resistance of these polycrystalline 1D nanostructures limits its photocatalytic and electronic applications.

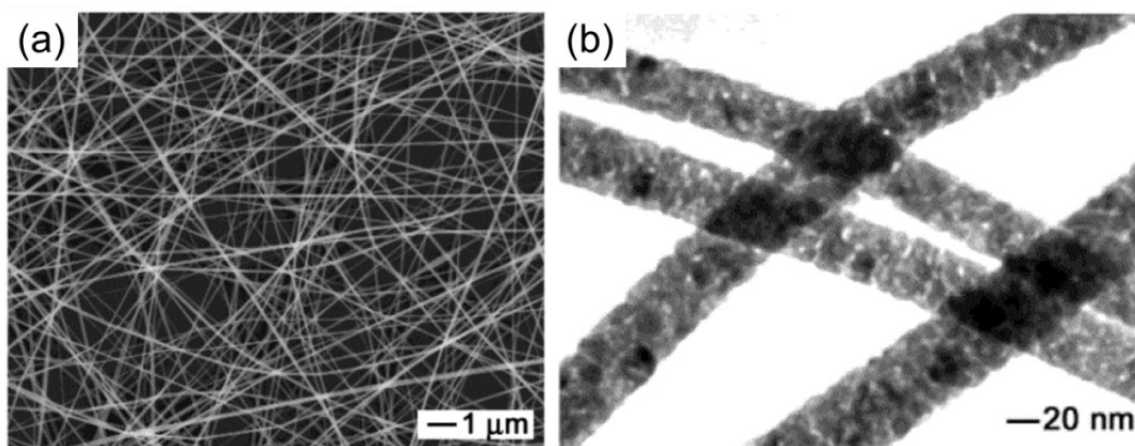


Figure 1.6 (a) SEM image and (b) TEM image of 1D TiO_2 nanostructure prepared by a typical wet-chemistry method. TEM image shows that the as-grown nanowires are composed of nanoparticles of TiO_2 .^{60**}

In contrast, nanostructures produced by dry deposition techniques that make use of gas-phase reactions as in chemical vapour deposition and thermal evaporation have several advantages over solution-based methods. As the nanostructures can often be grown directly onto a desired substrate, this allows for easy integration into an existing device or product during the manufacturing process. Additionally, the higher growth temperature often employed in these methods provides a higher degree of crystallinity, producing single-crystalline materials. As a tighter control over chemical reactants requires more precise gas flow in chemical vapour deposition, or the use of 100% pure source materials in thermal evaporation technique, more reproducible growth outcome can be achieved when compared to the wet-chemistry method. As a result, a number of vapor-phase assisted growth methods, including chemical vapor deposition and physical vapor deposition, have been developed for the preparation of high-quality 1D TiO_2 nanostructures on a desirable substrate.^{61,62}

Of the vapor-phase growth methods, the vapor-liquid-solid (VLS) growth mechanism⁶³ is the most widely used growth technique for synthesizing single-crystalline 1D nanostructures. Wagner and Ellis first used the VLS mechanism in 1964 to account for the growth of Si nanowhiskers using Au as the catalyst on a Si(111) substrate (Figure 1.7).⁶³ In the VLS growth method, a vaporized

** Reproduced with the permission from: Shi, J.; Wang, X. *Cryst. Growth Des.* **2011**, *11*, 949–954. Copyright (2003) by the American Chemical Society.

source material is used. A metal catalyst in the liquid phase provides preferential deposition sites for the vaporized source material, which enable the chemical adsorption and confinement required for one-dimensional growth. The liquid droplet, formed by the eutectic reactions between the source material and the catalyst, is prerequisite for the VLS growth. The vaporized source material initially adsorbed on the surface of the catalyst droplet is subsequently absorbed into the droplet. Once the amount of the source material has exceeded the finite solubility limit of the source material in the droplet, the excess source material diffuses to the liquid-solid interface of the substrate, creating nucleation sites for 1D nanostructural growth. The enhanced confinement of the vapor species on and into the liquid catalyst facilitates a higher reaction rate (of the constituents for nanostructure formation) at the liquid droplet than that of the surrounding area, confining the growth to one dimension. Upon cooling, the liquid catalyst solidifies, producing a cap at the tip of the nanostructure.

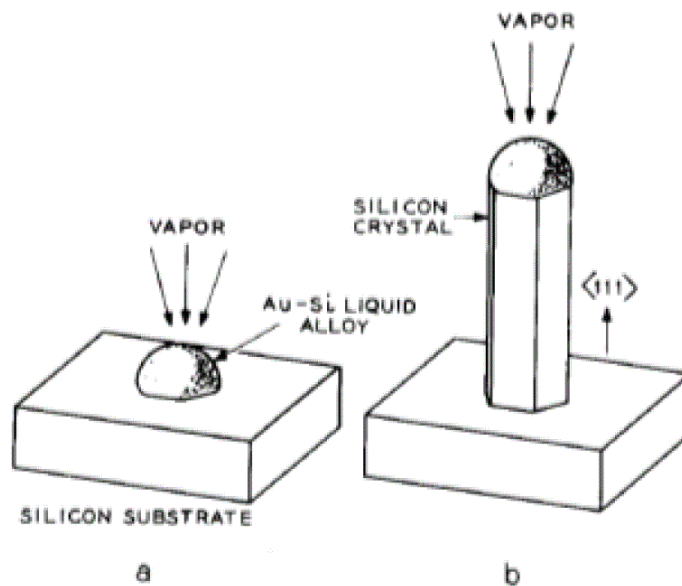


Figure 1.7 Schematic representation of the growth of Si nanowhiskers by the vapor-liquid-solid growth mechanism. (a) Initial droplet formation at the catalyst site. (b) Growth of nanowires with metallic alloy at the tip. ^{63††}

^{††} Reproduced with the permission from: Wagner, R. S.; Ellis, W. C. *Appl. Phys. Lett.* **1964**, *4*, 89–90. Copyright (1964) by the American Institute of Physics.

Similarly, TiO₂ nanowires have been grown by the VLS growth mechanism using Au as the liquid catalyst.⁶⁴ Due to the high melting points of Ti (1668 °C) and TiO₂ (1843 °C), a protective buffer layer (with thickness greater than 60 nm) is often employed to activate the substrate-sensitive catalyst, in order to grow the nanowire at high temperature by traditional vapour deposition techniques such as chemical vapour deposition and thermal evaporation. For example, a SiO₂, TiO₂ or TiN layer has been used as the buffer layer, on which a thin layer of Ni,⁶⁵⁻⁶⁸ Cu⁶⁹ or Au^{17,61} has been used as the catalysts to promote VLS growth of TiO₂ nanowires (on a Si substrate). However, the presence of a dielectric or insulating buffer layer that is too thick on a conductive substrate could have adverse effects on the growth characteristics,⁷⁰ oxygen vacancy,⁷¹ and charge collection efficiency,⁷² all of which could also negatively impact the electronic properties of the nanodevices. Controlled synthesis of a 1D TiO₂ nanostructure on a conductive substrate at a lower temperature with a buffer layer of an appropriately chosen thickness (<10 nm) by an alternative vapour deposition method is therefore extremely important for future technological applications.

As the lower charge collection efficiency⁷² of the dielectric or insulating buffer layer limits the application of VLS growth of 1D TiO₂ nanostructures, VLS-grown TiO₂ nanowires have not been studied for photoelectrochemical water splitting property. The reported work on photoelectrochemical water splitting property is mainly performed by using 1D TiO₂ nanostructures prepared by the aforementioned wet-chemistry (hydrothermal, sol-gel, electrospinning or anodization) methods.²³ Similar to TiO₂ thin films and nanoparticles, oxygen vacancies can also be created in 1D TiO₂ nanostructures by annealing in hydrogen. The hydrogen-treated TiO₂ nanowires with stable oxygen vacancies have been found to exhibit a photocurrent density 3.5 times that of pristine TiO₂ nanowires (Figure 1.8).¹² However, the incident-photon-to-current-conversion efficiency (IPCE) was found to be only 3% in the visible light region (> 400 nm). It is therefore extremely important to create oxygen vacancies in the bulk of TiO₂, instead of just the surface layer as obtained, e.g., by hydrogenation, in order to achieve high performance in the visible light region.

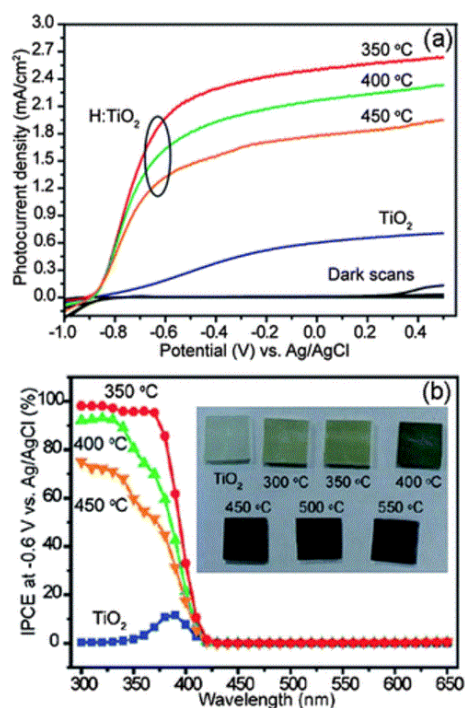


Figure 1.8 (a) Photocurrent densities and (b) IPCE spectra for the pristine TiO_2 nanowires, and TiO_2 nanowires after annealing in H_2 at 350, 400, and 450 $^\circ\text{C}$, as a function of applied potential vs. Ag/AgCl , along with their photographs (insets).^{12‡‡}

Of all the synthesis techniques of 1D nanostructures (hydrothermal, sol-gel, anodization, chemical vapour deposition, and thermal evaporation) and the post-treatment methods of creating the oxygen vacancies (hydrogen treatment, high-energy particle bombardment, doping, and thermal annealing in reduced oxygen pressure), the majority of the defects are created within the surface region (a few nanometers from the surface) of these nanostructures. Although the overall reactivity can be increased due to the higher specific surface area, improved light harvesting ability, and enhanced charge transfer property of these 1D TiO_2 nanostructures (i.e., less recombination), especially when compared to (planar) thin films and nanoparticles, the photocatalytic activity is still limited to just the ultraviolet region of the solar spectrum due to the large band gaps. To overcome this critical shortcoming, it is therefore important to introduce appropriate band gap states in order to capture the visible light and to enhance its efficiency in this region. New synthetic methods that are

^{‡‡} Reprinted with the permission from: Wang, G.; Wang, H.; Ling, Y.; Tang, Y.; Yang, X.; Fitzmorris, R. C.; Wang, C.; Zhang, J. Z.; Li, Y. *Nano Lett.* **2011**, *11*, 3026–3033. Copyright (2011) by the American Chemical Society.

capable of inherently creating oxygen vacancy defects inside the 1D nanostructures, along with capability to introduce such rough surface morphologies as corrugated nanowires, nanocrystal-decorated nanowires, and hierarchical nanowires would therefore be highly desirable. These methods will provide novel photocatalysts capable of absorption of more visible light (due to more defect states in the band gap) and provision for more reaction sites, both of which would ultimately improve the photoelectrochemical water splitting reaction performance in the visible light region.

1.2.2 ZrO₂ as a photocatalyst for photoelectrochemical water oxidation

1.2.2.1 Properties of stoichiometric ZrO₂ nanostructures

ZrO₂ is known to occur in three polymorphs at atmospheric pressure: the monoclinic, tetragonal, and cubic phases.⁷³ At room temperature, the most stable phase of ZrO₂ is the monoclinic phase, which occurs naturally as the mineral Baddeleyite, and is stable up to ~1478 K. At 1480 K and ambient pressure, the tetragonal phase becomes thermodynamically stable, and it transforms into the cubic calcium fluoride structure at 2650 K. The crystal structures of these polymorphs are shown in Figure 1.9. Evidently, the tetragonal and the monoclinic structures can be considered as distorted cubic structures. Both tetragonal and cubic phases can be stabilized at lower temperature by reducing the crystallite size and by introducing phase-stabilizing impurities in the bulk and at the crystal surface.^{74,75} The zirconium-oxygen phase diagram is shown in Figure 1.10. Like TiO₂, ZrO₂ can be reduced easily, and the Zr-O phase diagram¹⁸ is very rich with multiple stable phases containing a variety of crystal structures. The reduced monoclinic and tetragonal ZrO₂ nanostructures are the focus of the present study.

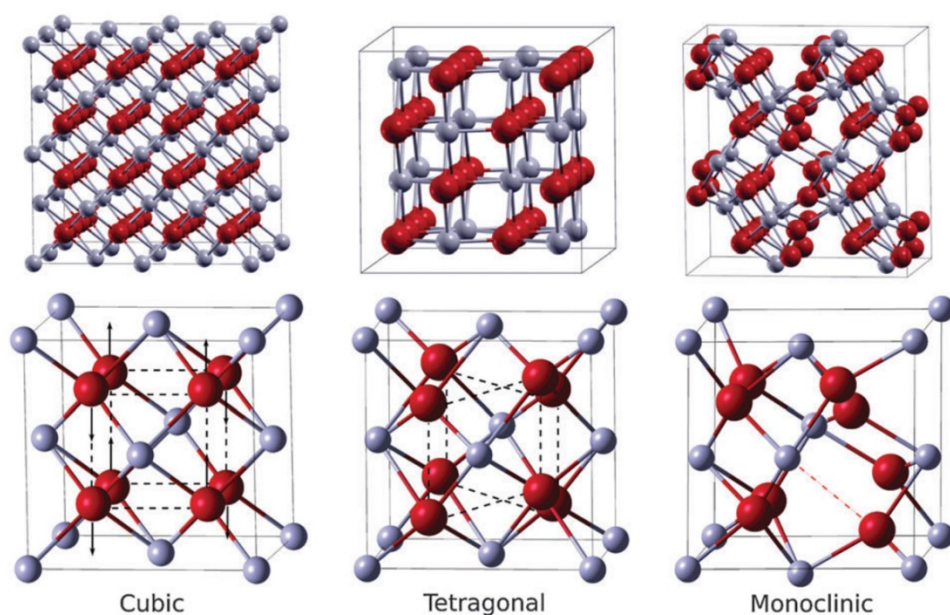


Figure 1.9 Cubic, tetragonal and monoclinic ZrO_2 lattice structures (lower panel). In the upper panel, the individual polymorph cells are space-expanded to provide a better view of the three different phases. In the lower panel, the cubic cell is taken as reference to show the deformation of the oxygen sublattice for tetragonal and monoclinic ZrO_2 (dashed lines and arrows). Large dark red spheres and small light grey spheres represent O and Zr atoms, respectively.^{76§§}

^{§§} Reproduced with the permission from: Gallino, F.; Valentin, C. Di; Pacchioni, G. *Phys. Chem. Chem. Phys.* **2011**, *13*, 17667–17675. Copyright (2011) by the Royal Society of Chemistry.

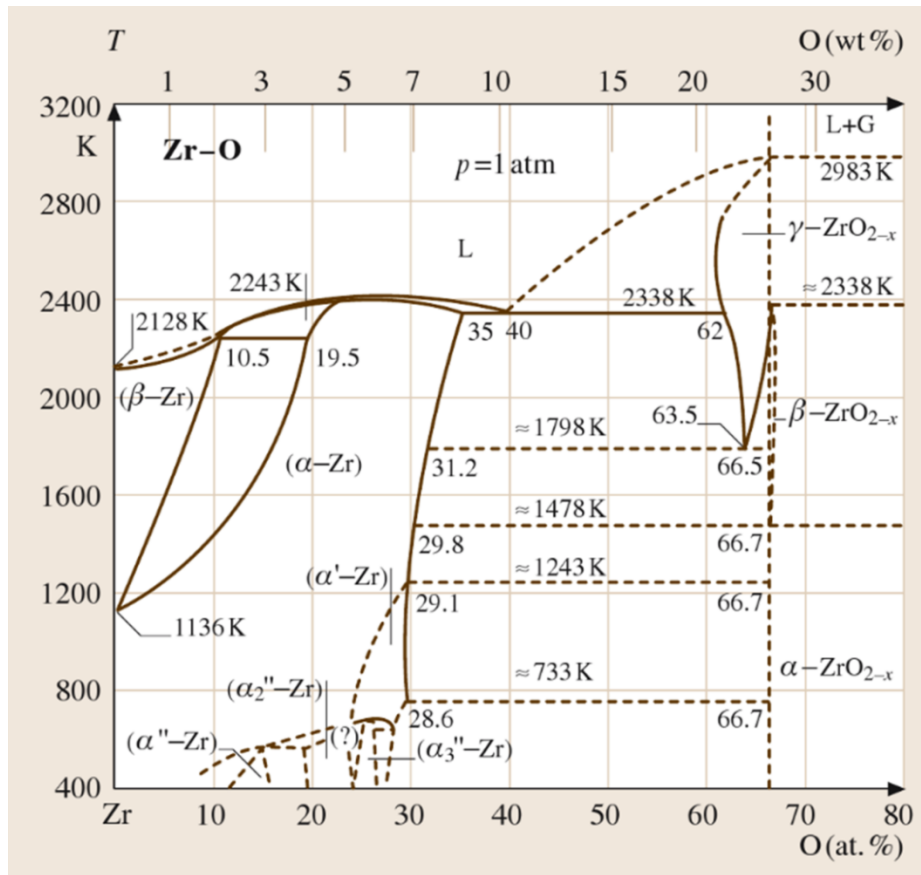


Figure 1.10 Zr-O phase diagram. At room temperature, zirconium exhibits a hexagonally close packed crystal structure, α -Zr, which changes to β -Zr, a body-centered cubic crystal structure, at 1163 K. Zirconium exists in the β -phase until the melting point. The phase transitions between the monoclinic and tetragonal phases and between the tetragonal and cubic phases are observed at 1478 K and 2650 K, respectively.^{18***}

Zirconium oxide is currently used in a variety of applications, for example, as a solid electrolyte in oxygen sensors⁷⁷ and solid oxide fuel cells operating at low temperatures,⁷⁸ thermal barrier coatings for gas turbine jet engines,⁷⁹ host material for nuclear waste containment,⁸⁰ as a gate dielectric material in metal-oxide semiconductor devices (generally in combination with hafnium),⁸¹ and as a catalytic support medium.⁸² As stoichiometric ZrO_2 has a band gap (monoclinic

*** Reproduced with the permission from: Warlimont, H.; Martienssen, W. (Eds.). Springer Handbook of Condensed Matter and Materials Data; Springer: Berlin, 2005. Copyright (2005) by the Springer Berlin Heidelberg.

4.99 eV, tetragonal 5.56 eV, cubic 4.62 eV)⁸³ considerably higher than TiO₂ (rutile 3.0 eV, anatase 3.4 eV, and brookite 3.3 eV), ZrO₂ can only be used as photocatalysts under UV light irradiation and its application in visible-light-driven photocatalysis is severely limited.

1.2.2.2 Strategies to improve the visible light activity of ZrO₂ nanostructures

(a) Doping

In order to improve the visible-light-driven photocatalytic water splitting performance, the impurity band created by the defects (introduced by dopants or hydrogen annealing) inside the host band structure should satisfy two criteria: a conduction band minimum sufficiently negative for H₂ generation and a band gap sufficiently narrow for the absorption of visible light. The band gap of ZrO₂ could be effectively reduced by doping with a variety of metal elements, such as Cr, Mn, Fe, Co and Ni.^{84–86} However, due to the hybridization of the atomic orbitals, almost all of the transition metal dopants in ZrO₂ creates impurity bands far below the redox potentials of water splitting (0 V versus NHE) (Figure 1.11).⁸⁷ As oxygen vacancies usually create an impurity band just below the conduction band minimum, in contrast to the deep donor band produced by the transition metal dopants, introducing oxygen vacancy defects into ZrO₂ could therefore provide an important solution to the above problem. Active efforts should therefore be placed on band gap narrowing of ZrO₂.

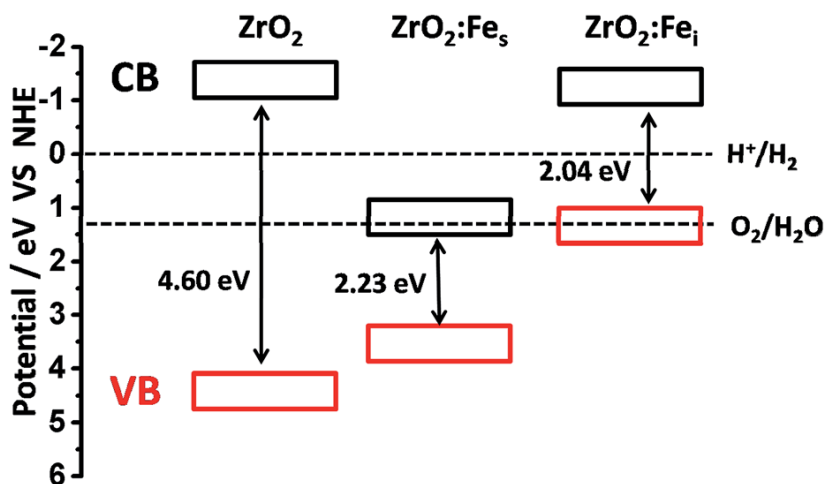


Figure 1.11 Calculated band-edge positions of pure ZrO₂, ZrO₂:Fe_s, and ZrO₂:Fe_i. ZrO₂:Fe_s and ZrO₂:Fe_i represent ZrO₂ doped with Fe atoms in substitutional and interstitial positions, respectively.^{87†††}

††† Reprinted with the permission from: Xiao, M.; Li, Y.; Lu, Y.; Ye, Z. *J. Mater. Chem. A* **2015**, *3*, 2701–2706. Copyright (2015) by the Royal Society of Chemistry.

(b) Developing defect-rich single-crystalline ZrO_2 nanostructures with high specific surface areas

Several wet-chemistry methods, including sol-gel,⁸⁸⁻⁹⁰ precipitation,⁹¹⁻⁹³ and hydrothermal synthesis,^{94,95} have been developed for the preparation of ZrO_2 powder nanomaterials and thin films.^{94,95} These methods all require long reaction times and post-annealing at high temperature to complete the crystallization of ZrO_2 . Dry deposition methods such as sputtering,⁹⁶ chemical vapor deposition,⁹⁷ atomic layer deposition,⁹⁸ liquid phase deposition,⁹⁹ and pulsed laser deposition¹⁰⁰ have also been used for the preparation of thin films of ZrO_2 . For 1D ZrO_2 nanostructures, there have been only a few reports about their synthesis, which include two-step anodization of superimposed Al/Zr films,¹⁰¹ hydrolysis and condensation of zirconium sol on tubular alumina template,^{101,102} and chemical vapour deposition of ZrCl_4 powders at 1000 °C.¹⁰³ As an example, Figure 1.12 illustrates the basic procedure of fabricating integrated arrays of highly ordered zirconia nanowires by tubular alumina template.¹⁰¹ Superimposed Al/Zr layers sputter-deposited on glass substrates were used as the starting specimen (Figure 1.12 A-a). The specimen was then subjected to a constant-potential anodization in a strong acidic electrolyte (Figure 1.12 A-b). Upon complete Al anodization, a highly ordered porous anodic alumina film with the desired pore dimension was obtained. This was then followed by a second constant-current anodization in a weak acid electrolyte to produce a zirconia nanowire array due to the highly anti-corrosive nature of Zr metal. Confining Zr anodization to only the pore base of the porous anodic alumina film allowed the external growth of solid zirconia along these alumina nanopores (Figure 1.12 A-c). Finally, the porous anodic alumina template was selectively removed by chemical etching to expose the integrated zirconia nanowire array on glass (Figure 1.12 A-d). The resulting zirconia nanowire template exhibits an average nanowire diameter of 40 nm and a pitch spacing of 120 nm, and the nanowires reach a height of 310 nm, with a height-to-diameter aspect ratio of 7.75 (Figure 1.12 B). However, the major disadvantages of this¹⁰¹ and other methods such as hydrolysis and condensation of zirconium sol (sol-gel) on tubular alumina template¹⁰² are that the as-grown nanowires are polycrystalline and the precursor materials are incorporated into the final structure as impurities.

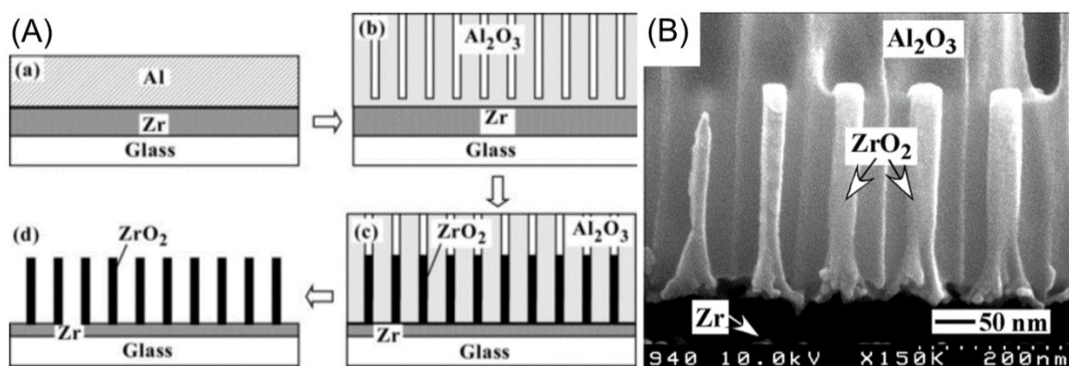


Figure 1.12 (A) Schematic drawing of the fabrication procedure of zirconia nanowire arrays on glass substrates by a tailored two-step anodization process. (B) Scanning electron micrograph of a fractured cross-section of a highly ordered anodic zirconia nanowire array partially embedded in a porous alumina film.^{101†††}

In the case of dry deposition methods, ZrO₂ nanowires grown by chemical vapour deposition¹⁰³ (involving ZrCl₄ powders at 1000 °C) were found to be amorphous. In addition, due to extremely low vapour pressure and high melting point of ZrO₂,¹⁰⁴ the vapour-liquid-solid (VLS) growth⁷¹ of 1D ZrO₂ nanostructures by traditional chemical vapour deposition and thermal evaporation techniques, as two of the most promising and reproducible growth methods to prepare highly crystalline 1D nanostructures, has not been successful. It is therefore important to develop an alternative vapour deposition technique for producing 1D nanostructures by the VLS growth mechanism at lower temperature than the traditional vapour deposition techniques.

The pulsed laser deposition technique can be a suitable solution for this problem due to its many unique advantages over other dry deposition methods. Unlike thermal evaporation and chemical vapor deposition, pulsed laser deposition involves direct laser ablation of the target material into the gaseous form without affecting its stoichiometry. The absorption of a high-intensity laser energy pulse by a small volume of target material leads to vaporization in the thermally non-equilibrium regime. As a result, activation of the catalyst could occur at a lower temperature, thus allowing the formation of 1D nanostructures at a lower temperature than other vapour deposition methods. Furthermore, variable substrate temperature, oxygen partial pressure and reductive growth

††† Reprinted with the permission from: Chu, S.-Z.; Wada, K.; Inoue, S.; Segawa, H. *J. Electrochem. Soc.* **2011**, *158*, C148. Copyright (2011) by the Electrochemical Society.

environment during pulsed laser deposition growth can be used to control not only the rate of deposition but also the morphology and the amount of oxygen-related defects.¹⁰⁵

There has been no study on the photoelectrochemical properties of oxygen vacancy defect-rich, single-crystalline 1D ZrO₂ nanostructures. These reduced ZrO₂ 1D nanostructures are expected to show similar advantages (such as enhanced electron transport properties, reduced charge-carrier recombination, and visible-light driven photoactivity) as oxygen-deficient 1D TiO₂ nanostructures, discussed above. Intense efforts should therefore be made to synthesize single-crystalline 1D ZrO₂ nanostructures in order to achieve the optimum performance for photocatalysis and other technological applications.

1.3 Transparent dilute ferromagnetic semiconductor oxides

1.3.1 Prospects and challenges in the development of transparent dilute ferromagnetic semiconductor oxides

In most semiconductor devices, the charge of the electron is used to carry and transport information. If the semiconducting material is ferromagnetic, the electron spin of this material can also be exploited. The use of both charge and spin of the semiconductor material would provide an additional degree of freedom for building novel electronic devices, where logic and memory operations could in principle be seamlessly integrated onto a single device. One of the most interesting new magnetic materials to emerge in the past few years is dilute ferromagnetic semiconductors with Curie temperatures (T_c) well above room temperature. This family of materials encompasses traditional binary and tertiary semiconductors and wide-bandgap semiconductor oxides, in which a sizable portion of the host lattice atoms are substituted by transition metals or rare earth metals (lanthanides), producing localized magnetic moments in the semiconductor matrix. Usually, the magnetic moments are originated from the 3d and 4f open shells of the transition metal and rare earth metal atoms, respectively. Some examples of dilute magnetic semiconductors are Ga_{1-x}Mn_xAs, Cd_{1-x}Co_xTe, Pb_{1-x}Eu_xTe, and transition-metal-doped TiO₂, ZrO₂, and ZnO.¹⁰⁶⁻¹⁰⁸ It has been suggested that a strong spin-dependent coupling between the band structures and localized states accounts for the giant spin splitting of the electronic states, formation of magnetic polarons, and exchange interactions between the magnetic moments.¹⁰⁹ Owing to the possibility of controlling and probing the magnetic properties by manipulating the electronic subsystems of the band structures, dilute magnetic

semiconductors have become a fertile testing ground for investigating a number of fundamental questions about the nature of the exchange interactions between electrons of the band structures and of the localized states.¹¹⁰

In 1970s, Manganese has been employed in growing bulk II-VI Mn-based alloys by various modifications of the Bridgman method (a single-crystal growth method).¹¹¹ Research on dilute ferromagnetic semiconductors has since been extended to materials containing magnetic elements other than Mn and to other host semiconductors, including group IV elemental semiconductors as well as III-VI, IV-VI and III-V compound semiconductors.¹¹²⁻¹¹⁴ In early 1990s, there was rapid progress in dilute ferromagnetic semiconductor research as the result of development of crystal growth methods that could produce crystals far from thermal equilibrium. These methods include molecular beam epitaxy and laser ablation, and they have made it possible to synthesize dilute ferromagnetic semiconductors with the content of the magnetic impurity beyond the solubility limits of thermal equilibrium.¹¹⁵ For example, low-temperature molecular beam epitaxy has been used to produce thin films of $\text{Ga}_{1-x}\text{Mn}_x\text{As}$ with x up to 0.07 and the hole concentration in excess of 10^{20} cm^{-3} , the ferromagnetic ordering of which has been observed up to 173 K.¹¹⁶

In 2000, a theoretical study suggested that high-temperature ferromagnetism could be possible in Mn-doped ZnO (a wide-bandgap semiconductor oxide).¹¹⁷ Soon thereafter, it was proposed that the entire series of transition metals could be used to partially substitute for Zn in ZnO to produce room-temperature ferromagnetism,¹¹⁸ and the experimental evidence for this system was later obtained in 2003.¹¹⁹ The first experimental evidence for room-temperature ferromagnetism was, however, obtained in laser-ablated Co-doped TiO_2 thin films in 2001.¹²⁰ However, the observed magnetic moment was very small, $0.3 \mu_B$ per Co atom. Since then, a lot of studies have been carried out for doped transparent conductive oxide thin films, in search of materials that might exhibit a large magnetic moment at or above room temperature.^{114,121}

The most studied system is transition metal-doped TiO_2 thin films.¹²² All of the transition metal-doped TiO_2 thin films have been found to be ferromagnetic above room temperature, and the observed magnetic moments are quite large (Figure 1.13). The largest value of $4.2 \mu_B$ per dopant atom found for V-doped TiO_2 films (Figure 1.13, inset) is particularly noteworthy because vanadium atom itself is known to be nonmagnetic. This suggests that the observed ferromagnetism must therefore be of intrinsic nature and not due to the dopants. Similarly, In_2O_3 thin films doped with V or Cr also showed room-temperature ferromagnetic behaviour.¹²³ Since V and Cr metals are themselves

nonmagnetic, it is therefore unlikely that the ferromagnetism observed in the V or Cr-doped In_2O_3 films could come from the dopant metals even if they were to form localized clusters.

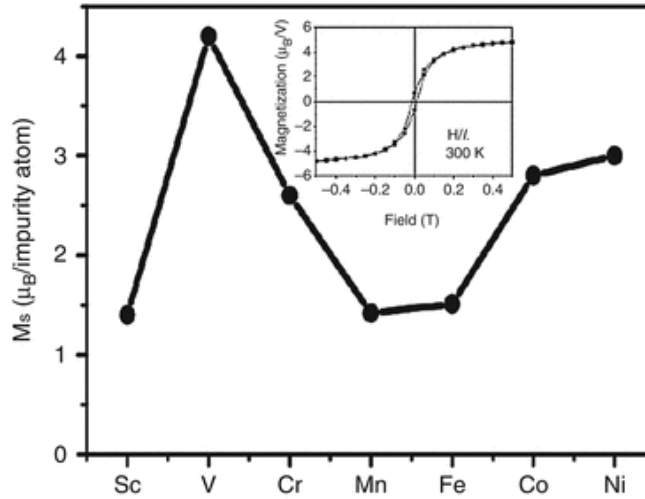


Figure 1.13 Saturated magnetization (at 300 K) for transition metal-doped TiO_2 thin films grown on a LaAlO_3 substrate at 923 K. The inset shows the magnetization curve taken at 300 K for a V-doped TiO_2 film (with the magnetic field applied parallel to the surface of the film).^{122§§§}

Growth conditions have been found to affect and can therefore be used to tune the magnetic properties of dilute ferromagnetic semiconductor oxides. The saturation magnetization for V-doped ZnO thin films obtained with the growth temperature increased by only 50 °C have been reported to increase by an order of magnitude.¹²⁴ In a separate study, it has been found for Mn-doped ZnO ($\text{Zn}_{0.9}\text{Mn}_{0.1}\text{O}$) thin films that the growth temperature and oxygen partial pressure during the deposition could be used to control the ferromagnetism.¹²⁵ For instance, the film grown at 650 °C with an oxygen pressure of 0.1 Torr was found to be ferromagnetic, while no ferromagnetism has been observed for the film grown at 400 °C with an oxygen pressure of 10^{-6} Torr. These results therefore suggest that instead of dopants, the growth conditions (growth temperature and oxygen pressure) might provide the necessary defects and/or oxygen vacancies to effect the observed ferromagnetism. This hypothesis is in accord with the theoretical report that vacancies are the necessary ingredient to create additional bands inside the semiconductor band structure that are

^{§§§} Reproduced with permission from: Hong, N. H.; Sakai, J.; Prellier, W.; Hassini, A.; Ruyter, A.; Gervais, F. *Phys. Rev. B* **2004**, *70*, 195204. Copyright (2004) by the American Physical Society.

responsible for ferromagnetism.¹²⁶ To further confirm the role of transition metal dopants as the ferromagnetic impurities in transition metal doped-semiconducting thin films, a series of X-ray absorption spectroscopy¹²⁷ and X-ray magnetic circular dichroism measurements¹²⁸ on Cr-, Mn-, or Co-doped TiO₂ films were carried out at the Cr, Mn, and Co $L_{2,3}$ edges.¹²⁹ These results reveal the paramagnetic behaviour of dopants (Cr, Mn, and Co) in these Cr-, Mn-, or Co-doped TiO₂ films,¹²⁹ and the observed ferromagnetic signal must therefore come from defects in the doped matrix. Very similar results have also been obtained for the Co-doped ZnO film, with the Co contribution to the magnetic property of the doped film found to be paramagnetic.¹³⁰ More importantly, while annealing in oxygen could evidently improve the crystallinity of the Cr-doped ZnO film, this post-growth treatment also reduced the ferromagnetic ordering.¹³¹ In this system, improving the crystallinity (elimination of structural imperfection) and removing oxygen vacancies both greatly degrade ferromagnetism. Indeed, structural defects and oxygen vacancies must play a critical role in tuning the ferromagnetic behaviour in doped transparent dilute ferromagnetic semiconductor oxides (TDFSOs). These results therefore suggest that the ferromagnetism of TDFSOs does not depend appreciably on the type and concentration of dopants. Indeed, it is the oxygen vacancy defects, induced by the presence of dopants, that mainly control the ferromagnetic ordering in doped TDFSOs.

Very similar results were also obtained for undoped TDFSOs. The observed ferromagnetism is induced by structural defects and/or oxygen vacancies that are formed mostly at or near the surface of the thin films^{5,132,133} and powder nanomaterials.¹³⁴⁻¹³⁶ In addition, the effect of confinement as imposed by the nanostructure also plays an important role in ferromagnetic ordering.^{134,137} For example, a 10 nm-thick ZnO film was found to exhibit almost 200 times higher saturation magnetization than a 375 nm-thick ZnO film.¹³⁷ In other cases, a specific crystal phase⁵ and the amount of oxygen vacancy defects^{134,137} are found to be the dominant factors for ferromagnetic ordering in a particular nanostructure.⁵ For example, ferromagnetism has been observed only in tetragonal ZrO₂ thin films, but not in monoclinic ZrO₂ thin films (Figure 1.14). In almost all the thin films and powder nanomaterials, the ferromagnetic ordering has been found to increase with increasing oxygen vacancy concentration.^{134,137}

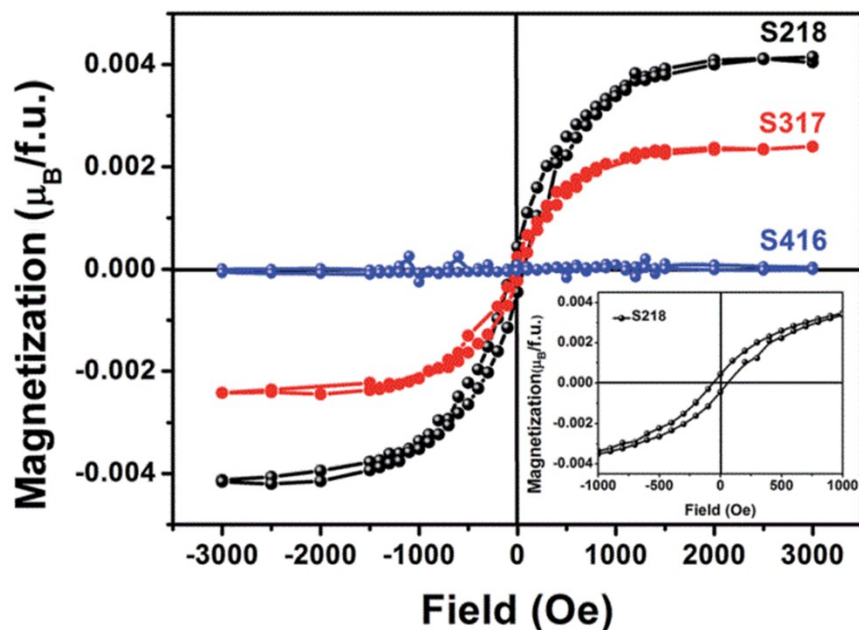


Figure 1.14 Magnetization vs magnetic field curves for ZrO₂ thin films with different crystal phases: S218 – completely tetragonal ZrO₂, S317 – mixture of monoclinic and tetragonal ZrO₂, and S416 – completely monoclinic ZrO₂. Inset shows the enlarged hysteresis loop of S218.^{5****}

1.3.2 Existing models of ferromagnetism in TDFSOs

To date, the mechanism that governs the magnetic interactions in the transparent dilute ferromagnetic semiconductor oxide (TDFS) systems is far from clear, and it remains under intense debate.^{131,138,139} The discovery of ferromagnetism in oxygen vacancy defect-rich ZrO₂,⁵ TiO₂,¹³² and ZnO¹⁴⁰ thin films and powder nanomaterials have attracted special attention in the field of nanoscale magnetism, which begs the key question: Is doping really necessary for introducing ferromagnetism in these materials? Or rather, does doping really just enhance the magnetism that already exists in the oxide host in the form of a thin film or nanoparticle? Furthermore, as the observed ferromagnetism could only be found in low-dimensional systems, the role of confinement effects should not be overlooked.

To explain the ferromagnetism in TDFSs, various models have been proposed. The very first model for doped TDFSs considered that the dopant cations (with d electrons) have well-

**** Reproduced with the permission from: Ning, S.; Zhang, Z. *RSC Adv.* **2015**, *5*, 3636–3641. Copyright (2015) by the Royal Society of Chemistry.

localized magnetic moments and they couple with each other ferromagnetically (i.e., through long-range-ordered interactions) via the $2p$ holes or $4s$ electrons of the valence band.¹¹⁷ As the dopants in semiconducting oxides could have a paramagnetic moment, this model does not seem to work for ferromagnetism in TDFSOs. In addition, given the very small amount of dopants (a few percent), it is unlikely that the exchange interaction could be that significant. On the other hand, the observed magnetization has been reported to be independent of the dopant concentration,^{129,130} which suggests that the Ruderman-Kittel-Kasuya-Yosida interaction may not be the main cause of ferromagnetism in TDFSOs. This model therefore fails to explain the origin of ferromagnetism in TDFSOs.

In the so-called polaron percolation model, the defects in doped TDFSOs are taken into account.¹⁴¹ The model treats the carriers (of the host semiconductor and dopants) as localized carriers in a semiconductor impurity band, in contrast to the free-carrier mean-field approach.^{142,143} Exchange interaction of the host semiconductor localized holes with magnetic impurities leads to the formation of bound magnetic polarons (Figure 1.15).^{109,144,145} This model is also applicable to host semiconductor localized electrons (not just to localized holes). Since the concentration of magnetic impurities is much larger than the hole concentration, a bound magnetic polaron consists of one localized hole surrounded by a large number of magnetic impurities. The localized holes of these polarons act on the magnetic impurities surrounding them, thus producing an effective magnetic field for these impurities. An energy minimum is reached when the impurity spins become parallel to the spins of localized holes. At sufficiently low temperature, the system could therefore reach a state in which the neighbouring magnetic polarons start to overlap and interact with each other via interaction with impurities between them (as illustrated by lens-shaped region in Figure 1.15). A ferromagnetic transition would occur when the cluster of correlated polarons reaches the size of the sample (the so-called infinite cluster limit). However, this model cannot explain how T_C in dilute ferromagnetic semiconductor oxides can become so high or how semiconducting oxides without any transition metal dopants (i.e. without any d electrons) can be ferromagnetic.

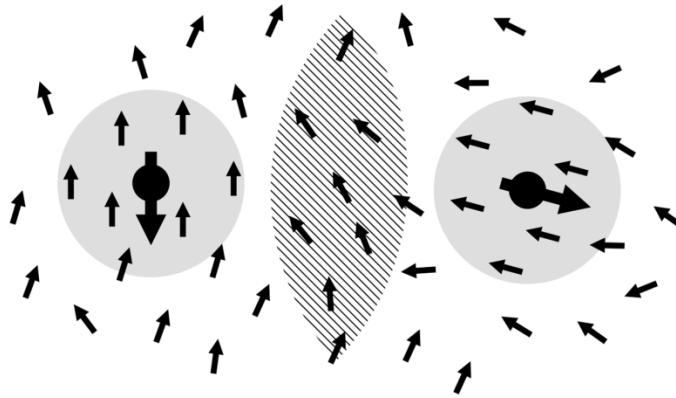


Figure 1.15 Interaction of two magnetic polarons. The polarons are shown as grey circles, while the small and large arrows represent impurity and holes spins, respectively.^{141††††}

Very recently, a new model has been proposed to explain the ferromagnetism in defect-rich semiconducting oxides. This so-called charge transfer ferromagnetism model is based on an impurity band introduced by defects, with the assumption that the presence of a charge reservoir in the system would facilitate hopping of electrons to or from the impurity band leading to spin splitting (Figure 1.16).¹⁴⁶ For dilute ferromagnetic semiconducting oxides, this reservoir is also consistent with doped semiconducting oxides (such as Mn-doped ZnO). However, this model still cannot explain how ferromagnetism could occur in undoped TCOs such as HfO₂, TiO₂, ZnO, SnO₂, because of the absence of a charge reservoir in these pristine oxides.

^{††††} Reproduced with the permission from: Kaminski, A.; Das Sarma, S. *Phys. Rev. Lett.* **2002**, *88*, 247202. Copyright (2002) by the American Physical Society.

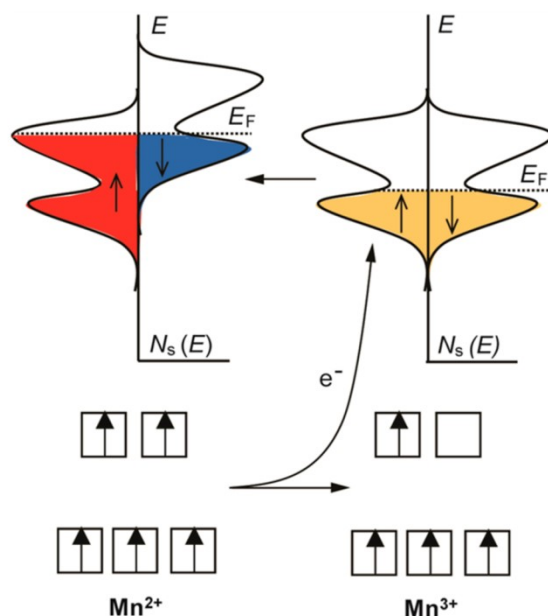


Figure 1.16 Schematic representation of the proposed charge-transfer ferromagnetism model for TDFSOs containing mixed-valence transition metal dopants such as manganese. This mechanism involves electron transfer from Mn^{2+} to the local density of states ($N_s(E)$) associated with the interfacial structural defects, raising the Fermi level to a peak in $N_s(E)$ and causing Stoner splitting (an exchange interaction that splits the energy of states with different spins and states near the Fermi level are polarized) of the defect band (indicated with red and blue colors).^{143****}

While all of the aforementioned models could account for some aspects of the observed ferromagnetism in these intriguing materials, a complete picture of the origin of ferromagnetism in pure (i.e. undoped) dilute ferromagnetic semiconducting oxides remains unclear. While one particular model could account for observation in one system (such as doped semiconducting oxides), it fails to explain the other systems (such as undoped semiconducting oxides). This area of research therefore represents one of the most interesting and challenging areas in nanomagnetism and is an exciting area in nanoscience in general. Fundamental understanding of the origin of ferromagnetism in these important materials promises new advances in spin-based applications including spinelectronics, quantum information processing, and targeted drug delivery and biomonitoring.

**** Reproduced with the permission from: Farvid, S. S.; Sabergharesou, T.; Hutfluss, L. N.; Hegde, M.; Prouzet, E.; Radovanovic, P. V. *J. Am. Chem. Soc.* **2014**, *136*, 7669–7679. Copyright (2014) by the American Chemical Society.

1.4 Motivations and Scope of the Thesis

Among all the defects identified in TCOs, oxygen vacancy is found to be one of the most important and is supposed to be the prevalent defect, as the properties of TCOs, including its light absorption, charge transport, photocatalytic performance, and magnetic properties, are all closely related to oxygen vacancy defects. For these reasons, there is a great interest in the development of controllable synthesis of TCO nanostructures rich with oxygen vacancy defects. As discussed in Section 1.2.2.2, reduced TiO_2 with oxygen vacancies can be produced by hydrogen thermal treatment, high-energy particle bombardment or thermal annealing under oxygen depleted condition, by which oxygen vacancies can be effectively created on the surface of TiO_2 . However, surface oxygen vacancies are not stable and are susceptible to oxidation upon long-term exposure to air or by dissolved oxygen in water. For this reason, creating oxygen vacancies in the bulk of TiO_2 offers a superior approach to achieve a stable reduced TiO_2 photocatalyst. In addition, the dependence of properties, such as optical, photoelectrochemical, and magnetic properties, on the surface morphology, and oxygen vacancy defects of the one dimensional TCOs are also not well understood. Further efforts are required to rationally engineer the oxygen vacancy defects in TCOs, with the goal to manipulate its properties deemed desirable for advancing magnetic and energy-related applications.

In the present work, we use catalyst-assisted pulsed laser deposition method for the synthesis of oxygen vacancy-rich 1D TiO_2 and ZrO_2 nanostructures on Si substrates. The use of a high vacuum system, and precise control of the gold nanoisland size, interfacial SiO_2 layer thickness, growth temperature and Ar flow have enabled us to produce, for the first time, oxygen vacancy-rich, single-crystalline nanostructured films with different morphologies and composition of oxygen vacancy defects (neutral, singly charged, and doubly charged defects) in one step. A series of detailed studies are performed to optimize the growth morphology, amounts and composition of oxygen vacancy defects, and to understand the underlying growth mechanism (vapour-liquid-solid versus vapour-solid growth) of different nanostructures, including TiO_2 nanobelts, nanosheets, and nanowires (corrugated, straight, and TiO_2 nanocrystal decorated), and ZrO_2 nanopopcorns, nanospikes, and nanowires (regular and hierarchical). Our objectives are two-fold: (a) to develop fundamental understanding of their structure-property relations through precise control of the growth parameters, and (b) to exploit the novel properties of these defect-rich nanostructures for visible-light driven photoelectrochemical water splitting and spin-dependent magnetic properties.

After a brief introduction to the general properties of defect-rich 1D TiO₂ and ZrO₂ nanostructures and their synthesis methodologies (Chapter 1) and a short description of the experimental setup and characterization techniques used in this work (Chapter 2), we present the results of three different studies on oxygen vacancy defect-rich TiO₂ and ZrO₂ nanostructures. In the Chapter 3, we report the controlled growth of 1D TiO₂ nanostructures with different morphologies and with incorporation of oxygen vacancy defects on a Si substrate by a one-step, catalyst-assisted pulsed laser deposition method. By manipulating the thickness of the SiO₂ buffer layer, together with optimized growth temperature and growth environment, we are able to synthesize TiO₂ nanobelts, corrugated nanowires, straight nanowires, and tapered TiO₂ nanowires decorated with TiO₂ nanocrystallites. We demonstrate direct correlation between morphology, oxygen vacancy defects, and the photoelectrochemical water splitting properties. The different amounts of oxygen vacancies of the as-grown nanostructured films cause their colour to change from lighter blue for nanobelts to deep blue for straight nanowires and to greyish black for decorated nanowires. Photoelectrochemical water splitting measurement under simulated sunlight shows that the decorated nanowires provide one of the highest anodic photocurrent densities of TiO₂ nanomaterials reported to date. We further demonstrate that the decorated nanowires exhibit the highest photoactivity in the visible region (>430 nm), which represents 87% of the overall photocurrent. The higher activity in the visible region can be attributed to the more conductive TiO₂ nanostructures (i.e., with a larger amount of oxygen vacancy defects), and to the enhanced charge transfer from the nanocrystallites to the core of the decorated nanowire.

The strategy of intentionally making defect-rich TiO₂ nanowires that are highly photoactive in the visible region in a one-step method inspires us to explore the present synthesis technique for making defect-rich ZrO₂ nanostructures. In Chapter 4, we present the development of an ultra-active photocathode for photoelectrochemical water splitting for H₂ production. Consisting of individual ZrO₂ nanowires decorated with ZrO₂ nanoplates, this photocathode is also synthesized by one-step catalyst-assisted pulsed laser deposition through the vapour-liquid-solid growth mechanism with aid of a SiO₂ buffer layer on a Si substrate. The already superior composition of oxygen vacancy defects, charge carrier transport resistance, and specific surface area of the as-grown single-crystalline hierarchical nanowires have been further improved by a hydrofluoric acid treatment, which causes partial delamination or flaking of the as-grown nanostructured film. X-ray photoelectron spectroscopy reveals the presence of different types of oxygen vacancies (neutral, singly charged and doubly charged defects) and their compositional correlation to the Zr^{x+} oxidation states ($4 > x > 1$), which are

found to affect the charge transfer process, the p-type conductivity, and the photocatalytic activity of ZrO₂ nanostructured film. The partially delaminated hierarchical nanowire film electrode provides the highest cathodic photocurrent of 22.1 mA/cm² (at -0.8 V vs reversible hydrogen electrode) in the visible light (>400 nm) reported to date, which represents 76% of the overall photocurrent. This electrode also exhibits a stable cathodic current even after 2 h continuous illumination and super-high water splitting performance with the Faradaic efficiency estimated to be nearly 100%.

In Chapter 5, defect-rich, dopant-free nanostructures of ZrO₂ with different specific surface areas and amounts of oxygen vacancy defects, including nanobricks, nanopopcorns, nanospikes, and nanowires, have been prepared by catalyst-assisted pulsed laser deposition method. We show that the nanowires exhibit remarkably high saturation magnetization (5.9 emu/g) and coercivity (99 Oe) at room temperature at a very small external magnetic field (2000 Oe). These novel properties are attributed to the large amount of defects and high specific surface area. More importantly, Curie temperature (T_c) considerably above room temperature is also observed for these ZrO₂ nanostructures, including nanowires (700 K), nanospikes (650 K), nanopopcorns (550 K), and nanobricks (400 K). We also provide the first experimental evidence that it is the amount of defects in and not the phase of ZrO₂ that controls the ferromagnetic order in undoped ZrO₂ nanostructures. The presence of different types of oxygen vacancies (neutral, singly and doubly charged defects) and their correlation to the Zr^{x+} oxidation states (4>x>1) are found to affect the exchange interactions and the formation of ferromagnetic bound magnetic polarons, similar to that exerted by dopants in transparent dilute ferromagnetic semiconductor oxides. A new direct correlation between ferromagnetism and the types of oxygen vacancy defects in both monoclinic and tetragonal ZrO₂ nanostructures is therefore established.

The present work therefore not only introduces a new simple strategy to intentionally create oxygen vacancy defects in fabricating defect-rich TiO₂ and ZrO₂ nanostructures, but also provides new opportunities in a variety of solar energy driven applications. New insights into magnetic ordering in dopant-free transparent dilute ferromagnetic semiconductor oxides are also obtained, which promises new design of exotic magnetic and novel multifunctional materials.

Chapter 2

Experimental Techniques

In this Chapter, we outline the experimental techniques used for synthesis and characterization of TiO₂ and ZrO₂ nanostructured materials, as well as evaluation of their photoelectrochemical water splitting performance and magnetic properties. A brief description of each of the relevant methods follows.

2.1 Pulsed Laser Deposition

Figure 2.1 shows the Pulsed Laser Deposition (PLD) system (NanoPLD, PVD Products) used for depositing TiO₂ and ZrO₂ nanostructures.¹⁴⁷ Equipped with a turbomolecular pump that delivers a base pressure better than 1×10^{-7} Torr, the PLD system consists of a high-power UV pulsed laser, transfer optics and a multiport deposition chamber. A KrF excimer laser (248 nm, Lambda Physik COMpex 205) operating with an energy of 100-600 mJ per pulse and a repetition rate of 1-50 Hz is used to vaporize the material of interest. The laser light is aligned and focused on the target by focusing lenses and a rastering mirror. The laser pulses pass through a fused silica window before entering into the vacuum deposition chamber. Inside the deposition chamber, a six-target carousel, with each target holder capable of rotating around the target axis, provides uniform ablation of the entire surface of the target, by rastering the laser beam across the diameter of the target. The deposition chamber is equipped with four gas flow meters for four different feed gases, a current source for the substrate heaters, a thermocouple to measure the temperature of the substrate holder, and an external pyrometer to monitor the temperature of the substrate mounted on the substrate holder. An assembly of infrared lamps is used to provide radiative heating of the substrate up to 900 °C. The substrate is mounted facing down towards the target on the substrate holder with the lamp assembly mounted at the backside. The substrate-to-target separation can be varied by moving the substrate holder vertically with a linear-motion manipulator. A four-channel mass flow controller (MKS 247D) is used to control the flow meters, which in combination with a variable leak valve deliver the set pressure of the process gases to the deposition chamber. TiO₂ and ZrO₂ targets are prepared by cold-pressing their respective commercially available powders (Aldrich, 99.99% purity) with a pressure of 20 MPa followed by sintering in air at 1100°C for 24 h. Typically, TiO₂ and ZrO₂ are deposited on the substrate, which is kept 25 mm from the target, by operating the laser at a fluence

of 350 mJ/pulse with a repetition rate of 5 Hz for a period of 90 min, while the substrate temperature is varied between 600 and 770 °C.

To evaluate the effect of surface SiO₂ layer on nanostructural growth, commercial p-type Si(100) chips (resistivity 0.001-0.002 ohm-cm, Siegert Wafer) are modified to produce three different substrates: (RCA-Si) chemically oxidized Si obtained after RCA cleaning,¹⁴⁸ (H-Si) H-terminated Si obtained by etching with 1 M hydrofluoric acid; and (Ox-Si) thermally oxidized Si by annealing RCA-Si in O₂ at 850 °C for 120 min. To produce the catalytic seed layer to facilitate the appropriate growth mode of interest, gold nanoislands (GNIs) are synthesized on the three modified Si(100) substrates by magnetron sputtering a gold target typically for 4-20 s followed by annealing in N₂ and/air at 500-600 °C for 30-60 min, and we designate the resulting templates as GNI/RCA-Si, GNI/H-Si, and GNI/Ox-Si. Minor variations of these preparation procedures are given in later chapters, wherever relevant. The size distributions of the GNIs can be determined by processing their scanning electron microscopy images with the ImageJ software.¹⁴⁹

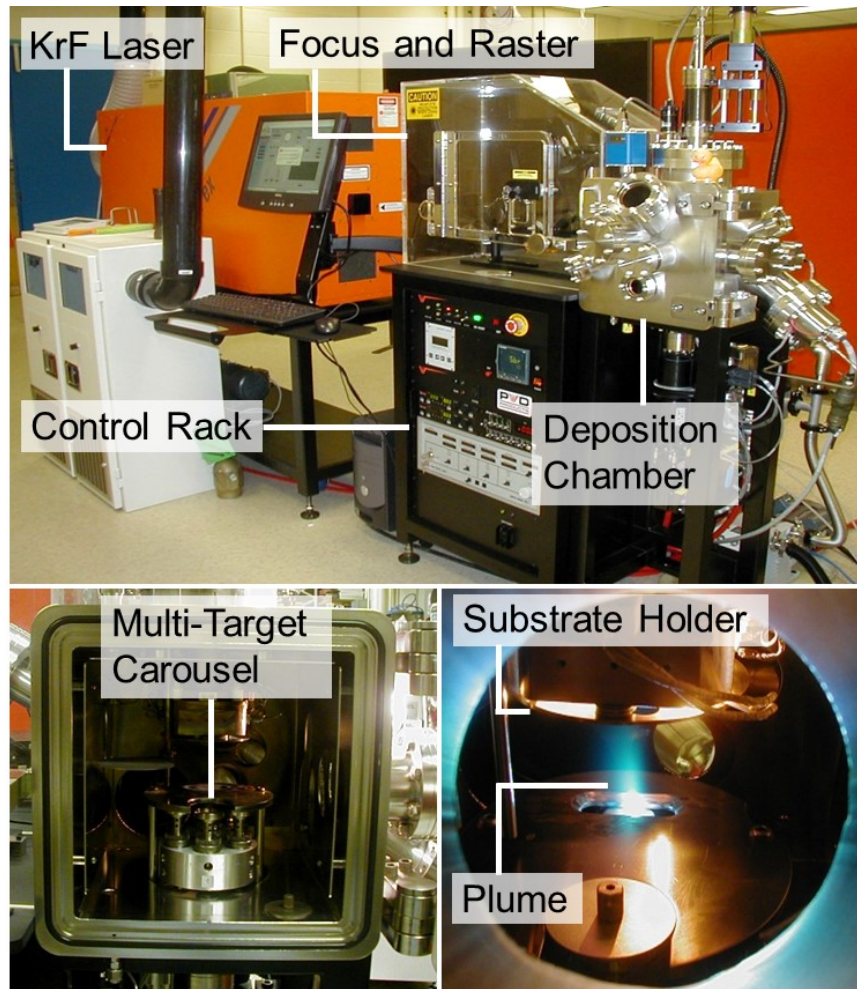


Figure 2.1 Photographs of (top) the pulsed laser deposition system, consisting of the KrF excimer laser, the alignment, focusing and rastering optics, and the vacuum deposition chamber, along with the electronic control rack and gas box; (bottom left) the multi-target carousel and substrate mount assembly inside the chamber; and (bottom right) the ablation laser plume of the target during deposition.

2.2 Characterization of Physical Properties

The morphologies and crystal structures of PLD-grown TiO₂ and ZrO₂ nanostructures have been extensively studied by electron and ion microscopies and X-ray diffraction, in order to investigate the growth mechanisms, structure-property relations and shape-dependent properties of the nanostructures.

2.2.1 Scanning electron microscopy

Scanning electron microscopy (SEM) is used to analyze the morphology and elemental composition of a nanostructured film.¹⁵⁰ Studying the morphology and surface features of nanostructures is of great importance to investigating the growth characteristics and structure-property relationship of nanostructures. A photograph of the Zeiss Merlin field-emission microscope used for the present work is shown in Figure 2.2. The core of the Merlin is the enhanced Gemini II electron optics column, which is equipped with a double condenser lens system to deliver an ultrahigh spatial resolution of 0.8 nm for imaging and a probe current of up to 300 nA for nanoanalytics applications. The unique charge compensation system of the Merlin also enables high-resolution imaging of non-conductive samples. The complete detection system combines three different in-lens detector systems for the analysis of a wide variety of samples: (a) SE detector for (low-energy) secondary electrons used for high-resolution imaging, (b) EsB detector for energy-selective detection of (high-energy) backscattered electrons for contrast identification based on electron energy loss transitions, and (c) AsB detector for angle-selective detection of backscattered electrons for enhancing crystallographical contrast. The Merlin is also equipped with an EDAX energy-dispersive X-ray (EDX) analysis system, which provides elemental identification based on detection of X-ray emission at element-specific characteristic photon energies from the sample upon excitation by the high-energy electron beam. The X-ray emission spectra so obtained can also be used for quantifying the elemental composition of the sample through the intensities of their characteristic X-ray emission features.

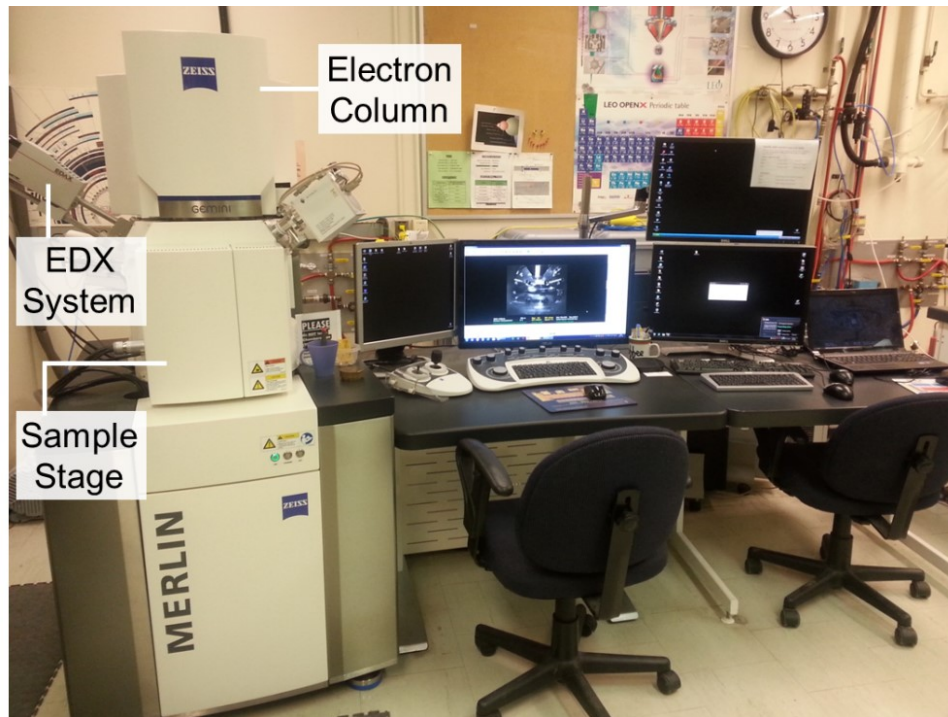


Figure 2.2 Photograph of the Zeiss Merlin field-emission scanning electron microscope, equipped with both in-lens and out-of-lens secondary electron detectors, an energy-selective (EsB) and an angle-selective (AsB) backscattered detectors, and an EDAX energy-dispersive X-ray analysis system.

2.2.2 Helium ion microscopy

Helium ion microscopy (HIM) is very similar to a scanning electron microscope, except that it employs a helium ion beam as the illuminating particle source instead of an electron beam.¹⁵¹

Figure 2.3 shows a Zeiss Orion Plus microscope that is capable of an ultrahigh spatial resolution of 0.35 nm due to the considerably shorter de Broglie wavelength of the helium ions than electrons at the same kinetic energy (30 keV). The source consists of a sharpened needle held at a high positive voltage (25 kV) and low temperature (~80 K) in the presence of helium gas. A special source formation procedure is used to create a near-atomically sharp tip with just three atoms (the trimer) at the apex. The electric field density is sufficiently intense at these tip atoms that the impinging gaseous helium atoms undergo field ionization and become helium ions. Selecting one of these atoms in the trimer as the source delivers a beam with a source size below an angstrom and a brightness exceeding $5 \times 10^9 \text{ A}/(\text{cm}^2 \text{sr})$ at 20 keV, an order of magnitude beyond even a cold field electron emitter.¹⁵² The

ion beam is then collimated and focused through a double electrostatic lens column onto the sample surface. The beam landing energy can be set typically to 25-35 keV, with a typical beam current of 0.1-10 pA. The column is used to produce a focused helium ion beam with a spot size of about 0.25 nm. As the advantage of HIM is the much shorter de Broglie wavelength of the He^+ ions compared to electrons (at the same kinetic energy), He^+ ions do not scatter as much as electrons.¹⁵¹ This leads to a better spatial resolution and also a greater depth of focus because of the considerably higher forward scattering cross section of He^+ compared to the electron. The increased depth-of-focus is of great importance to imaging one-dimensional nanostructures with micron-sized height differences. As high-energy ion impact creates secondary electrons in the near surface, these secondary electrons can be collected by an Everhardt-Thornley (secondary electron) detector, while the Rutherford backscattered ions are detected by using a microchannel plate detector. Similar to the secondary electrons detected in SEM, the secondary electrons collected by the Everhart-Thornley detector provide the morphology and electron density information about the surface, while the backscattered ions offer image contrast based on the atomic number of the elements.

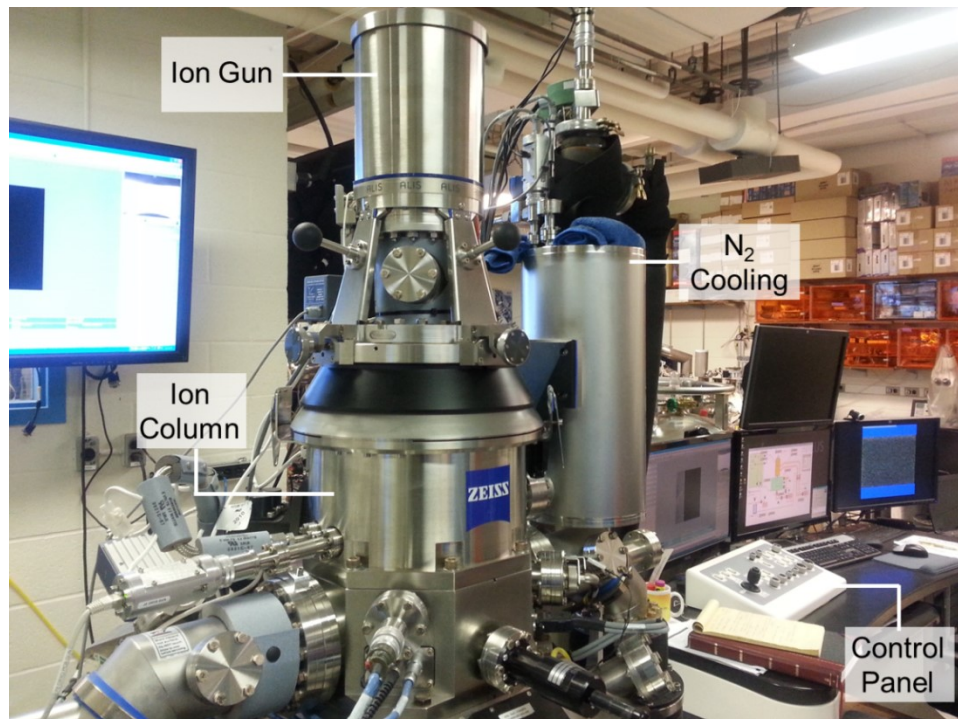


Figure 2.3 Photograph of a Zeiss Orion Plus helium ion microscope.

2.2.3 Transmission electron microscopy

Transmission electron microscopy (TEM) measurements have been performed for studying the crystal structure, phase identification, and determination of surface planes of TiO₂ and ZrO₂ nanostructures.¹⁵³ In the present work, both low-magnification and high-resolution bright-field TEM images have been collected by using a Zeiss Libra 200 MC microscope, shown in Figure 2.4.¹⁵⁴ The Libra system is capable of producing high resolution, high contrast images by taking advantage of Zeiss' proprietary electron gun monochromator (MC) and Kohler illumination systems as well as the double-corrected in-column omega energy filter technology. The monochromator is used to reduce the energy width of the primary electrons to less than 0.2 eV, thereby providing one of the highest energy resolution systems for electron energy loss spectroscopy (EELS). In TEM, a high-energy (200 kV) electron beam is transmitted through an ultra-thin specimen (usually less than 100 nm thick). An image is formed from the interactions of the transmitted electrons with the atomic columns in the specimen.¹⁵⁵ To prepare our samples for TEM analysis, the deposited nanostructured samples are scraped off from the substrates and then dispersed in methanol. After sonication for 10 min, the resulting solution is then dispensed onto the holey carbon TEM grids for imaging in the TEM.

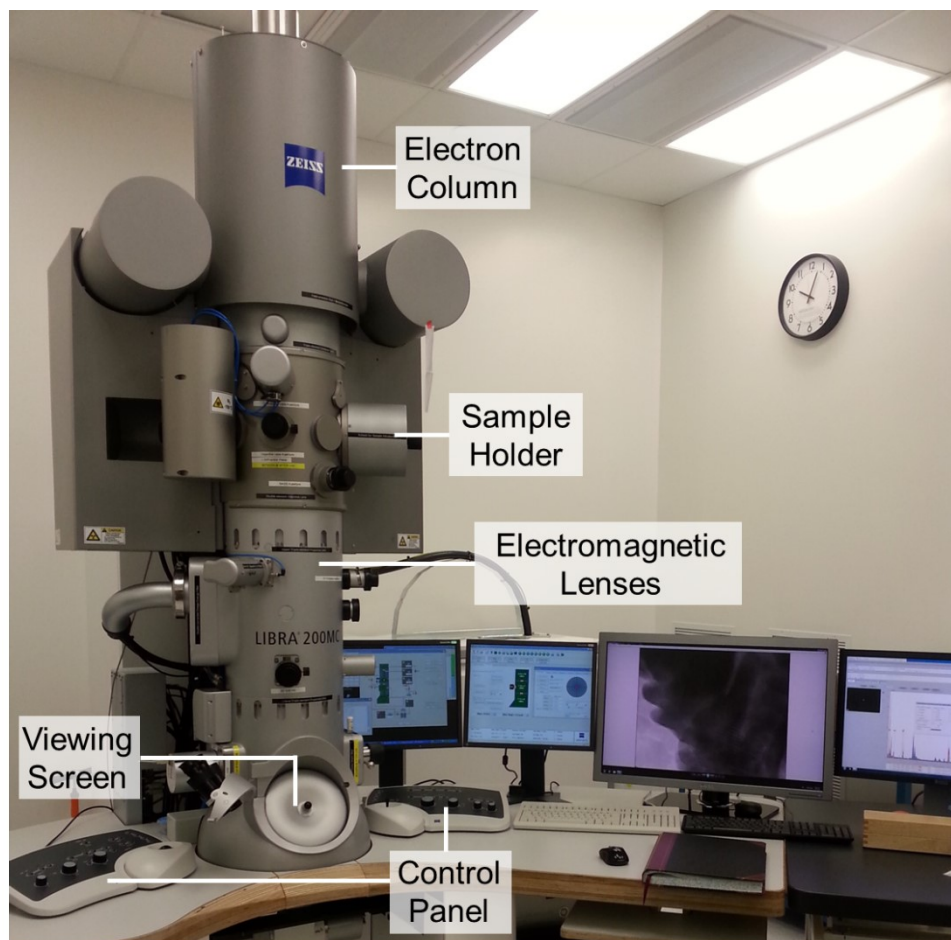


Figure 2.4 Photograph of a Zeiss Libra 200 MC transmission electron microscope.

2.2.4 X-ray diffraction crystallography

X-ray diffraction (XRD) is a powerful technique for identification and characterization of the crystal structure of a bulk material as hard X-rays could penetrate deep into the materials in order of millimeters.¹⁵⁶ X-ray diffraction is based on constructive interference of monochromatic X-rays with a crystalline lattice in the material. High-energy electron-impact excitation of a Cu anode is used to generate Cu $K\alpha$ X rays (1.54 Å). In the present work, we use a PANalytical X'Pert Pro MRD diffractometer to identify the crystalline phases and to determine the preferred growth orientations of the nanostructures (Figure 2.5). There are different optics and diffraction geometries available for this system. Due to the very small amount of sample (deposited on a substrate) and the nanometer size of the crystallites, the signal strength from these nanostructured materials is usually very weak and

dominated by the signal from the substrate. In order to reduce the signal from the substrate, glancing incidence X-ray diffraction is used to examine the crystal structure of the supported nanostructures. In this method, the incidence angle (ω) of the X-ray beam is kept at a very shallow angle (i.e., close to the critical angle of the scattering geometry), while the detector is swept over the 2θ angular direction. Since the incidence angle is below the critical angle, an evanescent wave is formed. This evanescent wave only penetrates into a thin layer (less than 100 nm) of the sample and travels on the surface of the sample, leading to an increased interaction of the X-ray beam with the nanostructured materials supported on the substrate and consequently to a greater signal.¹⁵⁷ For this purpose, a parallel beam geometry involving an X-ray mirror in the incident beam side and a parallel-plate collimator in the diffracted beam side is used. This configuration allows glancing incidence X-ray diffraction measurements at a typical incidence angle of 0.3° , which is used for the majority of the samples studied in this work.

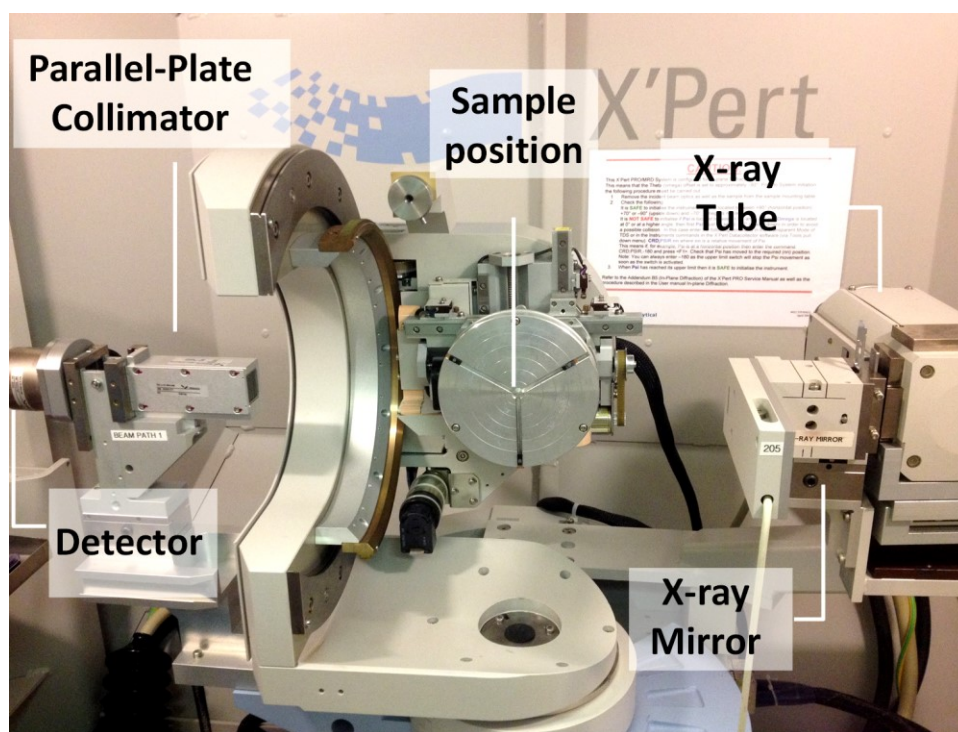


Figure 2.5 Photograph of the Panalytical X'pert Pro MRD X-ray diffractometer used for crystal structure characterization of the as-prepared supported nanostructures. The instrument is set up in the parallel beam geometry employing an X-ray mirror as the incident beam optics and a parallel plate collimator as the diffracted beam optics.

2.3 Chemical-state Composition Analysis

X-ray photoelectron spectroscopy (XPS) is performed in order to examine the elemental composition, empirical formula, chemical state and electronic state of the nanostructured film.¹⁵⁸ The XPS instrument used for these measurements is a Thermo-VG Scientific ESCALab 250 Microprobe (Figure 2.6), equipped with a monochromatic Al K α X-ray source (1486.6 eV) operated at a typical energy resolution of 0.4-0.5 eV full-width-at-half-maximum. XPS spectra are obtained by irradiating the sample surface with an X-ray beam while collecting electrons ejected typically from the top 1-10 nm of the material being analyzed as a function of the kinetic energy of the ejected electrons. A photoelectron spectrum is recorded by counting the number of these ejected electrons (the photoelectrons) as a function of electron kinetic energy, E_K , as determined by using a hemispherical electron energy analyzer. The corresponding binding energy, E_B , is calculated by using the Einstein equation, as follows: $E_B = h\nu - (E_K + \phi)$, where $h\nu$ is the photon energy (i.e. 1486.6 eV for Al K α ; h is the Planck constant and ν is the light frequency), and ϕ is the work function.¹⁵⁹

Photopeaks at characteristic binding energies correspond to individual chemical states. When compared with the appropriate standards, shifts in the binding energy (the so-called chemical shifts) contain information about the local chemical environments.¹⁶⁰ The energies and intensities of the photopeaks enable identification and quantification of all surface elements (except hydrogen) in the material environment. Using an Argon ion source to sputter away materials interleavingly between XPS spectral measurements, i.e. XPS depth profiling, it is possible to follow the chemical-state composition change as a function of sputtering depth and thereby in the depth direction in the near-surface region of the sample.

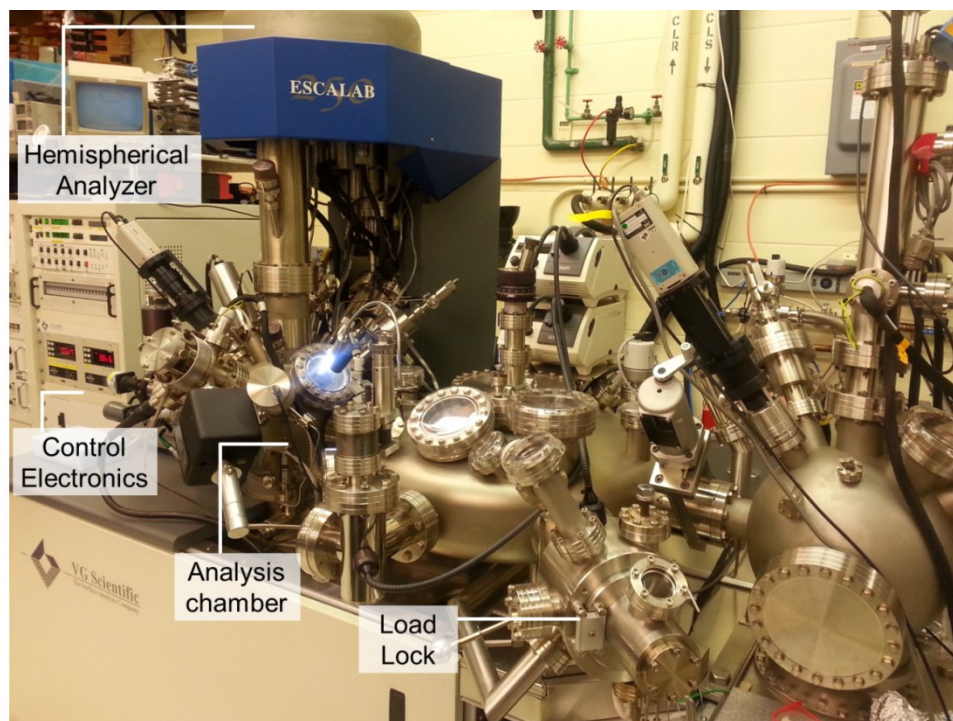


Figure 2.6 Photograph of the Thermo-VG Scientific ESCALAB 250 X-ray Photoelectron Microprobe used for chemical-state quantification of nanostructured materials.

2.4 Characterization of Electrical, Optical and Magnetic Properties

For the electrical characterization of nanomaterials and particularly those used in the photoelectrochemical water splitting reaction, a number of electrochemical methods have been used.

2.4.1 Electrochemical techniques for analysis

To study the photocatalytic activity of the TiO_2 and ZrO_2 nanostructured films for photoelectrochemical water splitting reaction, we perform chronoamperometry, in which the potential of the working electrode is scanned in a stepwise fashion while the current resulting from the faradic processes at the electrode (caused by the potential step) is monitored as a function of time.¹⁶¹ A CH Instruments electrochemical station (CHI 660E) is used (Figure 2.7). Employing a standard three-electrode configuration, the TiO_2 or ZrO_2 nanostructures grown on the modified Si templates, a saturated Ag/AgCl electrode, and a platinum wire are used as the working, reference, and counter electrodes, respectively, along with a 1.0 M KOH solution used as the electrolyte. The photocurrent spectra are obtained over an illuminated sample area of 0.2 cm^2 under simulated sunlight illumination,

as provided by a 300 W solar simulator, consisting of a 300 W Xenon lamp (Newport-Oriel Instruments, Model 68811) coupled with an AM 1.5G filter.

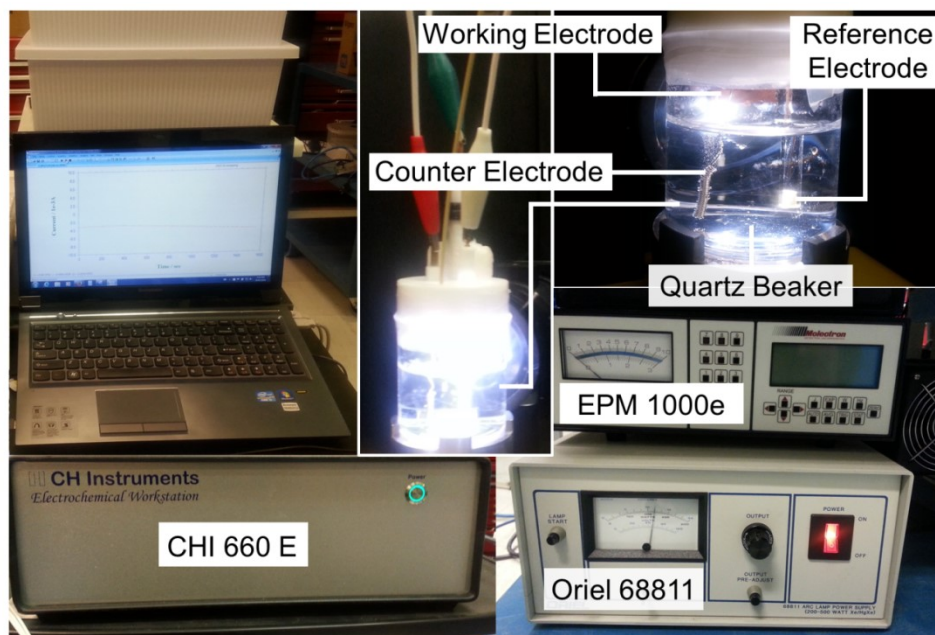


Figure 2.7 Photograph of an electrochemical station (CHI 660E) connected to a three-electrode electrochemical cell in typical photoelectrochemical water splitting reaction setup. The nanostructured sample is used as the working electrode, in the presence of a Pt wire counter electrode and an Ag/AgCl reference electrode. A 300 W solar simulator (Newport-Oriel Instruments, Model 68811) was used to provide the AM 1.5G solar light. The light intensity of the solar simulator was calibrated to 1 sun (100 mW cm^{-2}) using a power meter (Molectron, EPM 1000e).

To confirm the stoichiometric photoelectrochemical splitting of water, in-situ quantification of the evolved gases is performed by using an Universal Gas Analyser (Stanford Research Systems, SRS-UGA) (Figure 2.8).¹⁶² As the measurement is conducted with the three-electrode configuration in a sealed quartz beaker, a capillary is inserted above the liquid electrolyte to sample the gases generated by the reaction. The UGA is a state-of-the-art benchtop mass spectrometer that operates from above atmospheric pressure to ultrahigh vacuum. The UGA system is also simple to operate and maintain, and it is ideal for on-line monitoring and analysis of gas mixtures. The UGA system consists of two main subsystems: a gas handling system and a gas analyzer. The gas analyzer is a quadrupole mass spectrometer that can only operate in high vacuum. The gas handling system

consists of a capillary, a pinhole, pumps and valves that deliver the sample gas to the analyzer. The UGA employs two separate diaphragm pumps for each stage in order to completely separate the high pressure sample line from the high vacuum analysis system (Figure 2.8). All the components can be controlled from both the front-panel and remotely by a computer. To sample the gases at atmospheric pressure, the UGA system uses a two-stage pressure reduction scheme. At the first stage, the sample at atmospheric pressure is drawn through a capillary (1.8 m long, 175 μm ID), which drops the pressure by 3 decades. In the second stage, a small amount of the gas sample is drawn through a pinhole (40 μm) into the analyzer region pumped by a turbomolecular pump, which reduces the pressure to $\sim 10^{-6}$ Torr (the mass spectrometer operating pressure), while most of the inlet gas (about 99.9%) flows directly to the bypass diaphragm pump. In this way, the inlet continuously samples the gases at low flow rates (several milliliters per minute), making the instrument ideal for real-time on-line analysis. A change in the gas composition at the inlet can be detected in ~ 0.2 s.

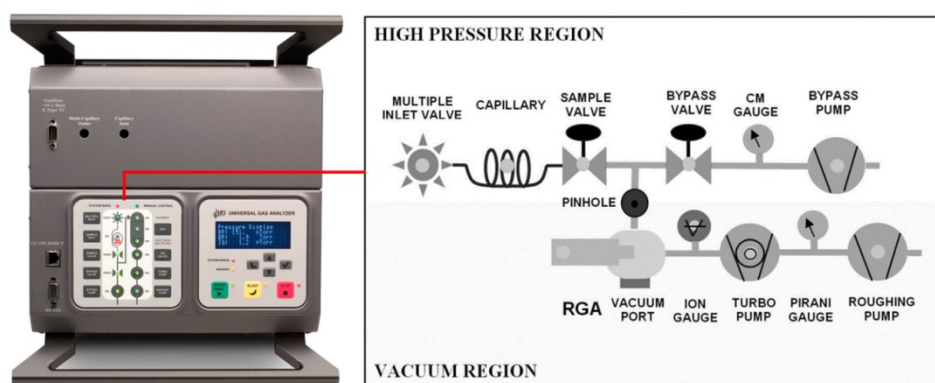


Figure 2.8 Photograph of the SRS-UGA gas analyzer with a two-stage pressure reduction scheme.

2.4.2 Electrochemical impedance spectroscopy

Electrochemical Impedance Spectroscopy (EIS) is a powerful technique in the studies of corrosion, semiconductors, batteries, electroplating, and electro-organic synthesis.¹⁶³ In general, EIS measures the response of an electrochemical circuit to an alternating current or voltage as a function of frequency. In an electrochemical cell, slow electron kinetics, slow preceding chemical reactions, and diffusion can all impede the electron flow. The components in an electrochemical cell can be considered analogous to the resistors, capacitors, and inductors that impede the flow of electrons in an alternating current (AC) circuit. In direct current (DC) circuit, however, only resistors could produce

this effect. The total impedance in the circuit is the combined opposition of all its resistors, capacitors, and inductors to the flow of electrons. Impedance can be expressed as a complex number, where the resistance is the real component and the combined capacitance and inductance represents the imaginary component. Capacitors and inductors affect not only the magnitude of an alternating current but also its time-dependent characteristics or phase. When most of the opposition to the current flow comes from its capacitive reactance, the circuit is said to be largely capacitive and the current leads the applied voltage by a phase angle.¹⁶⁴ When most of the opposition to current flow comes from its inductive reactance, the circuit is said to be largely inductive and the current lags the applied voltage by a phase angle. The more inductive is the circuit, the closer would the current be 90° out of phase with the voltage.

In the case of an ideal resistor (i.e., when the frequency is set to 0 Hz), the resistance R can be calculated using Ohm's law as the ratio between the voltage V and the current I, i.e. $R = V/I$. The electrochemical impedance is calculated by measuring the current through the cell when an AC potential is applied at different frequencies, f (Hz). Typically, the current response to a sinusoidal potential is also a sinusoid at the same frequency but with a phase shift. The change in potential E_t at time (t) is related to the maximum potential E_0 as a function of the radial frequency ω (radian/second), as follows:

$$E_t = E_0 \sin(\omega t),$$

where $\omega = 2\pi f$. On the other hand, the current at time t (I_t) is shifted in phase and is related to the maximum current (I_0) according to:

$$I_t = I_0 \sin(\omega t + \varphi),$$

where φ is the phase shift. Consequently, the impedance of the system (Z) is given by:

$$Z = E_t / I_t = E_0 \sin(\omega t) / [I_0 \sin(\omega t + \varphi)] = Z_0 [\sin(\omega t) / \sin(\omega t + \varphi)],$$

where $Z_0 = E_0/I_0$. The impedance can also be expressed as a complex number with the real part (Z_{Re}) and imaginary part (Z_{Im}) given at different frequencies, where

$$Z(\omega) = E/I = Z_0 \exp(j\varphi) = Z_0 (\cos \varphi + j \sin \varphi), \text{ where } j = \sqrt{-1}$$

As different working electrodes are employed for the photoelectrochemical water splitting application, the determination of electrical resistance of the nanomaterials deposited on the substrates is therefore important to understanding the performance of the photoelectrode. A typical photoelectrochemical cell can be commonly simulated as an equivalent circuit in order to better quantify the effects of different parameters that are crucial to improving the cell performance. A

typical equivalent circuit model is shown in Figure 2.9b. In a typical photoelectrochemical cell, the series resistance is an important factor for the overall performance of the photoelectrochemical cell. This series resistance (R_s) could be due only to the resistance of photoelectrode (i.e. the working electrode), or to the combination of the contact resistances of counter, working and reference electrodes. In addition, as ions diffuse in an electrolyte solution, they would adsorb onto the electrode surface forming a double layer. The existence of this electrical double layer at the interface effectively separates the ions from the charged electrode by an insulating space, forming a chemical capacitance element (CPE). Parameters such as ionic concentration, electrode potential, and impurity adsorption could affect the magnitude of the capacitor.^{165,98} Finally, the Warburg impedance (Z_w) corresponds to the diffusional impedance for one-dimensional linear diffusion. In contrast to the Helmholtz layer resistance and double layer capacitance, the Warburg impedance is a non-ideal circuit element because it depends on the frequency of the potential change. At a high frequency, the Warburg impedance is small as the diffusing reactants do not have to travel very far, in contrast to that at a low frequency with an increasing Warburg impedance. However, the identification of Z_w is difficult because it is always accompanied by the charge-transfer resistance and double-layer capacitance.

There are several ways to display frequency response data, including the Bode' plots and Nyquist plots. Bode' plots display the amplitude and phase separately as functions of the frequency, while a Nyquist plot shows the imaginary part of impedance, Z_{Im} , as a function of the real part, Z_{Re} , obtained for different frequencies, ω . In a standard Nyquist plot, the semicircle portion at higher frequencies corresponds to the electron transfer limited process, while the series resistance can be found by reading the real axis value at the high frequency intercept. Figure 2.9a shows an example of a Nyquist plot obtained for a TiO_2 nanowire film grown on a Si substrate by catalyst-assisted pulsed laser deposition method.⁷¹ The same electrochemical station used for the photoelectrochemical measurement is also used for the electrical impedance measurement and modelling by electrochemical impedance spectroscopy.

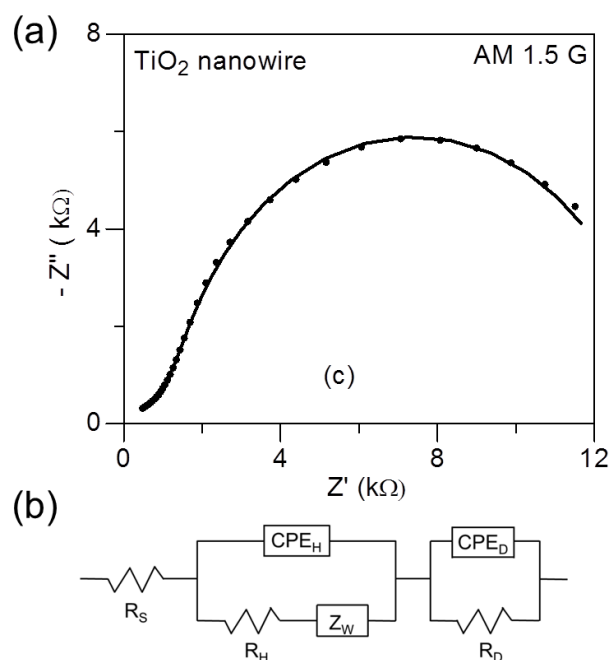


Figure 2.9 (a) Typical Nyquist plot for a TiO₂ nanowire film under illumination of simulated sunlight (100 mW/cm²). The experimental data (solid circles) are collected in a frequency range between 0.01 Hz and 100 Hz with an AC voltage amplitude of 10 mV and a DC bias of -0.5 V, and they are fitted with (b) an equivalent circuit model (solid line). The equivalent circuit consists of a series resistance (R_S), an RC circuit with a resistance (R_D) and a chemical capacitance element (CPE_D) for the semiconductor depletion layer, along with a second RC circuit containing the charge transfer resistance for the Helmholtz layer (R_H) and the Warburg diffusion impedance (Z_W), and the capacitance for the electrochemical double layer (CPE_H) in a second RC circuit connected in series.

2.4.3 Hall effect measurements

For carrier type and carrier concentration measurements, a Hall effect measurement system (Ecopia HMS-5300) employing the four-point probe method in a van der Pauw configuration is used,¹⁶⁶ as shown in Figure 2.10. The system can be used to measure the carrier concentration, carrier mobility, resistivity and conductivity, and the Hall coefficient as functions of temperature. To assure good electrical connections for these measurements, aluminum and platinum contacts are sputter-

§§§§ Reproduced with the permission from: M.A. Rahman, S. Bazargan, S. Srivastava, X. Wang, M. Abd-Ellah, J.P. Thomas, N.F. Heinig, D. Pradhan, and K.T. Leung, *Energy Environ. Sci.* 8, 3363 (2015). Copyright (2015) by the Royal Society of Chemistry.

deposited by magnetron sputtering (with a current of 50 mA for 120 s) onto the corners of the deposited nanostructured materials on Si substrates.

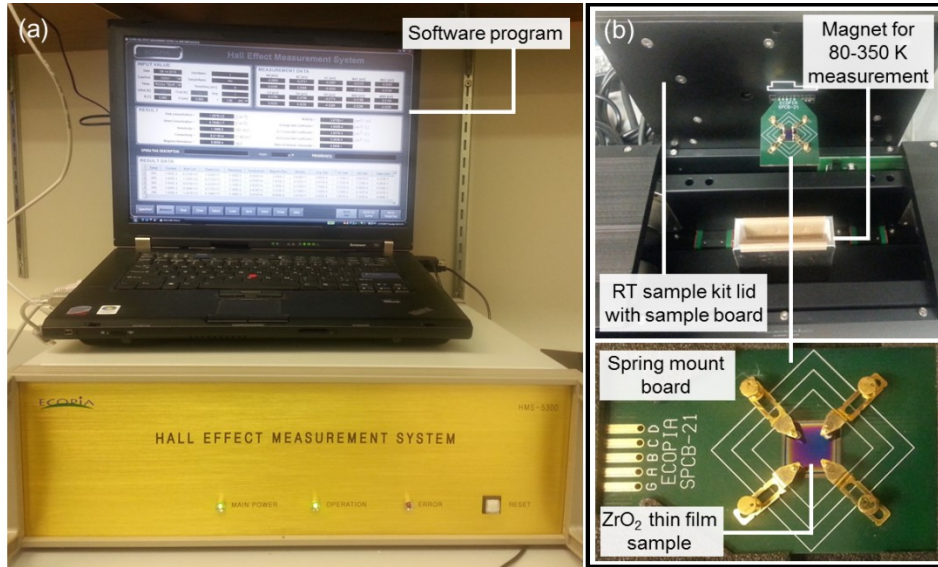


Figure 2.10 (a) Photograph of the Ecopia HMS-5300 Hall effect measurement system, (b) sample mounting fixture with upper cooling reservoir.

2.4.4 Ultra-Violet/Visible (UV/Vis) spectroscopy

In the present study, we use a Perkin-Elmer Lambda 1050 UV/Vis/NIR spectrophotometer to measure the optical properties of the as-prepared materials, including their light absorbance and reflectance (Figure 2.11).¹⁶⁷ The double-beam scanning spectrophotometer consists of a double monochromator, and three detectors for optimum energy detection across the entire UV/Vis/NIR range (175-3300 nm) with a UV/Vis resolution of 0.05 nm and a NIR resolution up to 0.20 nm. A gridless photomultiplier detector is used for detection in the UV/Vis range (175-860 nm), while either a Peltier-cooled InGaAs detector (860-2500 nm) or a Peltier-cooled PbS detector (860-3300 nm) is used for the detection in the near-infrared (NIR) region. This spectrophotometer offers the best combination of scanning speed and photodynamic range that can be achieved on a given sample type.

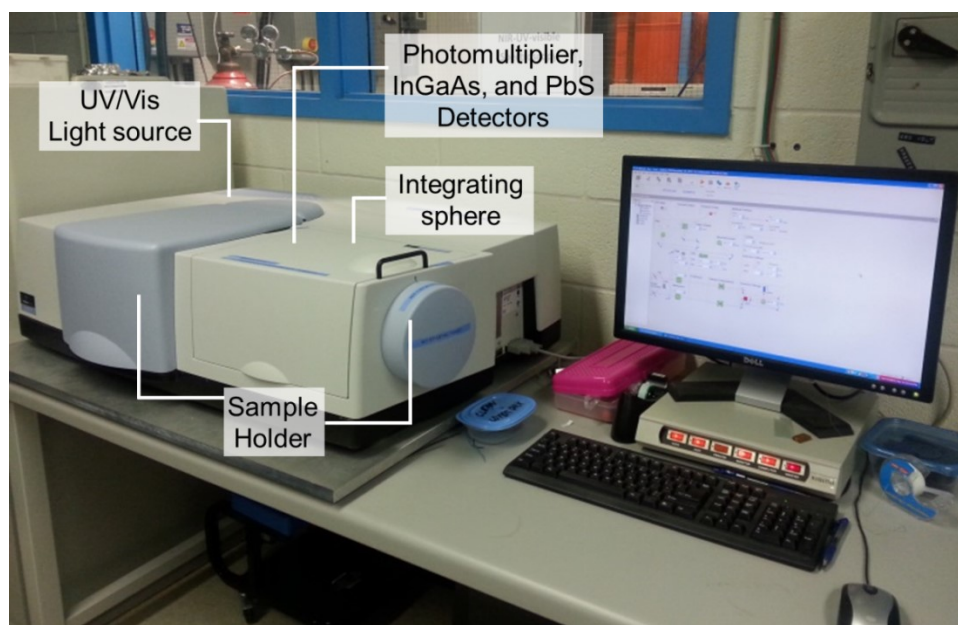


Figure 2.11 Photograph of the Perkin-Elmer Lambda 1050 UV/Vis/NIR spectrophotometer.

2.4.5 Measurement of magnetic properties

A 7-Tesla Quantum Design EverCool Magnetic Property Measurement System (MPMS), utilizing the Superconducting Quantum Interference Device (SQUID) technology, is used to characterize the magnetic properties of TiO_2 and ZrO_2 nanostructured films (Figure 2.12).¹⁶⁸ The magnetic moments of the samples are measured as a function of temperature in the 1.8-400 K range with the sensitivity of 1×10^{-8} emu. The SQUID and the superconducting magnet must both be cooled with liquid helium, which is provided by an integrated pulse-tube cryocooler-dewar system. Liquid helium is also used to cool the sample chamber. The sample should be smaller than a maximum size of $5 \times 5 \text{ mm}^2$ in order to be inserted inside the bore of the magnet and the sample is appropriately positioned such that the sample vibration occurs in the homogeneous part of the magnetic field. It should be noted that only plastic tweezers and quartz holders have been used during the sample preparation and magnetic measurement to avoid any unintentional ferromagnetic contamination.

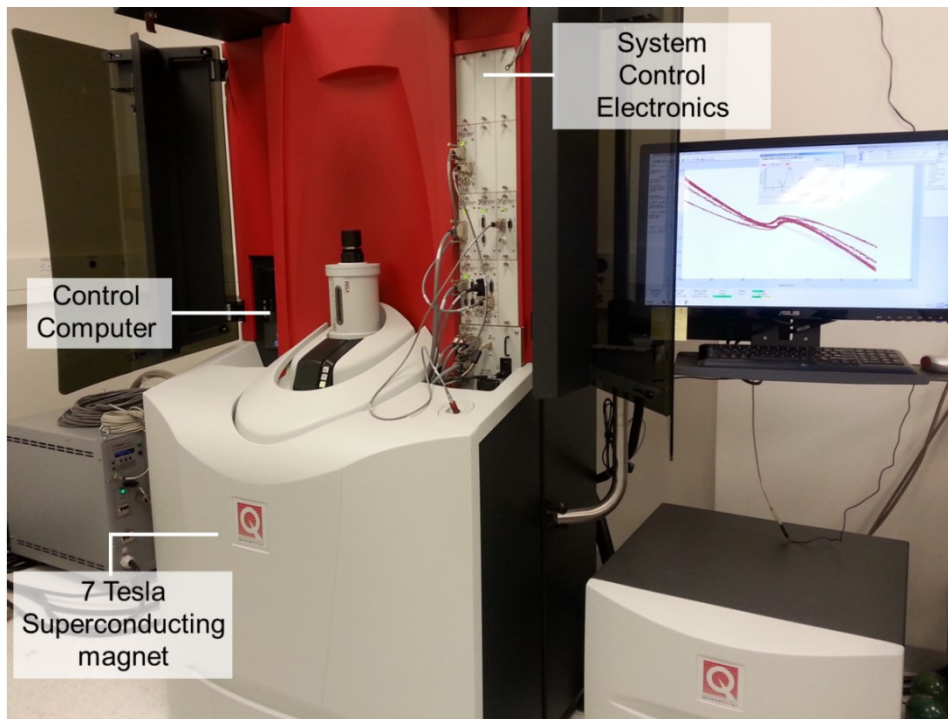


Figure 2.12 Photograph of the Quantum Design MPMS SQUID VSM system with Evercool technology.

Chapter 3

Defect-rich Decorated TiO₂ Nanowires for Super-efficient Photoelectrochemical Water Splitting Driven by Visible Light ^{*****}

3.1 Introduction

Over the past two decades, TiO₂ has been extensively studied as a photoanode for photoelectrochemical water splitting reaction due to its compatible band-edge positions, high photocatalytic activity, high resistance to photocorrosion, low cost, and lack of toxicity.¹⁶⁹ However, TiO₂ has too wide a band gap (3.0 eV)²⁴ to absorb sunlight in the visible region, which limits its photocatalytic activity to ultraviolet illumination. Several attempts have been made to extend the light absorption of this catalyst, and they include doping,¹⁷⁰ hydrogen treatment,⁸ and plasmonic nanoparticle sensitization.¹⁷¹ All of these efforts have only managed to produce a photocurrent density no greater than 0.1 mA/cm² in the visible region (>430 nm). The dependence of photoelectrochemical activity on the surface morphology and oxygen vacancy of these 1D TiO₂ nanostructures are also not well understood. As the surface morphology and electronic properties of TiO₂ nanostructures can affect the space charge regions differently, they are especially important to the overall charge collection efficiency by influencing the recombination velocity and the chemical reaction dynamics.¹⁷² Furthermore, these nanostructures (such as nanobelts and nanowires) can also be used to enhance light harvesting and to suppress charge carrier recombination while maintaining a high surface area necessary to improve the photoresponse.⁵⁹

There are a variety of techniques to synthesize 1D TiO₂ nanostructures, including anodization of titanium foil or wires,¹⁷³ electrodeposition or solution precipitation,¹⁷⁴ hydrothermal methods,^{175,176} thermal evaporation,^{62,66,177–179} and chemical vapour deposition.¹⁸⁰ One major limitation of wet-chemistry methods is that the precursor materials often incorporated into the final structure as an impurity.^{174,181} As a result, the charge transport efficiency and material stability are significantly reduced due to poor crystallinity, and grain boundaries. However, large-scale controlled synthesis of 1D TiO₂ nanostructures by vapour deposition is challenging due to the extremely low vapour pressures and high melting points of Ti and TiO₂. A protective buffer layer such as SiO₂, TiO₂ or TiN

***** Reproduced with permission: Rahman, M. A.; Bazargan, S.; Srivastava, S.; Wang, X.; Abd-Ellah, M.; Thomas, J. P.; Heinig, N. F.; Pradhan, D.; Leung, K. T. *Energy Environ. Sci.* **2015**, *8*, 3363–3373. Copyright © 2015 by the Royal Society of Chemistry.

is often employed to activate the substrate-sensitive catalyst, including Ni,^{65,66} Cu,⁶⁹ or Au,^{17,61} in order to promote vapour-liquid-solid (VLS) growth of TiO₂ nanowires. In the absence of a buffer layer, the catalyst would quickly become poisoned, thus inhibiting VLS growth.¹⁷⁷ However, the presence of a dielectric or insulating buffer layer that is too thick on a conductive substrate has adverse effects on the growth characteristics¹⁸² and charge collection efficiency,⁷² which negatively impact the electronic properties of the nanodevices. A simple, alternative vapour deposition method to provide controlled synthesis of a 1D TiO₂ nanostructure on a conductive substrate with a buffer layer, of an appropriately optimized thickness (<50 nm), could therefore significantly advance future technological applications.

Unlike thermal evaporation and chemical vapour deposition, pulsed laser deposition (PLD) involves direct laser ablation of the target material, without affecting its stoichiometry, into the gaseous form, which is then exposed to the substrate held at a specified temperature. The absorption of a high-intensity laser energy pulse by a small volume of material leads to vaporization in the thermally non-equilibrium regime. As a result, activation of the gold catalyst could occur at a lower temperature, thus allowing the formation of 1D TiO₂ nanostructures at a lower temperature than other vapour deposition methods. Furthermore, variable substrate temperature, oxygen partial pressure and reductive growth environment during PLD can be used to control not only the rate of deposition but also the crystallinity, morphology and the amount of oxygen-related defects.¹⁰⁵ Oxygen vacancies are highly desirable for metal oxides because oxygen vacancy defects increase light absorption, act as electron donors and therefore enhance the electrical conductivity and charge transport property,⁴³ which can significantly improve their catalytic performance for photoelectrochemical water splitting reactions.⁸

Here, we use catalyst-assisted pulsed laser deposition (PLD) to synthesize defect-rich 1D TiO₂ nanostructures with a wide range of morphology on a Si substrate by controlling a SiO₂ buffer layer of appropriately optimized thickness and the growth temperature. We further demonstrate the remarkable photoelectrochemical catalytic performance of these defect-rich nanostructures for the first time in the visible light region (> 430nm) in a water splitting reaction.

3.2 Materials and Methods

The catalyst-assisted PLD technique used to synthesize the 1D TiO₂ nanostructures has been described in detail elsewhere.¹⁸³ Briefly, the NanoPLD system (PVD Products) used in the present

study was equipped with a KrF excimer laser (248 nm wavelength), and was operated at a fluence of 350 mJ/pulse with a repetition rate of 5 Hz. The TiO₂ target was prepared by cold-pressing rutile TiO₂ powders (Aldrich, 99.99% purity) at a pressure of 25 MPa, followed by sintering in air at 900 °C for 12 h. The temperature of the substrate could be varied from room temperature to 900 °C by radiative heating from infrared heat lamps. The target-to-substrate distance was maintained at 25 mm with the substrate temperature kept at 675, 700, 720 or 750 °C to facilitate growth of nanostructures with different morphologies. Argon gas was let into the growth chamber at a constant flow rate of 19.8 sccm by using a mass flow controller to maintain a pressure of ~180 mTorr.

To evaluate the effect of surface SiO₂ layer, we modified commercial p-type Si(100) chips (resistivity 0.001-0.002 ohm-cm, Siegert Wafer) to produce three different substrates: (RCA-Si) chemically oxidized Si obtained after RCA cleaning; (H-Si) H-terminated Si obtained by etching with hydrofluoric acid; and (Ox-Si) thermally oxidized Si by annealing H-Si in O₂ at 850 °C for 120 min. Using a Filmetrics F-40 UV reflectometer, we estimated the respective oxide layer thicknesses for H-Si, RCA-Si and Ox-Si to be 1 nm, 3 nm and 30 nm. Gold nanoislands (GNIs) were produced on the three modified Si(100) substrates by magnetron sputtering a gold target for 4 s followed by annealing in N₂ at 500 °C for 30 min, and we designate the resulting templates as GNI/RCA-Si, GNI/H-Si, and GNI/Ox-Si. The size distributions of the GNIs were measured by processing their SEM images with the ImageJ software.

The surface morphologies of the as-grown TiO₂ nanostructures on the three templates were characterized by field-emission scanning electron microscopy (SEM) in a Zeiss Merlin microscope. The crystal structures of the nanostructures were analyzed by glancing-incidence X-ray diffraction at an incidence angle of 0.3° using a PANalytical X'Pert Pro MRD diffractometer with Cu K α radiation (1.54 Å). Transmission electron microscopy (TEM) study of the as-deposited structures was conducted in a Zeiss Libra 200 MC microscope. Reflectance spectra were recorded using a Perkin-Elmer Lambda 950 UV-Vis-NIR spectrometer with a Labsphere integrating sphere detector. The chemical-state compositions of the nanostructures were characterized by X-ray photoelectron spectroscopy (XPS) in a VG Scientific ESCALab 250 microprobe with a monochromatic Al K α X-ray source (1486.6 eV).

Photoelectrochemical measurements for the water splitting reaction using the TiO₂ nanostructures as the photocatalysts were carried out in an electrochemical station (CH Instruments, CHI 660E). We employed a standard three-electrode configuration, in which the TiO₂ nanostructures

grown on the aforementioned templates, a saturated Ag/AgCl electrode, and a platinum wire were used as the working, reference, and counter electrodes, respectively, and a 1.0 M KOH solution was used as the electrolyte. A 300 W solar simulator (Newport-Oriel Instruments, Model 68811) was used to provide the AM 1.5G solar spectral illumination. Light intensity of the solar simulator was calibrated to 1 sun (100 mW/cm^2) with a power meter (Moletron, EPM 1000e). The SRS-UGA system is used to analyze a gas sample at atmospheric pressure via a specially designed 6 feet long capillary tube ($175 \text{ }\mu\text{m}$ ID). The measurement is done with the same three-electrode electrochemical cell in a sealed quartz beaker, with the capillary inserted to sample the gases generated by the reaction. A short-pass ($< 400 \text{ nm}$) or a long-pass ($> 430 \text{ nm}$) filter (Oriel) was coupled with the AM 1.5G filter to isolate the UV or visible part of the simulated sunlight spectrum. Before each measurement, the electrolyte was thoroughly flushed with N_2 gas to remove any dissolved oxygen. The same electrochemical station was also used for the electrical impedance measurement by electrochemical impedance spectroscopy.

3.3 Results and Discussions

3.3.1 Growth of defect-rich 1D Nanostructures

The SEM images shown in Figure 3.1 illustrate the effect of a SiO_2 buffer layer with different thickness on PLD growth of TiO_2 nanostructures at $700 \text{ }^\circ\text{C}$. On a pristine H-Si substrate, laser ablation of the rutile TiO_2 target for 90 min produces nanobricks with an edge length of 150-250 nm and thickness of 80-150 nm (Figure 3.1a1). Similar film morphology is also observed on pristine RCA-Si (Figure 3.1b1) and Ox-Si substrates (Figure 3.1c1), which indicates that the presence of a SiO_2 layer, irrespective of its thickness, appears to have no significant effect on the TiO_2 film growth. In Figure 3.1, we show that the mean diameters of the GNIs as-formed on the respective pristine substrates [$4 \pm 3 \text{ nm}$ for H-Si (Figure 3.1a2), $8 \pm 3 \text{ nm}$ for RCA-Si (Figure 3.1b2), and $11 \pm 3 \text{ nm}$ for Ox-Si (Figure 3.1c2)] increase with increasing SiO_2 buffer layer thickness. The formation of much smaller GNIs on H-Si than RCA-Si and Ox-Si is due to the relative ease of Au silicide formation on the H-Si surface with the thinnest SiO_2 layer.¹⁸⁴ PLD growth of TiO_2 on the GNI/H-Si template for 90 min at $700 \text{ }^\circ\text{C}$ produces mainly flake-like nanostructures (Figure 3.1a3), 300-400 nm long and 3-8 nm thick. The corresponding back-scattered electron images show that no GNI is present at the edges of these nanoflakes (Figure 3.1a4). The presence of reactive Si dangling bonds at high temperature

causes the Au atoms to bond strongly to the Si substrate,¹⁸⁴ and the resulting GNIs are therefore less prone to be lifted off. In contrast to the nanobrick film obtained on the pristine H-Si substrate (Figure 3.1a1), the growth of nanoflakes on the GNI/H-Si template suggests that GNIs act as the nucleation sites and lower the surface energies of crystal growth planes, which consequently enhance the adsorption rate of gaseous species and promote the growth of flake-like nanostructures.¹⁸⁵ On the other hand, PLD growth on the GNI/RCA-Si template under the same deposition conditions produces TiO₂ nanowires that are notably different from flake-like nanostructures (Figure 3.1b3, 3.1b4). The surfaces of these straight nanowires appear smooth, and each individual wire has a cross-sectional diameter of 10-15 nm along its entire length of several hundred nanometers. The length of the nanowires can be controlled by changing the deposition time. Evidently, the nanowires, indicating a vapour-liquid-solid (VLS) growth mechanism for these nanowires.¹⁸⁶ However, the presence of a small amount of Au at the RCA-Si substrate interface (Figure 3.1b4, inset), as in the case of GNI/H-Si (Figure 3.1a4, inset), suggests that a fraction of Au has diffused through the interfacial SiO₂ layer at high temperature during the GNI formation and/or during TiO₂ deposition, producing Au-silicides at the interface. Interestingly, PLD growth on the GNI/Ox-Si template at 700 °C produces TiO₂ nanobelts, typically 10-20 nm thick, 50-80 nm wide and several hundred nm long (Figure 3.1c3, 3.1c4). The nanobelt has a pointy, triangular tip, with periodic sawtooth faceting along the sidewalls, the latter reflecting a remarkable oscillatory growth process.¹⁸⁷ Unlike the RCA-Si and H-Si templates, the thicker SiO₂ layer on the Ox-Si template prevents Au diffusion and the subsequent Au-silicide formation, as supported by the absence of Au at the interface (Figure 3.1c4, inset).

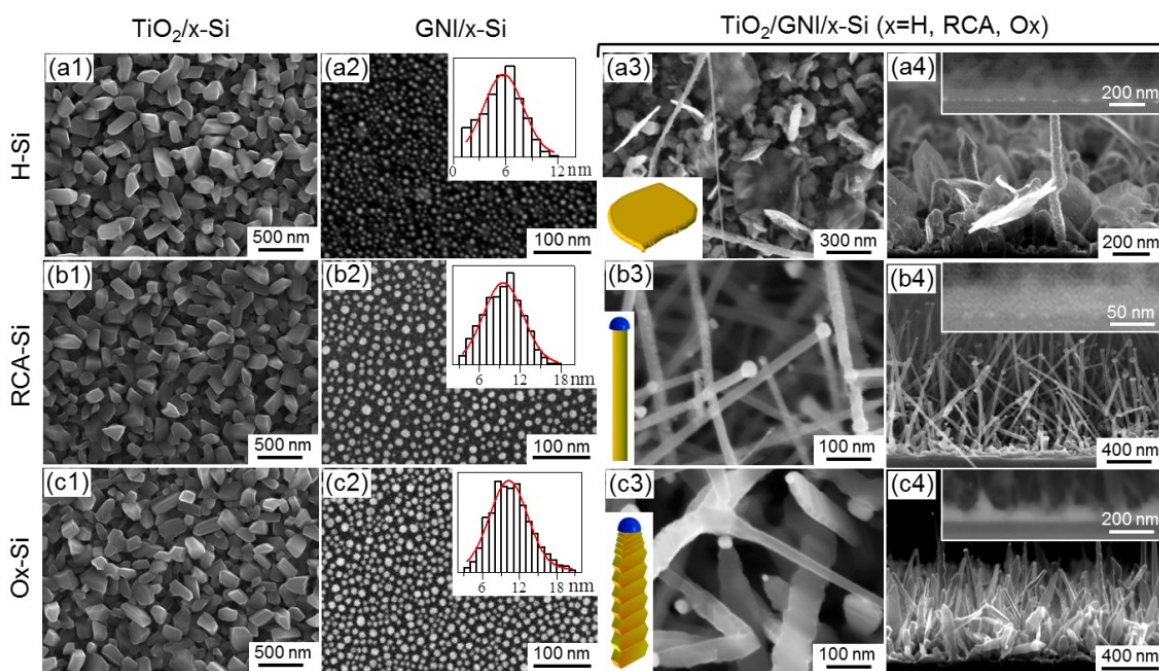


Figure 3.1 SEM images of (a1, b1, c1) typical TiO_2 nanobricks deposited in 200 mTorr Ar at 700 °C and (a2, b2, c2) typical gold nanoislands (GNIs), with the corresponding near-Gaussian size distributions (insets), formed on H-Si (top row), RCA-Si (middle row) and Ox-Si (bottom row). SEM images of the TiO_2 nanostructures grown in 200 mTorr of Ar at 700 °C on GNI/H-Si (top row), GNI/RCA-Si (middle row), and GNI/Ox-Si templates (bottom row) taken as (a3, b3, c3) top view and (a4, b4, c4) cross-sectional view. Insets in (a3, b3, c3) schematically show the respective nanostructures. Insets in (a4, b4, c4) show the corresponding cross-sectional backscattered electron images.

We have also studied the effect of deposition (substrate) temperature on the nanostructure growth. Figure 3.2 shows the SEM images of TiO_2 nanostructures grown on the three templates at 675 °C, 720 °C, and 750 °C, in addition to those obtained at 700 °C (already shown in Figure 3.1a3, 3.1b3, 3.1c3). Deposition at 675 °C produces, on all three templates, tapered corrugated nanowires with stacking faults distributed along the growth direction (Figure 3.2a1, 3.2b1, 3.2c1). Similar types of structures have also been reported for SiC ¹⁸⁸ and ZnO nanowires.¹⁸⁹ On the other hand, deposition at 720 °C on GNI/H-Si produces pebble-like particles (Figure 3.2a3), which is likely caused by complete consumption of the thin SiO_2 layer (~1 nm) via silicide formation.¹⁹⁰ As reported in earlier studies, annealing SiO_2 on Si in high vacuum condition leads to decomposition of SiO_2 via the interfacial reaction: $\text{Si} + \text{SiO}_2 = 2\text{SiO}(\text{g})$,^{191,192} and the decomposition rate is further enhanced by the presence of Au.¹⁹³ The surfaces of these pebble-like particles are decorated with small nanoparticles.

Interestingly, PLD growth at the same temperature (720 °C) on GNI/RCA-Si (Figure 3.2b3) and GNI/Ox-Si templates (Figure 3.2c3) leads to tapered nanowires also decorated with nanocrystallites on the surface, in marked contrast to the straight nanowires with smooth surfaces found on GNI/RCA-Si at 700 °C (Figure 3.2b2). The nanocrystallites are also been confirmed by helium ion microscopy images (not shown). These decorated nanowires are found to be 0.8-1.5 μm long, with an average diameter of 50-70 nm. Closer examination reveals that the nanocrystallites on these decorated nanowires are more concentrated at the base, and the surface of the decorated nanowires grown on GNI/Ox-Si (Figure 3.2c3) appears to be rougher than that of the decorated nanowires on GNI/RCA-Si (Figure 3.2b3). Deposition on the GNI/H-Si template at a higher temperature (750 °C) produces pebble-like structures (Figure 3.2a4) similar to those obtained at 720 °C (Figure 3.2a3). On GNI/RCA-Si, nanoflakes and pebble-like particles are observed at 750 °C (Figure 3.2b4) and 770 °C (not shown), respectively, likely due to the gradual consumption of thin SiO_2 layer (3 nm) via the interfacial reaction. In contrast to the GNI/H-Si (Figure 3.2a4) and GNI/RCA-Si templates (Figure 3.2b4), nanowires decorated with larger nanocrystallites grown on GNI/Ox-Si at 750 °C (Figure 3.2c4) or higher temperature are observed. In Figure 3.3, we schematically summarize the different 1D TiO_2 nanostructures obtained on the three templates: GNI/RCA-Si, GNI/H-Si and GNI/Ox-Si, with the respective estimated thicknesses for the SiO_2 buffer layer of 1 nm, 3 nm, and 30 nm, at different growth temperatures.

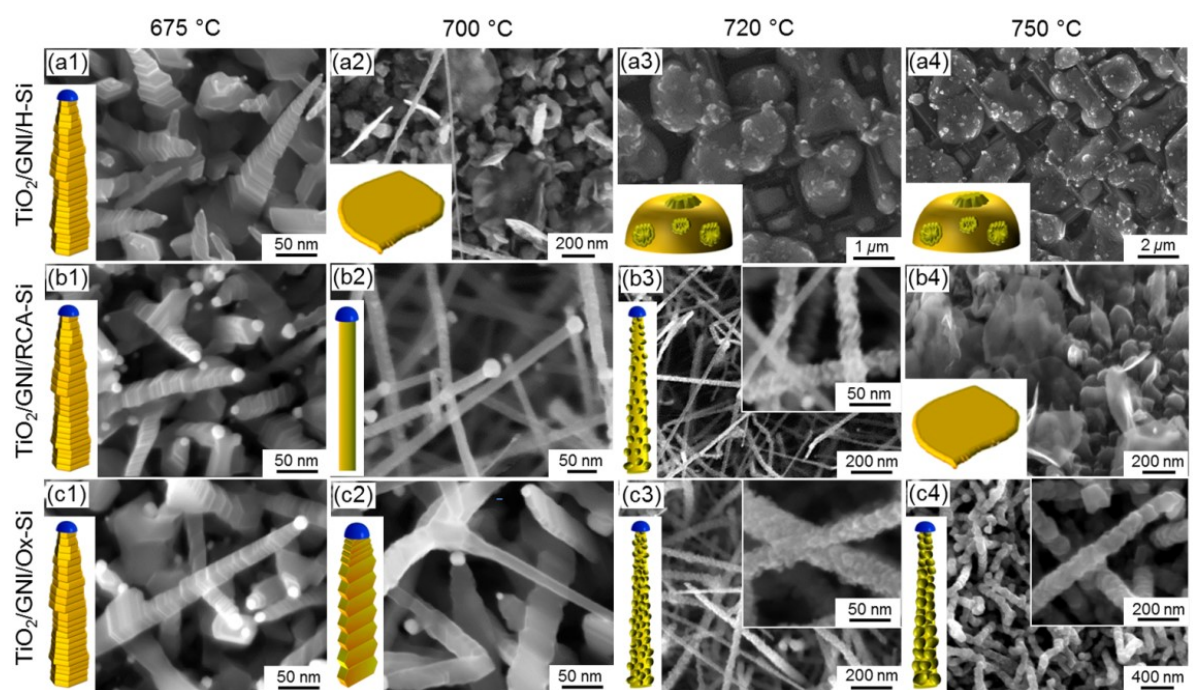


Figure 3.2 SEM images of TiO₂ nanostructures grown in 20 mTorr Ar at (a1, b1, c1) 675 °C, (a2, b2, c2) 700 °C, (a3, b3, c3) 720 °C, and (a4, b4, c4) 750 °C on GNI/H-Si (top row), GNI/RCA-Si (middle row) and GNI/Ox-Si templates (bottom row). The corresponding lower left insets show schematic models of the respective as-grown nanostructures, with the magnified SEM images of selected nanostructures shown in the upper right insets.

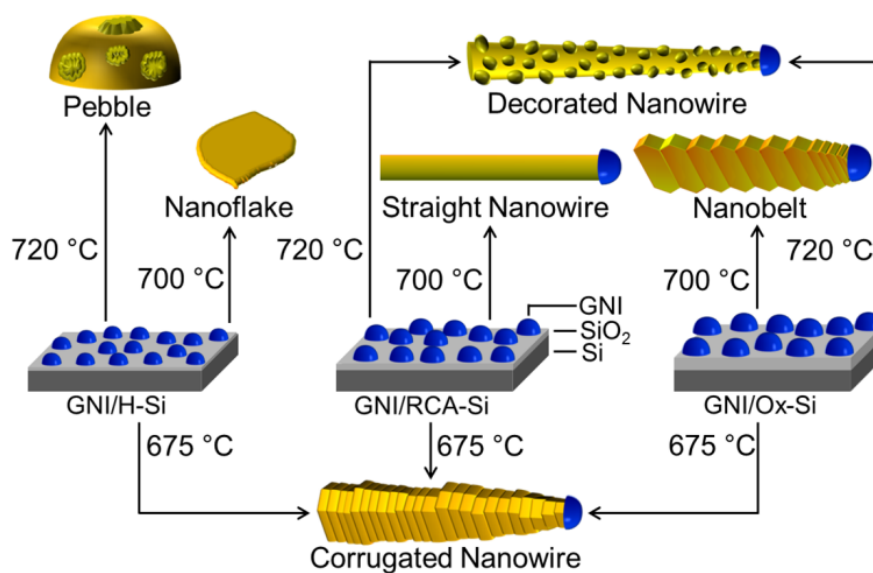


Figure 3.3 Schematic models of TiO₂ nanostructures grown on gold nanoisland (GNI) modified Si(100) templates at 675, 700 and 720 °C.

Figure 3.4 shows the corresponding transmission electron microscopy (TEM) images of representative TiO₂ nanostructures, including corrugated nanowires (Figure 3.2b1), straight nanowires (Figure 3.2b2), decorated nanowires (Figure 3.2b3), and nanobelts (Figure 3.2c2). The rugged edges of the nanobelts (Figure 3.4a) and corrugated nanowires (Figure 3.4b) are clearly observed, while the surface of the straight nanowires appears to be smooth (Figure 3.4c). For the decorated nanowires (Figure 3.4d), the outer shell consists of nanocrystallites of 3-5 nm in size. The corresponding high-resolution TEM images (Figure 3.4, insets) show that all the nanostructures are single-crystalline and have an interplanar spacing of 3.2 Å, corresponding to the (110) plane of bulk rutile TiO₂. Interestingly, the same rutile TiO₂ interplanar spacing is also found for individual nanocrystallites on the decorated nanowire (Figure 3.4d, top inset). The corresponding lattice planes appear to be not perfectly aligned and disordered at the edges of the nanocrystallite (Figure 3.4d, top inset), indicating the presence of crystalline defects, including dislocations and local strains.¹⁹⁴ To further investigate the nature of crystallinity of the predominant nanostructures, we compare the glancing-incidence X-ray diffraction (XRD) patterns of as-deposited nanostructures in Figure 3.5. The prominent diffraction peaks are in good accord with the typical rutile structure of TiO₂ (PDF2 00-021-1276) and FCC phase of metallic Au (PDF2 00-041-0784). Of particular interest is the remarkably different relative peak intensities of the prominent peaks at 27.4° (110), 36° (101) and 54.3° (211) with respect to the reference pattern of powder TiO₂ (PDF2 00-021-1276). Evidently, the higher intensity ratios of the (110) peak to (101) peak in all the nanowires and of (110) peak to (211) peak in nanobelts than those in the reference pattern indicates that they have a preferred (110) growth orientation (in good accord with our TEM data).

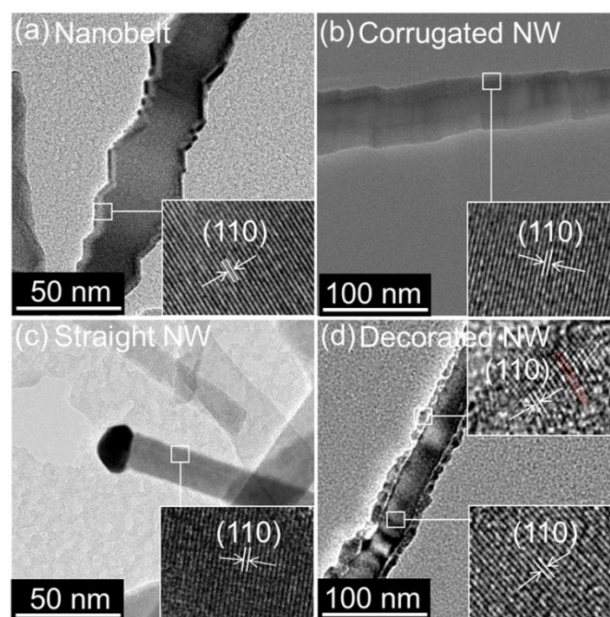


Figure 3.4 TEM images of a typical (a) TiO_2 nanobelt, (b) corrugated nanowire (NW), (c) straight nanowire, and (d) decorated nanowire. Lower-right insets show the corresponding high-resolution TEM images, while the upper-right inset in (d) depicts the high-resolution TEM image of a nanocrystallite.

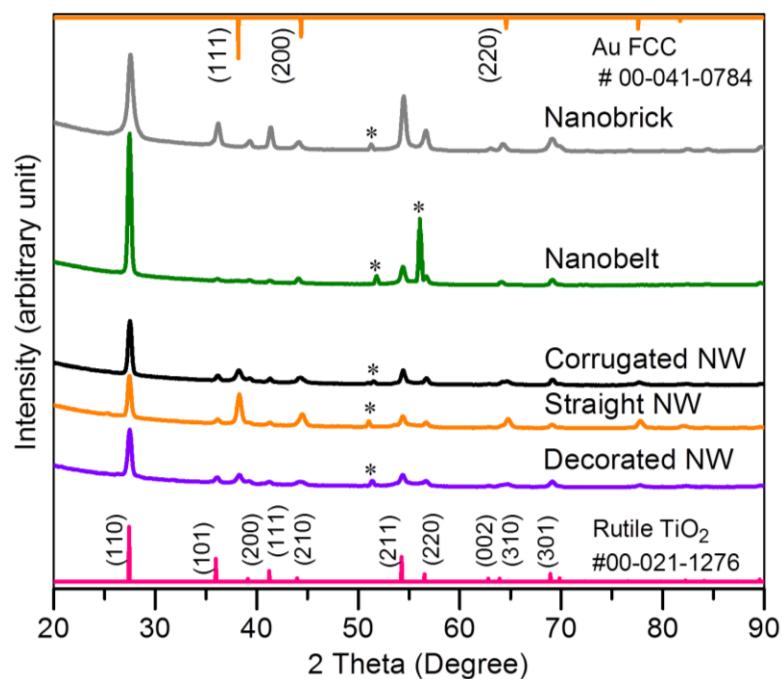


Figure 3.5 Glancing-incidence XRD patterns of different rutile TiO_2 nanostructures obtained at an incidence angle of 0.4° . The PDF2 reference patterns of the FCC phase of Au (#00-041-0784) and of rutile TiO_2 (#00-021-1276) are shown as top and bottom bar graphs, respectively. The features marked by asterisks (*) correspond to the modified Si substrate.

As noted previously for other material systems,^{195,196} the growth temperature can affect the catalyst state and, consequently, the predominant growth mode, i.e. vapour-solid growth below the eutectic temperature or VLS growth at or above the eutectic temperature, which ultimately governs the length and diameter of the nanowire. It has been observed that both vapour-solid and VLS growth can occur simultaneously, with the vapour-solid growth generally 10-100 times slower than VLS growth at the same precursor partial pressure and temperature.¹⁹⁶ In the present study, the growth temperature (675-750 °C) for the nanowires is lower than the lowest eutectic temperature in the bulk Au-Ti binary system (832 °C).¹⁹⁷ It should be noted that VLS growth could occur concurrently, the VLS growth predominates at the higher growth temperature and the slower vapour-solid growth at a particular growth temperature could perturb and thus introduce variations into the general morphology of the nanowires. Formation of tapered shape for the decorated nanowires has been attributed to the additional uncatalyzed vapour-solid growth occurring at the sidewall, and to the longer exposure of the vapour to the base area compared to the tip area that ultimately affects the cross sectional shape of the nanowires.⁶³ The presence of a greater number of nanocrystallites on the decorated nanowires as-grown on GNI/Ox-Si than those on GNI/RCA-Si at a particular growth temperature suggests that the thicker, thermally grown SiO₂ layer (on Ox-Si) is rougher and has a different heat transfer efficiency than RCA-grown SiO₂, which ultimately affects the surface mobility, nucleation sites, and supersaturation rate of TiO₂, all of which control the morphology of the 1D nanostructures at a given temperature.¹⁹⁸ Our results also suggest that a minimum SiO₂ layer thickness of 3 nm (as formed on the RCA-Si substrate) is necessary for enabling VLS nanostructure growth in the PLD method, and a thicker SiO₂ or protective buffer layer is required for the growth of nanowires at a higher temperature. A buffer layer has been used in thermal evaporation and other methods for similar reasons,⁷ but the thickness of the buffer layer so employed has been considerably larger than 3-5 nm.^{66,177} For example, TiO_x nanowires on Si interaction between GNI and Si substrate in terms of Au silicide formation and to provide a source of oxygen during growth in Ar ambient. The thickness of the SiO₂ buffer layer therefore plays a critical role in the growth of TiO₂ nanowires on a Si substrate. Formation of different 1D nanostructures at different growth temperatures on GNI/RCA-Si (corrugated nanowires at 675 °C, straight nanowires at 700 °C, and decorated nanowires at 720 °C) and on GNI/Ox-Si (corrugated nanowires at 675 °C, nanobelts at 700 °C, and decorated nanowires at 720 °C or higher temperature) therefore confirms that both the growth temperature and the thickness of the SiO₂ buffer layer can be used complementarily to control the morphology of the 1D nanostructures.

In Figure 3.6a, we show the changes in the colour of the as-deposited nanostructured films from blue (corrugated nanowires) to deep blue (straight nanowires) to greyish black (decorated nanowires), and then to lighter blue (nanobelts and nanobricks). It should be noted that the colours so observed for these nanostructured films remain unchanged for the respective films obtained with deposition longer than 40 min. Moreover, the samples retain their individual colour upon storage at ambient atmosphere for over a year, indicating the robustness of these nanostructured films and that Ti^{3+} and/or oxygen vacancy defects are located in the bulk and not just at the surface of these nanostructures. Similar colour changes in TiO_2 due to difference in growth temperature and oxygen partial pressure as employed in flame reduction method have also been reported.¹⁹⁹ Furthermore, hydrogen treatment has been used to create a high density of oxygen vacancies, which changed the colour of rutile TiO_2 from white to yellowish green and finally to black.⁸ Recently, Ti^{3+} -related bulk defects in rutile TiO_2 have been found to exhibit five different colours, and the crystal colour appeared to correlate directly with the amount of defects.²⁰⁰ Based on these studies and our experimental results, we hypothesize that the different colours for corrugated (light blue), straight (dark blue) and decorated nanowires (greyish black) are due to the differences in the amount of defects.

This series of colours should correlate with the respective degree of sub-stoichiometry of TiO_2 in these nanostructured films,²⁰¹ which is in good accord with our X-ray photoelectron data shown in Figure 3.6b. For all the samples, the prominent Ti $2p_{3/2}$ peak at 459.4 eV corresponds to the Ti^{4+} state attributable to TiO_2 , while the shoulder at 458.0 eV could be assigned to Ti^{3+} state in TiO_x ($2 > x > 1$).^{202,203} Four O 1s peaks at 530.7, 531.1, 532.6 and 533.3 eV correspond to TiO_2 , TiO_x , SiO_2 , and SiO_x , respectively.^{203,204} The fitted O 1s intensity ratios for $\text{TiO}_x/\text{TiO}_2$ and $\text{SiO}_x/\text{SiO}_2$ of the nanowires prepared on the GNI/RCA-Si template follow the ordering: decorated nanowires (720 °C) > straight nanowires (700 °C) > corrugated nanowires (675 °C), in close correlation with the growth temperature and sample colour (Figure 3.6a). The Si $2p_{3/2}$ ($2p_{1/2}$) peaks at 102.6 (103.3) and 103.5 (103.2) eV correspond to SiO_2 and SiO_x , respectively.²⁰⁴ For decorated nanowires, the Ti $2p_{3/2}$ peak width is found to be discernibly larger (Figure 3.7), which further supports the presence of a larger amount of oxygen vacancy defects in decorated nanowires than the other nanostructures.²⁰⁵ The higher the growth temperature, the more reduced TiO_2 has become in the present synthesis conditions. On the other hand, the O 1s intensity ratio for $\text{TiO}_x/\text{TiO}_2$ of the nanobelts, deposited at the same temperature as that for straight nanowires on GNI/RCA-Si (700 °C) but on a GNI/Ox-Si template, is found to be smaller, which is consistent with the thicker SiO_2 layer on the GNI/Ox-Si

template serving as a source of oxygen during growth in an Ar atmosphere. Less oxygen vacancy defects can therefore be expected in nanobelts than the nanowires grown on GNI/RCA-Si templates. As a result, the colour of the nanobelt film is lighter than the nanowire film (Figure 3.6a). The corresponding reflectance spectra of the nanostructures all exhibit broadband absorption, starting at 330 nm and extending into visible region of the spectrum (Figure 3.8). The intensity of the reflectance band increases with decreasing growth temperature for the nanowires, and with larger interfacial SiO₂ layer thickness for the nanobelts, which is also consistent with the colour change of the samples. We have also calculated the bandgaps by using the Tauc plots (Figure 3.9). The band gap is determined to be 2.68 eV for the decorated nanowire, 2.86 eV for straight nanowire, 2.91 eV for corrugated nanowire, and 2.98 eV for the nanobelt. The visible light absorbance of the TiO₂ nanowires could be mainly attributed to the existence of defect states in the TiO₂ band gap,^{11,182} likely due to the presence of Ti³⁺ defects and oxygen vacancies in accordance with the XPS analysis.

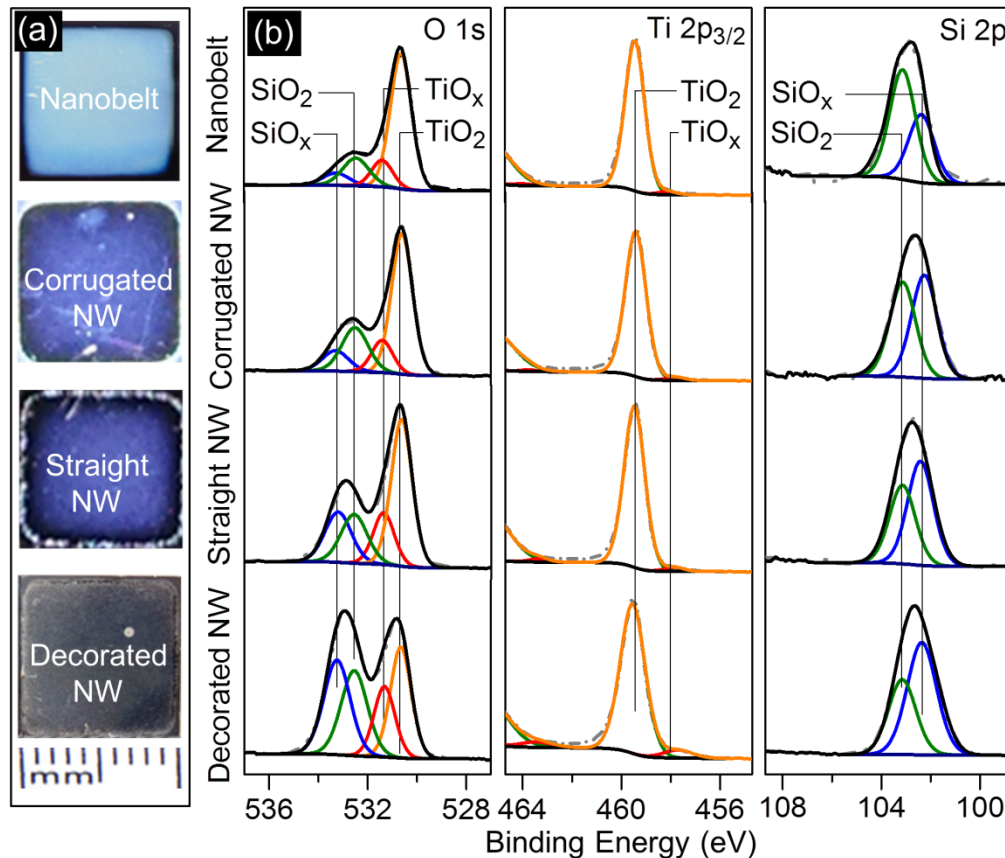


Figure 3.6 (a) Photographs and (b) XPS spectra of O 1s, Ti 2p_{3/2}, and Si 2p regions of TiO₂ nanostructured films consisting of nanobelts, corrugated nanowires (NWs), straight NWs, and decorated NWs.

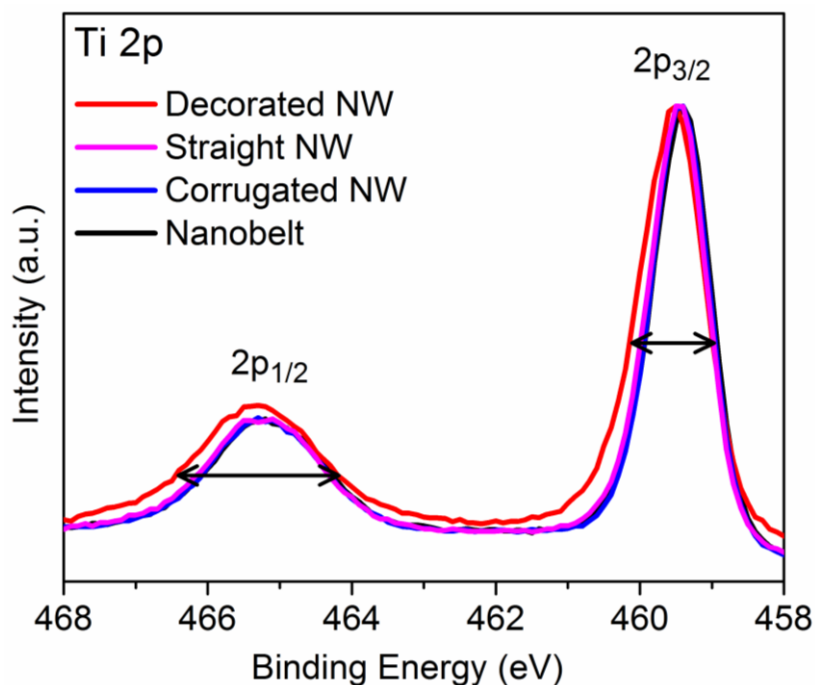


Figure 3.7 XPS spectra of the Ti 2p region, relatively normalized at the Ti 2p_{3/2} peak maxima, for TiO₂ nanobelts, corrugated nanowires (NWs), straight NWs, and decorated NWs. The arrows indicate the full widths at half maxima of 2p_{3/2} and 2p_{1/2} peaks of the decorated NWs.

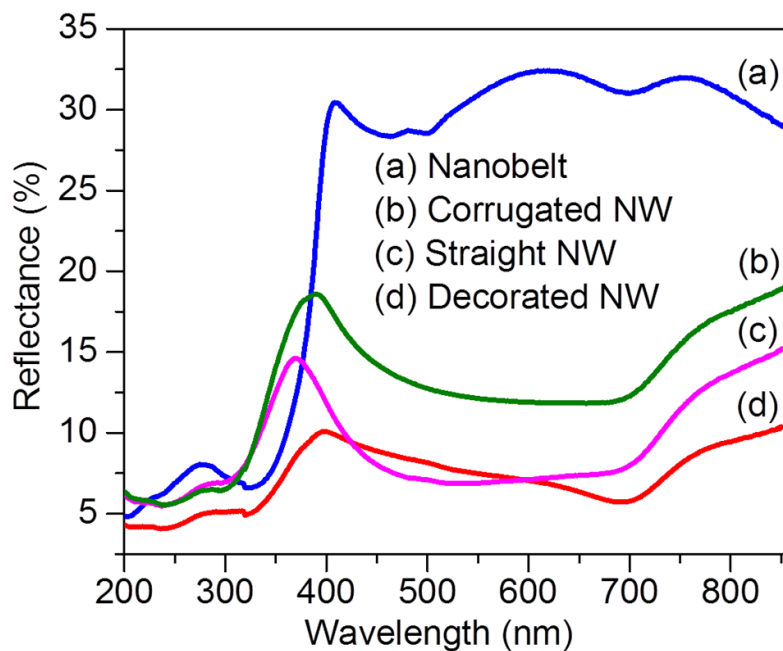


Figure 3.8 UV-Vis reflectance spectra of TiO₂ nanobelts, corrugated nanowires (NWs), straight NWs, and decorated NWs.

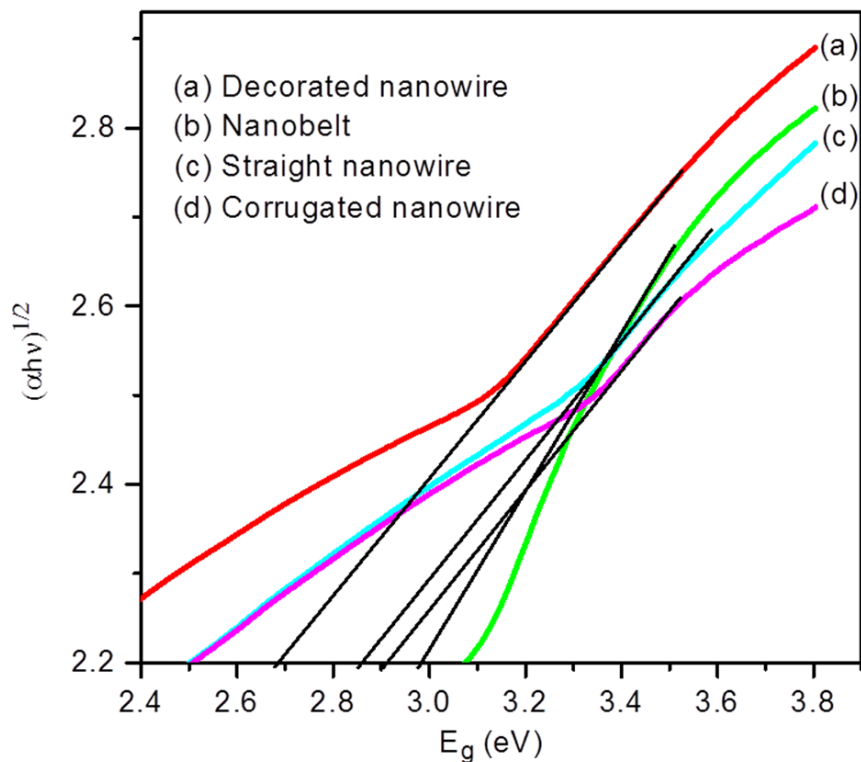


Figure 3.9 Tauc plots for PLD-grown 1D TiO₂ nanostructured films.

The slight deviation from perfect stoichiometry could result in a significant change in the electrical property of the TiO₂ nanostructured films.¹⁰ Figure 3.10a shows the corresponding Nyquist plots for the nanostructured films under simulated sunlight illumination obtained by potentiostatic electrochemical impedance spectroscopy. Using the equivalent circuit model shown in Figure 3.10b, we determine the series resistance (R_S), the resistance (R_D) and chemical capacitance (CPE_D) of the semiconductor depletion layer in an RC circuit, along with the charge transfer resistance in the Helmholtz layer (R_H), the Warburg diffusion impedance (Z_W), and the capacitance of the electrochemical double layer (CPE_H) in a second RC circuit in series. The electrical parameters obtained by fitting the experimental data with the equivalent circuit are summarized in Table 3.1. The fitted data shows that the charge transfer resistances (R_S , R_D , and R_H) increase (while the capacitance decreases) in the following ordering: decorated nanowires < straight nanowires < corrugated nanowires < nanobelts, in close correlation with the observed oxygen vacancy and crystal colour. The higher charge transfer resistances of nanobelts might also be caused by the thicker interfacial SiO₂

layer, which ultimately reduces the collection efficiency of photogenerated electrons. Interestingly, the charge transfer resistance (R_D) at the depletion layer of decorated nanowires has become significantly smaller while the corresponding capacitance (CPE_D) has increased concomitantly, which suggests that the nanocrystallites of the decorated nanowires contain a large amount of oxygen vacancy defect states, likely in the band gap of the TiO_2 nanocrystallites. The sub-stoichiometric TiO_x ($2 > x > 1$) therefore possesses numerous advantages over stoichiometric TiO_2 because reduced TiO_x has higher absorbance, wettability,²⁰⁶ and conductivity that are important to photoelectrochemical applications.

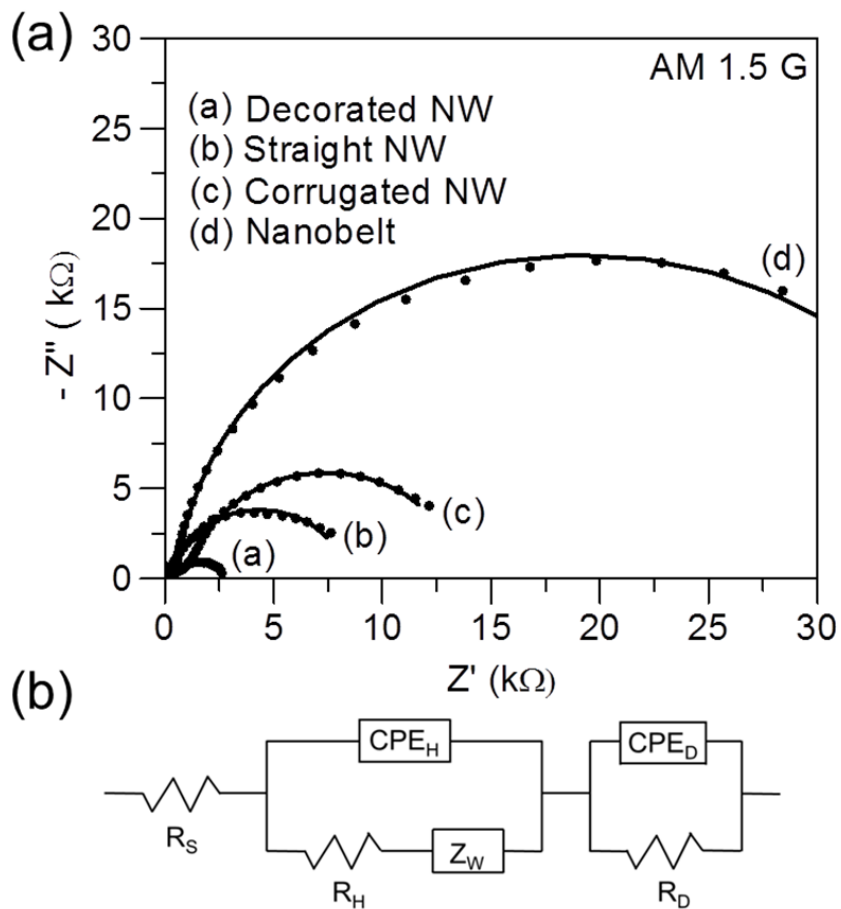


Figure 3.10 Nyquist plots of predominant TiO_2 nanostructured films (a) under illumination of simulated sunlight (100 mW/cm^2). The experimental data (symbols) are collected in a frequency range between 0.01 Hz and 100 Hz with an ac voltage amplitude of 10 mV and a dc bias of -0.5 V , and they are fitted with (b) an equivalent circuit model (solid lines).

Table 3.1 Parameters extracted from fitted results of electrochemical impedance spectra for TiO₂ nanostructured films under simulated sunlight.

| | AM 1.5 G | | |
|---------------------|--------------------|--|--|
| | R _S (Ω) | R _H (kΩ) CPE _H (μF) | R _D (kΩ) CPE _D (μF) |
| Nanobelt | 254 | 20 110 | 33 2.7 |
| Corrugated Nanowire | 35.0 | 2.1 130 | 8.0 56 |
| Straight Nanowire | 32.8 | 1.6 221 | 6.9 92 |
| Decorated Nanowire | 20.5 | 1.4 264 | 1.3 210 |

3.3.2 Photoelectrochemical properties

To study the photocatalytic activity of the aforementioned nanostructures for photoelectrochemical water splitting reaction, we employ, as photoanodes, TiO₂ nanobricks (grown on a pristine RCA-Si substrate, Fig. 1b1), corrugated nanowires (on a GNI/RCA-Si template, Fig. 2b1), straight nanowires (on a GNI/RCA-Si template, Fig. 2b2) and decorated nanowires (on a GNI/RCA-Si template, Fig. 2b3), as well as nanobelts (produced on a GNI/Ox-Si template, Fig. 2c2). The photocurrent spectra have been obtained over an illuminated sample area of 0.2 cm² under simulated sunlight illumination at 100 mW/cm² from a 300 W xenon lamp coupled with an AM 1.5G filter. In-situ quantification of the evolved gases by using an Universal Gas Analyser (Stanford Research Systems, SRS-UGA) (Figure 3.11). As shown in the Figure 3.11, we monitor the partial pressures of H₂, O₂, N₂, H₂O and CO₂ with light off and light on during the water-splitting

reaction. Evidently, only H₂ and O₂ pressures are found to increase as the reaction commences (with light on) while those of all the other gases remain flat and unchanged. The pressure change for H₂ ($\Delta P = 18 \times 10^{-8}$ Torr) is found to be almost twice (1.8 times) that of O₂ ($\Delta P = 10 \times 10^{-8}$ Torr), which confirms stoichiometric splitting of water. It should be noted that the amount of time for the evolved gases to reach saturation will depend on the amount of catalysts on the sample and the efficiency of gas production (both of which will affect the amounts of H₂ and O₂ produced by the water-splitting reaction), as well as the volume of space above the liquid solution in the beaker. Evidently, it only takes about 20 minutes for the produced gases to displace the air in the volume above the solution.

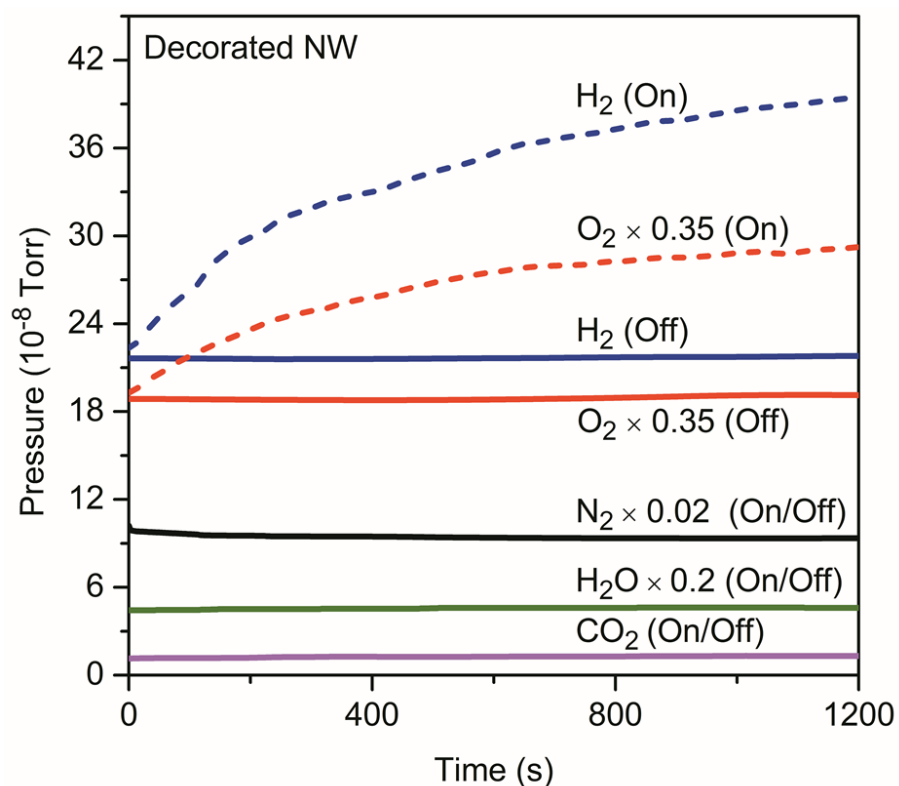


Figure 3.11 Quantification of gas evolution for photoelectrochemical water splitting reaction with decorated TiO₂ nanowires as the photoanode with light on and light off.

The photocurrent density measured at 0.5 V (vs Ag/AgCl) for the decorated nanowires (1.5 mA/cm²) is found to be 8.3, 6.0, 2.5, and 1.6 times those of nanobelts (0.18 mA/cm²), nanobricks (0.25 mA/cm²), straight nanowires (0.6 mA/cm²), and corrugated nanowires (0.94 mA/cm²),

respectively (Figure 3.12a). We also characterize and obtain essentially no photocatalytic activity for the pristine RCA-Si substrate and GNI/RCA-Si template under the same conditions (Figure 3.12a). The photogenerated holes in Si cannot be easily transferred to the valence band of TiO₂, likely due to a significant barrier at the junction resulting in carrier recombination in Si.²⁰⁷ The higher photocurrent density observed for the decorated nanowires (and other nanostructures) can therefore be attributed only to the photogenerated charge carriers from the TiO₂ nanostructures themselves. The decorated nanowires provide one of the best photoelectrochemical performance among the TiO₂ nanostructures reported to date. The measured photocurrent density for the decorated nanowires (1.5 mA/cm² at 0.5 V) in the present work is higher than those for most TiO₂ nanomaterials, including a modified rutile TiO₂ nanowire array obtained by depositing an epitaxial rutile TiO₂ shell onto a hydrothermally prepared rutile TiO₂ nanowire array (1.1 mA/cm² at 0.5 V),¹⁷² a hierarchical branched rutile TiO₂ nanorod array with the surface of the TiO₂ nanorod trunks covered by short needle-shaped TiO₂ branches (0.83 mA/cm² at 0.7 V),²⁰⁸ a N-modified rutile TiO₂ nanowire array with a cobalt cocatalyst (0.8 mA/cm² at 0.7 V),¹⁷⁰ a TiO₂ nanoforest prepared by depositing dense TiO₂ nanorods along the entire TiO₂ nanotube trunk (0.75 mA/cm²),²⁰⁹ and an anatase TiO₂ nanotube array decorated with Ag nanoparticles (0.05 mA/cm²).²¹⁰ Our current density is also comparable to that of flame-reduced TiO₂ nanowires (1.5 mA/cm² at 0.58 V), where a complicated flame reduction method was used to control the oxygen vacancies by manipulating a minute variation of reduction time (a few seconds) or by adjusting slight change in the fuel-to-air ratio.²¹¹

To quantitatively evaluate the efficiency of photoelectrochemical hydrogen generation from our TiO₂ nanostructures, the photoconversion efficiency is calculated by using the equation,²¹² $\eta (\%) = j_p \frac{(1.23-V)}{I_0} \times 100$, where j_p is the photocurrent density (in mA/cm²) at the applied voltage V [vs reversible hydrogen electrode (RHE)], and I_0 is the illumination intensity (i.e. 100 mW/cm² for AM 1.5G).^{8,170} A maximum photoconversion efficiency of 2.4% at -0.3 V vs Ag/AgCl (or 0.7 V vs RHE) is found for the decorated nanowires, followed by the corrugated nanowires (1.8% at -0.4 V vs Ag/AgCl), straight nanowires (0.95% at -0.33 V vs Ag/AgCl), nanobricks (0.32 % at -0.44 V vs Ag/AgCl), and nanobelts (0.11% at -0.09 V vs Ag/AgCl), as shown in Figure 3.12b. The lowest maximum photocurrent density found for the nanobelts can be attributed to the thicker SiO₂ buffer layer on the GNI/Ox-Si template, which impedes the photogenerated carrier transfer from the TiO₂ surface to the Pt counter electrode. The lower photocatalytic activity of the nanobricks on the RCA-Si template compared to nanowires is due to a shorter average length and a

lower density of the as-grown nanobricks, and therefore a smaller specific surface area available for the water oxidation reaction. On the other hand, the higher photocatalytic activities of the decorated nanowires and corrugated nanowires compared to straight nanowires are attributed to the different morphologies of the nanowires. For the decorated nanowire, the shell consisting of densely packed ultrasmall nanocrystallites (3-5 nm) introduces jagged surface at the nanowire. The “bumpy” surface evidently provides extra surface area for the photoelectrochemical reaction, while the junctions between the nanocrystallites act as additional active sites for oxygen production reaction.²¹³ Similarly, rugged surface and nanojunctions in corrugated nanowires account for the observed higher catalytic activity than straight nanowires, but less than the decorated nanowires. Furthermore, to investigate the chemical and structural stabilities during photoelectrochemical water splitting, we perform chronoamperometric (current vs time) studies with light on/off cycles at 100 mW/cm² at 0 V vs Ag/AgCl (or 1.0 V vs RHE), at which potential the photocurrent density has reached a plateau region (Figure 3.12a). A typical measurement on the decorated nanowires shows a stable photocurrent density of 1.06 mA/cm² with degradation of only 2.0% after 9 on/off cycles (Figure 3.12c). (The corresponding Faradaic efficiency is estimated to be 95.1%.) The catalysts remain active even after six hours of photoelectrochemical water-splitting reaction (Figure 3.13). Similar stability tests have also been made on other nanostructures and they show virtually no degradation over repeated cycling and extended use.

The decorated nanowires have high surface area, which reduces the required current density per unit surface area, but it may also introduce more surface recombination. So the final improvement on performance may come from the coupled effects of charge separation and oxidation on surface. To verify the recombination loss, we perform an experiment with the presence of a hole scavenger (0.5 M Na₂SO₃) for the decorated nanowire and straight nanowire samples (the latter has a smaller surface area than the former). As shown in the Figure 3.14, no significant change in the saturation photocurrent density and onset potentials is observed in the presence of the hole scavenger for both decorated and straight nanowire samples. For the straight nanowire sample, the two curves are essentially the same, which indicates insignificant recombination loss. For the decorated nanowire sample, we observe a minor amount of recombination current (as evidenced from the difference of the saturated current density potentials), which indicates the increase in surface area plays a more important role in photocurrent enhancement than that in recombination loss.

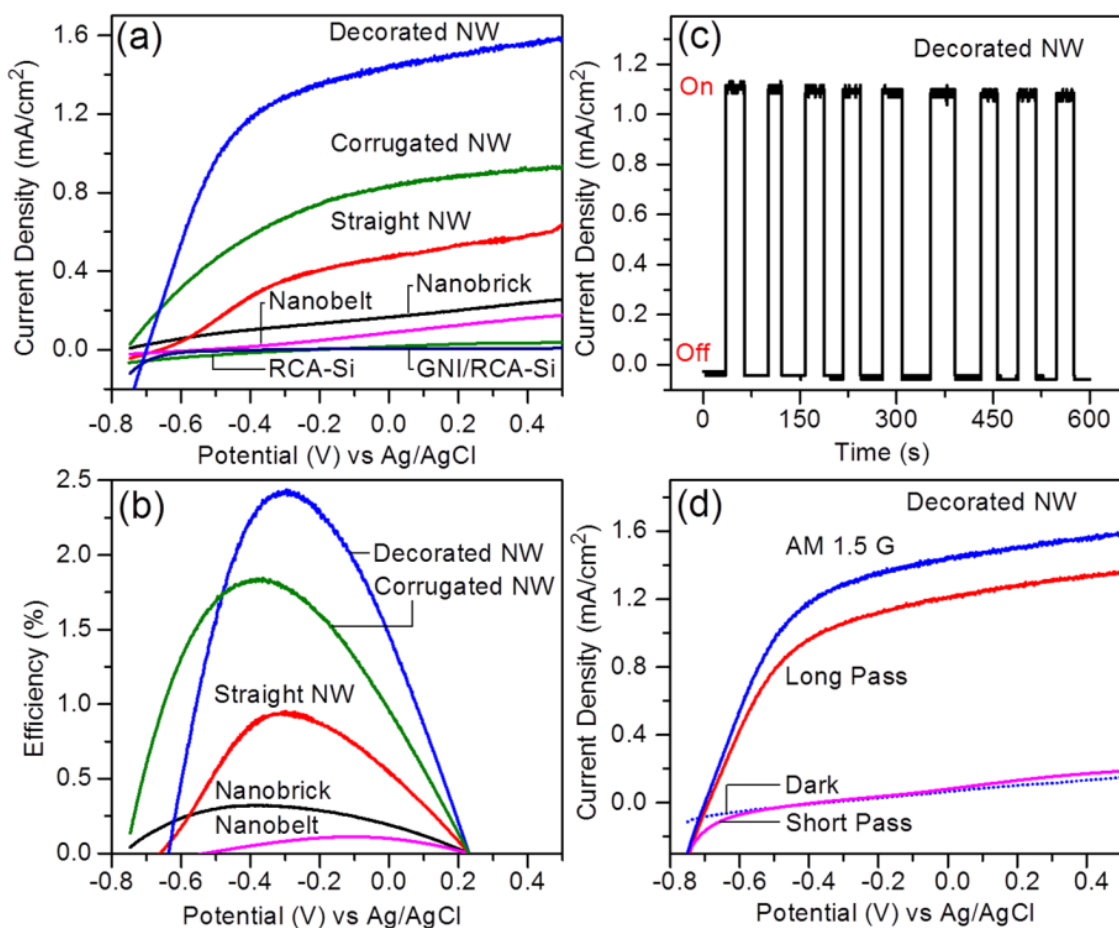


Figure 3.12 (a) Current density and (b) the corresponding photoconversion efficiency measured as a function of applied potential from different TiO₂ nanostructured photoanodes and from pristine RCA-Si, and RCA-Si/GNI templates (used as the control). The measurements are performed in a 1M KOH solution with a scan rate of 10 mV/s under 100 mW/cm² simulated sunlight illumination with a AM 1.5G filter. (c) Photocurrent density of decorated nanowires for repeated on/off cycles of simulated sunlight illumination. (d) Linear sweep voltammograms of decorated TiO₂ nanowire photoanode from an AM 1.5 G light (100 mW/cm²) and with long-pass (>430 nm) and short-pass (<400 nm) filters.

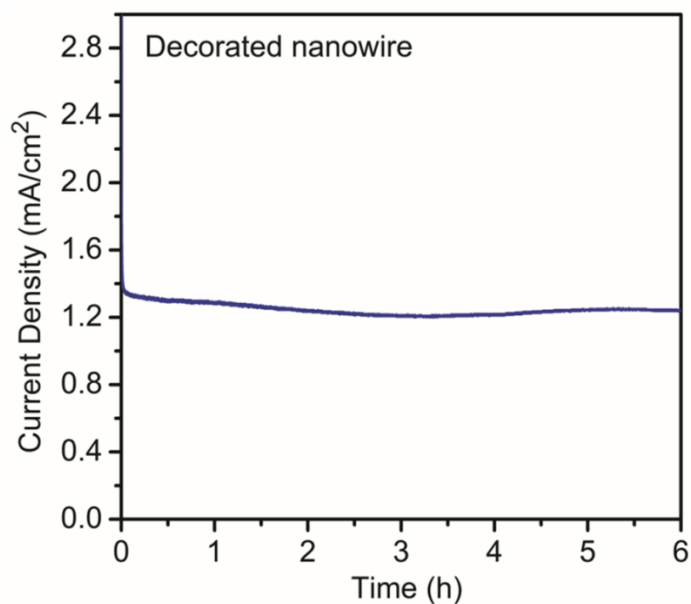


Figure 3.13 Photocurrent density of decorated TiO_2 nanowire at -0.2 V versus Ag/AgCl in 1 M KOH solution under simulated sunlight.

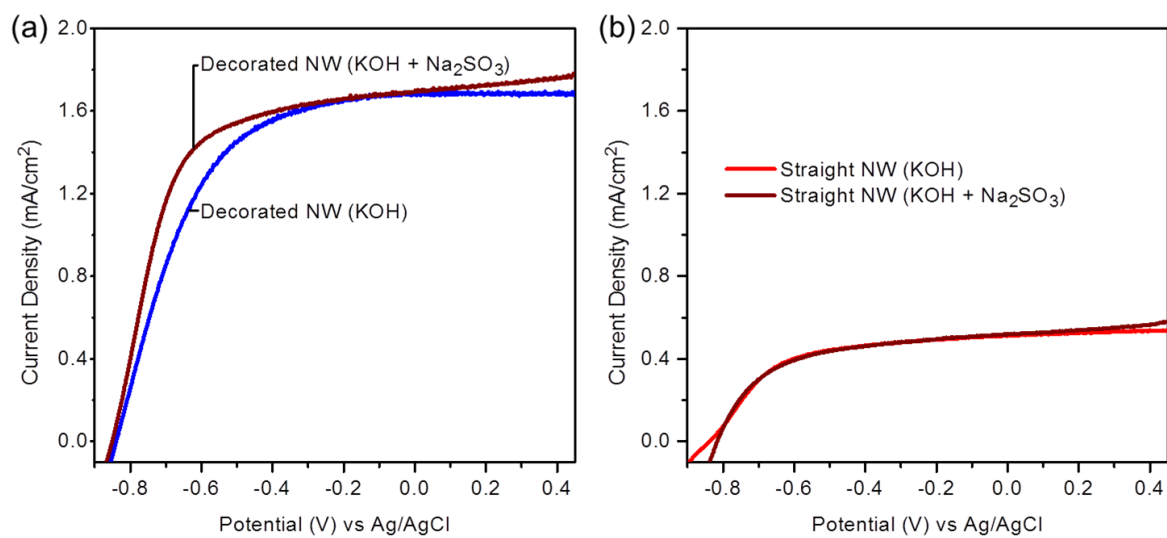


Figure 3.14 Current density measured as a function of applied potential for (a) decorated and (b) straight nanowires in 1M KOH and 1M KOH-0.5M Na_2SO_3 under simulated solar light illumination.

Since TiO₂ is expected to be photoelectrochemically active mainly under UV light illumination due to its wide band gaps: 3.2 eV (388 nm) for anatase and 3.0 eV (410 nm) for rutile phase, and given that the AM 1.5G light contains only a small UV component, we determine the photocurrent densities arising from separate UV and visible spectral illuminations by coupling the AM 1.5G light with appropriate short-pass (<400 nm) and long-pass filters (>430 nm), respectively. As shown in Figure 3.12d, the photocurrent density of decorated nanowires is reduced slightly from 1.5 mA/cm² to 1.4 mA/cm² when a long-pass filter is coupled with the AM 1.5G filter, and to effectively dark current density (0.18 mA/cm²) when a short-pass filter is used. The photocurrent density observed for the decorated nanowire sample therefore mainly comes from the longer wavelength region (>430 nm), i.e. the visible light region. This is a significant result, because unlike the previously reported case for rutile TiO₂ nanowire arrays decorated with Au nanoparticles,¹⁷¹ where the observed photocurrent density (1.8 mA/cm²) in AM 1.5G light was found to reduce by nearly 50% to 0.96 mA/cm² with UV light component (<430 nm) and to 0.00267 mA/cm² with visible light component (>430 nm), we observe only a 13% reduction with just the visible light component in the present work. Our visible light current density is also significantly higher than those reported for highly dense Si core TiO₂ shell nanowire arrays, obtained by depositing a polycrystalline anatase TiO₂ layer on a Si nanowire array, which gave zero photocurrent density under visible light.²⁰⁷ Similarly, for H₂-treated TiO₂ nanowires⁸ and Sn-doped TiO₂ nanowires,²¹⁴ almost zero photocurrent density were observed in the visible light (> 430 nm). These results verify that our decorated nanowire sample is the top photoelectrochemical catalysis performer in the visible light (>430 nm) reported to date.

It has been reported that the band gap of TiO₂ and the amount of oxygen vacancy defects depend on the crystallite size. For example, when the crystallite size is decreased from 17 to 3 nm, the band gap is reported to increase from 3.2 to 3.6 eV and the deviation from stoichiometry (due to the presence of oxygen vacancies) has also increased with increasing Ti³⁺ concentration.¹⁹⁹ Meanwhile, oxygen vacancies are found to introduce defect states below the conduction band of TiO₂.^{11,182} The smaller (3-5 nm) rutile nanocrystallites on the decorated nanowires would therefore have a larger band gap than the single-crystalline nanowire host but possess defect states close to the conduction band minimum. A schematic band alignment diagram for the enhancement mechanism of photoelectrochemical properties of decorated nanowires is shown in Figure 3.15. When the decorated nanowires are irradiated with AM 1.5G light, electron transfer takes place from both valence band (VB) and oxygen vacancy defect states to the conduction band (CB) of TiO₂ nanocrystallites. The

photon-excited electrons in the nanocrystallites are then injected into the conduction band of the core nanowires, while the photogenerated holes of nanocrystallites react with the donor species of the electrolyte. Owing to the single-crystalline nature of the nanowire core, the electrons in the conduction band of the nanowire could migrate easily to the Si substrate and ultimately to the counter electrode. The higher photocurrent density obtained from the decorated TiO₂ nanowires can therefore be attributed to the dense mat of nanowires²¹⁵ with densely packed TiO₂ nanocrystallites at the outer surface. These nanocrystallites offer excellent light-trapping characteristics, a large contact area with the electrolyte, and a highly conductive pathway for charge carrier collection, while the presence of a large number of oxygen vacancy defects in these nanocrystallites provides superior photoelectrochemical performance in the visible region.

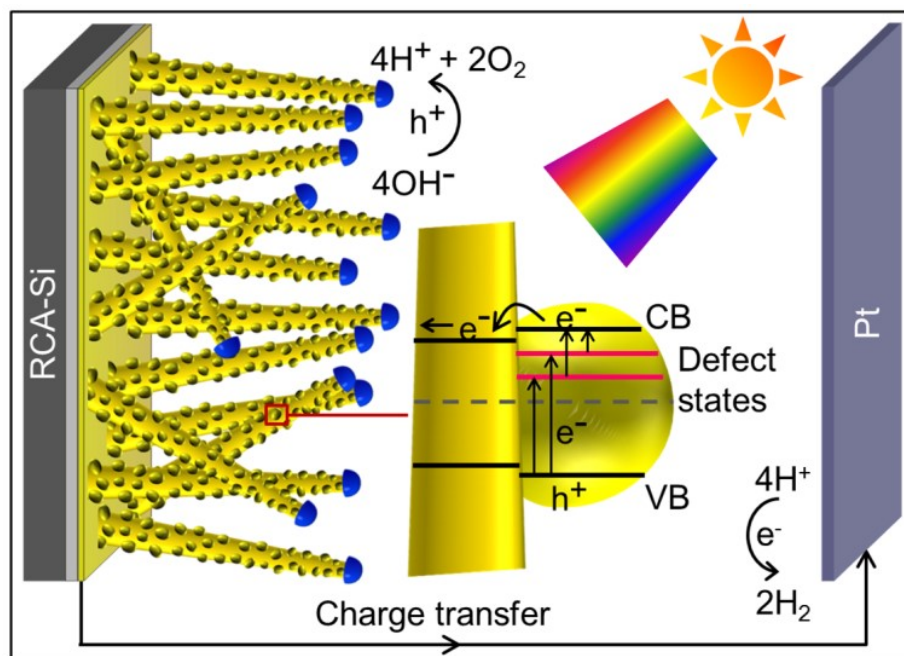


Figure 3.15 Schematic diagram for the charge separation and migration process in TiO₂ decorated nanowires in a photoelectrochemical water splitting reaction driven by visible light irradiation.

3.4 Summary

By tuning the interfacial SiO₂ layer thickness and growth temperature, we synthesize a variety of 1D nanostructured TiO₂ films, including nanobelts, corrugated nanowires, straight

nanowires, and decorated nanowires, by using catalyst-assisted PLD method. The use of a high vacuum system and the precise control of growth temperature and Ar flow have enabled us to produce (oxygen vacancy) defect-rich TiO₂ nanostructured film. We further demonstrate that the amount of oxygen vacancy defects depends on the growth temperature, and the electrochemical impedance measurement confirms the lower charge transfer resistances at the depletion layer of the decorated nanowires. Photoelectrochemical measurement under simulated sunlight (100 mW/cm²) shows that these decorated nanowires exhibit a low onset potential of 0.3 V (vs RHE) and a total energy photoconversion efficiency of 2.4%. More importantly, the photocurrent density of defect-rich decorated nanowires is reduced only slightly from 1.6 mA/cm² to 1.4 mA/cm² when the ultraviolet light component (<430 nm) is filtered out. Unlike the previously reported cases for sub-10 nm rutile nanoparticles,²¹⁶ Fe₂TiO₅ coated TiO₂ nanotube arrays,²¹⁷ (W, C) co-doped TiO₂ nanowires,²¹⁸ and Au nanoparticle decorated TiO₂ nanowire arrays,¹⁷¹ where the observed photocurrent densities in AM 1.5G light were found to reduce by over 50% with just visible light illumination, we observe only a 13% reduction for the decorated nanowires. These defect-rich decorated nanowires therefore have the best photoelectrochemical catalytic performance in the visible region reported to date and are expected to have a significant impact on the design of super-efficient photoanodes for photoelectrochemical applications driven by visible light.

The present photocurrent density of TiO₂ nanowires can be further increased with a longer PLD deposition time. When the deposition time for the decorated nanowires is increased from 90 minutes to 130 minutes, the current density increases from 1.6 mA/cm² to 2.2 mA/cm² (i.e. by 32%). This performance is especially remarkable when considering that the length and density of the nanowires are both smaller than most of the high-performance TiO₂ nanowire samples reported in the literature.^{8,214} While the latter samples exhibit a current density of 2-3 mA/cm², these nanowires also have a higher aerial density and average length of 5-15 μm, the larger amount of which inherently provides more active sites for the photoelectrochemical reaction. Furthermore, the present nanowires are prepared with one distinct advantage, i.e. without the need for any post-synthesis modification or treatment, in marked contrast to most of the aforementioned TiO₂ nanowire samples, all of which required post-treatment (such as annealing in a reductive environment) or doping with secondary materials. In our case, the photocurrent density and hence the efficiency could easily be increased further by increasing the aerial density of the nanowires (e.g., by increasing the GNI density) and/or the length of the nanowires (e.g., by increasing the deposition time). An even higher efficiency can be achieved by controlling doping with a second material (e.g., Sn, Zn, Fe, or Cu) in the TiO₂ target.

Furthermore, fabricating hybrid and/or core-shell nanowires and synthesizing binary or tertiary nanowires could also enhance the photoelectrochemical efficiency and can be easily accomplished by switching the targets (using a multi-target holder) during the growth of the TiO₂ nanowires. The present approach of intentionally growing defect-rich TiO₂ nanostructures by catalyst-assisted PLD method could be extended to other wide-band gap semiconductors, which could offer viable alternatives for TiO₂ in a variety of solar energy driven applications, including photoelectrochemical water splitting, photocatalysis, and solar cells.

Chapter 4

Defect-rich Delaminated p-type ZrO₂ Hierarchical Nanowires for Super-efficient Photoelectrochemical Water Reduction under Visible Light

4.1 Introduction

With increasing global energy demand and climate change impact of CO₂ emission from fossil fuels, the production of chemical fuels from alternative clean and renewable energy supplies has become one of the most urgent challenges for the modern world.^{219–221} Photoelectrochemical splitting of water into hydrogen and oxygen by direct use of sunlight is an ideal renewable method of hydrogen production, and it represents an attractive, sustainable solution to the renewable energy challenge.²²² Considerable efforts have been made in the past decade to achieve a solar-to-hydrogen conversion efficiency of more than 10% in order to become viable for practical applications.²²³ Among the various efforts involved in improving a photoelectrochemical water splitting system, appropriate choice of photoelectrode materials (usually p-type or n-type semiconductors) compatible with solar energy conversion, particularly in the visible spectral region, is especially important. This is because material properties, such as optical absorption characteristics, energy band positions and chemical stability, could greatly affect the system performance.^{21,30,224,225} For commercially viable solar energy harvesting, the photoelectrochemical system must also be low-cost and be fabricated from abundant elements using a scalable manufacturing process.^{226,227}

Due to their low cost and ready availability, many metal oxides, such as Fe₂O₃,²²⁴ TiO₂,²¹ ZrO₂,²²⁵ and Cu₂O,³⁰ have attracted a lot of attention as possible photoelectrode materials for photoelectrochemical conversion of solar energy into chemical fuels. However, these oxides suffer from low solar visible light absorption due to their large bandgap (~3 eV) and relatively fast electron–hole recombination, which limits their photoconversion efficiency to less than 0.1% in the visible region of the solar spectrum.^{228,229} To overcome these drawbacks, several strategies have been attempted and they include: doping with impurity elements,^{230,231} use of semiconductor heterojunctions,^{232,233} thermal annealing in a reductive environment,⁸ and surface passivation.³⁰ Although these strategies are capable of improving light absorption of these metal oxides, the

resulting overall water splitting efficiencies fall well below the respective theoretical maximum efficiencies of 10-20%.^{30,234} This discrepancy could be due to low specific surface area, imperfection from single crystallinity, generation of only surface defects instead of bulk defects in reductive environments, and presence of large numbers of recombination centers in doped and heterojunction semiconductors.^{30,231,233,235} Moreover, the photoelectrochemical activity of thin-film electrode is generally restricted to the top surface, because electroactive species of the electrolyte can only come in contact with the top surface of the electrode. As the underside (i.e. the bottom) surface of the base film is in direct contact with the conductive substrate, it is out of reach of the electrolyte and it therefore remains unusable for photoelectrochemical reactions. On the other hand, by partially delaminating the thin film, it is possible to expose the bottom surface of the base film, thereby potentially doubling the active area, for photoelectrochemical reactions. To improve the charge-carrier collection, it is also extremely important to develop a photocatalyst material with not only high crystallinity and large surface area, but also a large amount of oxygen vacancies, short charge-transfer length, and special morphology for enhancing performance in photoelectrochemical water splitting. One-dimensional (1D), single-crystalline hierarchical nanostructures with high oxygen vacancy defect composition provide the apparent advantages of not only enhanced transport and separation of photoexcited charge carriers, but also an abundant number of surface reaction sites, all of which are crucial to obtaining high solar energy conversion efficiency.

Zirconium dioxide (ZrO_2) is one of the most promising water reduction materials because of its easy availability, low cost, strong photo-reducing power, high photo-stability, non-toxicity, and favourable band-edge positions that are compatible with the hydrogen evolution potential.²³⁶ However, the synthesis of 1D single-crystalline ZrO_2 nanowires by catalyst-assisted vapour-liquid-solid (VLS) growth,⁷¹ as the most popular, reproducible approach to synthesize single-crystalline nanostructures, has thus far been unsuccessful. This is because of the difficulties caused by the low vapour pressures and high melting points of Zr (1789 °C) and ZrO_2 (2715 °C).¹⁰⁴ Moreover, in order to fabricate 1D nanostructures by the VLS growth approach above 1079 °C (the eutectic point of Au-Zr),²³⁷ a dielectric buffer layer for the Si substrate is required to prevent the formation of silicides with the sensitive catalysts (e.g. Au).⁶¹ Such a dielectric buffer layer could, however, impede direct flow of photogenerated carriers from the nanostructured film to the conductive substrate. In the present work, we demonstrate that the use of a buffer layer with the appropriate thickness provides the key to achieving VLS growth without greatly affecting the carrier transport.

Here, we synthesize highly oxygen-deficient, p-type ZrO₂ hierarchical nanowires on Si substrates by one-step catalyst-assisted pulsed laser deposition using gold nanoislands as the catalysts, which are predeposited on a SiO₂ buffer layer of appropriately optimized thickness. In laser ablation, the absorption of a high-intensity laser pulse by a small volume of the target material leads to vaporization in the thermally non-equilibrium regime, which allows activation of the gold catalysts at a lower temperature and the formation of 1D nanostructures to proceed at a lower temperature (via VLS growth) than other vapour deposition methods.⁷¹ We demonstrate that the as-grown ZrO₂ hierarchical nanowires provide the highest photoelectrochemical water splitting performance under simulated sunlight among all the nanostructured transparent conductive oxide photoelectrodes reported to date.²³⁸ Furthermore, the photoelectrochemical performance could be significantly improved even further by partially delaminating the as-grown ZrO₂ nanostructured film. By partial dissolution of the interfacial SiO₂ layer in HF, we produce a flaky nanostructured film with considerably larger surface area by partially exposing the underside surface of the nanostructured film. More importantly, partial removal of the SiO₂ layer enables better contact of the nanostructured film with the substrate, thus significantly improving the carrier transport. We demonstrate the ultrahigh photocatalytic performance of these flaky, defect-rich hierarchical nanowire films in a photoelectrochemical water splitting reaction for the first time. Even more extraordinary are that their photoactivity is predominantly driven by visible light (>400 nm) and that 99.5% Faradaic efficiency and 17.1% solar-to-hydrogen conversion efficiency are achieved.

4.2 Experimental details

Catalyst-assisted pulsed laser deposition (PLD) is used to synthesize ZrO₂ hierarchical nanowires on an oxidized Si(100) substrate in a NanoPLD system (PVD Products) with a base pressure of 1×10^{-7} Torr. A KrF excimer laser (248 nm wavelength) operated with a laser fluence of 350 mJ/pulse at a repetition rate of 5 Hz is used to ablate a ZrO₂ target, which is prepared by cold-pressing ZrO₂ powders (Aldrich, 99.99% purity) at a pressure of 25 MPa followed by sintering at 1000°C for 48 h in air. A silicon chip (10×10 mm², 525 ± 25 μm thick), pre-cut from a Si(100) wafer (p-type, B-doped, with a resistivity of < 0.005 Ω cm), is chemically oxidized in H₂O₂ and NH₄OH solutions following a RCA cleaning procedure.²³⁹ The resulting SiO₂ buffer layer on the Si substrate, identified as RCA-Si, is found to have a thickness of 3 nm. Gold nanoisland (GNI) catalysts are fabricated on an RCA-Si substrate by magnetron sputtering a thin layer of Au for 3-15 s followed by

annealing in O₂ at 600°C for 1 h. The SiO₂ layer thickness has increased to 10 nm after the synthesis of GNIs, and the resulting template is designated here as GNI/Ox-Si. The substrate is mounted perpendicular to the expansion direction of the laser plume on a windowed substrate holder. The target-to-substrate separation is kept at 30 mm, with the substrate positioned in close proximity to the top of the visible region of the laser plume. During deposition, the substrate temperature is kept at 770 °C by radiative heating of infrared heat lamps from the backside of the substrate. Deposition is carried out on the GNI/Ox-Si template for 90 min in 0.2 Torr of Ar at a flow rate of 10 sccm.

Surface morphology of the sample is examined by field-emission scanning electron microscopy (SEM) in a Zeiss Merlin microscope. The corresponding crystal structure is characterized by glancing-incidence X-ray diffraction (XRD) in a PANalytical MRD X'pert Pro diffractometer with a Cu K α source, by using a parallel X-ray beam setup with an incidence angle of 0.3°. The crystalline structure of ZrO₂ nanowires is also studied by transmission electron microscopy (TEM) in a Zeiss Libra 200MC microscope operating at 200 kV. For these measurements, the samples are scraped off the substrate using a sharp blade, mixed with high-performance liquid chromatography grade methanol in an eppendorf tube and sonicated for 10 min, and the resulting suspension is then transferred onto a holey carbon copper grid. Chemical-state compositions of the nanostructured films are analyzed by X-ray photoelectron spectroscopy (XPS) in a Thermo-VG Scientific ESCALab 250 microprobe with a monochromatic Al K α X-ray source (1486.6 eV). The Hall coefficient is measured by an Ecopia HMS-5300 Hall effect measurement system with a magnetic field of 0.5 T and an electric current of 1 mA. To assure good electrical connections for these measurements, aluminum and platinum contacts are sputter-deposited onto the corners of the deposited nanostructured materials on Si substrates.

Photoelectrochemical measurements for the water splitting reaction using the ZrO₂ nanostructures as the photocatalysts are carried out in a standard three-electrode quartz cell connected to an electrochemical workstation (CH Instruments, Model 660E). The ZrO₂ nanostructures grown on a GNI/Ox-Si template, a saturated Ag/AgCl electrode, and a platinum wire are used as the working, reference, and counter electrodes, respectively, and a 0.1 M H₂SO₄ + 0.01 M K₂SO₄ solution is used as the electrolyte. A 300 W solar simulator (Newport-Oriel Instruments, Model 68811) is used to provide the AM 1.5G solar spectral illumination. Light intensity of the solar simulator is calibrated to 1 sun (100 mW/cm²) with a power meter (Molelectron, EPM 1000e). All the electrode potentials are reported with reference to the reversible hydrogen electrode (RHE). The potential measured with

respect to Ag/AgCl can be converted to that with respect to RHE by using the equation: $E_{\text{RHE}} = E_{\text{Ag/AgCl}} + 0.059 \text{ pH} + E_{\text{Ag/AgCl}}^{\circ}$ (where $E_{\text{Ag/AgCl}}^{\circ} = +0.199 \text{ V}$, $\text{pH} = 1.89$). A short-pass ($< 400 \text{ nm}$) and a long-pass ($> 400 \text{ nm}$) filters (Oriol) are used to couple with the AM 1.5G filter to isolate, respectively, the UV and visible parts of the simulated sunlight spectrum. To isolate the specific wavelength components of the visible region, bandpass filters of 400, 500, 600, 700, and 800 nm are used in conjunction with the AM 1.5 G filter. Before each measurement, the electrolyte solution is thoroughly flushed with N_2 gas to remove any dissolved oxygen. The same electrochemical station is also used for electrical impedance measurement by electrochemical impedance spectroscopy.

4.3 Results and Discussions

4.3.1 Growth and Characterization of ZrO_2 Hierarchical Nanowires

GNI have been fabricated on the Ox-Si substrate by magnetron sputtering a thin layer of Au for 4 s followed by annealing at $600 \text{ }^{\circ}\text{C}$ in air for 1 h. The resulting GNIs exhibit a near-Gaussian size-distribution, with a mean diameter of $50 \pm 10 \text{ nm}$ (Figure 4.1a). Evidently, the corresponding ZrO_2 nanowires, grown on the GNI/Ox-Si template at $770 \text{ }^{\circ}\text{C}$, are found to be randomly oriented with respect to the substrate plane and the nanowires appear tapered (Figure 4.1b). Closer examination reveals that individual nanowire corresponds to a string of nanoplates stacked horizontally on top of one another with a gap spacing of $\sim 3 \text{ nm}$ (Figure 4.1b, inset). The nanoplate appears to have a cross section with a distorted polygon shape and a thickness of $\sim 6 \text{ nm}$. The SEM images in Figure 4.1c1-4.1c4 show that the angle, size and distribution of the stacking nanoplates along the main trunks of the nanowires could change from nanowire to nanowire. In some nanowires, the nanoplates are stacked almost perpendicularly ($\sim 90^{\circ}$) along the core nanowire length (Figure 4.1c2), while the angles in the other nanoplates range from 45 to 70° (Figure 4.1c3). A mixture of two orientations is also observed in some of the nanowires (Figure 4.1c4). Smaller nanoplates with side lengths of $10\text{-}20 \text{ nm}$ are observed at the tip while those at the base are found to be larger with side lengths of $50\text{-}70 \text{ nm}$, and the tip of the nanowire trunk is covered by more nanoplates than the base. The corresponding TEM image confirms the overall tapered structure of the nanowire and the presence of the nanoplates stacking in parallel with respect to one another along the nanowire trunk direction (Figure 4.1d). Close inspection reveals that the nanoplates have their roots inside the core nanowire trunk surface and they appear firmly attached to the nanowire trunk. The corresponding high-resolution TEM

image demonstrates the single-crystalline nature of the nanoplates, with an interplanar spacing (5.1 Å) consistent with the (100) plane of monoclinic ZrO₂ (Figure 4.1d, inset).

In a separate experiment, we perform PLD growth of ZrO₂ on an Ox-Si substrate without any GNI catalysts. The corresponding SEM image (Figure 4.1e) shows that the resulting film consists of nanobricks of typical lengths of 10-30 nm, while the TEM images of selected regions of the nanobricks (Figure 4.1e, inset) show interplanar spacings of 2.9 Å and 2.5 Å, corresponding to the (101) and (110) planes of tetragonal ZrO₂, respectively. Closer examination of the hierarchical nanowire film shown in Figure 4.1b reveals the presence of similar nanobricks among the bases of the hierarchical nanowires. This suggests concurrent vapour-solid growth of nanobricks in regions where there is no catalyst in the nanowire sample. However, PLD growth at 770 °C on a GNI/Ox-Si template with the SiO₂ layer thickness below ~10 nm produces mainly nanopopcorn-like film (not shown), which is due to the formation of Au-silicide by interfacial reaction between GNI and Si.¹⁹⁰ The thicker SiO₂ layer (10 nm) on the Ox-Si template prevents Au diffusion into the substrate and the subsequent Au-silicide formation. A SiO₂ layer with the appropriate thickness (of ~10 nm) is therefore extremely important for enabling VLS growth in the present PLD method.

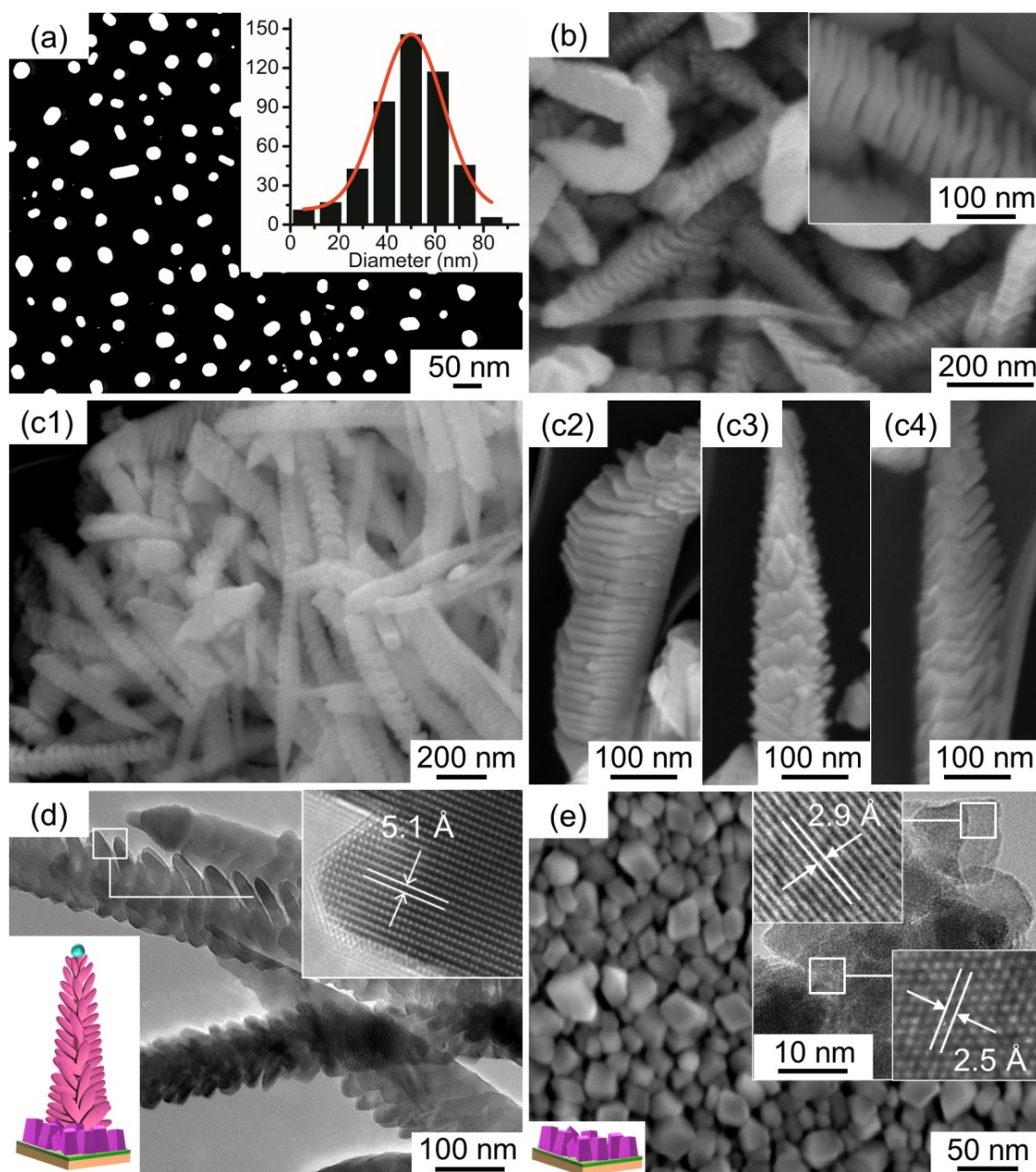


Figure 4.1 SEM images of (a) typical gold nanoislands (GNIs), with its corresponding near-Gaussian size distribution (inset), formed on the Ox-Si substrate, (b) PLD-grown ZrO_2 hierarchical nanowires on the GNI/Ox-Si template at 770°C in 200 mTorr of Ar for 90 min, and (c1 – c4) ZrO_2 hierarchical nanowires scrapped-off from the GNI/Ox-Si template, taken after dispersing onto holey carbon TEM copper grids. TEM images of (d) a typical ZrO_2 hierarchical nanowire. (e) SEM image of ZrO_2 nanobricks PLD-grown in the absence of GNIs on bare Ox-Si substrate in 200 mTorr of Ar at 770°C for 90 min. In (d) and (e), the lower-left insets show schematic representations of the respective PLD-grown nanostructures, while the upper-right insets show high-resolution TEM images of selected areas of the respective nanostructures.

The size of the nanoplates and consequently the morphology of hierarchical nanostructures can be tuned by varying the size of the GNI catalysts. The average size of the GNIs is controlled by the thickness of the gold layer and the annealing temperature. Figure 4.2a1, 4.2b1, and 4.2c1 show the SEM images of GNIs on Ox-Si templates, prepared by sputter-coating thin layers of Au for 3, 6 and 15 s, respectively, followed by annealing at 600°C in air for 1 h. The respective mean diameters of GNIs are measured to be 15 ± 5 nm (Figure 4.2a1), 30 ± 10 nm (Figure 4.2b1), and 90 ± 20 nm (Figure 4.2c1). Evidently, PLD growth of ZrO_2 at 770 °C on a GNI/Ox-Si template with smaller GNIs (15 ± 5 nm) produces regular nanowires with a uniform cross section along the length and without any nanoplates (Figure 4.2a2). The corresponding magnified TEM image further confirms that there is no plate-like structure at the exterior of the nanowire (Figure 4.2a2, inset) and that the ZrO_2 nanowires are single-crystalline and have the monoclinic phase, with an interplanar spacing of 2.6 Å corresponding to the (002) plane of bulk monoclinic ZrO_2 (Figure 4.3). On the other hand, PLD growth on a GNI/Ox-Si template with 30 ± 10 nm GNIs produces hierarchical nanowires with nanoplates with side lengths of 25-35 nm at the base and 10-15 nm at the tip of the nanowire. While this structural characteristic may not be easily seen in the high-magnification SEM image (Figure 4.2b2), due to the small spacing between the nanoplates (2-3 nm), it can be clearly observed in the high-resolution TEM image (Figure 4.2b2, inset). For GNI/Ox-Si template with further increase in the average gold catalyst size to 90 ± 20 nm, octopus-like nanowire assemblies are formed (Figure 4.2c2), of which more than one hierarchical nanowires are grown from a single large Au particle (Figure 4.2c2, inset), and the size of the nanoplates varies from wire to wire (not shown). These results therefore illustrate the importance of delicate control of the catalyst size in effecting the desired morphologies of the as-grown ZrO_2 nanostructures. A critical GNI size of 30-60 nm is necessary for the successful formation of the hierarchical nanowires while any GNI size less than 20 nm or greater than 70 nm would be ineffective in producing the hierarchical nanowires.

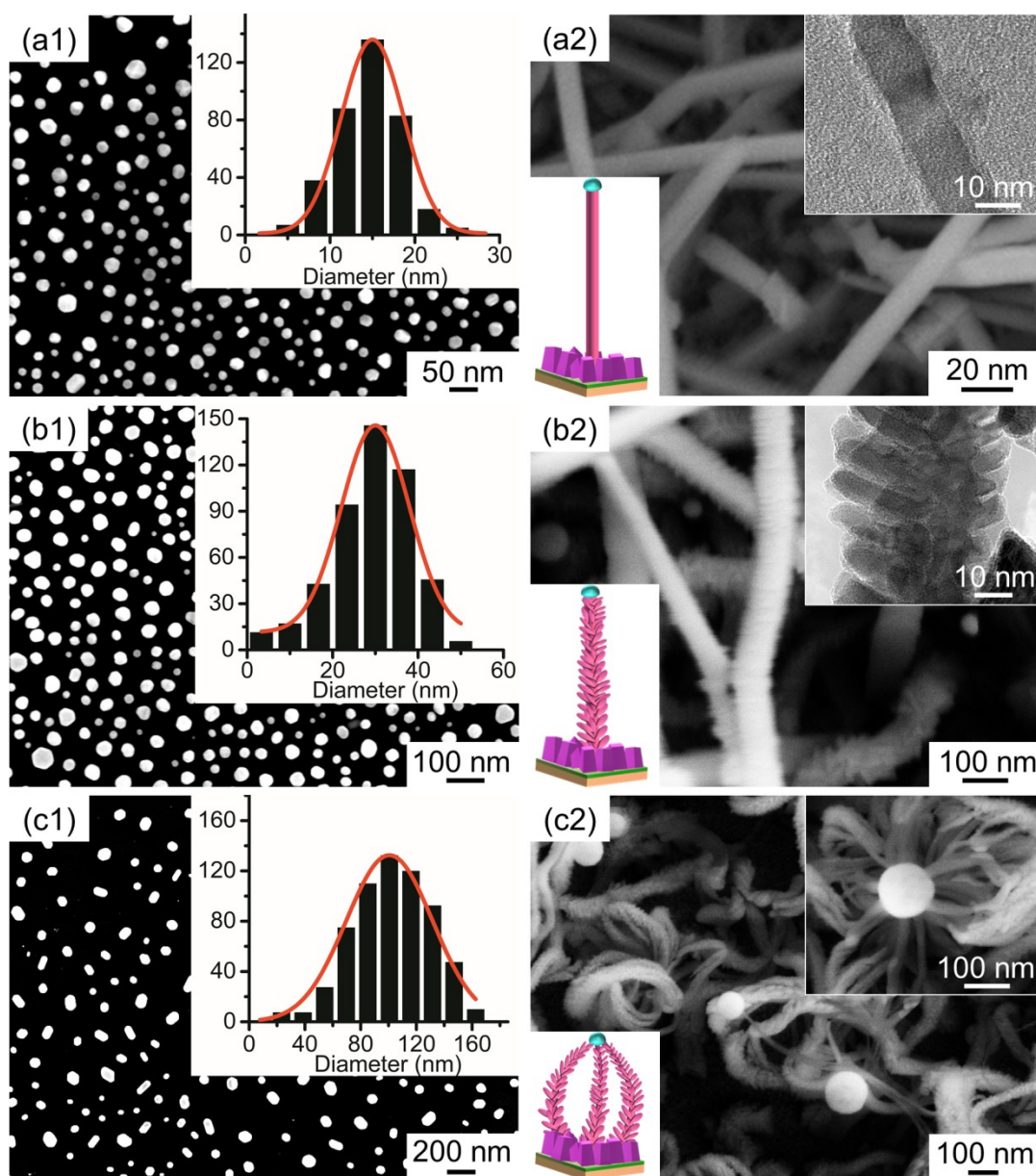


Figure 4.2 SEM images of (a1, b1, c1) typical gold nanoislands (GNIs), with the corresponding near-Gaussian size distributions (insets), formed on Ox-Si templates by magnetron sputtering a gold target for (a1) 3 s, (b1) 6 s, and (c1) 15 s followed by annealing in air at 600 °C for 1 h. SEM images of (a2) regular nanowires, (b2) hierarchical nanowires, and (c2) octopus-like nanowires PLD-grown in 200 mTorr Ar at 770 °C for 90 min on the respective GNI/Ox-Si templates shown in (a1, b1, c1). The corresponding lower-left insets show schematic models of the as-grown nanostructures, while the upper-right insets in (a2, b2) and in (c2), respectively, depict the magnified TEM images and SEM image of the respective as-grown nanostructures.

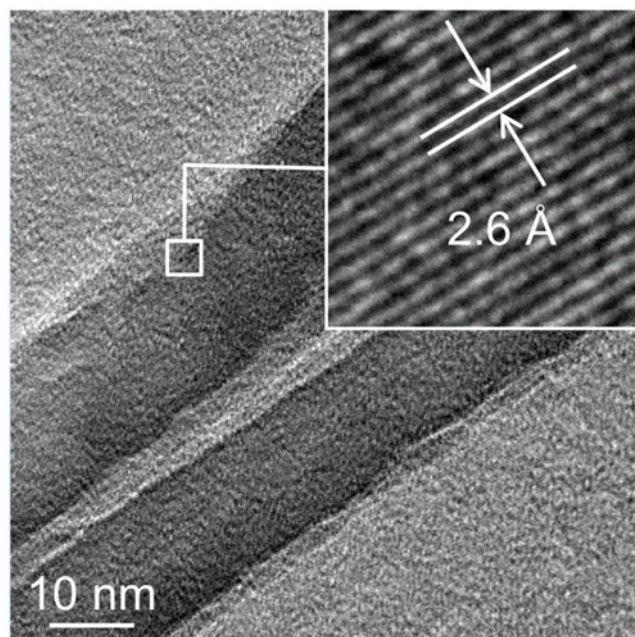


Figure 4.3 TEM image of as-grown regular ZrO_2 nanowires, with a high-resolution TEM image of a selected area of an individual nanowire shown in inset.

Our proposed growth mechanism for the hierarchical ZrO_2 nanowires is shown schematically in Figure 4.4. The initial gold nanoisland formation on the Ox-Si substrate provides the essential catalysts for VLS growth (Figure 4.4a). At the start of the VLS growth, a ZrO_2 nanowire trunk pushes up and detaches a GNI from the Ox-Si substrate (Figure 4.4b). As the VLS growth continues, a fraction of the Au atoms are evaporated from the bulk Au catalyst at the tip of the nanowire trunk, and they then get re-adsorbed on the surface of nanowire trunk (Figure 4.4c). These re-adsorbed Au atoms become additional nucleation sites, enhance the absorption rate of incoming ZrO_2 vapours, and promote ZrO_2 nanoplate formation (Figure 4.4d). The longer exposure of the base to the incoming ZrO_2 vapour compared to the tip results in larger nanoplates at the base and smaller nanoplates at the tip of the nanowire trunk, thus accounting for the observed tapered shape of the hierarchical nanowire structure.

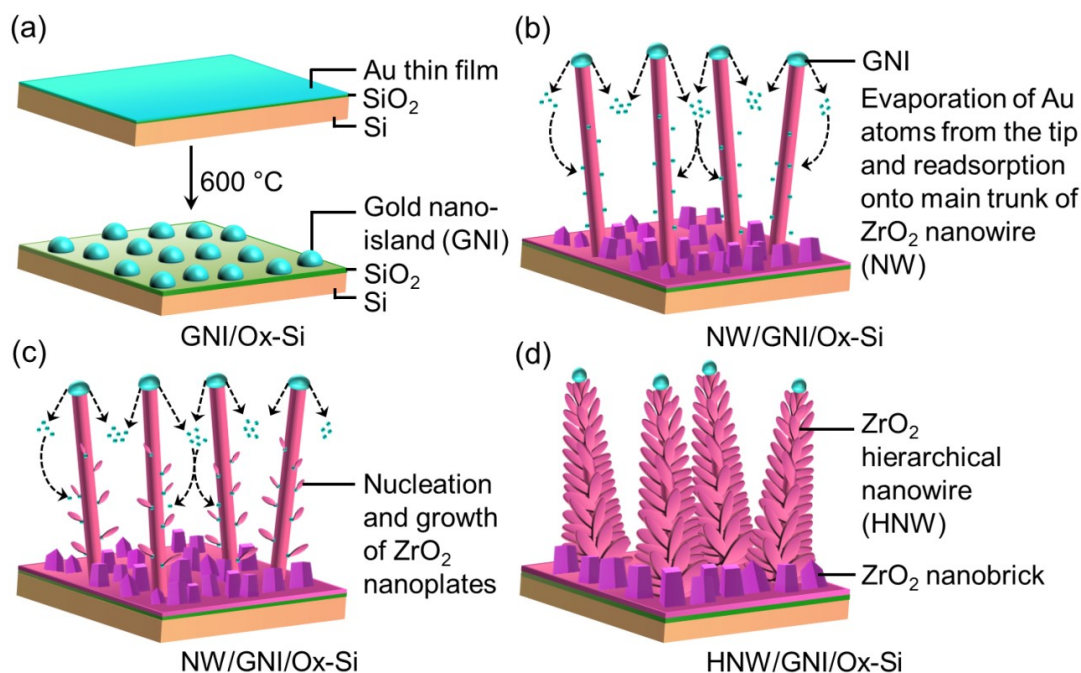


Figure 4.4 Schematic diagram of proposed catalyst-assisted vapour-liquid-solid growth mechanism for typical ZrO₂ hierarchical nanowires.

Figure 4.5 shows the corresponding glancing-incidence X-ray diffraction (XRD) patterns of the as-grown hierarchical nanowires (Figure 4.1b) and nanobricks (Figure 4.1e). The prominent diffraction peaks of the hierarchical nanowire and nanobrick films are found to be in excellent accord with the monoclinic (PDF2 #01-083-0940) and tetragonal ZrO₂ reference patterns (PDF2 #01-080-0784), respectively. The additional minor contributions from the tetragonal ZrO₂ phase and FCC phase of metallic Au (PDF2 #03-065-8601) in the hierarchical nanowire films can be attributed to the presence of the nanobricks between the nanowires and that of the GNI catalysts, respectively. As with the hierarchical nanowires (Figure 4.1b), the regular nanowires without nanoplate (Figure 4.2a2), the hierarchical nanowires with small nanoplates (Figure 4.2b2), and octopus-like hierarchical nanowires (Figure 4.2c2) also exhibit similar XRD patterns with predominant monoclinic ZrO₂ features (not shown). The XRD and TEM results therefore both support that the PLD-grown ZrO₂ regular

nanowires and hierarchical nanowires are predominantly monoclinic, while the nanobricks among these nanostructures (similar to those that make up the nanobrick film) are predominantly tetragonal ZrO_2 . Moreover, the single-crystalline nature of the nanowires suggests that the main trunks of individual hierarchical nanowires are also single-crystalline, monoclinic ZrO_2 .

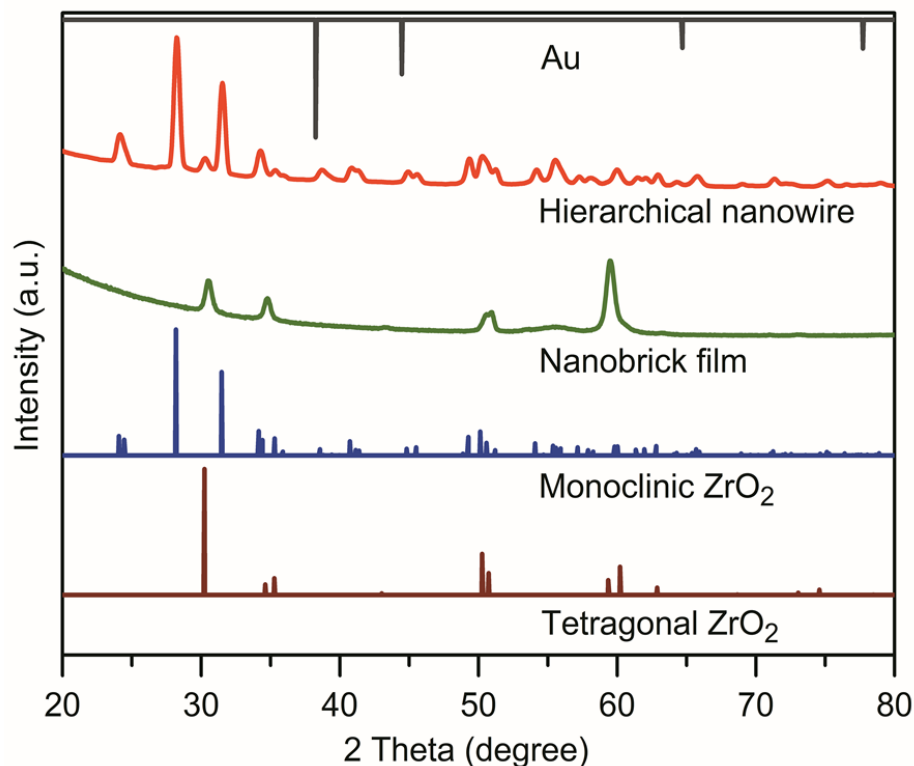


Figure 4.5 Glancing-incidence XRD patterns of ZrO_2 hierarchical nanowire and nanobrick films obtained at an incidence angle of 0.3° . The PDF2 reference patterns of the FCC phase of Au (#03-065-8601), and of the monoclinic phase (#01-083-0940) and tetragonal phase (#01-080-0784) of ZrO_2 are shown as top, and bottom bar graphs, respectively.

The presence of secondary structures such as the nanoplates around the trunk of the nanowire has dramatically increased the surface area of the hierarchical nanowire relative to the regular nanowire. These secondary nanoplates are therefore expected to greatly increase the amount of catalytically active sites (per illumination photocathode-area) and consequently photoelectrochemical water splitting activity. Among the base of the hierarchical nanowires are the nanobricks, and the entire ZrO_2 nanostructured film is attached to the Si substrate through a 10 nm thick interfacial SiO_2 layer (Figure 4.6a, 4.6c). The presence of a relatively thick dielectric layer between the ZrO_2

nanostructured film and the Si substrate is expected to impede direct transfer of photogenerated charge carriers from the nanostructured film to the substrate. To get collected by the external contact (placed at the edge and on the top of the film), the charge carriers photogenerated in the film must travel across the base layer to the external contact point (Figure 4.6c). Consequently, a majority of the charge carriers might be lost due to recombination at the defect sites in the base layer. As with the majority of the thin-film-based photoelectrodes, the electrolyte is exposed to and therefore photoelectrochemical activity is restricted to the top side of the film (Figure 4.6c). In contrast, as the underside surface of a partially delaminated thin film is partially detached from the substrate or supporting layer (Figure 4.6d), the electrolyte is in contact with and could therefore access both the top side and underside surfaces of the film. The resulting photoactivity is expected to increase considerably depending on the extent of the delamination. This partial delamination architecture could also improve light absorption, because a more textured film could scatter the light more efficiently than a more planar film. More importantly, for the substrate-sensitive nanostructured growth (as in the present case), partial delamination could remove part of the dielectric layer such that transport of the photogenerated carriers could proceed directly between those parts of the delaminated nanostructured film that are in better contact with the conductive substrate and the external contact (Figure 4.6d).

To date, there is no report on direct method of creating partially delaminated nanostructured thin films. Here, we develop a facile post-treatment to create such a nanoarchitecture to massively increase the photoactivity and the charge transport for photoelectrochemical reactions, by simply soaking the as-grown ZrO_2 hierarchical nanowire film in a 0.01 M HF solution for 1 h. Evidently, the HF treatment causes cracking to develop across the film, likely along fault lines with poor adhesion between the film and substrate (Figure 4.6b, inset), converting the smooth film (Figure 4.6a) into a “flaky” film with a random-stone-like pattern (Figure 4.6b). Partial dissolution of the underlying SiO_2 layer also causes residual compressive stress near the edge of the flakes as a result of the mismatched strains between the detached and attached portions of the film. This mismatched strain occurs upon cooling from high-temperature deposition and arises as a result of the differences in the thermal expansion coefficients of the film and the supporting SiO_2 layer (and/or the substrate). As the supporting layer (and/or the substrate) is much more massive than the film itself, it contracts more freely and consequently imposes a strain on the film in all directions parallel to the interface. As a result, extension of channel cracks and buckling in the film occur (at the edges of the flakes) in the absence of the SiO_2 layer. Similar results are also obtained for the nanobrick and nanowire films (not

shown). Both X-ray diffraction and TEM analysis show that the HF treatment does not affect the crystallinity of the films.

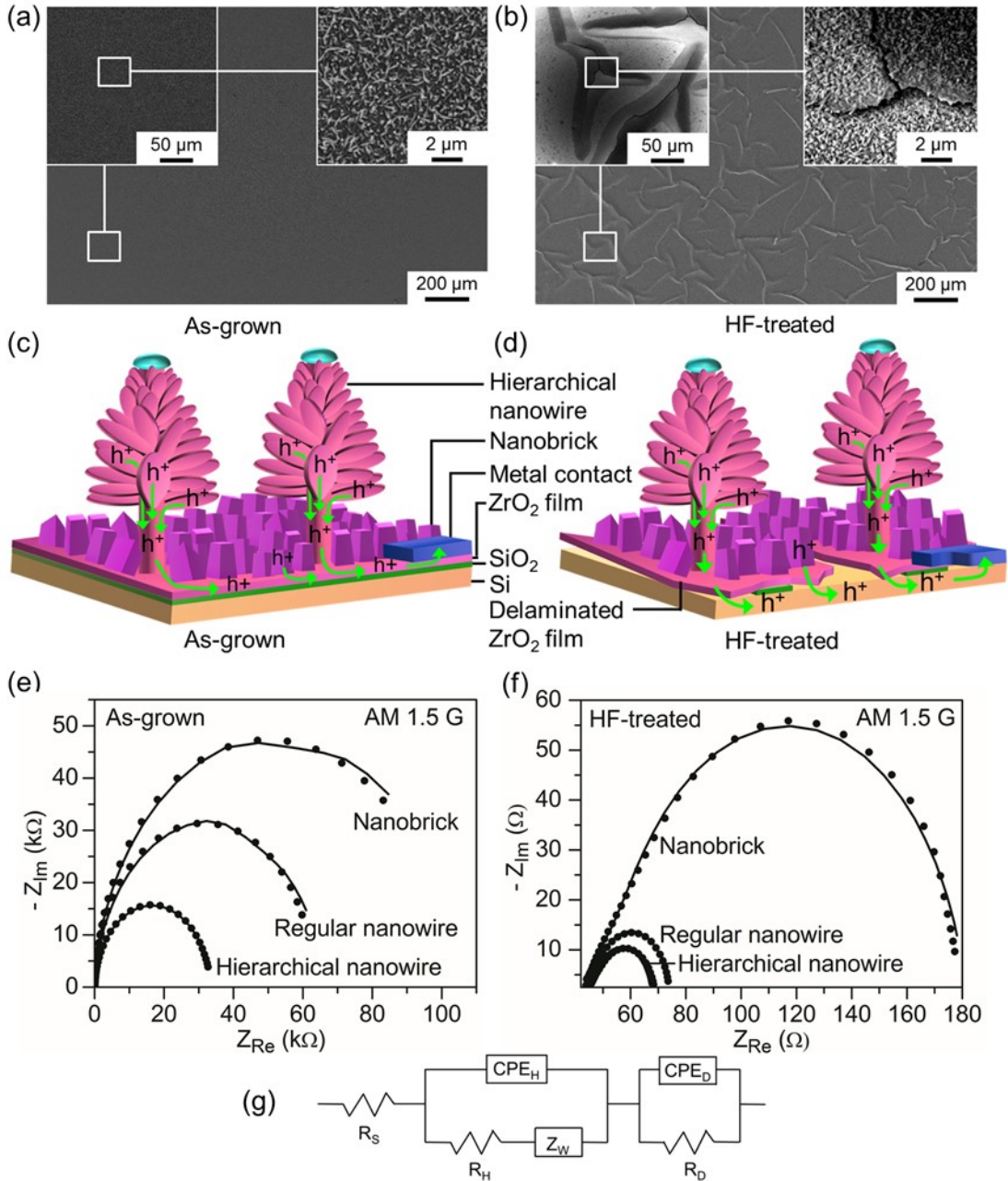


Figure 4.6 SEM images of (a) as-grown and (b) HF-treated ZrO_2 hierarchical nanowire films, with magnified views of selected areas in insets. Schematic models of the hierarchical nanowire film (c) before and (d) after the HF treatment. Nyquist plots of (e) as-grown and (f) HF-treated hierarchical nanowire samples under illumination of simulated sunlight (100 mW/cm^2). The experimental data (solid circles) are collected in a frequency range between 0.01 Hz and 100 Hz with an AC voltage

amplitude of 10 mV and a DC bias of -0.9 V, and they are fitted with (g) an equivalent circuit model (solid lines).

To identify the chemical nature of ZrO_2 hierarchical nanowire film before and after the HF treatment, we compare, in Figure 4.7, the X-ray photoelectron spectroscopy (XPS) spectra of the Zr 3d and O 1s regions of the nanobrick, regular nanowire, and hierarchical nanowire films. The prominent Zr $3d_{5/2}$ peak at 182.4 eV corresponds to the Zr^{4+} state for ZrO_2 , while the residual intensity between the Zr^{4+} feature (at 182.4 eV) and metallic Zr^0 feature (at 178.3 eV) could be fitted with two components: ZrO_{x1} ($2 > x1 > 1.5$) and ZrO_{x2} ($1.5 \geq x2 > 1$). The prominent O 1s peak located at 530.3 eV is attributed to O^{2-} in ZrO_2 , while the residual O 1s intensity between 532.0 eV and 530.9 eV can be assigned to oxygen anions in the oxygen-deficient ZrO_{x1} and ZrO_{x2} species within the matrix, with the O 1s intensity above 533.0 eV attributed to the SiO_x ($2 > x > 1.5$) species. The apparent relative increase of SiO_x species in the HF-treated sample is due to cracks and openings in the partially delaminated film, which allow more exposure of the underlying Si substrate compared to the as-grown nanowires.

Due to a fairly attractive Madelung potential of excess electrons in oxygen-deficient ZrO_2 ,²⁴⁰ the oxygen vacancy defects of ZrO_2 can have three different charge states: neutral, singly-charged, and doubly-charged defects. The formation of a neutral oxygen vacancy would result in two electrons to remain at the oxygen vacancy site, and there is therefore no apparent effect on the neighbouring Zr^{4+} oxidation states. For the singly-charged oxygen vacancy, one electron would remain at the singly-charged oxygen vacancy site, with the other electron in the corresponding Zr atom leading to a Zr^{3+} ($4d^1$) ion. For the doubly-charged oxygen vacancy, two electrons from the vacancy site could be located at two nearest-neighbour Zr sites [leading to two Zr^{3+} ($4d^1$) ions] or both at one Zr site [leading to a Zr^{2+} ($4d^2$) ion]. Different lattice relaxations associated with the differently charged oxygen vacancies change the corresponding O 1s and Zr 3d binding energies in oxygen-deficient ZrO_2 . Density functional theory calculations have also confirmed that the singly and doubly charged oxygen vacancies have larger lattice relaxation effects than the neutral oxygen vacancies.²⁴⁰ The decrease in electron charge density for the $\text{O}-\text{Zr}^{3+}$ bond (relative to the $\text{O}-\text{Zr}^{4+}$ bond) results in less screening of the O 1s electrons, which consequently increases the effective nuclear charge and leads to an increase in the O 1s binding energy and a corresponding decrease in the Zr 3d binding energy. The O 1s and the corresponding Zr 3d peaks for ZrO_{x1} and ZrO_{x2} therefore correspond to the singly-charged and doubly-charged oxygen vacancies, respectively, while those for the neutral oxygen

vacancy defect reside with the respective features for ZrO_2 . Along with the discernible intensity variations found for the O 1s and Zr 3d states for the ZrO_{x1} and ZrO_{x2} components, the minor differences in the binding energy positions and in the full-width half maxima reflect the differences in the relative compositions of these different types of oxygen vacancies in a particular sample. The O 1s and the Zr 3d intensity percentages for the ZrO_{x1} and ZrO_{x2} components of the respective total intensities [i.e., $\text{ZrO}_2 + \text{ZrO}_{x1} + \text{ZrO}_{x2}$] for the nanostructures, as-grown and after the HF treatment, are summarized in Table 4.1. The total defect intensity is found to increase after the HF treatment for all three nanostructured samples. This can be attributed to the flaking and buckling as a result of residual compressive stress caused by removal of the SiO_x layer, which generate a larger amount of defects in the partial delamination process. For the as-grown and HF-treated samples, the summed defect intensity ($\text{ZrO}_{x1} + \text{ZrO}_{x2}$) appears to follow the descending trend: hierarchical nanowires > regular nanowires > nanobricks, which is consistent with a similar trend in the specific surface area.

The increase in the defect density and the higher surface roughness due to buckling also change the colours of the HF-treated samples. For the as-grown nanostructured samples, the colour changes from light blue (nanobrick) to bluish black (regular nanowire), and to greyish black (hierarchical nanowire), due to the increasing amount of oxygen vacancy defects within the nanostructures (Figure 4.7a, insets). Similarly, in the partially delaminated samples, the colour also changes due to differences in the compositions of the oxygen vacancies and in the surface roughness of the films. The contrast differences between the HF-treated samples and the respective as-deposited samples further confirm the buckling-driven delamination process. The corresponding reflectance spectra follow essentially the same profile over the 320 – 680 nm range, with the magnitude following the descending trend: nanobrick > regular nanowire > hierarchical nanowire, and the absorbance following the opposite trend (Figure 4.8). However, the HF-treated samples exhibit ~10% lower reflectance than the respective as-deposited samples, which could be due to more scattering and higher absorption caused by buckling of the delaminated films. The absorbance of the ZrO_2 nanostructures in the visible region could therefore be attributed to the existence of defect states within the bandgap, the overlap and hybridization of which could lead to impurity bands within the bandgap.²⁴¹ Moreover, both the as-grown and HF-treated ZrO_2 samples retain their individual color profiles upon storage in ambient atmosphere for over a year, indicating that the defects are located in the bulk and not just at the surface of these nanostructures.

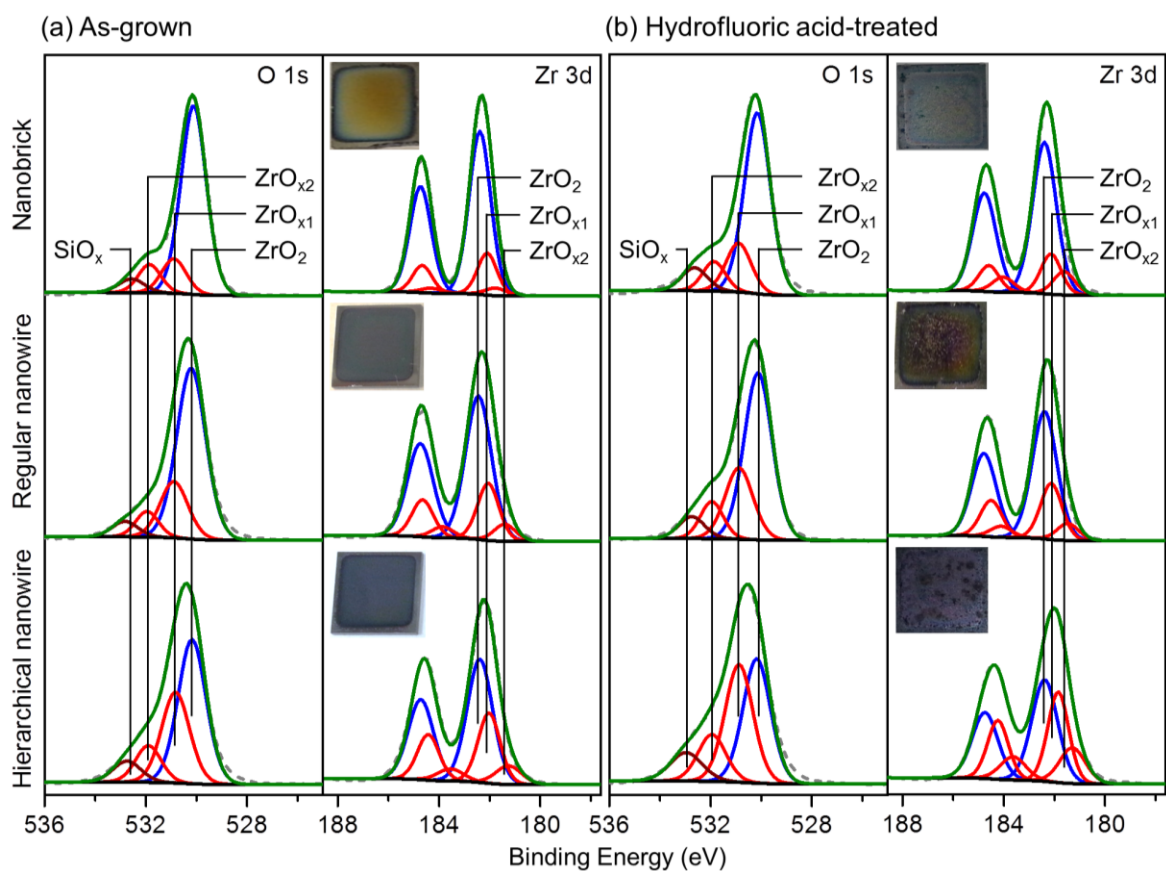


Figure 4.7 XPS spectra of Zr 3d and O 1s regions of (a) as-deposited, and (b) HF-treated ZrO₂ nanobrick (top row), regular nanowire (middle row) and hierarchical nanowire films (bottom row). In addition to the ZrO₂ and SiO_x ($2 > x > 1.5$) features, two sets of oxygen vacancy defect features corresponding to ZrO_{x1} ($2 > x1 > 1.5$) and ZrO_{x2} ($1.5 \geq x2 > 1$) are used to fit the residual intensities. Photographs of the as-grown and HF-treated nanostructured samples are shown as insets in (a) and (b), respectively.

Table 4.1 Comparison of the relative percentages of the Zr 3d and O 1s peak intensities for oxygen vacancy defect features: ZrO_{x1} ($2 > x1 > 1.5$) and ZrO_{x2} ($1.5 \geq x2 > 1$),[#] for the as-grown and HF-treated ZrO_2 nanostructured films.

| ZrO ₂ nanostructured film | As-grown [HF-treated] (%) | | | | | |
|--------------------------------------|------------------------------|-------------------|--|-------------------|-------------------|--|
| | Zr 4d | | | O 1s | | |
| | ZrO _{x1} | ZrO _{x2} | ZrO _{x1} + ZrO _{x2} | ZrO _{x1} | ZrO _{x2} | ZrO _{x1} + ZrO _{x2} |
| Nanobrick | 13.8 [17.5] | 3.5 [9.4] | 17.3 [26.9] | 15.9 [19.9] | 11.2 [11.6] | 25.3 [29.0] |
| Regular nanowire | 20.1 [25.5] | 7.1 [7.7] | 27.2 [33.2] | 22.6 [28.2] | 8.3 [11.7] | 29.0 [37.1] |
| Hierarchical nanowire | 29.3 [36.7] | 10.1 [13.5] | 39.4 [50.2] | 33.2 [41.3] | 13.5 [15.7] | 43.3 [53.2] |

[#] For the Zr 3d and O 1s features, the percentage of an individual component is calculated by dividing the peak area of that component by the total area for the ZrO₂, ZrO_{x1} and ZrO_{x2} features.

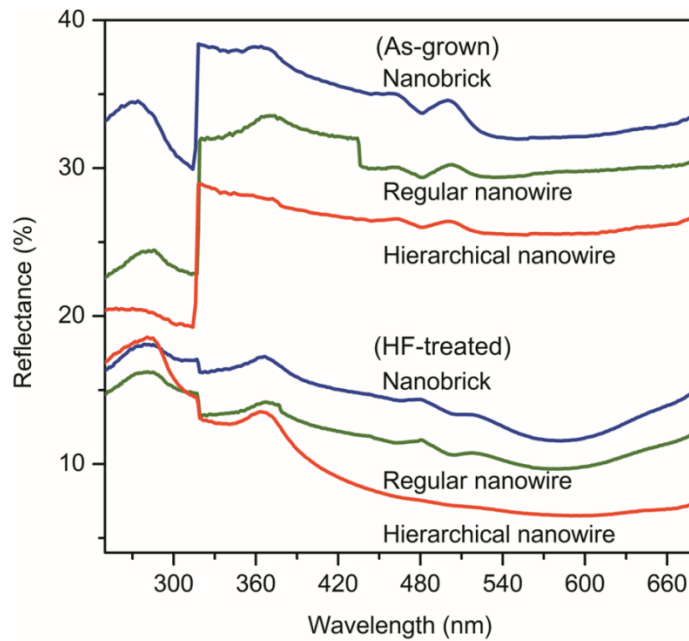


Figure 4.8 UV-Visible reflectance spectra of as-grown and HF-treated ZrO_2 nanostructured films.

The minor deviation from perfect stoichiometry and the improved electrical contact between the film and the Si substrate are expected to produce significant enhancements in the electrical and optical properties of these partially delaminated ZrO₂ nanostructured films.¹⁰ Figure 4.6e and 4.6f show the corresponding Nyquist plots for the nanostructured films before and after the HF treatment under simulated sunlight illumination obtained by potentiostatic electrochemical impedance spectroscopy. Using the equivalent circuit model shown in Figure 4.6g, we determine the series resistance (R_S), the resistance (R_D) and chemical capacitance or constant phase element (CPE_D) of the semiconductor depletion layer in an RC circuit, along with the charge-transfer resistance in the Helmholtz layer (R_H), the Warburg diffusion impedance (Z_W), and the capacitance of the electrochemical double layer (CPE_H) in a second RC circuit connected in series. The electrical parameters obtained by fitting the experimental data with the model equivalent circuit are summarized in Table 4.2. The fitted data shows that the charge transfer resistances R_D have decreased by four orders of magnitude while R_H have also decreased but to a lesser extent after the HF treatment. For both as-grown and HF-treated nanostructured films, the charge-transfer resistances decrease in the following order: nanobrick > regular nanowire > hierarchical nanowire, in close correlation with the opposite trends in the specific surface area, observed amounts of oxygen vacancy defects, and crystal colour. The substantial reduction in the charge-transfer resistance at the depletion layer (R_D) between regular nanowires and hierarchical nanowires indicates that the nanoplates of the hierarchical nanowires contain a larger amount of oxygen vacancy defect states. Interestingly, the reduction in R_D of the HF-treated hierarchical nanowires with respect to that of the HF-treated regular nanowires is considerably smaller than the reduction between these nanowires without HF treatment, which suggests that the partial removal of SiO_x in the delamination has a much greater effect in lowering the charge-transfer resistance.

Several defect bands may occur as a result of the overlap and hybridization of the defect states, which in effect lead to a reduction of the observed optical bandgap. These defect states and their imprint on the electronic band structure may also change the carrier type (p- or n-type) of the resulting sample. In the present study, all the nanostructured samples are found to have p-type conductivity with a Hall effect coefficient of $\sim 4.6 \times 10^{-4} \text{ cm}^3/\text{C}$. P-type conductivity suggests that the presence of singly-charged and doubly-charged oxygen vacancies creates an acceptor band above the valance band maximum, similar to that found for acceptor-impurities in metal oxides.²⁴² The improved visible light absorbance, lower charge-transfer resistance, and a larger amount of defects in

the partially delaminated, hierarchical nanowire sample promise an exceptional photocatalyst for visible sunlight-driven reactions and applications.

Table 4.2 Parameters determined from fitted results of electrochemical impedance spectra for as-grown and HF-treated ZrO₂ nanostructured films under AM 1.5G light.

| ZrO ₂ nanostructures | As-grown [HF-treated] | | |
|---------------------------------|-----------------------|---|---|
| | R _S (Ω) | R _H (Ω) CPE _H (μF) | R _D (Ω) CPE _D (μF) |
| Nanobrick | 46.9 [42.3] | 11900 [18.9] 34 [22] | 92100 [116.6] 1.0 [11] |
| Regular nanowire | 42.1 [41.0] | 8100 [6.5] 207 [81] | 62700 [26.4] 1.3 [101] |
| Hierarchical Nanowire | 41.3 [39.3] | 800 [5.7] 390 [161] | 32800 [20.4] 3.2 [238] |

4.3.2 Photoelectrochemical properties

In order to evaluate the photocatalytic activity of the aforementioned nanostructures for photoelectrochemical water splitting reaction, we employ as-grown and HF-treated ZrO₂ nanobrick, regular nanowire, and hierarchical nanowire films as photocathodes. The photocurrent spectra have been obtained for an illuminated sample area of 5×10 mm² under simulated sunlight illumination at 100 mW/cm² from a 300 W Xenon lamp coupled with an AM 1.5G filter. For the as-grown nanostructured films, the photocurrent density measured at -0.82 V vs RHE for the as-grown hierarchical nanowire film (12.1 mA/cm²) is found to be 5.8, and 1.9 times those of the as-grown nanobrick (2.1 mA/cm²) and regular nanowire films (6.4 mA/cm²), respectively (Figure 4.9a). It should be noted that the photocurrent density reported in the present work corresponds to the difference between light-on and dark current densities at -0.82 V vs RHE. On the other hand, the photocurrent density of the partially delaminated hierarchical nanowire film, obtained after the HF treatment, is found to increase stupendously to 42.4 mA/cm², i.e. nearly 3.5 times that of the as-grown hierarchical nanowire film (12.1 mA/cm², Figure 4.9b). For the delaminated regular nanowire and nanobrick films, the respective photocurrent densities have also increased to 19.8 mA/cm² (by 3.1 times from 6.4 mA/cm²) and to 4.8 mA/cm² (by 2.3 times from 2.1 mA/cm² of the respective as-grown nanostructured films). We have also characterized and obtained essentially no photocatalytic activity for the pristine Ox-Si substrate and GNI/Ox-Si template, and for the Si substrate after the as-grown hierarchical nanowire film has been completely delaminated under the same conditions (not

shown). The photogenerated holes in Si cannot be easily transferred to the valence band of the ZrO₂ nanobrick film, likely due to a significant barrier at the junction resulting in carrier recombination in Si.²⁰⁷ The significantly higher photocurrent density observed for the HF-treated hierarchical nanowires (and HF-treated regular nanowires) can therefore be attributed only to the photogenerated charge carriers from the ZrO₂ nanowires themselves and not the substrate. In-situ quantification of the evolved gases is also performed by using the HF-treated hierarchical nanowire film photoelectrode. As shown in Figure 4.10, only the partial pressures of H₂ and O₂ are found to increase as the reaction commences while those of the background gases (N₂, H₂O, and CO₂) remain flat and unchanged. The pressure change for H₂ ($\Delta P = 1.1 \times 10^{-7}$ Torr) is found to be almost twice that of O₂ ($\Delta P = 0.51 \times 10^{-7}$ Torr), which confirms the stoichiometric splitting of water. The corresponding Faradaic efficiency is estimated to be 99.5%. The solar-to-hydrogen conversion efficiency (η) is estimated to be 17.1% for HF-treated hierarchical nanowires from the equation,²³⁸ $\eta = [J_{ph} \times \eta_F (V_{th} - V_{app})] / P \times 100\%$, where J_{ph} is the photocurrent (mA/cm²) under AM 1.5G illumination, η_F is the Faradaic efficiency, V_{th} is the theoretical water-electrolysis voltage, V_{app} is the absolute value of the applied potential (vs. RHE), and P is the irradiance of the AM 1.5 G light (100 mW/cm²). Moreover, our photocatalysts are robust and remain active even after 2 hours of continuous photoelectrochemical water splitting reaction (Figure 4.11). Similar stability tests have also been made for other nanostructured films and they also show virtually no degradation over repeated cycling and extended use.

The lower photoelectrochemical activity of the as-grown nanostructured films, compared to the corresponding partially delaminated nanostructured films, could be attributed to the thicker SiO₂ buffer layer of the GNI/Ox-Si template, which impedes the direct transfer of photogenerated carriers from the ZrO₂ film to the Si substrate (and onto the Pt counter electrode). For the partially delaminated nanostructured films, the lower photocatalytic activity of the nanobrick film than the regular nanowire and hierarchical nanowire films is due to their smaller specific surface area available for the water reduction reaction. On the other hand, the higher photocatalytic activity of the hierarchical nanowire film compared to the regular nanowire film is attributed to the different morphologies of the nanowires. In the hierarchical nanowires, the densely packed nanoplates (3-6 nm thick) along individual nanowire trunks evidently provide significantly higher surface area for the photoelectrochemical reaction. In addition, the higher amount of oxygen vacancy defects in the hierarchical nanowires (Figure 4.7, Table 4.1) suggests the presence of more defect states in the bandgap, which ultimately enhance light absorption and generate more charge carriers for the water reduction reaction.

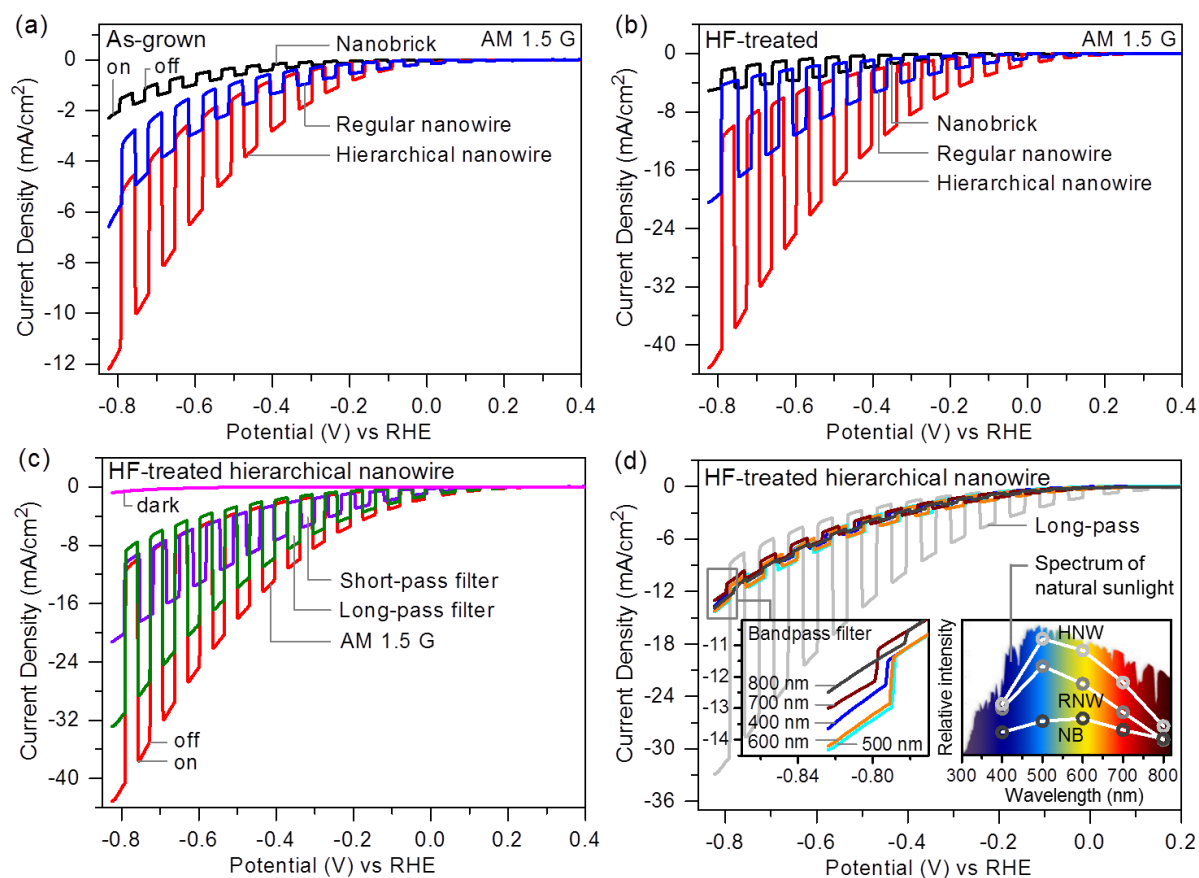


Figure 4.9 Current density measured by linear sweep voltammetry as a function of applied potential for (a) as-grown and (b) HF-treated ZrO_2 nanostructured film photocathodes, and for HF-treated hierarchical nanowire film photocathodes obtained with (c) short-pass and long-pass filters and (d) band-pass filters at 400, 500, 600, 700, and 800 nm. The measurements are performed in a ($0.1 \text{ M H}_2\text{SO}_4 + 0.01 \text{ M K}_2\text{SO}_4$) solution with a scan rate of 10 mV/s under 100 mW/cm^2 simulated sunlight illumination with repeated light-on/light-off cycles. The inset in (d) shows the relative photocurrent density vs wavelength profiles of hierarchical nanowire (HNW), regular nanowire (RNW), and nanobrick (NB) films with respect to the natural sunlight spectrum. The HNW profile is point-normalized to the maximum of the natural sunlight spectrum.

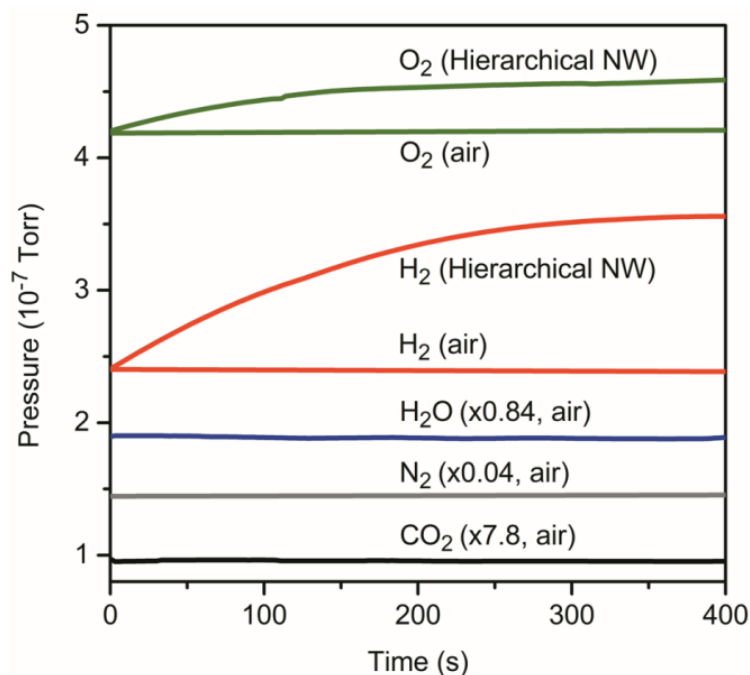


Figure 4.10 Quantification of gas evolution for photoelectrochemical water splitting reaction with HF-treated hierarchical ZrO₂ nanowire (NW) film as the photocathode. A Stanford Research Systems Universal Gas Analyzer system is used to analyze the gas sample at atmospheric pressure via a specially designed, 1.8 m-long capillary tube (175 μm ID). The measurement is performed with a three-electrode electrochemical cell in a sealed quartz beaker, with the capillary inserted to collect the gases generated by the reaction. The partial pressures for H₂, O₂, N₂, H₂O and CO₂ before and during the water-splitting reaction are monitored. Evidently, only the partial pressures of H₂ and O₂ are found to increase as the reaction commences, while those of the other gases remain flat and unchanged. It should be noted that the amount of time for the evolved gases to reach saturation depends on the amount of catalysts on the sample and the efficiency of gas production (both of which affect the amounts of H₂ and O₂ produced by the water-splitting reaction), as well as the volume of space above the liquid solution in the beaker. Evidently, it only takes ~20 minutes for the produced gases to displace the air in the volume above the solution.

With a photocurrent density of 12.1 mA/cm² (at -0.82 V vs RHE), the as-grown ZrO₂ hierarchical nanowire film is the best transparent conductive oxide nanostructured photocatalyst reported to date.²³⁸ Remarkably, the partially delaminated hierarchical nanowire film provides nearly 3.5 times the photocurrent density of the as-grown hierarchical nanowire film, outperforming not only the best such transparent conductive oxide based photocatalysts by a wide margin but indeed the best (arrayed) photocatalysts reported to date. The measured photocurrent density for the delaminated hierarchical nanowires (42.4 mA/cm² at -0.82 V vs RHE) in the present work is significantly higher than those modified p-type and n-type 1D nanomaterials, including a three-dimensional branched

ZnO/p-Si heterojunction nanowire array (8 mA/cm² at -1.5 V vs Ag/AgCl),²⁴³ a p-type Cu₂O/n-type TaON heterojunction nanorod array passivated with an ultrathin carbon sheath (5.3 mA/cm² at 1.5 V vs RHE),²³³ a three-dimensional heterojunction photoanode of CoO_x/C₃N₄/Ba-TaON (5.6 mA/cm² at 1.6 V vs RHE),²⁴⁴ and a TiO₂-nanocrystal-decorated TiO₂ nanowires (2.2 mA/cm² at 0.5 V vs Ag/AgCl).⁷¹ Moreover, the photocurrent density of the partially delaminated hierarchical nanowires is also higher than the best photocathodes reported to date, including Pt-nanoparticle-decorated p-Si nanowire array (28 mA/cm² at 0.1 V vs RHE),²⁴⁵ and a TiO₂/Ti/n⁺pp⁺-Si heterostructure (25 mA/cm² at 0 V vs RHE).²³² In order to obtain the hitherto highest photocurrent densities, these latter two studies require the use of expensive platinum catalysts and employ complicated multistep synthesis techniques for the preparation of the photoelectrodes. This is in marked contrast to the present work where a relatively inexpensive material and a one-step catalyst-assisted pulsed laser deposition technique are used.

Since stoichiometric ZrO₂ has wide bandgaps: monoclinic (3.58 eV), tetragonal (4.07 eV), and cubic (3.26 eV),⁸³ photoelectrochemical activity is expected to come mainly from UV light illumination. This creates an inherent disadvantage for ZrO₂ (and other transparent conductive oxide materials with similar wide bandgaps) for solar-light driven applications because UV light ($\lambda < 400$ nm) represents only 5%–8% of the overall AM 1.5G light. In order to determine the photoresponse arising from separate UV and visible spectral illuminations, we couple the AM 1.5G light with appropriate short-pass (<400 nm) and long-pass filters (>400 nm). As shown in Figure 4.9c, the photocurrent density of partially delaminated hierarchical nanowire film is reduced from 42.4 mA/cm² to 32.2 mA/cm² when the long-pass filter is coupled with the AM 1.5G filter, and to significantly lower current density (20.5 mA/cm²) when the short-pass filter is employed. The photocurrent density observed for the partially delaminated hierarchical nanowire sample therefore mainly comes from the visible light region (>400 nm). We also investigate the contribution of different wavelengths of the long-pass filtered light by coupling the AM 1.5 G filter separately with the 400, 500, 600, 700, and 800 nm bandpass filters (each with a full width half maximum of 10 nm). The photocurrent densities so obtained at specific wavelengths after excluding the capacitive currents (the difference between light-on and light-off currents near -0.8 V): 0.6 mA/cm² (400 nm), 1.7 mA/cm² (500 nm), 1.6 mA/cm² (600 nm), 1.1 mA/cm² (700 nm), and 0.5 mA/cm² (800 nm) (Figure 4.9d) closely correlate with the relative light intensity wavelength profile of natural sunlight, with the maximum at 500 nm (Figure 4.9d, inset). The HF-treated regular nanowire sample also shows similar profile but with the photocurrent density between 500-800 nm 20-50% lower than the HF-treated

hierarchical nanowire sample (Figure 4.9d, inset). For the HF-treated nanobrick film, a relatively “flat” photocurrent response profile with the maximum at 600 nm and a significantly lower photocurrent density (50-70%) than the HF-treated hierarchical nanowire sample is obtained (Figure 4.9d, inset). The lower photocurrent profiles found for the regular nanowire and nanobrick films can be attributed to their smaller surface areas, while the discernibly different photocurrent wavelength response observed for the nanobrick film suggests that the nanobricks might have different compositions of defects, leading to different defect state distributions in the band structure, compared to the regular nanowires and hierarchical nanowires. The relatively higher photocurrent response of the hierarchical nanowire sample at longer wavelength also suggests that they have more defect states in the band structure than the regular nanowire sample.

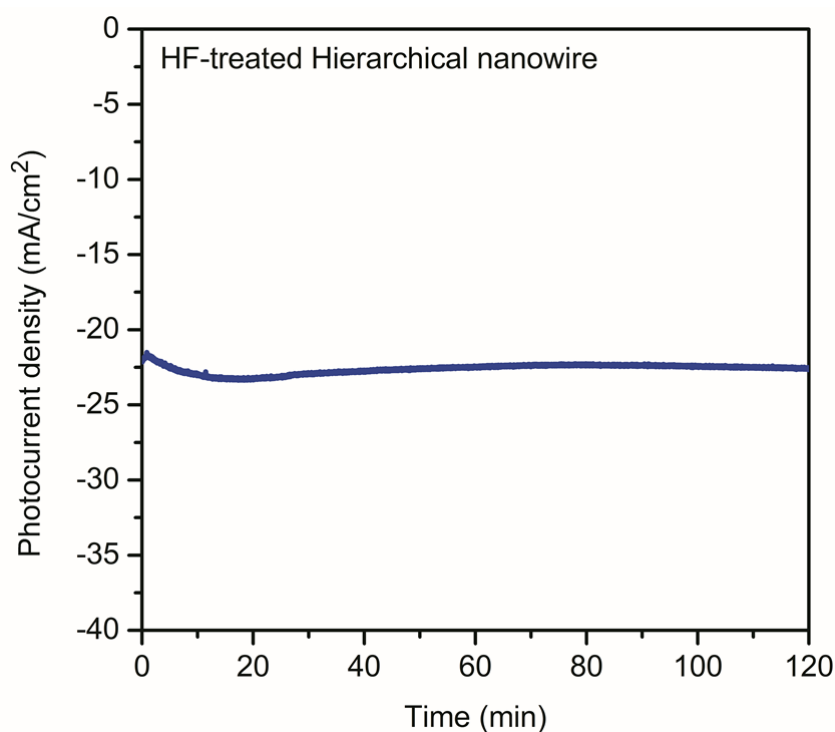


Figure 4.11 Photocurrent density of HF-treated hierarchical ZrO₂ nanowire film at -0.6 V vs RHE in 0.1 M H₂SO₄ + 0.01 M K₂SO₄ solution under simulated sunlight. Virtually no degradation in the photocurrent density is observed over the experiment period of 2 h.

The partially delaminated hierarchical nanowire film is therefore highly sensitive to the visible light component of the AM 1.5G spectrum. This is a significant result, because unlike the

previously reported case for N-doped TiO₂ nanotubes coated with a thin TaO_xN_y layer,²⁴⁶ where the observed photocurrent density, 2.5 mA/cm², in AM 1.5G light was found to reduce by nearly 80% to 0.4 mA/cm² with the visible light component (>420 nm), we observe only a 24% reduction with just the visible light component in the present work. Our visible-light-driven current density is also significantly higher than H₂-treated TiO₂ nanowires,⁸ and highly dense Si-core TiO₂-shell nanowire arrays²⁰⁷ which gave just 2-3% photocurrent density under visible light.⁵⁵ These results verify that our hierarchical nanowire sample is the top photoelectrochemical catalysis performer in the visible light region (>400 nm) of all the transparent conductive oxide photocatalysts reported to date.

As reported for the other material systems,²⁴⁷⁻²⁴⁹ both the bandgap and the deviation from stoichiometry (oxygen vacancy) increase with decreasing crystallite size.¹⁹⁹ In the hierarchical nanowire, the thickness of the nanoplates (3-6 nm) is much smaller than the diameter of the trunk of the nanowire (30-40 nm). The nanoplates are therefore expected to have a larger amount of oxygen vacancy defects and different bandgaps from the core nanowire. Meanwhile, the composition of the oxygen vacancy defects of ZrO₂ (i.e. the relative amounts of singly-charged, doubly-charged and neutral oxygen vacancies) could introduce defect-related bands below the conduction band minimum and above the valence band maximum of stoichiometric ZrO₂.^{11,250} As the singly-charged oxygen vacancy reduces Zr⁴⁺ ions to Zr³⁺ ions and generates one electron and one hole in the vacancy site while the doubly-charged oxygen vacancy leads to two Zr³⁺ ions or to one Zr²⁺ ion and two holes in the defect states, intermixing of the Zr⁴⁺, Zr³⁺ and Zr²⁺ ions and their corresponding holes at the defect sites could generate donor bands below the conduction band minimum and acceptor bands above the valence band maximum, respectively. The presence of the nanoplates on the nanowire backbone could therefore not just effectively improve the charge separation and/or transport but also extend the absorption edge into longer wavelength, which consequently improves the photoelectrochemical water splitting performance. Partial delamination improves the direct contact between the base of nanostructured film and the Si substrate, which in turn reduces the diffusion length of the photogenerated carriers and consequently the recombination losses, in contrast to the as-grown film where the photogenerated carriers have to travel across the entire film to reach the external contact.

A schematic diagram for the enhancement mechanism of photoelectrochemical water splitting reaction of the partially delaminated hierarchical nanowire film is shown in Figure 4.12. When the hierarchical nanowires are irradiated with AM 1.5G light, electron transfer takes place from both the valence band and oxygen vacancy defect states to the conduction band of ZrO₂. The photon-

excited electrons in the nanoplates react with the acceptor species (H^+) of the electrolyte and generate H_2 , while the photogenerated holes of the nanoplates injected into the valence band oxidize OH^- to produce O_2 at the Pt counter electrode. Owing to the single-crystalline nature of the core nanowire and to the direct contact between the nanostructured film and the Si substrate, the photogenerated holes in the valence band of the nanowire could migrate easily to the Si substrate and ultimately to the counter electrode. Similar process involving their corresponding defect states is also expected to occur in the trunks of these nanowires. The higher photocurrent density obtained from the partially delaminated hierarchical ZrO_2 nanowires can therefore be attributed to the dense mat of nanowires²¹⁵ with densely packed ZrO_2 nanoplates in individual nanowires. The presence of these nanoplates offers excellent light-trapping characteristics and a large contact area with the electrolyte, while the presence of a large number of oxygen vacancy defects in these nanoplates not only improves the efficiency of the charge separation process but also provides a highly conductive pathway for charge carrier collection. Their combined effects give rise to superior photoelectrochemical performance in the visible region.

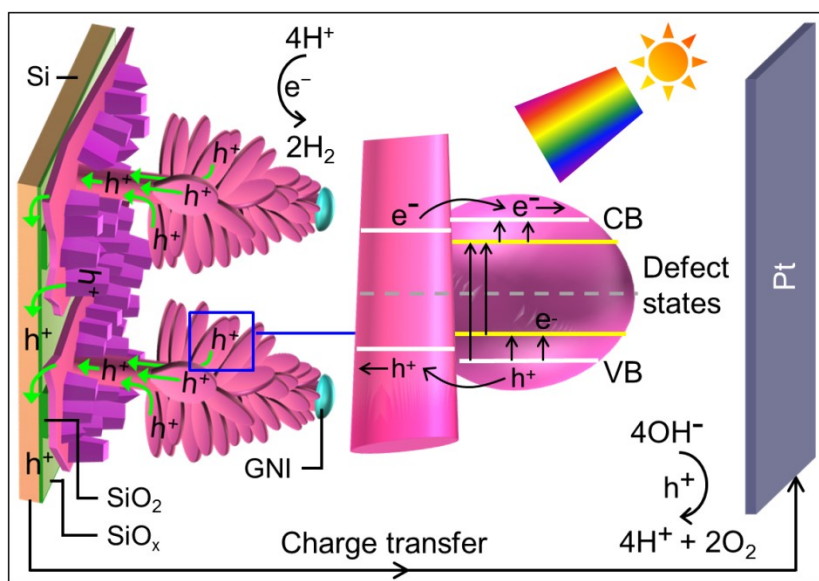


Figure 4.12 Schematic diagram for the charge separation and transfer process in the nanoplates of the HF-treated ZrO_2 hierarchical nanowires in a photoelectrochemical water splitting reaction driven by visible light irradiation. Similar process involving their corresponding defect states [located between the valence band minimum (VB) and conduction band maximum (CB)] is expected to occur also in the trunks of these nanowires.

4.3.3 Conclusion

In summary, by tuning the size of the GNI catalysts and the film thickness of the interfacial SiO₂ layer, we are able to synthesize nanoplate-decorated hierarchical ZrO₂ nanowires by a facile one-step catalyst-assisted pulsed laser deposition method. The use of a high vacuum system and precise control of the growth temperature and Ar flow have enabled us to produce, for the first time, defect-rich, single-crystalline nanostructured films with different composition of oxygen vacancy defects. We further demonstrate that post-treatment with dilute hydrofluoric acid solution could be used to dramatically reduce (by over three orders of magnitude) the charge transport resistance by partial removal of interfacial SiO₂ layer. The post-treatment also increases the surface area exposed to the electrolyte and the amount of oxygen vacancy defects due to buckling of the partially delaminated film. Photoelectrochemical measurement under simulated sunlight (100 mW/cm²) shows that the partially delaminated hierarchical nanowires exhibit an extraordinary photocurrent density (42.4 mA/cm²), 3.5 times that of the as-grown hierarchical nanowires (12.1 mA/cm²). This is the highest photocurrent ever obtained for both oxide-based and non-oxide-based photoelectrodes for photoelectrochemical water splitting under AM 1.5G simulated sunlight illumination. We also achieve the predominant photoactivity in the visible region and a Faradaic efficiency close to 100% for water reduction based on partial pressure measurements of the evolved gases, while stability tests show sustainedly high photocurrents even after 2 h of continuous operation. With an estimated 17.1% solar-to-hydrogen conversion efficiency, the present hierarchical ZrO₂ nanowire photocatalysts are therefore commercially viable for solar hydrogen production.

More importantly, the photocurrent density of partially delaminated hierarchical nanowires is reduced by only 24% from 42.4 mA/cm² to 32.2 mA/cm² when the ultraviolet light component (<400 nm) is filtered out and only visible light component is used. Unlike the previously reported cases for transparent conductive oxide photocatalysts, such as N-doped TiO₂ nanotubes coated with a thin TaO_xN_y layer,²⁴⁶ H₂-treated TiO₂ nanowires,⁸ Fe₂TiO₅ coated TiO₂ nanotube arrays,²¹⁷ and highly dense Si core TiO₂ shell nanowire arrays,²⁰⁷ where the observed photocurrent densities in AM 1.5G light were found to reduce by over 80% with just visible light illumination, the observed 24% reduction qualifies the partially delaminated hierarchical nanowires to be the best photocatalyst for photoelectrochemical water splitting driven by the visible light.

The record-high performance of the present photoelectrode (42.4 mA/cm²) is especially remarkable when considering that the length and density of the hierarchical nanowires are both

smaller than most of the hierarchical nanowire samples reported in the literature.^{233,243,245} In order to achieve a current density of 5-28 mA/cm², these latter hierarchical nanowires are produced with considerably higher areal density and average length of 5-15 μm, in order to provide more active sites for the photoelectrochemical reaction. The photocurrent density of our ZrO₂ hierarchical nanowires even in its present configuration is already the highest ever reported, and it can be easily increased further by increasing the areal density of the nanowires (e.g., by increasing the GNI areal density) and/or the length of the nanowires (e.g., by increasing the deposition time). An even higher efficiency can be achieved by adapting more elaborate strategies including fabricating hybrid and/or core-shell nanowires and synthesizing binary or tertiary nanowires, which can be easily accomplished by switching the targets (using a multi-target holder in our PLD system) during growth of the ZrO₂ nanowires. The present approach of intentionally growing defect-rich nanowires both chemically (by introducing oxygen vacancy defects) and mechanically (by partially delamination and introduction of hierarchical architectures) by catalyst-assisted PLD growth followed by simple HF treatment could be extended to other wide bandgap semiconductors. The defect-rich, partially delaminated ZrO₂ hierarchical nanowires promise viable alternatives for a variety of solar visible-light driven applications, including photoelectrochemical water splitting, photocatalysis, and solar cells.

Chapter 5

High- T_C Ferromagnetism in Defect-rich Dopant-free ZrO_2 Nanostructures

5.1 Introduction

Uncovering the harmony of different electronic properties of solid-state materials provides better understanding of new phenomena of fundamental interest to basic research and practical applications.^{251,252} Modern solid-state electronics is often developed in parallel with or directly through the development of structures based on their “champion” materials. The revolutions of microelectronics with Si, optoelectronics with GaAs, and display technology with liquid crystals are some of many examples. These conventional applications are based mainly on manipulating the electron charge. An intriguing alternative is the field of spin-based electronics, in which the manipulation of the electron spin in semiconductor devices promises a variety of emerging applications, such as non-volatile memory, quantum computing, and solid-state magneto-optical telecommunication devices.²⁵³ The success of spin-based electronics depends on establishing a champion material that combines the desirable properties of ferromagnets with those of semiconductors. Dilute ferromagnetic semiconductors belong to one such unique class of materials with special properties, such as giant Faraday rotation and Zeeman splitting.²⁵⁴ These dilute ferromagnetic semiconductors are usually semiconducting alloys with a small amount of their lattice atoms replaced by substitutional magnetic atoms (i.e., dopants). In contrast to magnetic semiconductors, dilute ferromagnetic semiconductors offer reliable control of not just stoichiometry but also the nature of carrier, impurity, and crystallographic structure, which can be used to provide interesting magneto-optical and transport properties.¹⁰⁸ Furthermore, existing techniques for fabricating semiconductor heterostructures enable incorporation of dilute ferromagnetic semiconductor layers into transistors, quantum wells, and other electro-optical devices, in which spin splitting can also be tuned by confinement energy and size quantization.^{255,256}

For dilute ferromagnetic semiconductors, the $Ga_{1-x}Mn_xAs$ and $In_{1-x}Mn_xAs$ systems have attracted the most attention.¹⁰⁸ These systems have provided a fertile ground to demonstrate spin injection, control of ferromagnetism by means of the electric field, and tunneling anisotropic magnetoresistance in planar junctions.²⁵⁷ The highest reported Curie temperature (T_C) for $Ga_{1-x}Mn_xAs$ is below 170 K, and even lower for $In_{1-x}Mn_xAs$.¹⁰⁸ As only ferromagnets with $T_C > 500$ K

are qualified for use in a room-temperature device,²⁵⁸ their low T_c becomes their main drawback for practical device applications. In contrast, transparent dilute ferromagnetic semiconductor oxides (TDFSOs) have generally higher T_c , with, e.g., 850-930 K reported for Cr-doped indium oxide thin film.²⁵⁹ TDFSOs therefore represent the alternative materials for future applications in spin-based electronics. However, there are major challenges in the development of dopant-based TDFSO systems, which include the low solubility limit of transition metal ion dopants (such as Mn, Fe, Co, Cr) in the host lattice, and their tendency to form clusters and to occupy sites other than the cation-substitutional ones.²⁶⁰ While the resulting systems may have collective magnetic property, the magnetism is often not uniform over the entire materials (due to dopant inhomogeneity). Furthermore, studies employing X-ray magnetic circular dichroism have revealed that dopants (Co, Mn, and Cr) with unpaired d electrons are not the origin of ferromagnetism, but rather it is the oxygen vacancy defects in the host oxide matrix that mainly contribute to ferromagnetism.^{129,130} More importantly, it has been found in a multilayer device structure that the dopants could migrate from the host layer to the adjacent layers during the operation of the device.²⁶¹ The elusive nature of dopants has therefore made practical implementation difficult. Clearly, there is an acute need for an alternative approach to the traditional method of incorporating dopants as a means to create the desirable properties of TDFSOs. In order to better understand and to exploit the spin-dependent properties of TDFSOs in spin-based electronic devices and other applications, it is crucial to prepare dopant-free TDFSOs, in which ferromagnetic ordering can be achieved (and controlled) at or above the room-temperature. This latter requirement has remained to be a major challenge.

A number of theoretical calculations and experimental studies have suggested that in addition to specific crystallographic phases or structures,⁵ dopants⁴ or/and defects¹³³ provide the main contribution to the ferromagnetic behavior of TDFSOs. Traditional mechanisms of ferromagnetism, such as phase segregation, super-exchange, and double exchange, cannot readily account for the long-range ordering in doped TDFSOs.²⁶² Despite a number of theoretical models developed to decipher the coupling mechanism responsible for the observed ferromagnetism in doped TDFSOs,^{6,126,133,263} the origin of ferromagnetism continues to be under intense debate.^{6,133} In more recent studies, ferromagnetism has also been observed in nanocrystalline TDFSOs that nominally do not contain any magnetic impurity.^{5,140} This begs the question of whether ferromagnetism is really due to just extrinsic effects such as doping and secondary phases, or it also has an intrinsic origin. While traditional descriptions of exchange interactions (double exchange, superexchange, and Ruderman-Kittel-Kasuya-Yosida interactions) cannot account for ferromagnetic ordering in undoped

TDFSOs,^{146,264} improved models involving bound magnetic polaron²⁵⁸ and charge transfer ferromagnetism¹⁴⁶ have also failed to address the important fundamental question of how pure semiconducting oxides, i.e. without any transition metal dopants (d electrons), can become ferromagnetic. These studies therefore suggest that other mechanisms must be responsible for ferromagnetism found in dopant-free TDFSOs.

For undoped TDFSOs, there are additional challenges in making use of their ferromagnetic properties. This is because ferromagnetism found in undoped TDFSOs thin films and nanoparticles has thus far been weak while discernible surface effects have also been observed.²⁶⁵ Compared to thin films, one-dimensional (1D) nanostructures, such as nanowires or nanospikes, with relatively large specific surface area offer abundant surface defects that could potentially enhance the intrinsic ferromagnetism. More importantly, 1D nanostructures also offer unique, physical properties arising from the nanoscale size and quantum confinement effects, all of which could affect carrier transport, exchange interaction of electron spins, and therefore ferromagnetic properties. Nanostructures with a large amount of defects are therefore expected to provide an excellent platform to investigate the origin of ferromagnetism in undoped TDFSOs.

In recent years, ZrO₂ thin films have attracted extensive research interest because of their compatibility with modern Si microelectronics.²⁶⁶ For 1D ZrO₂ nanostructures, however, there have been only a few reports about their synthesis, including two-step anodization of superimposed Al/Zr films,¹⁰¹ hydrolysis and condensation of zirconium sol on tubular alumina template,^{101,102} and chemical vapour deposition of ZrCl₄ powders at 1000 °C.¹⁰³ One major limitation of wet-chemistry methods is that the precursor materials are often incorporated into the final structure as an impurity.¹⁰¹ As a result, the charge transport efficiency and material stability are significantly reduced due to poor crystallinity and the presence of considerable amounts of grain boundaries. Because of the extremely low vapour pressures and high melting points of ZrO₂, vapour-liquid-solid (VLS)⁷¹ growth has not been successful for these 1D ZrO₂ nanostructures.¹⁰⁴ Unlike thermal evaporation and chemical vapour deposition, pulsed laser deposition (PLD) involves direct laser ablation of the target material into the gaseous form, and the absorption of a high-intensity laser pulse by a small volume of material leads to vaporization in the thermally non-equilibrium regime while keeping its stoichiometry intact. As activation of the gold nanocatalysts could occur at a lower temperature, the formation of 1D nanostructures could also proceed at a lower temperature (via VLS growth) than other vapour deposition methods.⁷¹ Furthermore, the substrate temperature, oxygen partial pressure, and reductive

growth environment during PLD can be varied to control not only the rate of deposition but also the crystallinity, morphology and the amount of oxygen-related defects.²⁴ Engineering defect-rich ZrO₂ nanostructures without addition of impurity atoms (dopants) removes such constraints^{267,268} as chemical incompatibility and any associated undesirable impurity diffusion in a multilayer structure, and it provides a new approach to producing highly stable TDFSO with desirable electrical transport and magneto-optical properties.

Similar to other TDFSOs, conflicting ferromagnetism mechanisms have been proposed for pristine ZrO₂ thin films.⁴⁻⁶ More importantly, the origin of ferromagnetic properties in undoped ZrO₂ nanostructures with a large specific surface area (such as nanobricks, nanospikes, and nanowires) and a large amount of oxygen vacancy defects remains unknown. With this objective in mind, we have prepared, for the first time, defect-rich, dopant-free nanostructures of ZrO₂ with different specific surface areas and amounts of defects, including nanobricks, nanopopcorns, nanospikes, and nanowires, on a Si substrate by catalyst-assisted PLD method. Here, we show that ferromagnetism is independent of the phase of ZrO₂, and is clearly related to the specific surface area of the nanostructure and to the amounts and types of oxygen vacancy defects in that particular nanostructure. A remarkably high saturation magnetization (5.9 emu/g at 2000 Oe) and a high T_C (700 K) are observed for ZrO₂ nanowires. Our results therefore not only firmly establish oxygen vacancy defects are primarily responsible for the origin of ferromagnetism in undoped TDFSO nanostructures, but also demonstrate the potential of controlling their magnetic properties by manipulating the composition of oxygen vacancy defects within the host lattice.

5.2 Materials and Methods

ZrO₂ nanostructures are synthesized on oxidized Si(100) template by catalyst-assisted pulsed laser deposition (PLD) method²¹⁵ in a NanoPLD system (PVD Products) with a base pressure of 1×10^{-7} Torr. A KrF excimer laser (248 nm wavelength) operated with a laser fluence of 350 mJ/pulse at a repetition rate of 5 Hz is used to ablate a ZrO₂ target, prepared by cold-pressing ZrO₂ powders (Aldrich, 99.99% purity) with a pressure of 25 MPa followed by sintering at 1000 °C in air for 48 h. A silicon chip (10×10 mm², 525 μm thick), pre-cut from a Si(100) wafer (p-type, B-doped, with a resistivity of <0.005 Ω cm, Siegert Wafer), is chemically oxidized using H₂O₂ and NH₄OH solutions following the RCA cleaning procedure.²³⁹ Gold nanoisland (GNI) catalysts are produced on the

resulting oxidized Si(100) substrate (denoted as Ox-Si) by magnetron sputtering a thin layer of Au followed by annealing in air.²⁶⁹ The Ox-Si substrate is mounted perpendicular to the expansion direction of the laser plume on a windowed substrate holder. During deposition, the substrate is in close proximity to the top of the visible region of the laser plume, with the target-to-substrate separation kept at 30 mm. The substrate temperature (i.e. growth temperature) can be varied between 550 and 770 °C by radiative heating of infrared heat lamps from the backside of the substrate. Deposition is carried out on the GNI template for 90 min in 200 mTorr of Ar at a flow rate of 10 sccm.

The morphology of the sample is examined by field-emission scanning electron microscopy (SEM) in a Zeiss Merlin microscope. Glancing-incidence X-ray diffraction (XRD) measurements are performed in a PANalytical MRD X'pert Pro diffractometer with a Cu K α source, by using a parallel X-ray beam setup with an incidence angle of $\omega=0.3^\circ$ over the selected 2θ range. The crystallinity of ZrO₂ nanostructures is studied by transmission electron microscopy (TEM) in a Zeiss Libra 200MC microscope. For TEM measurement, the nanostructures are scraped off the substrate using a sharp blade and mixed with liquid-chromatography-grade methanol in an Eppendorf tube and sonicated for 10 min, and the resulting suspension is then transferred onto a holey carbon TEM copper grid. The chemical-state compositions of the nanostructures are analyzed by X-ray photoelectron spectroscopy (XPS) in a Thermo-VG Scientific ESCALab 250 microprobe with a monochromatic Al K α X-ray source (1486.6 eV), operated with a typical energy resolution of 0.4–0.5 full width at half-maximum. The magnetic property is characterized at different temperature by using a superconducting quantum interference device (SQUID) magnetometer (Quantum Design MPMS SQUID-VSM), with the applied magnetic field direction parallel to the sample surface. It should be noted that only plastic tweezers and quartz holders have been used during sample preparation and magnetic measurement to avoid any unintentional ferromagnetic contamination. The diamagnetic contribution from the Si substrate and the quartz sample holder has been removed, and the magnetization of the ZrO₂ nanostructures is normalized by the mass of the measured sample, as estimated by assuming that the nanostructures are completely filled in the measured volume (i.e., without considering the filling factor) with a bulk density of 5.68 g/cm³.

5.3 Results and Discussion

The SEM images shown in Figure 5.1 illustrate the PLD growth of ZrO₂ nanostructures on the GNI/Ox-Si template. For all the depositions, GNIs have been deposited on the Ox-Si substrate for

the same amount of sputtering time (4 s) followed by annealing under the same conditions (at 600 °C in air for 30 min). The resulting GNI size distributions are found to be highly reproducible, with a mean diameter of 15-25 nm (Figure 5.1a). The thickness of the SiO₂ layer has also increased correspondingly from 3 nm after the RCA cleaning to 6 nm for the GNI/Ox-Si template. PLD growth on the GNI/Ox-Si template in 200 mTorr Ar for 90 min at 550 °C evidently produces ZrO₂ nanopopcorns, made up of distorted tetragonal-shaped nanobricks (Figure 5.1c1, inset). Each nanotetragon has well-defined facets with typical lengths of 15-30 nm, and their bases are joined to one another around a GNI as their common core in a flower-like morphology (Figure 5.1c2, inset). On the other hand, deposition at 650 °C produces spike-like nanostructures (Figure 5.1d1), the length and the base diameter of which are estimated to be several hundred nm and 40-50 nm, respectively (Figure 5.1d2). The backscattered-electron image further reveals its sharp tip with a tip diameter less than 10 nm, on top of which lies a Au nanoparticle (Figure 5.1d2, inset). This confirms that the GNI catalysts have been detached from the substrate, and they stay on top of the growing nanostructures, clearly revealing the VLS nanostructure growth mechanism.²⁷⁰ Interestingly, PLD growth at 770 °C produces slightly tapered nanowires with a nearly uniform cross section, the diameter of which decreases from 50-60 nm at the base to 40-50 nm at the tip along their typical lengths of 2-3 μm (Figure 5.1e1, 5.1e2). As for the nanopikes, the presence of Au nanoparticles at the tips of individual nanowires also supports the VLS growth mechanism for these nanowires. In a separate experiment, we perform PLD growth of ZrO₂ without the GNI catalysts on the Ox-Si substrate. Figure 5.1b shows that this leads to a nanoparticulate film with nanobricks of typical lengths of 10-30 nm. Closer examination of the nanostructured films shown in Figure 5.1c-5.1e also reveals the presence of similar type of nanobricks among the bases of the nanopopcorns, nanopikes and nanowires. This suggests a concurrent vapour-solid growth mechanism in regions where there is no catalyst. However, PLD growth at 550 – 750 °C on a GNI/Ox-Si template with the SiO₂ layer thickness less than 6 nm produces mainly nanopopcorn-like film (not shown), due to the formation of Au-silicide by the interfacial reaction of Au and Si.¹⁹⁰ The thicker SiO₂ layer on the Ox-Si template prevents Au diffusion and the subsequent Au-silicide formation. A SiO₂ layer with the appropriate thickness (of 6 nm) is therefore extremely important for enabling VLS growth in the present PLD method.

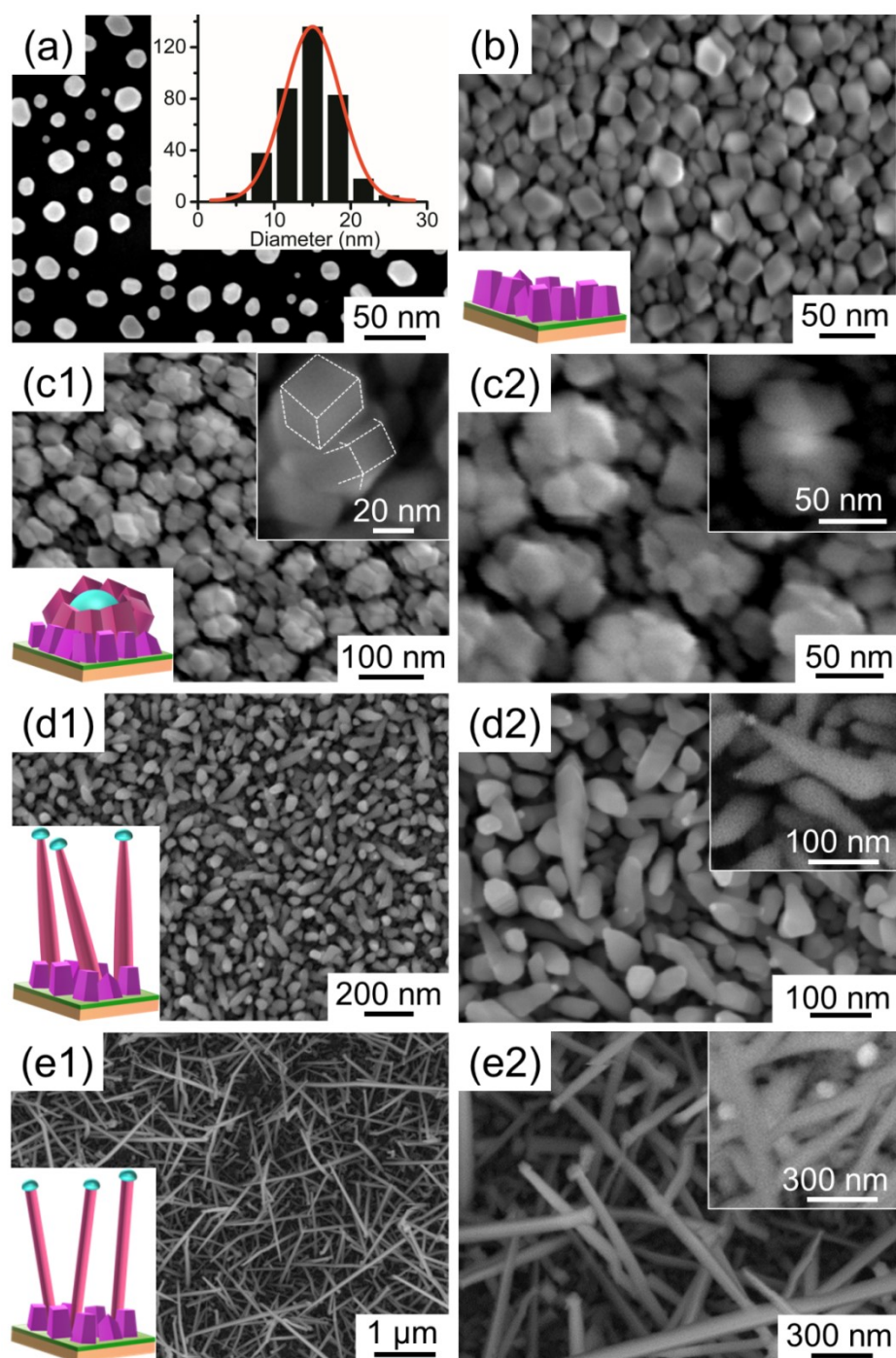


Figure 5.1 SEM images of (a) typical gold nanoislands (GNIs), with the corresponding near-Gaussian size distribution (inset), deposited on an Ox-Si template, (b) ZrO_2 nanobrick film PLD-grown on pristine Ox-Si template (without any GNI) at 770 °C, ZrO_2 nanopopcorns, nanospikes and nanowires PLD-grown on the GNI/Ox-Si templates in 200 mTorr Ar for 90 min at, respectively, (c1, c2) 550 °C, (d1, d2) 650 °C, and (e1, e2) 770 °C. The corresponding lower left insets show schematic models of

the respective as-grown nanostructures, with the backscattered electron images (upper right insets) depicting a gold nanoparticle (c2) at the core and (d2, e2) at the tips of the respective nanostructures. The SEM image in the upper right inset of (c1) illustrates the shape of the ZrO₂ nanopopcorns.

In the present study, the growth temperatures chosen for the nanostructures are all lower than the lowest eutectic temperature for the bulk Au-Zr binary system (863 °C).²³⁷ As observed previously for other material systems, both VLS and vapour-solid growth could occur simultaneously below the eutectic temperature, with the vapour-solid growth generally 10-100 times slower than the VLS growth at the same precursor partial pressure and temperature.¹⁹⁶ We therefore expect both growth mechanisms to be operative for the nanospikes and nanowires, while the nanopopcorn and nanobrick structures are evidently formed via the vapour-solid mechanism only. Although both vapour-solid and VLS growth occur concurrently, the VLS growth predominates at a higher growth temperature. The slower vapour-solid growth at a particular growth temperature¹⁹⁵ could, however, perturb and introduce variations in the general morphology of nanospikes and nanowires. The formation of shorter tapered-shape nanospikes at 650 °C and of longer nanowires at 770 °C therefore suggests that the catalysts remain semi-solid below 650 °C, which consequently reduces the diffusion rate of incoming atoms through the Au seeds and thus the VLS growth rate. As a result, VLS growth becomes less dominant below 650 °C. The thinner average diameter found for the nanowires than the nanospikes also suggests that the VLS growth rate is higher than the vapour-solid growth rate at a particular growth temperature above 650 °C. The present observation therefore illustrates that the PLD growth temperature can be used to effectively manipulate the dominant growth mode (vapour-solid vs VLS), and consequently the cross-sectional dimension and overall morphology of the deposited ZrO₂ nanostructures. In Figure 5.2, we schematically summarize the different ZrO₂ nanostructures on the two templates: Ox-Si and GNI/Ox-Si, obtained at three different growth temperatures.

Figure 5.3 shows the corresponding glancing-incidence X-ray diffraction (XRD) patterns of the as-deposited nanostructures. The prominent diffraction peaks of the nanobrick film are in excellent accord with the tetragonal ZrO₂ reference pattern (PDF2 #01-080-0784). For nanopopcorns, additional minor contributions from the monoclinic ZrO₂ features (PDF2 #01-083-0940), along with the features from the FCC phase of metallic Au (PDF2 #03-065-8601), are observed. These additional contributions from the monoclinic ZrO₂ features are found to increase for the nanospikes and nanowires. Of particular interest are the remarkably different relative peak intensity ratios of the

monoclinic (-111) peak at 28.18° to the tetragonal (101) peak at 30.24° among the nanopopcorns, nanopikes, and nanowires.

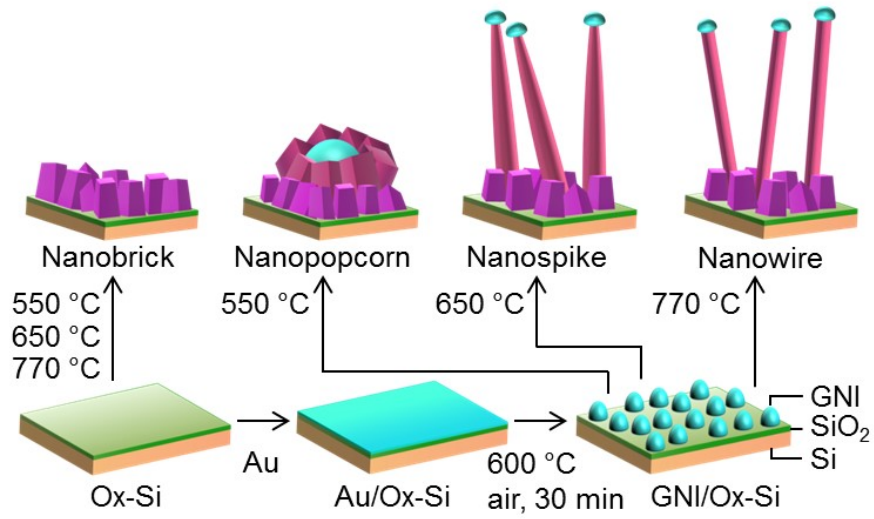


Figure 5.2 Schematic models of ZrO₂ nanostructures grown on Ox-Si templates without and with gold nanoislands (GNIs) in 200 mTorr Ar for 90 min at 550 °C, 650 °C, and 770 °C.

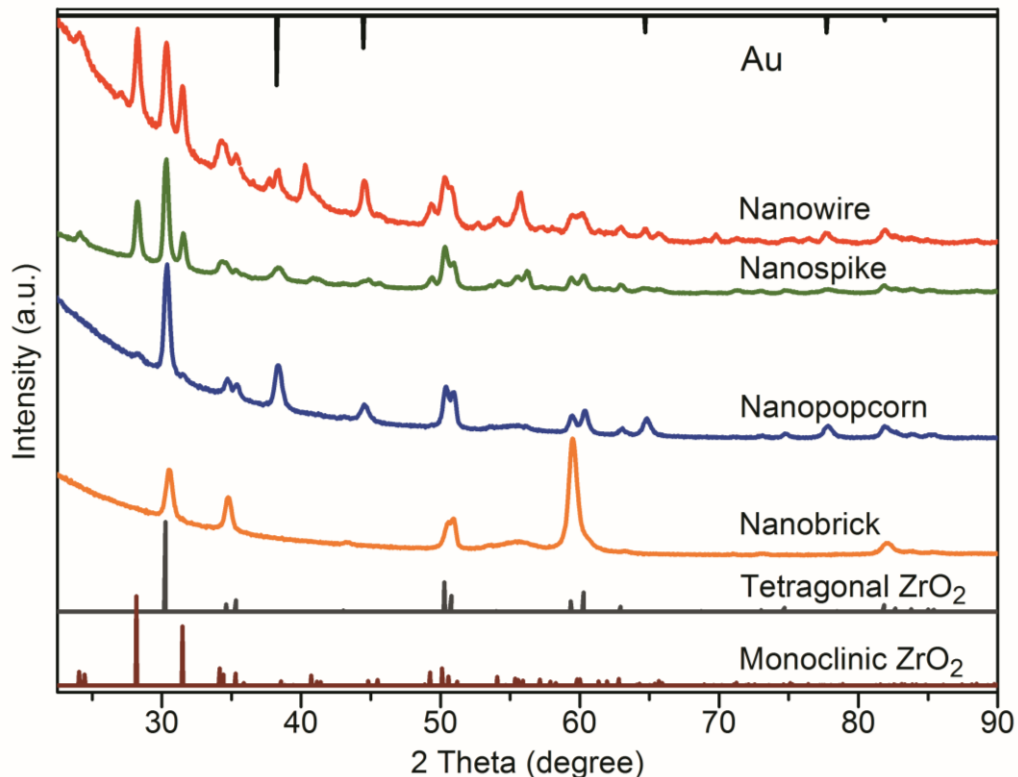


Figure 5.3 Glancing-incidence XRD patterns of different PLD-grown ZrO_2 nanostructures obtained at an incidence angle of 0.3° . The PDF2 reference patterns of the FCC phase of Au (#03-065-8601), and of the monoclinic phase (#01-083-0940) and tetragonal phase (#01-080-0784) of ZrO_2 are shown as top, and bottom bar graphs, respectively.

Further insight into the morphology and crystallography of the as-deposited nanostructures can be obtained by transmission electron microscopy (TEM). Figure 5.4a1 shows a typical low-magnification TEM image of the ZrO_2 nanopopcorns, in which clustering of several distorted nanotetragons (grey region) around a single gold nanoparticle core (dark region) is clearly observed without any evidence of gold at the edge of these tetragons. The size of these nanopopcorn structures is 80-140 nm while the typical dimension of the gold nanoparticles at the cores is 50-80 nm (Figure 5.4a1), in good accord with our SEM observation (Figure 5.4c1, 5.4c2). Figure 5.4a2 shows the high-resolution TEM image of two selected areas of a nanopopcorn. The lattice fringes of the nanotetragons at the perimeter indicate that the constituent particles are single-crystalline, and that their respective interplanar spacings of 3.2 Å and 2.6 Å correspond to those of the (-111) and (002) planes of monoclinic ZrO_2 . In Figure 5.4b1, the tapered shape of the nanospikes is clearly observed,

while the diameter of the nanowires appears nearly uniform along the entire length as shown in Figure 5.4c1. The corresponding high-resolution TEM images (Figure 5.4b2, 5.4c2) show that the nanopikes and nanowires are also single-crystalline and that their respective interplanar spacings of 2.8 Å and 2.6 Å correspond to the (111) and (002) planes of bulk monoclinic ZrO₂, respectively. Interestingly, the nanobricks in the gaps among the nanopopcorns, nanopikes and nanowires exhibit interplanar spacings of 2.9 Å and 2.5 Å, corresponding to the (101) and (110) planes of tetragonal ZrO₂, respectively (Figure 5.5). These results therefore suggest that the PLD-grown ZrO₂ nanopopcorns, nanopikes, and nanowires are predominantly monoclinic, while the nanobricks among these nanostructures (similar to those that make up the nanobrick film) are predominantly tetragonal ZrO₂. Indeed, our TEM results confirm the presence of both monoclinic and tetragonal XRD features for the ZrO₂ nanopopcorn, nanopike and nanowire films (Figure 5.3).

Figure 5.4d shows the room-temperature magnetization versus magnetic field (M - H) curves for the nanobricks, nanopopcorns, nanopikes, and nanowires when the external magnetic field is applied parallel to the respective sample surfaces (i.e. in-plane direction). Evidently, all the samples exhibit well-defined hysteresis loops, indicating room-temperature ferromagnetic behavior. More importantly, the film containing more monoclinic phase has a larger saturation magnetization. The saturation magnetization (M_s) measured at 2000 Oe for the nanowires (5.9 emu/g) is found to be 2.0, 4.9, and 9.8 times those of nanopikes (2.9 emu/g), nanopopcorns (1.2 emu/g), and nanobricks (0.6 emu/g), respectively, while the coercivity (H_c) for the nanowires (99 Oe) is approximately twice that of the nanobricks (50 Oe) (Figure 5.4d, inset). This is a significant result, because in marked contrast to the previously reported ZrO₂ planar thin films,^{5,271} of which the observed ferromagnetic behaviour was found to reduce with increased amount of the monoclinic phase, we observe increase in ferromagnetism with increase of the monoclinic phase in the ZrO₂ nanostructures here. More importantly, the saturation magnetization increases with increasing specific surface areas of the ZrO₂ nanostructures (Figure 5.4d). This apparent morphology dependence of room-temperature ferromagnetism further supports specific surface area effect and surface-state effect of these nanostructures on their magnetic behaviour. It should be noted that we also characterize and obtain essentially diamagnetic behavior for the pristine Ox-Si template, GNI/Ox-Si template, and quartz sample holder (used for the magnetization measurements) under the same conditions (not shown). In addition, to investigate the effect of the PLD growth temperature on the magnetization of these substrates, we examine pristine Ox-Si substrates annealed in 200 mTorr Ar at 770 °C for 90 min in the PLD chamber and confirm that they also do not exhibit any ferromagnetic behavior.

Recent studies have suggested that point defects, such as oxygen vacancies, could stabilize the tetragonal phase of ZrO_2 , providing the key to understand the origin of the observed room-temperature ferromagnetic behavior in undoped ZrO_2 .^{5,271} To date, ferromagnetism has only been observed in tetragonal ZrO_2 , and no ferromagnetism has ever been reported for monoclinic ZrO_2 with or without oxygen vacancy defects.⁵ For a mixture of monoclinic and cubic phases of ZrO_2 , the interfacial defects in the grain boundary region have, however, been suggested to play an important role in generating ferromagnetic order in undoped ZrO_2 .²⁷² There is, therefore, no consensus on the defect origin of room-temperature ferromagnetism in undoped ZrO_2 . Furthermore, room-temperature ferromagnetism is often observed only in post-annealed thin film and powders of TDFSO nanostructures, and it has been found to exhibit notable surface-dependent effects,²⁶⁵ particularly those related to surface defects.^{273,274} In the present study, we have observed ferromagnetism in undoped tetragonal ZrO_2 nanostructures and, for the first time, undoped monoclinic ZrO_2 nanostructures, and the magnetization appears to depend on the morphology, regardless of the phase of the ZrO_2 nanostructures. The dependence of the observed room-temperature ferromagnetic behavior on the morphology but not on the phase of these ZrO_2 nanostructures provides us with an important clue both to understand the origin of room-temperature ferromagnetism and to realize its controllability in undoped ZrO_2 nanostructures.

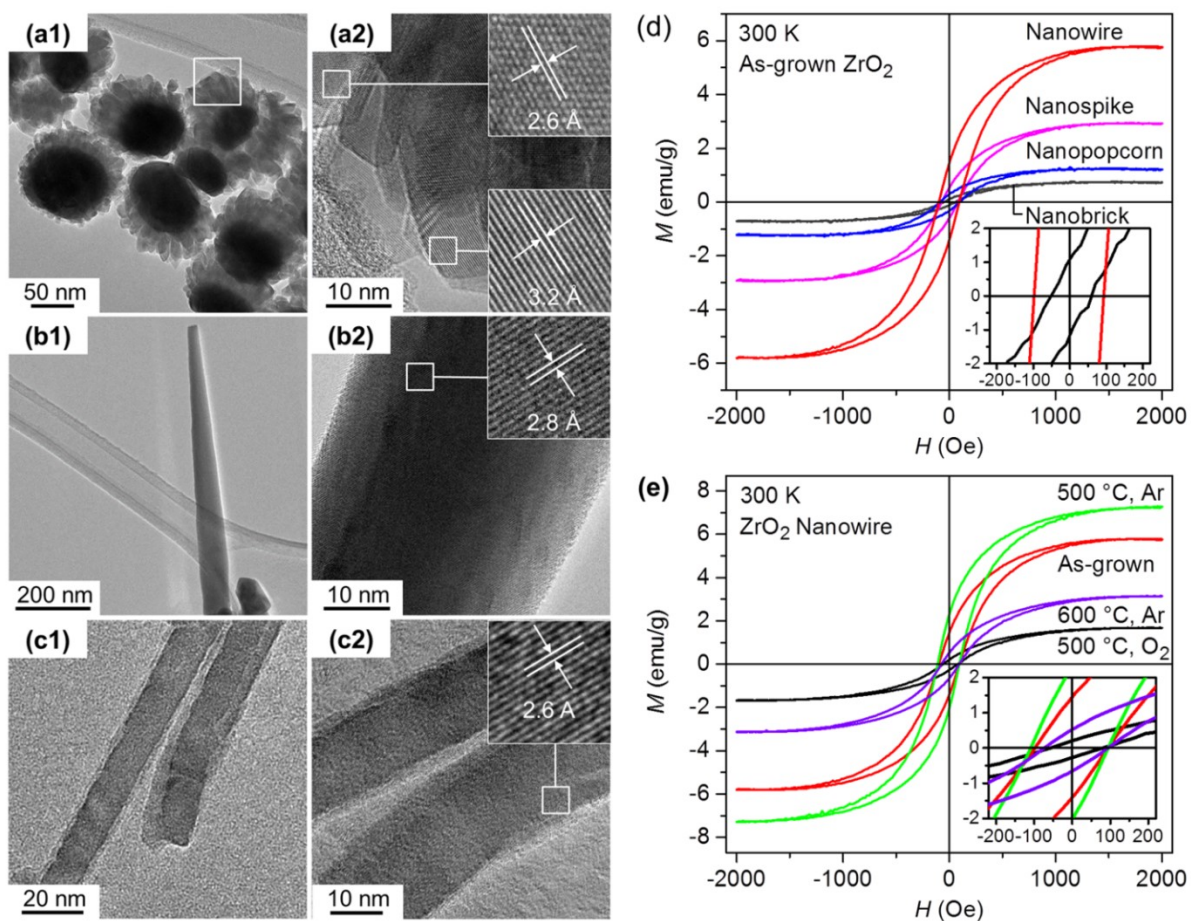


Figure 5.4 TEM images of typical (a1, a2) ZrO_2 nanopopcorns, (b1, b2) nanospikes, and (c1, c2) nanowires, with the corresponding high-resolution images of selected areas of individual nanostructures shown in insets. (d) Magnetization (M) vs magnetic field (H) curves of as-grown ZrO_2 nanostructures, with the enlarged view of the hysteresis loops for ZrO_2 nanobricks and nanowires given in inset. (e) M - H curves for as-grown and annealed ZrO_2 nanowires under different post-treatment conditions of annealing temperature and atmosphere, with the enlarged view of the respective hysteresis loops given in inset.

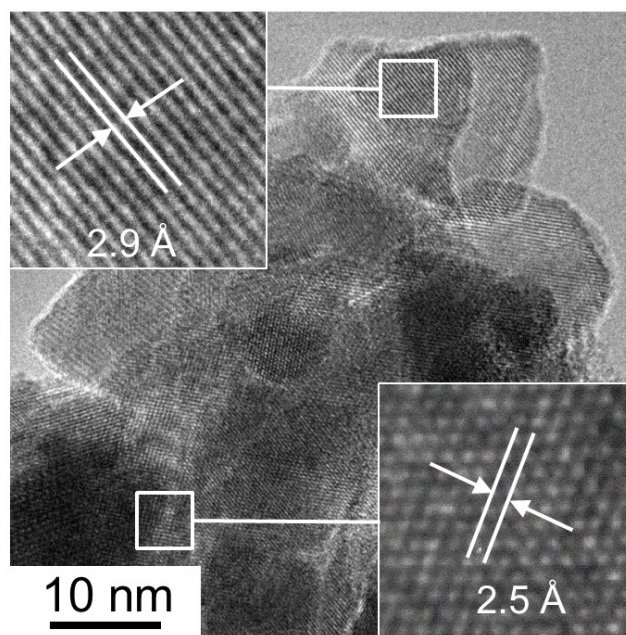


Figure 5.5 TEM image of ZrO_2 nanobricks located in the gap among the ZrO_2 nanowires. The corresponding insets showing the magnified images of individual nanobricks, with interplanar spacings of 2.9 Å and 2.5 Å, corresponding to the (101) and (110) planes of tetragonal ZrO_2 , respectively.

In order to determine the role of defects in room-temperature ferromagnetism for the PLD-grown ZrO_2 nanostructures, we perform X-ray photoelectron spectroscopy (XPS) study of the as-prepared samples. A representative survey spectrum of ZrO_2 nanowires shows that only Zr, O, Au, and C are present (Figure 5.6). More importantly, the absence of Mn 2p at 638.3 eV, Fe 2p at 706.8 eV, and Co 2p feature at 779.4 eV (binding energy) allows us to rule out any contamination caused by unwanted magnetic impurities in the sample. The chemical states of Zr and O in the samples are determined from the deconvoluted Zr 3d and O 1s spectra (Figure 5.7a). The prominent Zr 3d_{5/2} peak at 182.4 eV corresponds to the Zr^{4+} state for ZrO_2 , while the residual intensity between the Zr^{4+} feature (at 182.4 eV) and metallic Zr^0 feature (at 178.3 eV) could be generally fitted to two components: ZrO_{x_1} ($2 > x_1 > 1.5$) and ZrO_{x_2} ($1.5 \geq x_2 > 1$). The prominent O 1s peak located at 530.3 eV is attributed to O^{2-} in ZrO_2 , while the residual O 1s intensity between 532.3 eV and 530.9 eV can be assigned to oxygen anions in the oxygen-deficient ZrO_{x_1} and ZrO_{x_2} species within the matrix.

Density function theory (DFT) calculations show that excess electrons in oxygen-deficient ZrO_2 experience an attractive Madelung potential (as in MgO), which results into three favoured charge states of oxygen vacancies.²⁴⁰ Accordingly, we have therefore classified the overall oxygen

vacancy concentration to consist of neutral, singly-charged, and doubly-charged defect contributions (Figure 5.7c). The formation of a singly-charged oxygen vacancy would produce one electron in the singly-charged oxygen vacancy site, with the other electron in the corresponding Zr atom leading to a Zr^{3+} ($4d^1$) ion (Figure 5.7c2). For the doubly-charged oxygen vacancy, the two electrons from the vacancy site could be located at two nearest-neighbour Zr ions leading to two Zr^{3+} ($4d^1$) ions (Figure 5.7c3), or at one single Zr atom leading to a Zr^{2+} ($4d^2$) ion (Figure 5.7c4). For the neutral oxygen vacancy, the two electrons remain at the oxygen vacancy site and there is therefore no apparent effect on the Zr^{4+} ion (Figure 5.7c1).

It has also been found by DFT calculations that the singly and doubly charged oxygen vacancies have larger lattice relaxation effects than neutral oxygen vacancies.²⁴⁰ For instance, for the singly charged defect, the four Zr neighbors are found to move away from the vacancy by about 0.1 Å, while formation of a neutral oxygen defect leads to smaller relaxation of the neighboring Zr atoms with displacements of about 0.01–0.02 Å from the perfect crystal positions.²⁴⁰ The different extents of lattice relaxation associated with the differently charged oxygen vacancies change the corresponding O 1s and Zr 3d binding energies in oxygen-deficient ZrO_2 . The decrease in electron charge density for the O– Zr^{3+} bond (relative to the O– Zr^{4+} bond) results in less screening of the O 1s electrons, which consequently increases the effective nuclear charge. This leads to an increase in the O 1s binding energy and correspondingly a decrease in the Zr 3d binding energy. The O 1s peaks of ZrO_{x1} and ZrO_{x2} therefore correspond to the singly- and doubly-charged oxygen vacancies, respectively, while the neutral oxygen vacancy defect peak likely lies at or near the same position of the ZrO_2 peak. As the binding energy of Zr 3d peak of ZrO_{x2} is farther away from the metallic Zr, and the relative intensities (and concentrations) of O 1s and Zr 3d in ZrO_{x2} are significantly different from those in ZrO_{x1} , the doubly-charged oxygen vacancies are expected to lead to predominantly Zr^{3+} ions (Figure 5.7c3) instead of Zr^{2+} ions (Figure 5.7c4).

Along with the minor differences in the binding energy positions and in the full-width half maxima, the discernible intensity variations found for the O 1s and Zr 3d states for the ZrO_{x1} and ZrO_{x2} components therefore reflect the difference in the relative composition of these different types of oxygen vacancies in a particular sample. The O 1s and the Zr 3d intensity percentages for the ZrO_{x1} and ZrO_{x2} components of the respective total intensities [i.e., $\text{ZrO}_2 + \text{ZrO}_{x1} + \text{ZrO}_{x2}$] for the nanostructures are summarized in Table 5.1. For ZrO_{x1} [and the total defect intensity, neutral and ($\text{ZrO}_{x1} + \text{ZrO}_{x2}$)], the Zr 3d percentages appear to follow the descending trend: nanowire > nanospike >

nanopopcorn \cong nanobrick. The O 1s percentages for ZrO_{x1} follow the trend: nanowire \cong nanospike $>$ nanopopcorn $>$ nanobrick, while there appear no clear patterns in the Zr 3d and O 1s percentages for ZrO_{x2} .

The existence of trapped electrons also changes the colours of the as-deposited samples. Evidently, the sample colour has changed from light golden (nanobrick) to dark golden (nanopopcorn) to light blue (nanospike), and to deep blue (nanowire), due to the increasing amount of oxygen vacancy concentrations within the nanostructures (Figure 5.7a, insets). The corresponding reflectance spectra follow essentially the same “exponential-like” profile over the 300 – 600 nm range, with the magnitude following the descending trend: nanobricks $>$ nanopopcorns $>$ nanospikes $>$ nanowires, and the absorbance following the opposite trend (Figure 5.8). The reflectance of the Ox-Si template is found to be considerably higher than that of the nanobrick film, which indicates that our ZrO_2 nanostructured films could serve as excellent antireflective coatings. The absorbance of the ZrO_2 nanostructures in the visible region could therefore be attributed to the existence of defect states within the bandgap, the overlapping and hybridization of which lead to impurity bands within the band gap.²⁴¹ The stronger absorbance found for the nanowire sample also indicates that this defect-rich 1D nanomaterial could be an excellent photocatalysts in sunlight-driven reactions and applications. Moreover, these defect-rich ZrO_2 samples retain their individual colour profiles upon storage in ambient atmosphere for over a year, indicating that the defects are located in the bulk and not just at the surface of these nanostructures. Similar colour changes in defect-rich TiO_2 nanostructured films obtained by PLD growth with different growth temperatures and growth environments have also been observed.⁷¹

In Table 5.1, we compare the estimated specific surface areas (i.e. surface area-to-volume ratios) of individual nanostructures (Table 5.2), the relative percentages of ZrO_2 monoclinic and tetragonal phases as obtained from the XRD patterns (Figure 5.3), the relative compositions of oxygen vacancy defects as determined from the Zr 3d and O 1s XPS spectra (Figure 5.7), and the saturation magnetization and coercivity of the ZrO_2 nanostructures (Figure 5.4). The relations among these observed properties reveal several important trends about room-temperature ferromagnetism. First, the saturation magnetization increases with increasing relative amount of the monoclinic phase. However, the magnetization remains non-zero even when there is only tetragonal phase as in the nanobrick film, which shows that the magnetization is not exclusive to the monoclinic or tetragonal phase. Second, the presence of different charge states of oxygen vacancies (i.e., singly-charged,

doubly-charged, and neutral oxygen vacancies)²⁷⁵ enables both M_S and H_C to be tunable by manipulating their relative amounts, indicating that the relative compositions and not just the total amounts of these oxygen vacancy defects are important. Third, the observed ferromagnetism exhibits morphology (i.e. shape) dependency. As the surface usually contains more defects than the bulk, their relative amounts can be modulated by manipulating the specific surface areas, as dictated by the morphology of the nanostructures. Lastly, the different colours and the optical properties of the respective nanostructured films reveal that these nanostructures also have different amounts of bulk defects. The morphology and the electronic structure are therefore very important drivers for room-temperature ferromagnetism in undoped ZrO_2 nanostructured films as induced by defects created not just on the surface but also in the bulk. This insight could also be applied to understanding the manifestation of d^0 ferromagnetism in low-dimensional nanostructures or thin films with high specific surface areas.

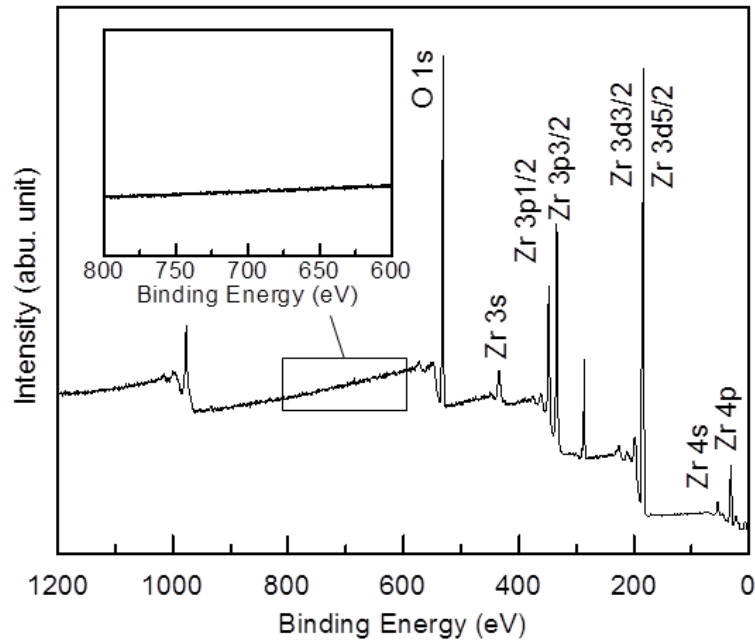


Figure 5.6 XPS survey spectrum for ZrO_2 nanowires. The corresponding inset shows the enlarged range from 600 eV to 800 eV, confirming the absence of any magnetic impurity.

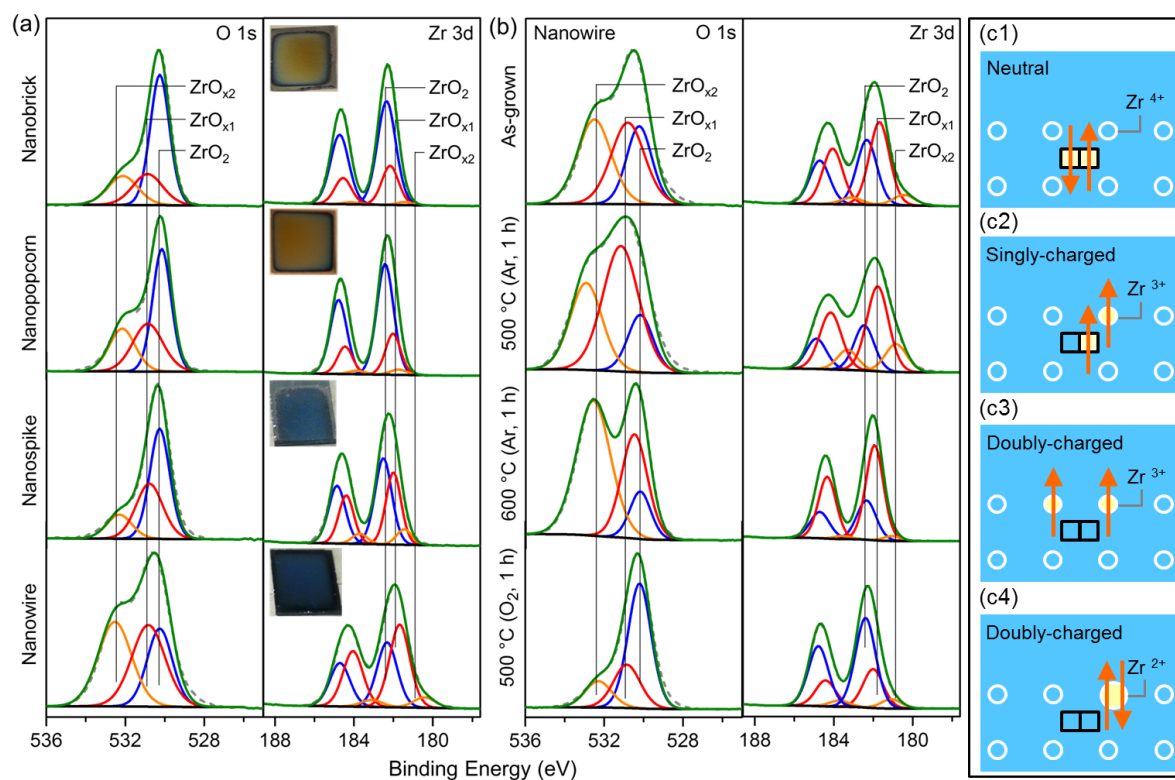


Figure 5.7 (a) XPS spectra of Zr 3d, and O 1s regions of (a) as-deposited ZrO_2 nanostructures, and (b) ZrO_2 nanowires as-deposited and post-annealed under different conditions. In addition to the ZrO_2 features, two sets of defect features corresponding to ZrO_{x_1} ($2 > x_1 > 1.5$) and ZrO_{x_2} ($1.5 \geq x_2 > 1$) are used to fit the residual intensities. The minor changes in the peak positions (and widths) of these defect features from the marked positions correspond to the changes in the defect distributions within the considered x_1 and x_2 ranges. Photographs of the as-grown nanostructured samples are shown as insets in (a). (c1-c4) Schematic representations of three plausible types of oxygen vacancies in ZrO_2 . The Zr^{4+} ions are marked by open white circles, and only the Zr^{3+} and Zr^{2+} ions [i.e. with relocation of electrons (with spin up and spin down as represented by up and down arrows, respectively) from the oxygen-vacancy defect sites] are shown as solid circles. In the interest of clarity, oxygen atoms are not shown, and the oxygen vacancy sites are marked as open squares.

Table 5.1 Comparison of the estimated specific surface area, percentages of the monoclinic and tetragonal phases, percentages of the Zr 3d and O 1s peak intensities for defect-related features (ZrO_{x1} , ZrO_{x2} , and their sums), and the saturated magnetization (M_s), remanence (M_r) and coercivity (H_c) measured at room temperature for the ZrO_2 nanostructured films as-deposited at the specified temperature and for ZrO_2 nanowires upon various post-treatments.

| ZrO ₂ Nano-structured Film | Estimated Specific Surface Area (nm ⁻¹) [#] | XRD* | | XPS ^{&} (%) | | | | | | Magnetic Properties | | |
|---|--|-----------------|-----------------|--------------------------|-------------------|---------------------------------------|-------------------|-------------------|---------------------------------------|---------------------|----------------|------------|
| | | Mono-clinic (%) | Tetra-gonal (%) | Zr 3d | | | O 1s | | | M_s (emu /g) | M_r (emu /g) | H_c (Oe) |
| | | | | ZrO _{x1} | ZrO _{x2} | ZrO _{x1} + ZrO _{x2} | ZrO _{x1} | ZrO _{x2} | ZrO _{x1} + ZrO _{x2} | | | |
| Nanobrick, 550-770 °C | 0.05 | 0 | 100 | 21.9 | 2.1 | 24.0 | 20.9 | 17.6 | 37.5 | 0.6 | 0.1 | 50 |
| Nano-popcorn, 550 °C | 0.08 | 32 | 68 | 22.9 | 2.8 | 25.7 | 28.7 | 22.9 | 51.6 | 1.2 | 0.3 | 73 |
| Nanospike, 650 °C | 0.11 | 57 | 43 | 32.2 | 8.3 | 40.5 | 31.6 | 15.5 | 47.1 | 2.9 | 0.5 | 77 |
| Nanowire, 770 °C (As-grown) | 0.13 | 75 | 25 | 49.3 | 7.4 | 56.7 | 36.5 | 37.1 | 73.6 | 5.9 | 1.5 | 99 |
| Nanowire (500 °C, Ar, 1 h) | | | | 55.5 | 16.2 | 71.7 | 54.1 | 32.4 | 86.5 | 7.3 | 2.3 | 113 |
| Nanowire (600 °C, Ar, 1 h) | | | | 69.4 | 2.7 | 72.1 | 31.9 | 55.9 | 87.8 | 3.2 | 0.6 | 71 |
| Nanowire (500 °C, O ₂ , 1 h) | | | | 24.3 | 7.7 | 32.0 | 26.6 | 14.7 | 41.3 | 1.6 | 0.2 | 54 |

[#] Only the exposed surface area of an “ideal” nanostructure of the specific shape and size is considered in the calculation, with details given in the Table 5.2.

* The relative phase percentages are obtained from the peak intensities of monoclinic (-111) and tetragonal (101) features using the X-pert HighScore software assuming random orientations.

[&] The percentages of individual components are calculated by dividing the peak area of that component with the total contribution of $ZrO_2 + ZrO_{x1} + ZrO_{x2}$.

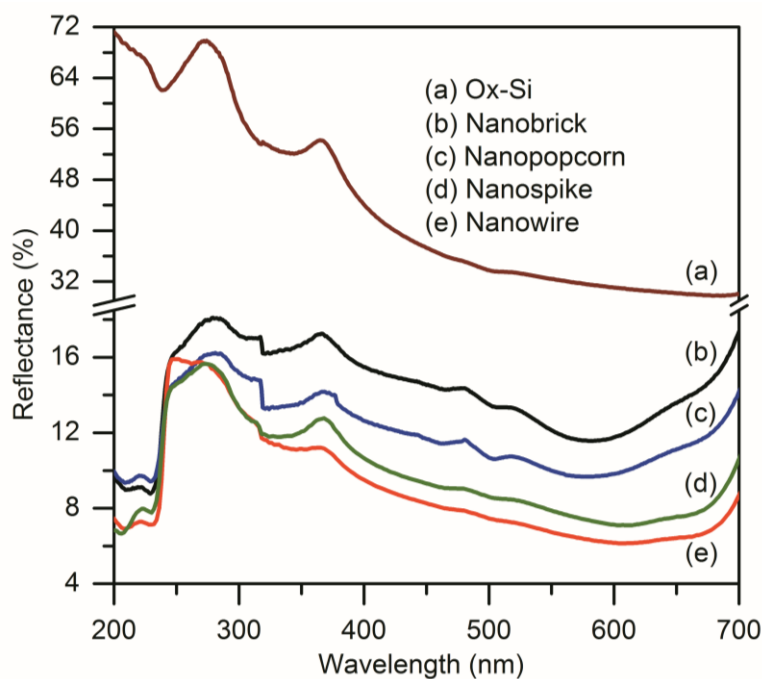
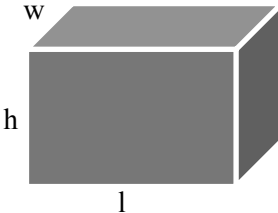

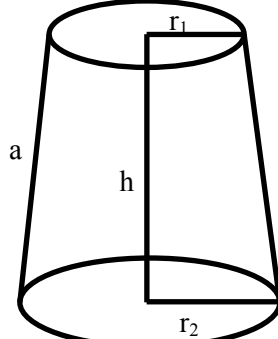
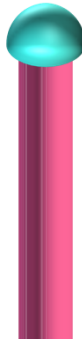
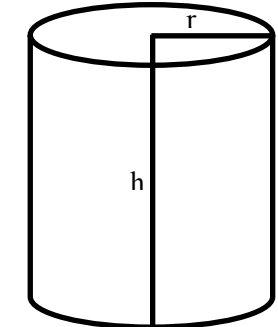


Figure 5.8 Comparison of UV-Vis-NIR reflectance spectra of as-deposited ZrO₂ nanostructured films, along with that of the pristine Ox-Si template.

Table 5.2 Calculations for specific surface areas of ZrO₂ nanostructures.

| Nano-structure | Comment and Procedure | Model |
|----------------|--|-------|
| Nanobrick | <p>In order to calculate the exposed surface area for cubic ZrO₂ nanobrick, we consider only one surface of the cube (the top surface) as the exposed face, because the nanobricks in the film are mostly attached to one another and are tightly packed.</p> <p>$a = 15 \text{ nm}$ exposed surface area = a^2 (top surface) volume = a^3 exposed surface area / volume = $225 \text{ nm}^2 / 3375 \text{ nm}^3 = 0.06 \text{ nm}^{-1}$</p> | |

| | | |
|---|---|---|
| <p>Nanopopcorn</p> | <p>A nanopopcorn is modelled as a cuboid (or a rectangular box) and the nanopopcorn structures are separated from one another. To calculate the exposed surface area, we ignore the bottom surface of the rectangle that is attached to the substrate.</p> <p>length (l) = 86 nm width (w) = 83 nm height (h) = 35 nm exposed surface area = $2(hw + lw + hl) - lw$ volume = lwh exposed surface area / volume = $18968 \text{ nm}^2 / 249830 \text{ nm}^3 = 0.08 \text{ nm}^{-1}$</p> |  |
| <p>Nanospike</p>  | <p>As a nanospike is tapered in shape, we consider its exposed area as the frustum of a cone truncated at both ends because the top end is terminated by a gold nanoparticle while the bottom end is in contact with the substrate. (http://www.mathinary.com/cone_frustum_volume_of_a_frustum_of_a_cone.jsp?calc_id=24&h=733&r1=7.5&r2=24&a=741&pi=Pi#calculator24)</p> <p>r_1 (radius of the smaller circular end plane) = 8 nm r_2 (radius of the larger circular end plane) = 26 nm h (height of the frustum) = 720 nm a (length of the lateral surface) = 733 nm area of the lateral surface = $\pi \times (r_1 + r_2) \times \sqrt{h^2 + (r_1 - r_2)^2}$ volume = $\frac{1}{3} \times \pi \times h \times (r_1^2 + r_2^2 + r_1 + r_2)$ surface area/volume = 0.12 nm^{-1}</p> |  |
| <p>Nanowire</p>  | <p>As the nanowire has a uniform cross section along the length, it can be considered as a straight cylinder with the two ends terminated by a gold nanoparticle and the substrate.</p> <p>$r = 16 \text{ nm}$ $h = 2000 \text{ nm}$ exposed surface area = $2\pi rh$ volume = $\pi r^2 h$ surface area/volume = 0.13 nm^{-1}</p> |  |

To further clarify the role of oxygen vacancy defects in determining the magnetic property, we carry out annealing experiments in an oxygen or Ar atmosphere at different temperatures for the as-deposited ZrO₂ nanowires. Initially, we anneal the as-deposited sample in an Ar atmosphere at 500 °C and 600 °C, each for 1 h, in order to introduce more oxygen vacancies into the nanowires. We also reduce the number of oxygen vacancy defects by annealing the as-deposited nanowire sample in O₂ at 500 °C for 1 h. X-ray diffraction analysis shows that there is no discernible change in the relative composition of the crystalline phases in the nanowires caused by these post-annealing treatments, regardless of the annealing temperature and environment (Table 5.1). The lower temperature (500 °C or 600 °C) employed in the post-annealing treatments than the growth temperature of the nanowires (770 °C) is not expected to improve crystallinity. On the other hand, the Zr 3d and O 1s XPS spectra show considerable differences in their relative intensity percentages related to ZrO_{x1} and ZrO_{x2} in the post-annealed samples (Figure 5.7b). Post-annealing the as-grown ZrO₂ nanowires in Ar at 500 °C increases the amount of oxygen vacancy defects (Figure 5.7b). As expected, the proportions of the types (i.e., the relative compositions) of oxygen vacancies corresponding to the ZrO_{x1} and ZrO_{x2} features have discernibly increased. However, further post-annealing the sample at 600 °C in Ar has increased the total oxygen vacancies (related to ZrO_{x1} + ZrO_{x2}), but the overall full-width half maximum of the Zr 3d peak has decreased significantly, and the O 1s and Zr 3d peaks corresponding to ZrO_{x1} is slightly shifted to lower and higher binding energy, respectively, all with respect to the as-grown features (Table 5.1). These results therefore suggest that post-annealing at 600 °C produces highly reduced ZrO₂ and favours the formation of more neutral oxygen vacancies than the as-grown and 500 °C Ar-annealed sample. For the ZrO₂ nanowires post-annealed in O₂, we should expect a significant decrease in the amount of oxygen vacancy defects, and this is indeed supported by the large reduction in the composition for the ZrO_{x1} and ZrO_{x2} XPS features (Figure 5.7b, Table 5.1). The changes in the defect type and its proportions caused by the post-treatments are found to greatly affect the magnetic properties. Indeed, Figure 5.4e shows that the reduction in the amounts of oxygen vacancies significantly decreases the saturation magnetization of the nanowires O₂-annealed at 500 °C. Furthermore, the saturation magnetization for the 500 °C Ar-annealed nanowires has increased but that for the 600 °C Ar-annealed sample has decreased significantly, due to the increase in neutral oxygen vacancies in the 600 °C Ar-annealed sample. These results therefore suggest that both the types (singly-charged, and doubly-charged, and neutral oxygen vacancy) and relative amounts of these oxygen vacancy defects play a crucial role for the observed room-temperature ferromagnetic behaviour in undoped ZrO₂ nanowire.

Figure 5.9a shows the magnetization vs magnetic field hysteresis loops for the as-grown ZrO_2 nanowires measured at different temperatures, $T = 5, 77, 200, 300,$ and 400 K. The presence of well-defined hysteresis loops supports strong ferromagnetic behavior over the entire temperature range, from 5 K to as high as 400 K (the maximum sampling temperature supported by our SQUID magnetometer). The characteristic features of ferromagnetism, such as remanence, coercivity, and saturation magnetization, have become much more prominent at the lower temperature (Figure 5.9a, insets). The coercivity (68 Oe), remanence (0.8 emu/g), and saturation magnetization (5.1 emu/g) observed at 400 K have nearly doubled, respectively, to 115 Oe, 1.7 emu/g, and 9.1 emu/g at 5 K. The small change in the coercivity (47 Oe) over the entire temperature range (395 K) is characteristic of dilute ferromagnetism (Figure 5.9a, insets), which affirms that PLD-grown defect-rich ZrO_2 nanowires exhibit the distinctive ferromagnetic order of TDFSOs.^{276,277} In addition, we have used Arrott plot (Figure 5.10a) and the power law (Figure 5.10b) to estimate the Curie temperature (T_c). As shown in Figure 5.10b, the model provides an excellent fit (solid line) to the experimental results (open circles), and the T_c for the as-grown ZrO_2 nanowires is determined to be 700 K. Similarly, T_c for ZrO_2 nanospikes, nanopopcorns, and nanobricks are found to be 650 K, 550 K, and 400 K, respectively (Figure 5.11). We also perform zero-field-cooled and field-cooled magnetization measurements for the ZrO_2 nanowires at an applied field of 100 Oe between 1.8 K and 400 K (Figure 5.9b). The wide separation of the zero-field-cooled and field-cooled magnetization curves over the entire temperature range suggests irreversibility of susceptibilities. The magnetic moments also do not drop to zero, indicating a high T_c above 400 K, in good agreement with the Arrott plot shown in Figure 5.10a. Since the zero-field-cooled magnetization appears to increase linearly with increasing temperature without any obvious peak, these ZrO_2 nanowires exhibit typical ferromagnetic behavior without any blocking temperature below 400 K. The absence of blocking temperature within this temperature range therefore confirms that ferromagnetism of the nanowires is of intrinsic origin and is not caused by extrinsic effects such as those arising from the presence of ferromagnetic impurities or dopants.²⁷⁷

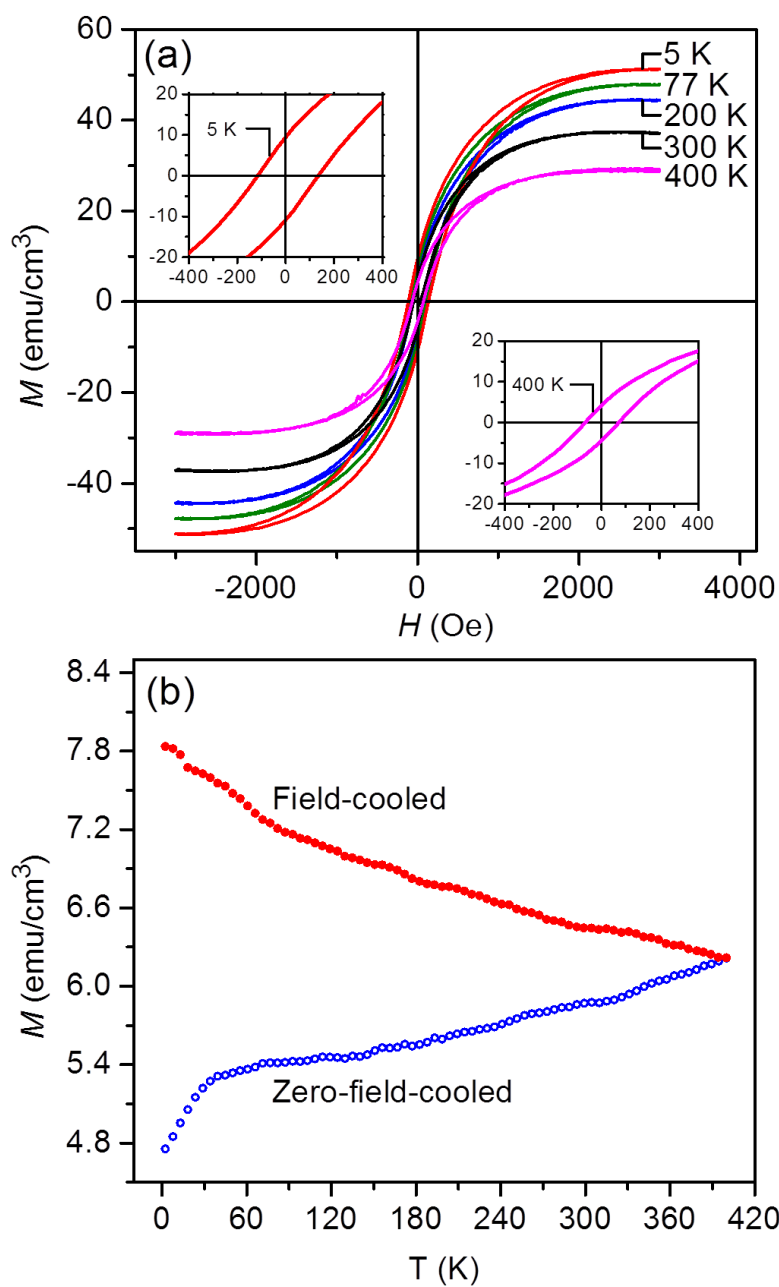


Figure 5.9 (a) M - H curves for ZrO₂ nanowires measured at 3000 Oe for temperature (T) = 5, 77, 200, 300, and 400 K. The insets show the magnified hysteresis loops near the origin at 5 K and 400 K. (b) Magnetization as a function of temperature following field-cooled and zero-field-cooled measurements at $H = 100$ Oe.

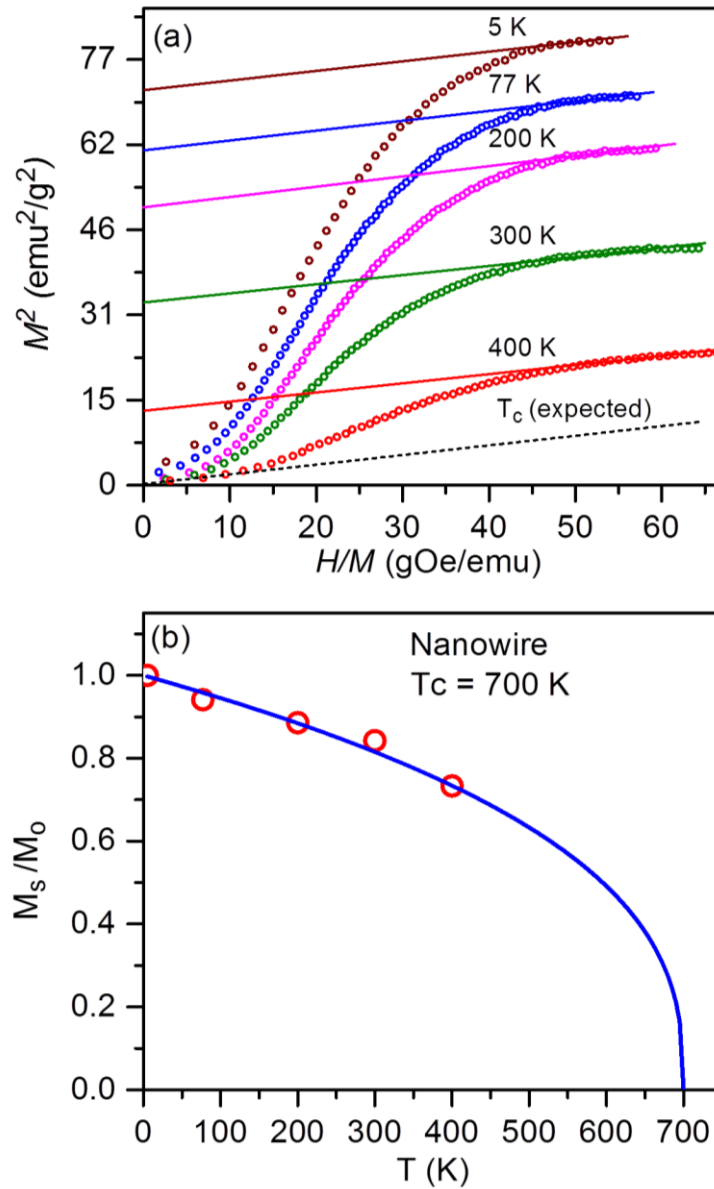


Figure 5.10 (a) Arrott plot for ZrO_2 nanowires measured at 3000 Oe for temperature (T) = 5, 77, 200, 300, and 400 K. (b) Normalized saturation magnetization (M_s/M_0) as a function of temperature, where M_0 is the saturation magnetization at 0 K. According to the Ginzburg-Landau mean field theory for ferromagnetism, the free energy of a ferromagnetic material close to the phase transition gives a relation for the magnetization order parameter: $M^2 = (1/b)(H/M) - (a/b)\epsilon$, where the magnetization M is the order parameter, H is the applied magnetic field, a and b are arbitrary constants, $\epsilon = (T-T_c)/T_c$, and T_c is the Curie temperature. In a plot of M^2 vs H/M (the Arrott plot) for various temperatures, the line without an intercept corresponds to the dependence at the Curie temperature. As shown in Figure 5.10a, the intercept is not zero even at 400 K, which means that T_c has yet to be reached. By using the instantaneous slope obtained at 400 K, a parallel dash line could be used to extrapolate to the origin, which indicates that T_c is above 400 K. Moreover, the

temperature dependence of the saturation magnetization (Figure 5.10b) enables estimation of T_c using a power-law equation from the critical behavior model:

$$\frac{M_s(T)}{M_0} = \left(1 - \frac{T}{T_c}\right)^\beta$$

where $M_0 \equiv M_s(T = 0) \sim M_s(T = 5 \text{ K})$, and $\beta = 0.365$ is the critical component in the 3D Heisenberg model.²⁷⁶ The model provides an excellent fit (solid line) to the experimental results (open circles), and the x-intercept gives $T_c = 700 \text{ K}$ for nanowires in Figure 5.10b and similarly $T_c = 650 \text{ K}$ for nanospikes, 550 K for nanopopcorns, 550 K for nanospikes, 550 K for nanopopcorns, and 400 K for nanobricks in Figure 5.11.

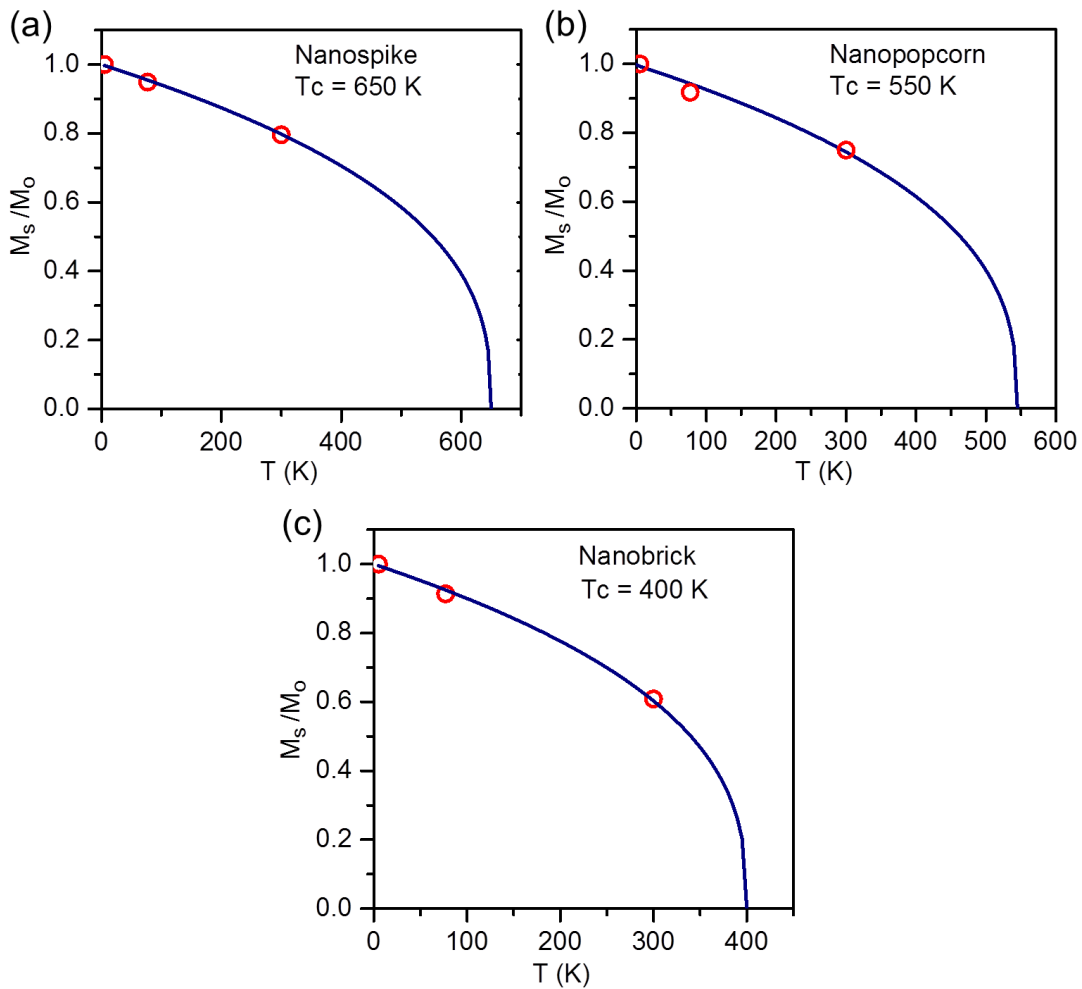


Figure 5.11 Normalized saturation magnetization (M_s/M_0) for ZrO_2 (a) nanospike, (b) nanopopcorn, and (c) nanobrick films as functions of temperature.

An original finding of this work is our observation of room-temperature ferromagnetism in both oxygen-deficient monoclinic ZrO₂ nanostructures (nanopopcorns, nanospikes, and nanowires) and oxygen-deficient tetragonal ZrO₂ nanobrick film, in marked contrast to earlier reports that room-temperature ferromagnetism can only be found for oxygen-deficient tetragonal ZrO₂ and not for oxygen-deficient monoclinic ZrO₂.^{5,271} Furthermore, we observe that the saturation magnetization and coercivity of monoclinic ZrO₂ nanowires are related to the total amounts and compositions of oxygen vacancy defects both on the surface and in the bulk of the nanostructures (Table 5.3). As the total amount of defects is related to the specific surface area (surface defects) and growth temperature (bulk defects) of the nanostructure, the larger saturation magnetization and coercivity are found for the nanowires with higher estimated specific surface area and higher growth temperature (0.13 nm⁻¹, 770 °C) than nanospikes (0.11 nm⁻¹, 650 °C), nanopopcorns (0.08 nm⁻¹, 550 °C), and nanobricks (0.05 nm⁻¹, 770 °C) (Table 5.4). These observations indicate that regardless of the phase of ZrO₂, it is the amount of defects in a particular ZrO₂ nanostructure that controls the room-temperature ferromagnetic behavior. This is consistent with recent report that no ferromagnetism was found for the pure monoclinic ZrO₂ thin film,²⁷¹ because the planar film inherently possesses a smaller amount of defects due to their lower specific surface area (and therefore with potentially less surface defects) when compared to nanostructured films. More importantly, our defect-rich ZrO₂ nanostructured films are novel, because our nanostructured samples require only 2000 Oe external field to reach saturation, making them the most responsive materials with the highest sensitivity to the external field reported to date. The observed saturation magnetization of our nanowire sample (5.9 emu/g) is significantly higher than those reported for undoped ZrO₂ (0.18 emu/g)⁵ and Mn-doped ZrO₂ (0.02 emu/g)²⁷⁸ thin films, undoped ZnO (0.4 emu/g)¹⁴⁰ and Mn-doped ZnO (0.05 emu/g)²⁷⁹ thin films, and undoped ZnO nanoparticulate film (0.003 emu/g),¹³⁴ all of the which were obtained with considerably higher applied magnetic field. Indeed, the saturation magnetization of our ZrO₂ nanowire film is also significantly higher than other nanostructured films, including ~26 times higher than the nanoporous pure TiO₂ nanoribbon film¹³⁵ and Cu-doped ZnO nanowire film (both 0.2 emu/g);²⁸⁰ and over 80 times higher than Fe and N co-doped TiO₂ nanorods (0.06 emu/g),¹⁰⁶ Cr-doped TiO₂ nanorods (0.07 emu/g),²⁸¹ and V-doped TiO₂ nanotubes (0.008 emu/g).²⁸² These results therefore demonstrate that our as-grown ZrO₂ nanowire sample has the best magnetization reported to date, and this remarkably high magnetic moment can be achieved by intentionally creating defects in undoped ZrO₂.

Defect-induced Bound Polaron Model

There have been a few theoretical studies^{6,126,133,263} on the origin of ferromagnetism in TDFSOs. In the very first model of TDFSOs, the Heisenberg model, the d electrons of the dopant (transition metal cations) are well localized, and they couple with one another ferromagnetically via long-range-ordered interactions among the free carriers (2p holes or 4s electrons).¹¹⁷ Given a small amount of dopants (a few percent), however, it is difficult to conceive how the exchange interaction could occur over a large separation between localized moments. Contrary to the Heisenberg model, the observed magnetization has already been reported to be independent of the dopant concentration,^{129,130} which suggests that the Ruderman-Kittel-Kasuya-Yosida interaction may not be the main cause of ferromagnetism in TDFSOs. In the so-called bound magnetic polaron model, the defects in doped-TDFSOs are taken into account. The ferromagnetic coupling is mediated by shallow donor electrons associated with defects via exchange interactions with the localized d electrons of the dopants.²⁵⁸ However, this model still cannot explain how T_C in dilute ferromagnetic semiconductor oxides can be so high (i.e. well above room temperature) or how semiconducting oxides without any transition metal dopants (i.e., without any unpaired d electrons) can be ferromagnetic. Very recently, a charge-transfer ferromagnetism model has been proposed as an extension to the bound magnetic polaron model.¹⁴⁶ This model assumes that the presence of defects introduces an impurity band, and the presence of dopants provides a charge reservoir in the system to facilitate hopping of electrons to or from the impurity band, which leads to splitting of spin states.¹⁴⁶ This model, however, cannot explain how ferromagnetism could occur in undoped TDFSOs because there is no charge reservoir due to the absence of dopants. Meanwhile, experiments using X-ray magnetic circular dichroism have revealed that the dopant (Co 3d, Mn 3d, and Cr 3d) sublattice is paramagnetic at all temperature down to 2 K, both at the surface and in the bulk of the films.^{129,130} As the dopants are evidently not the origin of ferromagnetism, ferromagnetism in doped semiconducting oxide thin films must therefore be related to defects.

Our experimental observations support the idea that both the total amount and the composition of oxygen vacancy defects (neutral, singly-charged, and doubly-charged oxygen vacancies) are responsible for the observed ferromagnetism in dopant-free ZrO_2 nanostructures. If only the total amount of oxygen vacancy defect is responsible, then ferromagnetic ordering is expected to remain unchanged after annealing the nanowire sample in Ar at 500 °C and 600 °C (Figure 5.4e). Instead, the corresponding XPS spectra (Figure 5.7) and magnetization data (Table 5.1)

suggest that the amounts of singly-charged and doubly-charged oxygen vacancies mainly control the ferromagnetism in the nanowire sample, because the saturation magnetization in the 500 °C Ar-annealed nanowire sample is increased with the increase of singly-charged and doubly-charged oxygen vacancies, compared to the as-grown nanowire sample. On the other hand, for the 600 °C Ar-annealed nanowire sample, the presence of more neutral oxygen vacancies reduces the saturation magnetization relative to that of the as-grown and 500 °C Ar annealed samples. The observed magnetization is therefore consistent with that among the different charge states of oxygen vacancies (neutral, singly-charged, and doubly-charged vacancies),^{283–285} the singly-charged and doubly-charged oxygen vacancies contribute more to magnetization, in contrast to the cancellation of paired electron spins in the neutral oxygen vacancies.^{283,286}

We hypothesize that narrow impurity bands could form below the conduction band minimum as a result of the overlap and hybridization of the defect states associated with these oxygen vacancies.²⁷⁵ In ZrO_2 , formation of a singly-charged oxygen vacancy would therefore result in one electron in the singly-charged oxygen vacancy site, with the other electron in the corresponding Zr atom leading to a Zr^{3+} ($4d^1$) ion. In such a system, either the singly-charged oxygen vacancy or the Zr^{3+} ($4d^1$) ion with one unpaired electron can effectively behave as a localized electron, similar to the unpaired d electrons of a dopant in doped-TDFSOs as proposed in earlier models. When these localized electrons are coupled with the conduction band electrons, the conduction band electrons became spin-polarized around the localized spins. Given that the stronger form of ferromagnetism usually requires localized rather than itinerant electrons, we expect ferromagnetic exchange interactions between the singly-charged oxygen vacancy electron and the $4d^1$ electron because the spins of all the carriers could assume the same direction. The parallel orientation of both localized spins therefore leads to the formation of a bound magnetic polaron at or near the defect site (Figure 5.12a), which causes both the conduction band and impurity band to split apart into a spin-up and a spin-down bands due to the difference in potential energies for the spin-up and spin-down electrons. Since the Fermi level is identical to both spin-up and spin-down bands, there is a small surplus of the type of spin in the resulting lower band (Figure 5.12b). This is in contrast to defect-free TDFSOs, in which an equal amount of spin-up and spin-down electrons would give rise to paramagnetic response (Figure 5.12b).¹³² Likewise, a doubly-charged oxygen vacancy would result in the relocation of these electrons to two nearest neighbouring Zr atoms, leading to formation of two Zr^{3+} (d^1) ions. The exchange interactions of these two d-electrons with each other and with the free carriers (electrons) could also lead to bound magnetron polaron formation and splitting of energy levels of the impurity

band around the vacancy defect. On the other hand, the anti-parallel electron spins of the neutral oxygen vacancies could only mediate weak antiferromagnetic exchange interactions due to cancellation of the paired electron spins. However, due to the quantum confinement effect in low-dimensional nanostructures, the neutral oxygen vacancies that have a triplet ground state or a low-lying triplet excited state could overlap to form a narrow impurity band and can be polarized by exchange with empty Zr 4d states.²⁸⁷ This is not supported by our XPS and magnetization data of the 600 °C Ar-annealed nanowire sample, which show that contribution from the neutral oxygen vacancies to the total ferromagnetism is negligibly small.

The mixing of the impurity band with the empty Zr 4d states therefore allows transfer of a fraction of electron density for each vacancy to the empty Zr 4d states. The localized electrons of Zr 4d¹ and oxygen vacancies would in turn polarize the conduction band electrons and provide the necessary ferromagnetic coupling.²⁵⁸ Moreover, the Curie temperature depends on the degree of hybridization, which corresponds to charge transfer from a donor-derived impurity band (oxygen vacancy) to the unoccupied *d* states at the Fermi level.²⁵⁸ The variation of the donor concentrations, i.e., compositions of the oxygen vacancy defects in the present case, could therefore change the T_c of the nanostructures. The higher T_c observed for the ZrO₂ nanowires, relative to those of nanobricks, nanopopcorns, and nanospikes, could therefore be attributed to the higher concentrations of singly-charged and doubly-charged oxygen vacancies in the nanowires.

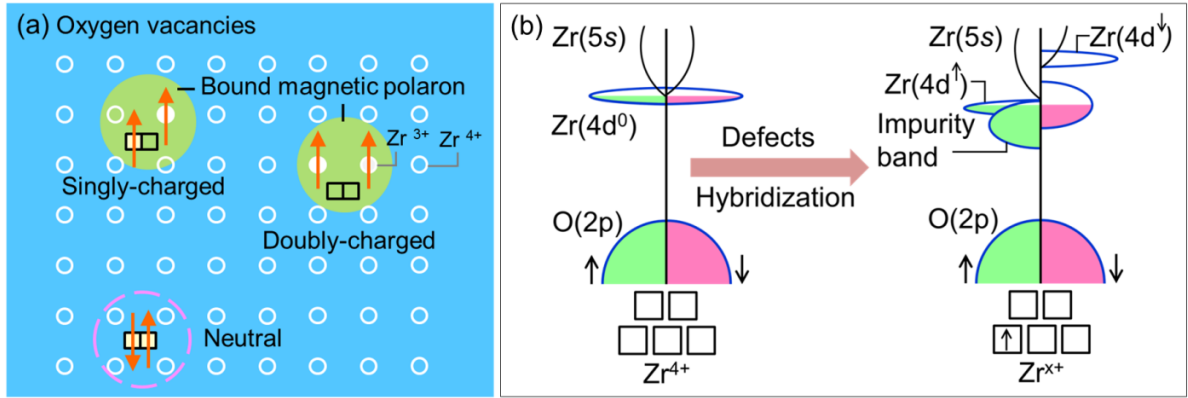


Figure 5.12 (a) Formation of bound magnetic polarons (marked by light green circles) by singly-charged and doubly-charged oxygen vacancies. The Zr^{4+} ions are marked by open white circles, while the Zr^{3+} ions are shown as solid white circles. In the interest of clarity, oxygen atoms are not shown, and the oxygen vacancy sites are marked by open white squares. The neutral oxygen vacancy site is highlighted by open dashed circle. The arrows indicate the direction of the spins. (b) Schematic representations of the proposed defect-induced bound polaron model for ferromagnetism in undoped ZrO_2 nanostructures containing oxygen vacancies and mixed-valence of Zr ions. This mechanism involves formation of an impurity band and its overlapping with Zr 4d states leading to ferromagnetic exchange coupling.

Our proposed model, as depicted in Figure 5.12, can be generally applicable to a wide range of undoped TDFSOs. The concept of impurity band formation and its hybridization with empty d states in undoped oxides suggests that magnetic ordering in semiconductor oxides could in principle be achieved by using different types of anion vacancy defects in the host lattice. In a separate study, we have indeed observed similar morphology and defect-dependent ferromagnetism in defect-rich, dopant-free TiO_2 nanostructures. For example, the magnetization in TiO_2 nanostructures is found to increase with increasing amounts and relevant types of oxygen vacancy defects within the nanostructures: nanobricks < nanobelts < corrugated nanowires < straight nanowires < decorated nanowires (not shown). These results therefore provide new insight to better mechanistic understanding of ferromagnetism in undoped TDFSOs and they also present viable opportunities for future applications of this new class of defect-rich nanomaterials in spin-based technologies. For examples, the present dopant-free, defect-rich ZrO_2 nanostructured films could be used to build more efficient spin transistors²⁸⁸ and spin-based logic circuits²⁸⁹ that could operate well above room temperature by taking advantage of their high saturated magnetization and high T_c capabilities. The high optical absorption property of these defect-rich nanomaterials also promises more efficient solar-

driven spin devices,²⁹⁰ in which the generation of spin currents by visible sunlight opens new door to solar-driven magneto-electronics.

5.4 Conclusion

In summary, we have synthesized a variety of undoped ZrO₂ nanostructures, including nanobricks, nanopopcorns, nanospikes, and nanowires, by catalyst-assisted PLD method. The use of a high vacuum system and precise control of the growth temperature and environment have enabled us to produce, for the first time, defect-rich, dopant-free nanostructured films with different compositions of oxygen vacancy defects. We further demonstrate that the growth mode (vapour-solid vs VLS) and the amounts and types of defects in these nanostructures critically depend on the growth temperature. Independent of the phase of ZrO₂ (tetragonal or monoclinic), these defect-rich nanostructured films are found to exhibit ferromagnetism with T_c considerably above room temperature. This is in marked contrast to previous report⁵ that only oxygen-deficient tetragonal ZrO₂ thin films could exhibit ferromagnetism. It is therefore the amounts and types of oxygen vacancy defects of the nanostructure that control the ferromagnetic property of ZrO₂. We hypothesize a new defect-induced bound polaron model for the observed high T_c ferromagnetism, in which the exchange interactions of singly and doubly-charged oxygen vacancy defects and reduced Zr 4d¹ ions lead to the formation of bound magnetic polarons nearby the vacancy sites. The essential feature of this mechanism is that regardless of the phase of ZrO₂, it is the specific surface area, the amounts and types of oxygen vacancy defects within the particular nanostructure that control the ferromagnetic ordering in undoped ZrO₂. The proposed model is generally applicable to other undoped TDFSO systems, including, e.g., undoped TiO₂ nanostructures, of which we have also observed similar morphology and defect-dependent ferromagnetism.

A large saturation magnetization (5.9 emu/g) has been observed for the as-grown ZrO₂ nanowires even with a very small external magnetic field (2000 Oe), consistent with their high specific surface area and higher concentration of defects. This is especially remarkable because not only is the magnetization significantly greater than other ZrO₂ nanomaterials reported to date, it is also at least an order of magnitude higher than the magnetization reported for other TDFSOs, including undoped TiO₂ nanoporous nanoribbons (0.2 emu/g),¹³⁵ α-MoO₃ nanofibers (0.015 emu/g),²⁹¹ CuO-ZnO heterostructures (0.002 emu/g),²⁹² 2H-SiC-α-Al₂O₃ nanowires (0.3 emu/g), hexagonal CeO₂ nanosheets (0.03 emu/g).¹³⁶ Even more extraordinary is that the observed magnetization is considerably higher than doped TDFSOs such as Ni-doped ZnO nanorods (1.0

emu/g).²⁹³ Furthermore, our magnetization values (Table 5.5) are estimated based on the sample volume, with the assumption that the nanostructures are tightly packed and densely distributed over the entire sampling area. If we consider that the nanowires only occupy ~20% of the presumed sample volume (Figure 5.1e2), the saturation magnetization should be ~5 times greater, making the magnetization reported here (29.5 emu/g for as-grown ZrO₂ nanowires and 36.5 em/g for Ar-annealed ZrO₂ nanowires) even greater. Indeed, the packing density and the overall amount of the nanowires could be greatly enhanced physically by increasing the areal density of the nanowires (e.g., by increasing the GNI density) and/or the length of the nanowires (e.g., by increasing the deposition time). In marked contrast to most of the aforementioned nanowire samples reported in the literature, all of which required post-treatment (such as annealing in a reductive environment) or doping with secondary materials, the present nanowires are prepared with one distinct advantage, i.e. without the need for any post-synthesis modification or treatment. The present facile synthesis process makes the fabrication of these defect-rich, dopant-free ZrO₂ nanostructured films easily scalable.

More importantly, as T_C found for the as-grown ZrO₂ nanowires (700 K) is significantly higher than room temperature, the nanostructured film can be readily incorporated into the fabrication protocol of room-temperature spin-based electronic devices that employ spins as the information carriers. For example, a spin transistor consisting of a conductor sandwiched between two TDFS contacts is expected to be faster and more efficient than a standard field effect transistor.²⁹⁴ Similarly, the semiconductor lasers fed by spin-polarized currents are expected to have better mode stability and lower carrier currents. As ZrO₂ is also chemical inert and highly biocompatible, the ferromagnetic ZrO₂ nanostructures could potentially be used in magnetically guided anti-cancer drug delivery system.²⁹⁵ Furthermore, fabricating hybrid and/or core-shell nanowires with a ferroelectric material would enable multiferroic (simultaneous ferroelectric and magnetic ordering) tunnel junction in a single nanowire, which could be used as a spin filter device with potential to be controlled both electrically and magnetically.²⁹⁶ This can be easily accomplished by switching the targets (using a multi-target holder) during the growth of ZrO₂ nanowires. The present approach of intentionally growing defect-rich, dopant-free ZrO₂ nanostructures by catalyst-assisted PLD method could be extended to build other novel dilute ferromagnetic semiconductors that promise new spin-based applications.

Chapter 6

Concluding Remarks and Future Work

6.1 Summary of Contributions

The objective of the present work is to design-and-build new materials with novel properties by engineering the surface morphology and the amount and composition of oxygen vacancy defects of the TiO_2 and ZrO_2 nanostructures for visible-light driven photoelectrochemical water splitting reaction and spin-electronic applications. The creation of unstable surface oxygen vacancies by post-treatment techniques, including hydrogen thermal treatment, high-energy particle bombardment and thermal annealing in oxygen depletion conditions, has motivated us to search for a reliable, one-step method that can be used to create stable oxygen vacancies not just at the surface but also in the bulk of TiO_2 and ZrO_2 nanostructures. In the present work, we have shown that the one-step catalyst-assisted pulsed laser deposition method can create highly oxygen-deficient TiO_2 and ZrO_2 nanostructures that are single crystalline, and exhibit a variety of surface morphologies and oxygen vacancy defect compositions. The use of a high vacuum system and Ar flow, and precise control of the gold nanoisland size, interfacial SiO_2 layer thickness and growth temperature has enabled us to produce nanosheets, nanobelts, nanopopcorns, nanospikes, and nanowires (corrugated, straight, TiO_2 nanocrystal-decorated, and hierarchical nanowires) of TiO_2 and similar ZrO_2 nanostructures with different oxygen vacancy defect compositions. The oxygen vacancy defects enhance the optical absorption and charge-transport properties by introducing additional defect states in the band structure, while the variation in neutral, singly charged, and doubly charged oxygen vacancies (due to the Madelung potential of the ionic crystal) leads to interesting magnetic properties found for these nanostructures. Meanwhile, the variations in the morphology of the as-grown single-crystalline nanostructures, together with the different oxygen vacancy defect compositions, also greatly influence the photoelectrochemical water splitting properties of these nanostructures.

Briefly, laser ablation of the rutile TiO_2 target at 700 °C on a pristine H-Si, RCA-Si, and Ox-Si substrates, with the respective thicknesses of the SiO_2 layers of 1, 3 and 30 nm, produces nanobricks, irrespective of the SiO_2 layer thickness. While under the same deposition conditions, PLD growth on GNI/H-Si, GNI/RCA-Si, and GNI/Ox-Si templates produces nanoflakes, nanowires and nanobelts, respectively. In contrast to nanobricks, the growth of nanoflakes and nanowires on substrates with GNIs suggests that GNIs act as the nucleation sites and lower the surface energies of

crystal growth planes, which consequently enhance the adsorption rate of gaseous species and promote the growth of nanostructures different than the nanobricks. The absence of Au on top of the nanoflake suggests that, Au remains mostly at the interface due to the thinner SiO₂ layer of the H-Si template and to the formation of Au-silicide, which leads to a vapour-solid growth process for these nanoflakes. The presence of gold at the tip of nanowires and nanobelts suggests that the GNIs are detached from the thicker SiO₂ layers on the substrate, indicating a VLS growth mechanism for nanowires and nanobelts. The growth of nanobelt structures on the GNI/Ox-Si template, nanoflake on GNI/H-Si, and nanowires on GNI/RCA-Si has therefore been attributed to the different SiO₂ layer thickness, surface roughness, and different heat-transfer efficiency that, ultimately affects the surface mobility, nucleation sites, and supersaturation rate of TiO₂.

We further demonstrate the effect of deposition temperature on the TiO₂ nanostructure growth. For all three templates, deposition at 675 °C produces tapered corrugated nanowires with stacking faults distributed along the growth direction. On the other hand, deposition at 720°C on GNI/H-Si produces pebble-like particles, due to the complete consumption of the thin SiO₂ layer (~1 nm) via silicide formation,¹⁹⁰ while the deposition at the same temperature on GNI/RCA-Si and GNI/Ox-Si templates leads to tapered nanowires also decorated with TiO₂ nanocrystallites on the surface, in marked contrast to the straight nanowires with smooth surfaces found on GNI/RCA-Si at 700°C. Similar to GNI/H-Si at 700 °C and 720 °C, deposition at a higher temperature on GNI/RCA-Si produces nanoflakes and pebble-like particles at 750°C and 770°C, respectively, likely due to the gradual consumption of thin SiO₂ layer (3 nm) via the interfacial reaction. For GNI/Ox-Si template, nanowires decorated with larger nanocrystallites are observed at 750°C or higher temperature, in contrast to the GNI/RCA-Si templates. These results suggest that a minimum SiO₂ layer thickness of 3 nm (as formed on the RCA-Si substrate) is necessary for enabling VLS nanostructure growth in the PLD method. The growth of these nanowires therefore occurs by both vapour-solid and VLS mechanisms as the catalyst state changes from a solid state to a liquid state through the temperature range. While both vapour-solid and VLS growth could occur concurrently, VLS growth predominates at the higher growth temperature and the slower vapour-solid growth at a particular growth temperature could perturb and thus introduce variations into the general morphology of the nanowires.

The fitted O 1s intensity ratios for TiO_x/TiO₂ and SiO_x/SiO₂ of the nanowires prepared on the GNI/RCA-Si template follow the ordering: decorated nanowires (720°C) > straight nanowires

(700°C) > corrugated nanowires (675°C), in close correlation with the growth temperature. The different amounts of oxygen vacancies of the as-grown nanostructured films also cause their colours to change from lighter blue for nanobelts to deep blue for straight nanowires and then greyish black for decorated nanowires. The slight deviation from perfect stoichiometry could result in a significant change in the electrical and photoelectrochemical property of the TiO₂ nanostructured films. The charge transfer resistances increase in the following ordering: decorated nanowires < straight nanowires < corrugated nanowires < nanobelts. The photocurrent density measured at 0.5 V (vs Ag/AgCl) for the decorated nanowires (1.5 mA/cm²) is found to be 8.3, 6.0, 2.5, and 1.6 times those of nanobelts (0.18 mA/cm²), nanobricks (0.25 mA/cm²), straight nanowires (0.6 mA/cm²), and corrugated nanowires (0.94 mA/cm²), respectively. The decorated nanowires provide one of the best photoelectrochemical performances among the TiO₂ nanostructures reported to date. Even more remarkable is that the photocurrent density of the decorated nanowires is reduced slightly from 1.5 mA/cm² to 1.4 mA/cm² when a long-pass filter is coupled with the AM 1.5G filter, which is 87% of the overall photocurrent. The higher photocurrent density of the decorated TiO₂ nanowires can be attributed to the dense mat of nanowires with densely packed TiO₂ nanocrystallites at the outer surface, which offer excellent light-trapping characteristics, a large contact area with the electrolyte, and a highly conductive pathway for charge carrier collection. At the same time, the presence of a large number of oxygen vacancy defects in these nanocrystallites provides superior photoelectrochemical performance in the visible region.

In the present work, we also explore the catalyst-assisted PLD growth for defect-rich ZrO₂ nanostructures. The variation of the GNI catalyst size allows us to prepare oxygen vacancy-rich ZrO₂ regular nanowires, hierarchical nanowires, and octopi-like hierarchical nanowires. We further demonstrate that the size of the nanoplates of hierarchical nanowires can be easily manipulated by controlling the GNIs catalyst size. In our proposed growth mechanism for these novel nanoplate-decorated 1D nanostructures, the initial gold nanoisland formation on the Ox-Si substrate provides the essential catalysts for VLS growth. At the start of the VLS growth, a ZrO₂ nanowire trunk pushes up and detaches a GNI from the Ox-Si substrate. As the VLS growth continues, a fraction of the Au atoms are evaporated from the bulk Au catalyst at the tip of the nanowire trunk, and they get re-adsorbed on the surface of nanowire trunk. These re-adsorbed Au atoms then become additional nucleation sites, enhance the absorption rate of incoming ZrO₂ vapours, and promote ZrO₂ nanoplate formation. The longer exposure of the base to the incoming vapour compared to the tip results in

larger nanoplates at the base and smaller nanoplates at the tip of the nanowire trunk, thus accounting for the observed tapered shape of the hierarchical nanowire structure.

Taking advantage of the significantly larger specific surface area and oxygen vacancy defect composition of the hierarchical nanowires, compared to the regular ZrO_2 nanowires, we employ these hierarchical nanowires as photoelectrode material for photoelectrochemical water splitting reaction. With their enhanced UV-Vis absorbance and large surface area, we obtain a photocurrent density of 6.0 mA/cm^2 , which is 2.5 times higher than that of regular nanowires (2.4 mA/cm^2). To further improve the photoelectrochemical performance, we perform a simple post treatment by dipping them in dilute hydrofluoric acid, in order to improve the contact between ZrO_2 nanostructured film and the Si substrate by partially removing the interfacial SiO_2 layer. The photocurrent density of the partially delaminated hierarchical nanowires, obtained after the HF treatment, is found to increase significantly to 29.4 mA/cm^2 , i.e. nearly five-fold that of the as-grown hierarchical nanowires (6.0 mA/cm^2). This is the highest photocurrent among all the transparent conductive oxide nanostructures ever reported to date. The lower activity of the as-grown nanostructured film, compared to the partially delaminated nanostructured film, could be attributed to the thicker SiO_2 buffer layer of the GNI/Ox-Si template, which impedes the direct transfer of photogenerated carriers from the ZrO_2 film to the Si substrate (and onto the Pt counter electrode). On the other hand, the higher photocatalytic activity of the hierarchical nanowires, compared to the regular nanowires, is attributed to the higher oxygen vacancy defects and densely packed nanoplates (3-6 nm thick) along individual nanowire trunks, which provide lower charge-transport resistances and significantly higher surface area for the photoelectrochemical reaction.

The variation of the PLD growth temperature also produces different ZrO_2 nanostructures with different amounts and compositions of oxygen vacancy defects. For example, PLD growth on the $15 \pm 5 \text{ nm}$ GNI/Ox-Si template at $550 \text{ }^\circ\text{C}$, $650 \text{ }^\circ\text{C}$ and $770 \text{ }^\circ\text{C}$ produces ZrO_2 nanopopcorns, nanospikes, and nanowires, respectively. In the absence of the GNI catalysts, nanobrick film is observed. As with TiO_2 , we therefore expect both vapour-solid and VLS growth mechanisms are operative for the nanospike and nanowire growth, while the nanopopcorn structures are evidently formed via the vapour-solid mechanism only.

Glancing-incidence X-ray diffraction and transmission electron microscopy reveal that the PLD-grown ZrO_2 nanopopcorns, nanospikes, and nanowires are predominantly monoclinic, while the nanobricks among these nanostructures (similar to those that make up the nanobrick film) are

predominantly tetragonal ZrO₂. The room-temperature magnetization versus magnetic field curves of the nanostructured films containing more monoclinic phase exhibit larger saturation magnetization. The saturation magnetization measured at 2000 Oe for the nanowires (5.9 emu/g) is found to be 2.0, 4.9, and 9.8 times those of nanospikes (2.9 emu/g), nanopopcorns (1.2 emu/g), and nanobricks (0.6 emu/g), respectively. This is a significant result, because in marked contrast to the previously reported ZrO₂ planar thin films, of which the observed ferromagnetic behaviour was found to reduce with increased amount of the monoclinic phase, we observe increase in ferromagnetism with increase of the monoclinic phase in the ZrO₂ nanostructures here. The observed saturation magnetization of nanowires (5.9 emu/g) is not only greater than other ZrO₂ nanomaterials reported to date, but also at least an order of magnitude higher than the undoped TiO₂ nanoporous nanoribbons (0.2 emu/g),¹³⁵ α-MoO₃ nanofibers (0.015 emu/g),²⁹¹ CuO-ZnO heterostructures (0.002 emu/g),²⁹² 2H-SiC-α-Al₂O₃ nanowires (0.3 emu/g), hexagonal CeO₂ nanosheets (0.03 emu/g),¹³⁶ and Ni-doped ZnO nanorods (1.0 emu/g).²⁹³

We further demonstrate that the origin of the ferromagnetism in undoped ZrO₂ nanostructure can be attributed to oxygen vacancy composition defects. The presence of different types of oxygen vacancies (neutral, singly charged and doubly charged defects) and their correlation to the Zr^{x+} oxidation states ($4 > x > 1$) are found to affect the exchange interactions and the corresponding magnetization. More importantly, T_c considerably above room temperature is also observed for these nanostructures: 700 K for nanowires, 650 K for nanospikes, 550 K for nanopopcorns, and 400 K for nanobricks. We hypothesize a new defect-induced bound polaron model for the observed high T_c ferromagnetism, in which the exchange interactions of singly charged and doubly charged oxygen vacancy defects and the reduced Zr 4d¹ ions lead to the formation of bound magnetic polarons around the vacancy sites. The essential feature of this mechanism is that regardless of the phase of ZrO₂, it is the specific surface area, the amounts and types of oxygen vacancy defects within the nanostructure that control the ferromagnetic ordering in these ZrO₂ nanostructure.

6.2 Suggestions for Future Work

The growth of defect-rich 1D TiO₂ and ZrO₂ nanostructures with different morphology and composition of oxygen vacancy defects by one-step catalyst-assisted pulsed laser deposition method has opened up new prospects of fabricating other defect-rich transparent conductive oxide semiconductor nanostructures by fully exploiting the deposition parameters. The present catalyst-assisted pulsed laser deposition technique is also not limited to the synthesis of just transparent

conductive oxide semiconductor nanostructures, and it can indeed be used to produce nanostructures of other materials, including group IV, group II-VI, and group III-V semiconductors. The random growth orientation of the nanowires obtained in the present growth technique is due to the amorphous nature of the interfacial SiO₂ layer, and this can be improved by epitaxial growth on lattice-matched single-crystal substrate. For example, single-crystalline LaAl₂O₃ and SrTiO₃ substrate can be used for epitaxial growth of TiO₂ nanowires while Al₂O₃ and MgO for ZrO₂. The vertically aligned 1D nanostructures so produced could maximize the optical absorption. As the photoelectrochemical performance and magnetic properties are mostly normalized on the area of the sample, the increase in the areal density of the nanowires could further improve the overall performance for the same sample. This could be done easily by increasing the density of the gold nanoislands by manipulating the gold film thickness and nanoisland formation temperature.

The other exciting opportunity that emerges from this catalyst-assisted pulsed laser deposition approach is the capability for doping the target material with the desirable carrier donors/acceptors (scandium/vanadium, or yttrium/niobium), optically active dopants (Pt, Ag), and dopants with special properties, which can be used as a means to introduce different and/or hybrid properties into these one-dimensional nanostructures. Another important future project is the fabrication of heterostructures by switching between multiple targets during the deposition, upon due consideration of lattice matching and the prospect of VLS growth of a selected phase by using Au or other catalysts. Fabrication of p-n junctions in a single nanowire is one of these exciting objectives in the synthesis of heterostructures, which would allow greater flexibilities in device design for applications such as the photocatalytic, photovoltaic,²⁹⁷ tunneling field-effect-transistors,²⁹⁸ and spin transistors.²⁹⁹ Both radial and longitudinal heterostructures can be deposited using this method. In combination with the variety of available n-type oxides, oxides with intrinsic or p-type doped carriers will be of special interest for the synthesis of p-n junctions. Among the p-type oxide semiconductors, ZrO₂ will be especially interesting because of the compositional similarities between the ZrO₂ and TiO₂ (the latter being an n-type oxide). Indeed, the present work has positioned us to attempt building such a radial nanostructured p-n junction device involving ZrO₂ and TiO₂. Other p-type oxides including NiO, Fe₂O₃, Cu₂O or ternary oxides can also be attempted. Enhanced photoactivity can be expected from these p-n junction nanowires, due to the extended light absorption and the effective separation of the photogenerated charge carriers driven by the photoinduced potential difference generated at the p-n junction interface. More importantly, by decorating the nanowire surface with a second catalyst, including noble metals (silver, gold or platinum), it may be possible to grow secondary nanowires at

the outer surface of the core nanowire. The creation of secondary nanowires of the same or different oxides might open new opportunities for the development of multifunctional one-dimensional nanostructures for a wide variety of applications.

In addition to the present focus on photoelectrochemical water splitting reactions and dilute ferromagnetism, future work is needed to explore the use of defect-rich TiO_2 and ZrO_2 nanostructures for other optoelectronic and sensing applications. The exceptional stability against photocorrosion upon optical excitation, the high thermal and chemical stability, and the low charge-transport resistances of defect-rich TiO_2 and ZrO_2 photoelectrodes could offer potential solution to reducing the efficiency decay problem in solar batteries. In addition, the current problem of spin-based devices²⁹⁹ is the requirement for low operational temperature, due to the low T_c of group III-V and II-VI semiconductors (<200 K), and to the low spin-injection efficiencies caused by the precipitation and migration of dopants from the host layer to the adjacent layers in a multilayer device (during the operation of the device).²⁶¹ By taking advantage of the high saturated magnetization and high T_c capabilities of the present dopant-free, defect-rich TiO_2 and ZrO_2 nanostructured films, it may also be possible to build more efficient spin transistors and spin-based logic circuits that could operate well above the room temperature. Finally, an exciting emerging area is solar spin devices, where the generation of spin currents by light opens the door to the integration of electronics and optics.²⁹⁰ This new approach to convert light of arbitrary polarization into spin current would allow an additional degree of freedom in spin transistors and spin-based logic circuits.

Appendix A

Permissions



RightsLink®

Home

Account
Info

Help



ACS Publications
Most Trusted. Most Cited. Most Read.

Title: The Stability, Electronic Structure, and Optical Property of TiO₂ Polymorphs
Author: Tong Zhu, Shang-Peng Gao
Publication: The Journal of Physical Chemistry C
Publisher: American Chemical Society
Date: May 1, 2014
Copyright © 2014, American Chemical Society

Logged in as:

Md Anisur Rahman

LOGOUT

PERMISSION/LICENSE IS GRANTED FOR YOUR ORDER AT NO CHARGE

This type of permission/license, instead of the standard Terms & Conditions, is sent to you because no fee is being charged for your order. Please note the following:

- Permission is granted for your request in both print and electronic formats, and translations.
- If figures and/or tables were requested, they may be adapted or used in part.
- Please print this page for your records and send a copy of it to your publisher/graduate school.
- Appropriate credit for the requested material should be given as follows: "Reprinted (adapted) with permission from (COMPLETE REFERENCE CITATION). Copyright (YEAR) American Chemical Society." Insert appropriate information in place of the capitalized words.
- One-time permission is granted only for the use specified in your request. No additional uses are granted (such as derivative works or other editions). For any other uses, please submit a new request.

If credit is given to another source for the material you requested, permission must be obtained from that source.

BACK

CLOSE WINDOW

Copyright © 2016 Copyright Clearance Center, Inc. All Rights Reserved. [Privacy statement](#), [Terms and Conditions](#).
Comments? We would like to hear from you. E-mail us at customercare@copyright.com



Title: Review of one-dimensional and two-dimensional nanostructured materials for hydrogen generation

Author: Veluru Jagadeesh Babu, Sesa Vempati, Tamer Uyar, Seeram Ramakrishna

Publication: Physical Chemistry Chemical Physics

Publisher: Royal Society of Chemistry

Date: Nov 28, 2014

Copyright © 2014, Royal Society of Chemistry

Logged in as:
Md Anisur Rahman

[LOGOUT](#)

Order Completed

Thank you for your order.

This Agreement between Md Anisur Rahman ("You") and Royal Society of Chemistry ("Royal Society of Chemistry") consists of your license details and the terms and conditions provided by Royal Society of Chemistry and Copyright Clearance Center.

Your confirmation email will contain your order number for future reference.

[Get the printable license.](#)

| | |
|----------------------------------|---|
| License Number | 3823890604719 |
| License date | Mar 07, 2016 |
| Licensed Content Publisher | Royal Society of Chemistry |
| Licensed Content Publication | Physical Chemistry Chemical Physics |
| Licensed Content Title | Review of one-dimensional and two-dimensional nanostructured materials for hydrogen generation |
| Licensed Content Author | Veluru Jagadeesh Babu, Sesa Vempati, Tamer Uyar, Seeram Ramakrishna |
| Licensed Content Date | Nov 28, 2014 |
| Licensed Content Volume | 17 |
| Licensed Content Issue | 5 |
| Type of Use | Thesis/Dissertation |
| Requestor type | non-commercial (non-profit) |
| Portion | figures/tables/images |
| Number of figures/tables/images | 1 |
| Distribution quantity | 1 |
| Format | print and electronic |
| Will you be translating? | no |
| Order reference number | None |
| Title of the thesis/dissertation | Defect-rich Titanium (IV) Oxide and Zirconium (IV) Oxide Nanostructures for Ultra-efficient Photocatalyst and High-Tc Dilute Ferromagnetic Semiconductor Applications |
| Expected completion date | May 2016 |
| Estimated size | 210 |
| Requestor Location | Md Anisur Rahman 200 University Ave W, Waterloo, ON N2L 3G1 Canada Attn: Md Anisur Rahman |
| Billing Type | Invoice |
| Billing address | Md Anisur Rahman 200 University Ave W, Waterloo, ON N2L 3G1 Canada Attn: Md Anisur Rahman |
| Total | 0.00 CAD |

[ORDER MORE](#)

[CLOSE WINDOW](#)

Copyright © 2016 Copyright Clearance Center, Inc. All Rights Reserved. [Privacy statement](#). [Terms and Conditions](#).
Comments? We would like to hear from you. E-mail us at customer care@copyright.com



Title: Size-Selected TiO₂ Nanocluster Catalysts for Efficient Photoelectrochemical Water Splitting
Author: Saurabh Srivastava, Joseph Palathinkal Thomas, Md. Anisur Rahman, et al
Publication: ACS Nano
Publisher: American Chemical Society
Date: Nov 1, 2014
Copyright © 2014, American Chemical Society

Logged in as:
Md Anisur Rahman

[LOGOUT](#)

PERMISSION/LICENSE IS GRANTED FOR YOUR ORDER AT NO CHARGE

This type of permission/license, instead of the standard Terms & Conditions, is sent to you because no fee is being charged for your order. Please note the following:

- Permission is granted for your request in both print and electronic formats, and translations.
- If figures and/or tables were requested, they may be adapted or used in part.
- Please print this page for your records and send a copy of it to your publisher/graduate school.
- Appropriate credit for the requested material should be given as follows: "Reprinted (adapted) with permission from (COMPLETE REFERENCE CITATION). Copyright (YEAR) American Chemical Society." Insert appropriate information in place of the capitalized words.
- One-time permission is granted only for the use specified in your request. No additional uses are granted (such as derivative works or other editions). For any other uses, please submit a new request.

If credit is given to another source for the material you requested, permission must be obtained from that source.

[BACK](#)

[CLOSE WINDOW](#)

Copyright © 2016 [Copyright Clearance Center, Inc.](#) All Rights Reserved. [Privacy statement](#). [Terms and Conditions](#). Comments? We would like to hear from you. E-mail us at customercare@copyright.com



Title: Fabrication of Titania Nanofibers by Electrospinning
Author: Dan Li, Younan Xia
Publication: Nano Letters
Publisher: American Chemical Society
Date: Apr 1, 2003
Copyright © 2003, American Chemical Society

Logged in as:
Md Anisur Rahman

[LOGOUT](#)

PERMISSION/LICENSE IS GRANTED FOR YOUR ORDER AT NO CHARGE

This type of permission/license, instead of the standard Terms & Conditions, is sent to you because no fee is being charged for your order. Please note the following:

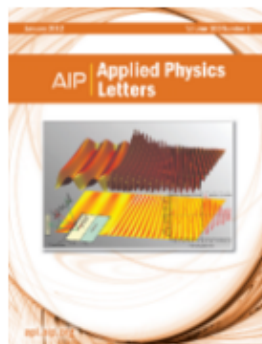
- Permission is granted for your request in both print and electronic formats, and translations.
- If figures and/or tables were requested, they may be adapted or used in part.
- Please print this page for your records and send a copy of it to your publisher/graduate school.
- Appropriate credit for the requested material should be given as follows: "Reprinted (adapted) with permission from (COMPLETE REFERENCE CITATION). Copyright (YEAR) American Chemical Society." Insert appropriate information in place of the capitalized words.
- One-time permission is granted only for the use specified in your request. No additional uses are granted (such as derivative works or other editions). For any other uses, please submit a new request.

If credit is given to another source for the material you requested, permission must be obtained from that source.

[BACK](#)

[CLOSE WINDOW](#)

Copyright © 2016 [Copyright Clearance Center, Inc.](#) All Rights Reserved. [Privacy statement](#). [Terms and Conditions](#).
Comments? We would like to hear from you. E-mail us at customer@copyright.com



Title: VAPOR-LIQUID-SOLID
MECHANISM OF SINGLE
CRYSTAL GROWTH
Author: R. S. Wagner, W. C. Ellis
Publication: Applied Physics Letters
Volume/Issue: 4/5
Publisher: AIP Publishing LLC
Date: Dec 23, 2004
Page Count: 2
Rights managed by AIP Publishing LLC.

Logged in as:
Md Anisur Rahman

LOGOUT

Order Completed

Thank you very much for your order.

Click [here](#) for Payment Terms and Conditions.

[Get a printable version for your records.](#)

| | |
|-------------------------------------|---|
| License Number | 3823891322353 |
| Order Date | Mar 07, 2016 |
| Publisher | AIP Publishing LLC |
| Publication | Applied Physics Letters |
| Article Title | VAPOR-LIQUID-SOLID MECHANISM OF SINGLE CRYSTAL GROWTH |
| Author | R. S. Wagner, W. C. Ellis |
| Online Publication Date | Dec 23, 2004 |
| Volume number | 4 |
| Issue number | 5 |
| Type of Use | Thesis/Dissertation |
| Requestor type | Student |
| Format | Print and electronic |
| Portion | Figure/Table |
| Number of figures/tables | 1 |
| Title of your thesis / dissertation | Defect-rich Titanium (IV) Oxide and Zirconium (IV) Oxide Nanostructures for Ultra-efficient Photocatalyst and High-Tc Dilute Ferromagnetic Semiconductor Applications |
| Expected completion date | May 2016 |
| Estimated size (number of pages) | 210 |
| Total | 0.00 CAD |

ORDER MORE...

CLOSE WINDOW

Copyright © 2016 Copyright Clearance Center, Inc. All Rights Reserved. [Privacy statement](#). [Terms and Conditions](#).
Comments? We would like to hear from you. E-mail us at customercare@copyright.com



Title: Hydrogen-Treated TiO₂ Nanowire Arrays for Photoelectrochemical Water Splitting
Author: Gongming Wang, Hanyu Wang, Yichuan Ling, et al
Publication: Nano Letters
Publisher: American Chemical Society
Date: Jul 1, 2011
Copyright © 2011, American Chemical Society

Logged in as:
Md Anisur Rahman

[LOGOUT](#)

PERMISSION/LICENSE IS GRANTED FOR YOUR ORDER AT NO CHARGE

This type of permission/license, instead of the standard Terms & Conditions, is sent to you because no fee is being charged for your order. Please note the following:

- Permission is granted for your request in both print and electronic formats, and translations.
- If figures and/or tables were requested, they may be adapted or used in part.
- Please print this page for your records and send a copy of it to your publisher/graduate school.
- Appropriate credit for the requested material should be given as follows: "Reprinted (adapted) with permission from (COMPLETE REFERENCE CITATION). Copyright (YEAR) American Chemical Society." Insert appropriate information in place of the capitalized words.
- One-time permission is granted only for the use specified in your request. No additional uses are granted (such as derivative works or other editions). For any other uses, please submit a new request.

If credit is given to another source for the material you requested, permission must be obtained from that source.

[BACK](#)

[CLOSE WINDOW](#)



Title: Band gap engineering of bulk ZrO₂ by Ti doping
Author: Federico Gallino, Cristiana Di Valentin, Gianfranco Pacchioni
Publication: Physical Chemistry Chemical Physics
Publisher: Royal Society of Chemistry
Date: Sep 7, 2011
 Copyright © 2011, Royal Society of Chemistry

Logged in as:
Md Anisur Rahman

LOGOUT

Order Completed

Thank you for your order.

This Agreement between Md Anisur Rahman ("You") and Royal Society of Chemistry ("Royal Society of Chemistry") consists of your license details and the terms and conditions provided by Royal Society of Chemistry and Copyright Clearance Center.

Your confirmation email will contain your order number for future reference.

[Get the printable license.](#)

| | |
|-------------------------------------|---|
| License Number | 3823881313822 |
| License date | Mar 07, 2016 |
| Licensed Content Publisher | Royal Society of Chemistry |
| Licensed Content Publication | Physical Chemistry Chemical Physics |
| Licensed Content Title | Band gap engineering of bulk ZrO ₂ by Ti doping |
| Licensed Content Author | Federico Gallino, Cristiana Di Valentin, Gianfranco Pacchioni |
| Licensed Content Date | Sep 7, 2011 |
| Licensed Content Volume | 13 |
| Licensed Content Issue | 39 |
| Type of Use | Thesis/Dissertation |
| Requestor type | non-commercial (non-profit) |
| Portion | figures/tables/images |
| Number of figures/tables/images | 1 |
| Distribution quantity | 1 |
| Format | print and electronic |
| Will you be translating? | no |
| Order reference number | None |
| Title of the thesis/dissertation | Defect-rich Titanium (IV) Oxide and Zirconium (IV) Oxide Nanostructures for Ultra-efficient Photocatalyst and High-Tc Dilute Ferromagnetic Semiconductor Applications |
| Expected completion date | May 2016 |
| Estimated size | 210 |
| Requestor Location | Md Anisur Rahman 200 University Ave W, Waterloo, ON N2L 3G1 Canada Attn: Md Anisur Rahman |
| Billing Type | Invoice |
| Billing address | Md Anisur Rahman 200 University Ave W, Waterloo, ON N2L 3G1 Canada Attn: Md Anisur Rahman |
| Total | 0.00 CAD |

ORDER MORE

CLOSE WINDOW

Copyright © 2016 Copyright Clearance Center, Inc. All Rights Reserved. [Privacy statement](#), [Terms and Conditions](#).
 Comments? We would like to hear from you. E-mail us at customercare@copyright.com



RSC Publishing

Title: Synthesis of ZrO₂:Fe nanostructures with visible-light driven H₂ evolution activity
Author: Mu Xiao,Yaguang Li,Yangfan Lu,Zhizhen Ye
Publication: Journal of Materials Chemistry A
Publisher: Royal Society of Chemistry
Date: Dec 3, 2014
Copyright © 2014, Royal Society of Chemistry

Logged in as:
Md Anisur Rahman
Account #:
3001006857

[LOGOUT](#)

Order Completed

Thank you for your order.

This Agreement between Md Anisur Rahman ("You") and Royal Society of Chemistry ("Royal Society of Chemistry") consists of your license details and the terms and conditions provided by Royal Society of Chemistry and Copyright Clearance Center.

Your confirmation email will contain your order number for future reference.

[Get the printable license.](#)

| | |
|----------------------------------|---|
| License Number | 3823940788009 |
| License date | Mar 07, 2016 |
| Licensed Content Publisher | Royal Society of Chemistry |
| Licensed Content Publication | Journal of Materials Chemistry A |
| Licensed Content Title | Synthesis of ZrO ₂ :Fe nanostructures with visible-light driven H ₂ evolution activity |
| Licensed Content Author | Mu Xiao,Yaguang Li,Yangfan Lu,Zhizhen Ye |
| Licensed Content Date | Dec 3, 2014 |
| Licensed Content Volume | 3 |
| Licensed Content Issue | 6 |
| Type of Use | Thesis/Dissertation |
| Requestor type | non-commercial (non-profit) |
| Portion | figures/tables/images |
| Number of figures/tables/images | 1 |
| Distribution quantity | 1 |
| Format | print and electronic |
| Will you be translating? | no |
| Order reference number | None |
| Title of the thesis/dissertation | Defect-rich Titanium (IV) Oxide and Zirconium (IV) Oxide Nanostructures for Ultra-efficient Photocatalyst and High-Tc Dilute Ferromagnetic Semiconductor Applications |
| Expected completion date | May 2016 |
| Estimated size | 210 |
| Requestor Location | Md Anisur Rahman 200 University Ave W, Waterloo, ON N2L 3G1 Canada Attn: Md Anisur Rahman |
| Billing Type | Invoice |
| Billing address | Md Anisur Rahman 200 University Ave W, Waterloo, ON N2L 3G1 Canada Attn: Md Anisur Rahman |
| Total | 0.00 USD |

[ORDER MORE](#)[CLOSE WINDOW](#)

Copyright © 2016 Copyright Clearance Center, Inc. All Rights Reserved. [Privacy statement](#). [Terms and Conditions](#).
Comments? We would like to hear from you. E-mail us at customercare@copyright.com



Title: Ferromagnetism in transition-metal-doped TiO2 thin films
Author: Nguyen Hoa Hong et al.
Publication: Physical Review B
Publisher: American Physical Society
Date: Nov 10, 2004
Copyright © 2004, American Physical Society

Logged in as: Md Anisur Rahman
Account #: 3001006857
LOGOUT

Order Completed

Thank you for your order.

This Agreement between Md Anisur Rahman ("You") and American Physical Society ("American Physical Society") consists of your license details and the terms and conditions provided by American Physical Society and Copyright Clearance Center.

Your confirmation email will contain your order number for future reference.

Get the printable license.

Table with license details including License Number (3823941072159), License date (Mar 07, 2016), Licensed Content Publisher (American Physical Society), Licensed Content Title (Ferromagnetism in transition-metal-doped TiO2 thin films), and Requestor Location (Md Anisur Rahman, 200 University Ave W, Waterloo, ON N2L 3G1, Canada).

ORDER MORE CLOSE WINDOW



Title: Phase-dependent and defect-driven d0 ferromagnetism in undoped ZrO2 thin films
Author: Shuai Ning,Zhengjun Zhang
Publication: RSC Advances
Publisher: Royal Society of Chemistry
Date: Nov 24, 2014
 Copyright © 2014, Royal Society of Chemistry

Logged in as:
Md Anisur Rahman
Account #:
3001006857

LOGOUT

Order Completed

Thank you for your order.

This Agreement between Md Anisur Rahman ("You") and Royal Society of Chemistry ("Royal Society of Chemistry") consists of your license details and the terms and conditions provided by Royal Society of Chemistry and Copyright Clearance Center.

Your confirmation email will contain your order number for future reference.

[Get the printable license.](#)

| | |
|----------------------------------|---|
| License Number | 3823950393379 |
| License date | Mar 07, 2016 |
| Licensed Content Publisher | Royal Society of Chemistry |
| Licensed Content Publication | RSC Advances |
| Licensed Content Title | Phase-dependent and defect-driven d0 ferromagnetism in undoped ZrO2 thin films |
| Licensed Content Author | Shuai Ning,Zhengjun Zhang |
| Licensed Content Date | Nov 24, 2014 |
| Licensed Content Volume | 5 |
| Licensed Content Issue | 5 |
| Type of Use | Thesis/Dissertation |
| Requestor type | non-commercial (non-profit) |
| Portion | figures/tables/images |
| Number of figures/tables/images | 1 |
| Distribution quantity | 1 |
| Format | print and electronic |
| Will you be translating? | no |
| Order reference number | None |
| Title of the thesis/dissertation | Defect-rich Titanium (IV) Oxide and Zirconium (IV) Oxide Nanostructures for Ultra-efficient Photocatalyst and High-Tc Dilute Ferromagnetic Semiconductor Applications |
| Expected completion date | May 2016 |
| Estimated size | 210 |
| Requestor Location | Md Anisur Rahman 200 University Ave W, Waterloo, ON N2L 3G1 Canada Attn: Md Anisur Rahman |
| Billing Type | Invoice |
| Billing address | Md Anisur Rahman 200 University Ave W, Waterloo, ON N2L 3G1 Canada Attn: Md Anisur Rahman |
| Total | 0.00 USD |

ORDER MORE

CLOSE WINDOW

Copyright © 2016 Copyright Clearance Center, Inc. All Rights Reserved. [Privacy statement](#). [Terms and Conditions](#).
 Comments? We would like to hear from you. E-mail us at customercare@copyright.com



Title: Polaron Percolation in Diluted Magnetic Semiconductors
Author: A. Kaminski and S. Das Sarma
Publication: Physical Review Letters
Publisher: American Physical Society
Date: May 31, 2002
 Copyright © 2002, American Physical Society

Logged in as:
 Md Anisur Rahman
 Account #: 3001006857
 LOGOUT

Order Completed

Thank you for your order.

This Agreement between Md Anisur Rahman ("You") and American Physical Society ("American Physical Society") consists of your license details and the terms and conditions provided by American Physical Society and Copyright Clearance Center.

Your confirmation email will contain your order number for future reference.

[Get the printable license.](#)

| | |
|--|---|
| License Number | 3823930512678 |
| License date | Mar 07, 2016 |
| Licensed Content Publisher | American Physical Society |
| Licensed Content Publication | Physical Review Letters |
| Licensed Content Title | Polaron Percolation in Diluted Magnetic Semiconductors |
| Licensed Content Author | A. Kaminski and S. Das Sarma |
| Licensed Content Date | May 31, 2002 |
| Licensed Content Volume | 88 |
| Type of use | Thesis/Dissertation |
| Requestor type | Student |
| Format | Print, Electronic |
| Portion | chart/graph/table/figure |
| Number of charts/graphs/tables/figures | 1 |
| Portion description | Interaction of two bound magnetic polarons (after Ref. [15]). The polarons are shown with gray circles; small and large arrows show impurity and hole spins, respectively |
| Rights for | Main product |
| Duration of use | Life of Current Edition |
| Creation of copies for the disabled | no |
| With minor editing privileges | no |
| For distribution to | Canada |
| In the following language(s) | Original language of publication |
| With incidental promotional use | no |
| Lifetime unit quantity of new product | 0 to 499 |
| The requesting person/organization | Md Anisur Rahman |
| Order reference number | None |
| Title of your thesis / dissertation | Defect-rich Titanium (IV) Oxide and Zirconium (IV) Oxide Nanostructures for Ultra-efficient Photocatalyst and High-Tc Dilute Ferromagnetic Semiconductor Applications |
| Expected completion date | May 2016 |
| Expected size (number of pages) | 210 |
| Requestor Location | Md Anisur Rahman 200 University Ave W, Waterloo, ON N2L 3G1 Canada Attn: Md Anisur Rahman |
| Billing Type | Invoice |
| Billing address | Md Anisur Rahman 200 University Ave W, Waterloo, ON N2L 3G1 Canada Attn: Md Anisur Rahman |
| Total | 0.00 USD |

ORDER MORE

CLOSE WINDOW

Request for Permission to Reproduce or Re-Publish ECS Material

Please fax this form to: The Electrochemical Society (ECS), Attn: Permissions Requests, 1.609.730.0629.
You may also e-mail your request to: copyright@electrochem.org. Include all the information as required on this form. Please allow 3-7 days for your request to be processed.

I am preparing a (choose one): paper chapter book thesis

entitled: "Defect-rich Titanium (IV) Oxide and Zirconium (IV) Oxide Nanostructures for Ultra-efficient Photocatalyst and

to be published by: High Tc Dilute Ferromagnetic Semiconductor Oxides." University of Waterloo

in an upcoming publication entitled: Thesis for the Degree of Philosophy

I request permission to use the following material in the publication noted above, and request nonexclusive rights for all subsequent editions and in all foreign language translations for distribution throughout the world.

Description of material to be used—Indicate what material you wish to use (figures, tables, text, etc.) and give the full bibliographic reference for the source publication. You may attach a separate list, organized by ECS title.

Figure 1. Schematic drawing of the fabrication procedures of zirconia nanowire arrays on glass substrate by a tailored anodization.

Journal of the Electrochemical Society, 158 95), C148-C157(2011)

Direct growth of highly efficient ordered crystalline zirconia nanowire arrays with high aspect ratios on glass by a tailored anodization

Signature:  Date: March 7, 2016

Name: Md Anisur rahman

Address: University of Waterloo, Chemistry Department, 200 University Ave W, Waterloo, ON N2L 3G1.

Telephone: 5199982871

Fax: _____

E-mail: ma5rahma@uwaterloo.ca

Permission is granted to reproduce the above-referenced material. Please acknowledge the author(s) and publication data of the original material, and include the words: "Reproduced by permission of The Electrochemical Society."

3/10/16
Date


James Ryan, Director of Publications



Title: Evidence of Charge-Transfer
Ferromagnetism in Transparent
Diluted Magnetic Oxide
Nanocrystals: Switching the
Mechanism of Magnetic
Interactions

Author: Shokouh S. Farvid, Tahereh
Sabergharesou, Lisa N. Hutfluss,
et al

Publication: Journal of the American Chemical
Society

Publisher: American Chemical Society

Date: May 1, 2014
Copyright © 2014, American Chemical Society

Logged in as:
Md Anisur Rahman
Account #:
3001006857

[LOGOUT](#)

PERMISSION/LICENSE IS GRANTED FOR YOUR ORDER AT NO CHARGE

This type of permission/license, instead of the standard Terms & Conditions, is sent to you because no fee is being charged for your order. Please note the following:

- Permission is granted for your request in both print and electronic formats, and translations.
- If figures and/or tables were requested, they may be adapted or used in part.
- Please print this page for your records and send a copy of it to your publisher/graduate school.
- Appropriate credit for the requested material should be given as follows: "Reprinted (adapted) with permission from (COMPLETE REFERENCE CITATION). Copyright (YEAR) American Chemical Society." Insert appropriate information in place of the capitalized words.
- One-time permission is granted only for the use specified in your request. No additional uses are granted (such as derivative works or other editions). For any other uses, please submit a new request.

If credit is given to another source for the material you requested, permission must be obtained from that source.

[BACK](#)

[CLOSE WINDOW](#)



Title: Defect-rich decorated TiO₂ nanowires for super-efficient photoelectrochemical water splitting driven by visible light

Author: Md Anisur Rahman, Samad Bazargan, Saurabh Srivastava, Xiongyao Wang, Marwa Abd-Ellah, Joseph P. Thomas, Nina F. Heinig, Debabrata Pradhan, Kam Tong Leung

Publication: Energy & Environmental Science
Publisher: Royal Society of Chemistry
Date: Sep 21, 2015

Copyright © 2015, Royal Society of Chemistry

Logged in as:
Md Anisur Rahman
Account #: 3001006857

[LOGOUT](#)

Order Completed

Thank you for your order.

This Agreement between Md Anisur Rahman ("You") and Royal Society of Chemistry ("Royal Society of Chemistry") consists of your license details and the terms and conditions provided by Royal Society of Chemistry and Copyright Clearance Center.

Your confirmation email will contain your order number for future reference.

[Get the printable license.](#)

| | |
|-------------------------------------|---|
| License Number | 3823940534190 |
| License date | Mar 07, 2016 |
| Licensed Content Publisher | Royal Society of Chemistry |
| Licensed Content Publication | Energy & Environmental Science |
| Licensed Content Title | Defect-rich decorated TiO ₂ nanowires for super-efficient photoelectrochemical water splitting driven by visible light |
| Licensed Content Author | Md Anisur Rahman, Samad Bazargan, Saurabh Srivastava, Xiongyao Wang, Marwa Abd-Ellah, Joseph P. Thomas, Nina F. Heinig, Debabrata Pradhan, Kam Tong Leung |
| Licensed Content Date | Sep 21, 2015 |
| Licensed Content Volume | 8 |
| Licensed Content Issue | 11 |
| Type of Use | Thesis/Dissertation |
| Requestor type | non-commercial (non-profit) |
| Portion | figures/tables/images |
| Number of figures/tables/images | 5 |
| Distribution quantity | 1 |
| Format | print and electronic |
| Will you be translating? | no |
| Order reference number | None |
| Title of the thesis/dissertation | Defect-rich Titanium (IV) Oxide and Zirconium (IV) Oxide Nanostructures for Ultra-efficient Photocatalyst and High-Tc Dilute Ferromagnetic Semiconductor Applications |
| Expected completion date | May 2016 |
| Estimated size | 210 |
| Requestor Location | Md Anisur Rahman 200 University Ave W, Waterloo, ON N2L 3G1 Canada Attn: Md Anisur Rahman |
| Billing Type | Invoice |
| Billing address | Md Anisur Rahman 200 University Ave W, Waterloo, ON N2L 3G1 Canada Attn: Md Anisur Rahman |
| Total | 0.00 USD |

[ORDER MORE](#)

[CLOSE WINDOW](#)

Copyright © 2016 Copyright Clearance Center, Inc. All Rights Reserved. [Privacy statement](#). [Terms and Conditions](#).
 Comments? We would like to hear from you. E-mail us at customercare@copyright.com

Bibliography

- (1) Wager, J. F.; Keszler, D. A.; Presley, R. E. *Transparent Electronics*; Springer US, **2008**.
- (2) Ginely, D.; Hosno, H.; Paine, D. C. (Eds.). *Handbook of Transparent Conductors*. Springer US, **2010**.
- (3) Wang, Z. L.; Kang, Z. C. *Functional and Smart Materials Structural Evolution and Structure Analysis*. Plenum Press. New York, **1998**.
- (4) Hong, N. H.; Park, C.; Raghavender, A. T.; Ruyter, A.; Chikoidze, E.; Dumont, Y. High Temperature Ferromagnetism in Cubic Mn-Doped ZrO₂ Thin Films. *J. Magn. Magn. Mater.* **2012**, *324*, 3013–3016.
- (5) Ning, S.; Zhang, Z. Phase-Dependent and Defect-Driven d⁰ Ferromagnetism in Undoped ZrO₂ Thin Films. *RSC Adv.* **2015**, *5*, 3636–3641.
- (6) Maca, F.; Kudrnovsky, J.; Drchal, V.; Bouzerar, G. Magnetism without Magnetic Impurities in Oxides ZrO₂. **2007**, *92*, 212503.
- (7) Baik, J. M.; Kim, M. H.; Larson, C.; Chen, X.; Guo, S.; Wodtke, A. M.; Moskovits, M. High-Yield TiO₂ Nanowire Synthesis and Single Nanowire Field-Effect Transistor Fabrication. *Appl. Phys. Lett.* **2008**, *92*, 242111.
- (8) Wang, G.; Wang, H.; Ling, Y.; Tang, Y.; Yang, X.; Fitzmorris, R. C.; Wang, C.; Zhang, J. Z.; Li, Y. Hydrogen-Treated TiO₂ Nanowire Arrays for Photoelectrochemical Water Splitting. *Nano Lett.* **2011**, *11*, 3026–3033.
- (9) Mongkolserm, P.; Pabchanda, S. Influence of Tin Doping on the Photocatalytic Activity of Zinc Oxide Thin Films under UV Light. *J. Chem. Chem. Eng.* **2012**, *6*, 631–637.
- (10) Radecka, M.; Trenczek-Zajac, A.; Zakrzewska, K.; Rekas, M. Effect of Oxygen Nonstoichiometry on Photo-Electrochemical Properties of TiO_{2-x}. *J. Power Sources* **2007**, *173*, 816–821.
- (11) Li, G.; Lian, Z.; Li, X.; Xu, Y.; Wang, W.; Zhang, D.; Tian, F.; Li, H. Ionothermal Synthesis of Black Ti³⁺-Doped Single-Crystal TiO₂ as an Active Photocatalyst for Pollutant Degradation and H₂ Generation. *J. Mater. Chem. A* **2014**, *00*, 1–9.
- (12) Wang, G.; Wang, H.; Ling, Y.; Tang, Y.; Yang, X.; Fitzmorris, R. C.; Wang, C.; Zhang, J. Z.;

- Li, Y. Hydrogen-Treated TiO₂ Nanowire Arrays for Photoelectrochemical Water Splitting. *Nano Lett.* **2011**, *11*, 3026–3033.
- (13) Ginsberg, D. M., (Eds.), Physical Properties of High Temperature Superconductors; *World Scientific: Singapore*, **1982**, *3*, 363.
- (14) Mo, S.; Ching, W. Y. Electronic and Optical Properties of Three Phases of Titanium Dioxide: Rutile, Anatase, and Brookite. *Phys. Rev. B* **1995**, *51*, 13023–13032.
- (15) Landmann, M.; Rauls, E.; Schmidt, W. G. The Electronic Structure and Optical Response of Rutile, Anatase and Brookite TiO₂. *J. Phys. Condens. Matter* **2012**, *24*, 195503.
- (16) Diebold, U. The Surface Science of Titanium Dioxide. *Surf. Sci. Rep.* **2003**, *48*, 53–229.
- (17) Zhu, T.; Gao, S. The Stability, Electronic Structure, and Optical Property of TiO₂ Polymorphs. *J. Phys. Chem. C* **2014**, *118*, 11385–11396.
- (18) Warlimont, H.; Martienssen, W. (Eds.). Springer Handbook of Condensed Matter and Materials Data; *Springer: Berlin*, **2005**.
- (19) Fujishima, A.; Honda, K. Electrochemical Photolysis of Water at a Semiconductor Electrode. *Nature* **1972**, *238*, 37–38.
- (20) Hoffmann, M. R.; Martin, S. T.; Choi, W.; Bahnemannt, D. W. Environmental Applications of Semiconductor Photocatalysis. *Chem. Rev.* **1995**, *95*, 69–96.
- (21) Khan, S. U. M.; Al-Shahry, M.; Ingler, W. B. Efficient Photochemical Water Splitting by a Chemically Modified n-TiO₂. *Science* **2002**, *297*, 2243–2245.
- (22) Srivastava, S.; Thomas, J. P.; Rahman, A.; Abd-ellah, M.; Mohapatra, M.; Pradhan, D.; Heinig, N. F.; Leung, K. T. Size-Selected TiO₂ Nanocluster Catalysts for Efficient Photoelectrochemical Water Splitting. *ACS Nano* **2014**, *8*, 11891–11898.
- (23) Babu, V. J.; Vempati, S.; Uyar, T.; Ramakrishna, S. Review of One-Dimensional and Two-Dimensional Nanostructured Materials for Hydrogen Generation. *Phys. Chem. Chem. Phys.* **2015**, *17*, 2960–2986.
- (24) Linsebigler, A. L.; Lu, G.; Yates, J. T. Photocatalysis on TiO₂ Surfaces: Principles, Mechanisms, and Selected Results. *Chem. Rev.* **1995**, 735–758.
- (25) Anpo, M. Use of Visible Light. Second-Generation Titanium Oxide Photocatalysts Prepared

- by the Application of an Advanced Metal Ion-Implantation Method. *Pure Appl. Chem.* **2000**, *72*, 1787–1792.
- (26) Fuerte, A.; Hernandez-Alonso, M. D.; Maira, A. J.; Martinez-Arias, A.; Fernandez-Garcia, M.; Conesa, J. C.; Soria, J. Visible Light-Activated Nanosized Doped-TiO₂ Photocatalysts. *Chem. Commun.* **2001**, 2718–2719.
- (27) Yu, J. C.; Zhang, L.; Zheng, Z.; Zhao, J. Synthesis and Characterization of Phosphated Mesoporous Titanium Dioxide with High Photocatalytic Activity. *Chem. Mater.* **2003**, *15*, 2280–2286.
- (28) Liu, Y.; Chen, X.; Li, J.; Burda, C. Photocatalytic Degradation of Azo Dyes by Nitrogen-Doped TiO₂ Nanocatalysts. *Chemosphere* **2005**, *61*, 11–18.
- (29) Ohno, T.; Mitsui, T.; Matsumura, M. Photocatalytic Activity of S-Doped TiO₂ Photocatalyst under Visible Light. *Chem. Lett.* **2003**, *32*, 364–365.
- (30) Paracchino, A.; Laporte, V.; Sivula, K.; Grätzel, M.; Thimsen, E. Highly Active Oxide Photocathode for Photoelectrochemical Water Reduction. *Nat. Mater.* **2011**, *10*, 456–461.
- (31) Hirai, T.; Suzuki, K.; Komasaawa, I. Preparation and Photocatalytic Properties of Composite CdS Nanoparticles–Titanium Dioxide Particles. *J. Colloid Interface Sci.* **2001**, *244*, 262–265.
- (32) Nah, Y.; Paramasivam, I.; Hahn, R.; Shrestha, N. K.; Schmuki, P. Nitrogen Doping of Nanoporous WO₃ Layers by NH₃ Treatment for Increased Visible Light Photoresponse. *Nanotechnology* **2010**, *21*, 105704.
- (33) Lam, S. W.; Chiang, K.; Lim, T. M.; Amal, R.; Low, G. The Effect of Platinum and Silver Deposits in the Photocatalytic Oxidation of Resorcinol. *Appl. Catal. B Environ.* **2007**, *72*, 363–372.
- (34) Niishiro, R.; Konta, R.; Kato, H.; Chun, W. J.; Asakura, K.; Kudo, A. Photocatalytic O₂ Evolution of Rhodium and Antimony-Codoped Rutile-Type TiO₂ under Visible Light Irradiation. *J. Phys. Chem. C* **2007**, *111*, 17420–17426.
- (35) Sun, L.; Zhao, X.; Cheng, X.; Sun, H.; Li, Y.; Li, P.; Fan, W. Evaluating the C, N, and F Pairwise Codoping Effect on the Enhanced Photoactivity of ZnWO₄: The Charge Compensation Mechanism in Donor-Acceptor Pairs. *J. Phys. Chem. C* **2011**, *115*, 15516–15524.

- (36) Abe, R.; Takami, H.; Murakami, N.; Ohtani, B. Pristine Simple Oxides as Visible Light Driven Photocatalysts: Highly Efficient Decomposition of Organic Compounds over Platinum-Loaded Tungsten Oxide. *J. Am. Chem. Soc.* **2008**, *130*, 7780–7781.
- (37) Kamat, P. V. Manipulation of Charge Transfer across Semiconductor Interface. A Criterion that cannot be ignored in Photocatalyst Design. *J. Phys. Chem. Lett.* **2012**, *3*, 663–672.
- (38) Serpone, N. Is the Band Gap of Pristine TiO₂ Narrowed by Anion- and Cation-Doping of Titanium Dioxide in Second-Generation Photocatalysts? *J. Phys. Chem. B* **2006**, *110*, 24287–24293.
- (39) Polarz, S.; Strunk, J.; Ischenko, V.; van den Berg, M. W. E.; Hinrichsen, O.; Muhler, M.; Driess, M. On the Role of Oxygen Defects in the Catalytic Performance of Zinc Oxide. *Angew. Chemie Int. Ed.* **2006**, *45*, 2965–2969.
- (40) Nakamura, I.; Negishi, N.; Kutsuna, S.; Ihara, T.; Sugihara, S.; Takeuchi, K. Role of Oxygen Vacancy in the Plasma-Treated TiO₂ Photocatalyst with Visible Light Activity for NO Removal. *J. Mol. ...* **2000**, *161*, 205–212.
- (41) Jing, L.; Xin, B.; Yuan, F.; Xue, L.; Wang, B.; Fu, H. Effects of Surface Oxygen Vacancies on Photophysical and Photochemical Processes of Zn-Doped TiO₂ Nanoparticles and their Relationships. *J. Phys. Chem. B* **2006**, *110*, 17860–17865.
- (42) Nowotny, J. Titanium Dioxide-Based Semiconductors for Solar-Driven Environmentally Friendly Applications: Impact of Point Defects on Performance. *Energy Environ. Sci.* **2008**, *1*, 565.
- (43) Nowotny, M. K.; Sheppard, L. R.; Bak, T.; Nowotny, J. Defect Chemistry of Titanium Dioxide . Application of Defect Engineering in Processing of TiO₂-Based Photocatalysts. *J. Phys. Chem. C* **2008**, *112*, 5275–5300.
- (44) Schaub, R.; Thostrup, P.; Lopez, N.; Lægsgaard, E.; Stensgaard, I.; Nørskov, J. K.; Besenbacher, F. Oxygen Vacancies as Active Sites for Water Dissociation on Rutile TiO₂ (110). *Phys. Rev. Lett.* **2001**, *87*, 266104.
- (45) Wang, J.; Liu, P.; Fu, X.; Li, Z.; Han, W.; Wang, X. Relationship between Oxygen Defects and the Photocatalytic Property of ZnO Nanocrystals in Nafion Membranes. *Langmuir* **2009**, *25*, 1218–1223.

- (46) Liu, H.; Ma, H. T.; Li, X. Z.; Li, W. Z.; Wu, M.; Bao, X. H. The Enhancement of TiO₂ Photocatalytic Activity by Hydrogen Thermal Treatment. *Chemosphere* **2003**, *50*, 39–46.
- (47) Naldoni, A.; Allieta, M.; Santangelo, S.; Marelli, M.; Fabbri, F.; Cappelli, S.; Bianchi, C. L.; Psaro, R.; Dal Santo, V. Effect of Nature and Location of Defects on Bandgap Narrowing in Black TiO₂ Nanoparticles. *J. Am. Chem. Soc.* **2012**, *134*, 7600–7603.
- (48) Pacchioni, G. Oxygen Vacancy: The Invisible Agent on Oxide Surfaces. *ChemPhysChem* **2003**, *4*, 1041–1047.
- (49) Eriksen, S.; Egdell, R. G. Electronic Excitations at Oxygen Deficient TiO₂(110) Surfaces: A Study by EELS. *Surf. Sci.* **1987**, *180*, 263–278.
- (50) Feibelman, M. L. K. and P. J. Ion Desorption by Core-Hole Auger Decay. *Phys. Rev. Lett.* **1978**, *40*, 2–5.
- (51) Soediono, B. Reinterpretation of Electron-Stimulated Desorption Data from Chemisorption Systems. *Physcial Rev. B* **1978**, *18*, 160.
- (52) Thompson, T. L.; Yates, J. T. TiO₂-Based Photocatalysis: Surface Defects, Oxygen and Charge Transfer. *Top. Catal.* **2005**, *35*, 197–210.
- (53) Onda, K.; Li, B.; Petek, H. Two-Photon Photoemission Spectroscopy of TiO₂(110) Surfaces Modified by Defects and O₂ or H₂O Adsorbates. *Phys. Rev. B* **2004**, *70*, 1–11.
- (54) Wu, Q.; Zheng, Q.; van de Krol, R. Creating Oxygen Vacancies as a Novel Strategy to Form Tetrahedrally Coordinated Ti⁴⁺ in Fe/TiO₂ Nanoparticles. *J. Phys. Chem. C* **2012**, *116*, 7219–7226.
- (55) Liu, L.; Zhao, C.; Li, Y. Spontaneous Dissociation of CO₂ to CO on Defective Surface of Cu(I)/TiO_{2-x} Nanoparticles at Room Temperature. *J. Phys. Chem. C* **2012**, *116*, 7904–7912.
- (56) Chang, H.; Wu, N.; Zhu, F. A Kinetic Model for Photocatalytic Degradation of Organic Contaminants in a Thin-Film TiO₂ Catalyst. *Water Res.* **2000**, *34*, 407–416.
- (57) Zhou, W.; Liu, H.; Boughton, R. I.; Du, G.; Lin, J.; Wang, J.; Liu, D. One-Dimensional Single-Crystalline Ti–O Based Nanostructures: Properties, Synthesis, Modifications and Applications. *J. Mater. Chem.* **2010**, *20*, 5993.
- (58) Feng, S.; Wu, J.; Hu, P.; Chen, Y.; Ma, B.; Peng, J.; Yang, J.; Jiang, H. Epitaxial Growth of

Successive CdSe Ultrathin Films and Quantum Dot Layers on TiO₂ Nanorod Arrays for Photo-Electrochemical Cells. *RSC Adv.* **2014**, *4*, 12154–12159.

- (59) Tian, J.; Zhao, Z.; Kumar, A.; Boughton, R. I.; Liu, H. Recent Progress in Design, Synthesis, and Applications of One-Dimensional TiO₂ Nanostructured Surface Heterostructures: A Review. *Chem. Soc. Rev.* **2014**, *43*, 6920-6937.
- (60) Li, D.; Xia, Y. Fabrication of Titania Nanofibers by Electrospinning. *Nano Lett.* **2003**, *3*, 555–560.
- (61) Shi, J.; Wang, X. Growth of Rutile Titanium Dioxide Nanowires by Pulsed Chemical Vapor Deposition. *Cryst. Growth Des.* **2011**, *11*, 949–954.
- (62) Shang, Z. G.; Liu, Z. Q.; Shang, P. J.; Shang, J. K. Synthesis of Single-Crystal TiO₂ Nanowire Using Titanium Monoxide Powder by Thermal Evaporation. *J. Mater. Sci. Technol.* **2012**, *28*, 385–390.
- (63) Wagner, R. S.; Ellis, W. C. Vapor-Liquid-Solid Mechanism of Single Crystal Growth. *Appl. Phys. Lett.* **1964**, *4*, 89–90.
- (64) Wu, J.; Wu, W.; Shih, H. C. Characterization of Single-Crystalline TiO₂ Nanowires Grown by Thermal Evaporation. *J. Electrochem. Soc.* **2005**, *152(8)*, G613-G616.
- (65) Amin, S. S.; Nicholls, A. W.; Xu, T. T. A Facile Approach to Synthesize Single-Crystalline Rutile TiO₂ One-Dimensional Nanostructures. *Nanotechnology* **2007**, *18*, 445609 (1–5).
- (66) Dupuis, A.; Jodin, L.; Rouvière, E. Catalytic Growth of TiO₂ Nanowires from a TiN Thin Film. *Appl. Surf. Sci.* **2006**, *253*, 1227–1235.
- (67) Wang, C.; Chen, J.; Wang, L.; Kang, Y.; Li, D.; Zhou, F. Single Crystal TiO₂ Nanorods: Large-Scale Synthesis and Field Emission. *Thin Solid Films* **2012**, *520*, 5036–5041.
- (68) Kim, M. H.; Baik, J. M.; Zhang, J.; Larson, C.; Li, Y.; Stucky, G. D.; Moskovits, M.; Wodtke, A. M. TiO₂ Nanowire Growth Driven by Phosphorus-Doped Nanocatalysis. *J. Phys. Chem. C* **2010**, *114*, 10697–10702.
- (69) Park, J.; Ryu, Y.; Kim, H.; Yu, C. Simple and Fast Annealing Synthesis of Titanium Dioxide Nanostructures and Morphology Transformation during Annealing Processes. *Nanotechnology* **2009**, *20*, 105608.

- (70) Jung, Y.; Jee, S.; Lee, J. Effect of Oxide Thickness on the Low Temperature (≤ 400 °C) Growth of Cone-Shaped Silicon Nanowires. *J. Appl. Phys.* **2007**, *102*, 046102.
- (71) Rahman, M. A.; Bazargan, S.; Srivastava, S.; Wang, X.; Abd-Ellah, M.; Thomas, J. P.; Heinig, N. F.; Pradhan, D.; Leung, K. T. Defect-Rich Decorated TiO₂ Nanowires for Super-Efficient Photoelectrochemical Water Splitting Driven by Visible Light. *Energy Environ. Sci.* **2015**, *8*, 3363–3373.
- (72) Mahanti, M.; Basak, D. Enhanced Emission Properties of Au/SiO₂/ZnO Nanorod Layered Structure: Effect of SiO₂ Spacer Layer and Role of Interfacial Charge Transfer. *RSC Adv.* **2014**, *4*, 15466–15473.
- (73) Application note. Temperature-Dependent Phase Transitions of ZrO₂. *Mater. Des.* **2009**, 1–4.
- (74) Li, P.; Chen, I.; Penner-hahn, J. E. Effect of Dopants on Zirconia Stabilization-An X-Ray Absorption Study: III, Charge-Compensating Dopants. *J. Am. Ceram. Soc.* **1994**, *77*, 1289–1295.
- (75) Bokhimi, X.; Morales, A.; Garcia-Ruiz, A.; Xiao, T. D.; Chen, H.; Strutt, P. R. Transformation of Yttrium-Doped Hydrated Zirconium into Tetragonal and Cubic Nanocrystalline Zirconia. *J. Solid State Chem.* **1999**, *142*, 409–418.
- (76) Gallino, F.; Valentin, C. Di; Pacchioni, G. Band Gap Engineering of Bulk ZrO₂ by Ti Doping. *Phys. Chem. Chem. Phys.* **2011**, *13*, 17667–17675.
- (77) Tanabe, K.; Yamaguchi, T. Acid-Base Bifunctional Catalysis by ZrO₂ and Its Mixed Oxides. *Catal. Today* **1994**, *20*, 185–198.
- (78) Charpentier, P.; Fragnaud, P.; Schleich, D. M.; Gehain, E. Preparation of Thin Film SOFCs Working at Reduced Temperature. *Solid State Ionics* **2000**, *135*, 373–380.
- (79) Clarke, D. R.; Levi, C. G. Materials Design for the next Generation Thermal Barrier Coatings. *Annu. Rev. Mater. Res.* **2003**, *33*, 383–417.
- (80) Meldrum, A.; Boatner, L. A.; Ewing, R. C. Nanocrystalline Zirconia Can Be Amorphized by Ion Irradiation. *Phys. Rev. Lett.* **2002**, *88*, 255031–255034.
- (81) Fiorentini, V.; Gulleri, G. Theoretical Evaluation of Zirconia and Hafnia as Gate Oxides for Si Microelectronics. *Phys. Rev. Lett.* **2002**, *89*, 266101.

- (82) Walter, E. J.; Lewis, S. P.; Rappe, A. M. First Principles Study of Carbon Monoxide Adsorption on Zirconia-Supported Copper. *Surf. Sci.* **2001**, *495*, 44–50.
- (83) Jiang, H.; Gomez-Abal, R. I.; Rinke, P.; Scheffler, M. Electronic Band Structure of Zirconia and Hafnia Polymorphs from the GW Perspective. *Phys. Rev. B Phys.* **2010**, *81*, 1–9.
- (84) Han, X. X.; Zhou, R. X.; Yue, B. H.; Zheng, X. M. Selective Hydrogenation of Cinnamaldehyde over Pt/ZrO₂ Catalyst Modified by Cr, Mn, Fe, Co and Ni. *Catal. Letters* **2006**, *109*, 157–161.
- (85) Kustov, A. L.; Rasmussen, S. B.; Fehrmann, R.; Simonsen, P. Activity and Deactivation of Sulphated TiO₂- and ZrO₂-Based V, Cu, and Fe Oxide Catalysts for NO Abatement in Alkali Containing Flue Gases. *Appl. Catal. B Environ.* **2007**, *76*, 9–14.
- (86) De Resende, V. G.; Legorreta Garcia, F.; Peigney, A.; De Grave, E.; Laurent, C. Synthesis of Fe-ZrO₂ Nanocomposite Powders by Reduction in H₂ of a Nanocrystalline (Zr, Fe)O₂ Solid Solution. *J. Alloys Compd.* **2009**, *471*, 204–210.
- (87) Xiao, M.; Li, Y.; Lu, Y.; Ye, Z. Synthesis of ZrO₂:Fe Nanostructures with Visible-Light Driven H₂ Evolution Activity. *J. Mater. Chem. A* **2015**, *3*, 2701–2706.
- (88) Ward, D. A.; Ko, E. I. Synthesis and Structural Transformation of Zirconia Aerogels. *Chem. Mater.* **1993**, *5*, 956–969.
- (89) Kundu, D.; Ganguli, D. Monolithic Zirconia Gels from Metal-organic Solutions. *J. Mater. Sci. Lett.* **1986**, *5*, 293–295.
- (90) Yoldas, B. E. Zirconium Oxides Formed by Hydrolytic Condensation of Alkoxides and Parameters That Affect Their Morphology. *J. Mater. Sci.* **1986**, *21*, 1080–1086.
- (91) Fisica, C.; Chimica, D.; Venezia, U.; Larga, C.; Dd, S. M. Preparation and Structural Characterization of Ultrafine Zirconia Powders. **1989**, *69*, 0–2.
- (92) Srinivasan, R.; Simpson, S. Discrepancies in the Crystal Structures Assigned to Precipitated Zirconia. *J. Mater. Sci. Lett.* **1991**, *10*, 352–354.
- (93) Woudenberg, F. C. M.; Sager, W. F. C.; Elshof, J. E.; Verweij, H. Nanostructured Dense ZrO₂ Thin Films from Nanoparticles Obtained by Emulsion Precipitation. **2004**, *1435*, 1430–1435.
- (94) Tahir, M. N.; Gorgishvili, L.; Li, J.; Gorelik, T.; Kolb, U.; Nasdala, L.; Tremel, W. Facile

- Synthesis and Characterization of Monocrystalline Cubic ZrO₂ Nanoparticles. *Solid State Sci.* **2007**, *9*, 1105–1109.
- (95) Scholz, S.; Kaskel, S. Surface Functionalization of ZrO₂ Nanocrystallites for the Integration into Acrylate Nanocomposite Films. *J. Colloid Interface Sci.* **2008**, *323*, 84–91.
- (96) Duc Huy, L.; Laffez, P.; Daniel, P.; Jouanneaux, A.; The Khoi, N.; Siméone, D. Structure and Phase Component of ZrO₂ Thin Films Studied by Raman Spectroscopy and X-Ray Diffraction. *Mater. Sci. Eng. B* **2003**, *104*, 163–168.
- (97) Thomas, R.; Milanov, A.; Bhakta, R.; Patil, U.; Winter, M.; Ehrhart, P.; Waser, R.; Devi, A. Liquid-Injection MOCVD of ZrO₂ Thin Films Using Zirconium Bis(diethylamido)-Bis(di-Tert-Butylmalonato) as a Novel Precursor. *Chem. Vap. Depos.* **2006**, *12*, 295–300.
- (98) Hausmann, D. M.; Gordon, R. G. Surface Morphology and Crystallinity Control in the Atomic Layer Deposition (ALD) of Hafnium and Zirconium Oxide Thin Films. *J. Cryst. Growth* **2003**, *249*, 251–261.
- (99) Kuratani, K.; Mizuhata, M.; Kajinami, A.; Deki, S. Synthesis and Luminescence Property of Eu³⁺/ZrO₂ Thin Film by the Liquid Phase Deposition Method. *J. Alloys Compd.* **2006**, *408-412*, 711–716.
- (100) Kotlyarchuk, B. K.; Popovych, D. I.; Savchuk, V. K.; Serednycki, A. S.; Pulsed Laser Deposition of ZrO₂ Thin Films for Application in Microelectronic Devices. *Physics and Chemistry of Solid State*, **2003**, *3*, 434–439.
- (101) Chu, S.; Wada, K.; Inoue, S.; Segawa, H. Direct Growth of Highly Ordered Crystalline Zirconia Nanowire Arrays with High Aspect Ratios on Glass by a Tailored Anodization. *J. Electrochem. Soc.* **2011**, *158*, C148-C157.
- (102) Tsai, M. C.; Lin, G. T.; Chiu, H. T.; Lee, C. Y. Synthesis of Zirconium Dioxide Nanotubes, Nanowires, and Nanocables by Concentration Dependent Solution Deposition. *J. Nanoparticle Res.* **2008**, *10*, 863–869.
- (103) Liao, L.; Bai, J.; Lin, Y.; Qu, Y.; Huang, Y.; Duan, X. High-Performance Top-Gated Graphene-Nanoribbon Transistors Using Zirconium Oxide Nanowires as High-Dielectric-Constant Gate Dielectrics. *Adv. Mater.* **2010**, *22*, 1941–1945.
- (104) Bauer, T. Thermophotovoltaics. Basic Principles and Critical Aspects of System Design.

Springer, Berlin 2011.

- (105) Zeng, J. N.; Low, J. K.; Ren, Z. M.; Liew, T.; Lu, Y. F. Effect of Deposition Conditions on Optical and Electrical Properties of ZnO₂ Films Prepared by Pulsed Laser Deposition. *Appl. Surf. Sci.* **2002**, *198*, 362–367.
- (106) Wang, H.; Wei, J.; Xiong, R.; Shi, J. Enhanced Ferromagnetic Properties of Fe+N Codoped TiO₂ Anatase. *J. Magn. Magn. Mater.* **2012**, *324*, 2057–2061.
- (107) Hong, N. H.; Park, C.; Raghavender, A.; Ruyter, A.; Chikoidze, E.; Dumont, Y. High Temperature Ferromagnetism in Cubic Mn-Doped ZrO₂ Thin Films. *J. Magn. Magn. Mater.* **2012**, *324*, 3013–3016.
- (108) Dietl, T. A Ten-Year Perspective on Dilute Magnetic Semiconductors and Oxides. *Nat. Mater.* **2010**, *9*, 965–974.
- (109) Durst, A. C.; Bhatt, R. N.; Wolff, P. A. Bound Magnetic Polaron Interactions in Insulating Doped Diluted Magnetic Semiconductors. *Phys. Rev. B* **2001**, *65*, 235205.
- (110) Dietl, T. Origin of Ferromagnetic Response in Diluted Magnetic Semiconductors and Oxides. *J. Phys. Condens. Matter* **2007**, *19*, 19.
- (111) Enkovaara, J.; Heczko, O.; Ayuela, A.; Nieminen, R. M. Coexistence of Ferromagnetic and Antiferromagnetic Order in Mn-Doped Ni₂MnGa. *Phys. Rev. B* **2003**, *67*, 212405.
- (112) Buschow, K.H.J. (Eds.). Handbook of Magnetic Materials. *Elsevier, Amsterdam* **2002**, *14*, 1–87.
- (113) Bauer, G.; Pascher, H.; Zawadzki, W. Magneto-Optical Properties of Semimagnetic Lead Chalcogenides. *Semicond. Sci. Technol.* **1999**, *7*, 703–723.
- (114) Prellier, W.; Fouchet, A.; Mercey, B. Oxide-Diluted Magnetic Semiconductors: A Review of the Experimental Status. *J. Phys. Condens. Matter* **2003**, *15*, R1583–R1601.
- (115) Ohno, H. Making Nonmagnetic Semiconductors Ferromagnetic. *Science*. **1998**, *281*, 951–956.
- (116) Wang, K. Y.; Campion, R. P.; Edmonds, K. W.; Sawicki, M.; Dietl, T.; Foxon, C. T.; Gallagher, B. L. Magnetism in (Ga, Mn)As Thin Films With T_c Up To 173K. *AIP Conf. Proc.* **2005**, *772*, 333.
- (117) Dietl, T. Zener Model Description of Ferromagnetism in Zinc-Blende Magnetic

- Semiconductors. *Science*. **2000**, *287*, 1019–1022.
- (118) Sato, K.; Katayama-Yoshida, H. Material Design for Transparent Ferromagnets with ZnO-Based Magnetic Semiconductors. *Japanese J. Appl. Physics*, **2000**, *39*, 555–558.
- (119) Schwartz, D. A.; Norberg, N. S.; Nguyen, Q. P.; Parker, J. M.; Gamelin, D. R. Magnetic Quantum Dots: Synthesis, Spectroscopy, and Magnetism of Co²⁺- and Ni²⁺-Doped ZnO Nanocrystals. *J. Am. Chem. Soc.* **2003**, *125*, 13205–13218.
- (120) Matsumoto, Y.; Murakami, M.; Shono, T.; Hasegawa, T.; Fukumura, T.; Kawasaki, M.; Ahmet, P.; Chikyow, T.; Koshihara, S.; Koinuma, H. Room-Temperature Ferromagnetism in Transparent Transition Metal-Doped Titanium Dioxide. *Science* **2001**, *291*, 854–856.
- (121) Janisch, R.; Gopal, P.; Spaldin, N. A. Transition Metal-Doped TiO₂ and ZnO—present Status of the Field. *J. Phys. Condens. Matter* **2005**, *17*, R657–R689.
- (122) Hong, N. H.; Sakai, J.; Prellier, W.; Hassini, A.; Ruyter, A.; Gervais, F. Ferromagnetism in Transition-Metal-Doped TiO₂ Thin Films. *Phys. Rev. B* **2004**, *70*, 195204.
- (123) Hong, N. H.; Sakai, J.; Huong, N. T.; Ruyter, A.; Brizé, V. Magnetism in Transition-Metal-Doped In₂O₃ Thin Films. *J. Phys. Condens. Matter* **2006**, *18*, 6897–6905.
- (124) Hong, N. H.; Sakai, J.; Hassini, A. Magnetism in V-Doped ZnO Thin Films. *J. Phys. Condens. Matter* **2005**, *17*, 199–204.
- (125) Hong, N. H.; Brizé, V.; Sakai, J. Mn-Doped ZnO and (Mn, Cu)-Doped ZnO Thin Films: Does the Cu Doping Indeed Play a Key Role in Tuning the Ferromagnetism? *Appl. Phys. Lett.* **2005**, *86*, 082505.
- (126) Das Pemmaraju, C.; Sanvito, S. Ferromagnetism Driven by Intrinsic Point Defects in HfO₂. *Phys. Rev. Lett.* **2005**, *94*, 4–7.
- (127) Yano, J.; Yachandra, V. K. X-Ray Absorption Spectroscopy. *Photosynth. Res.* **2009**, *102*, 241–254.
- (128) Carra, P.; Thole, B. T.; Altarelli, M.; Wang, X. X-Ray Circular Dichroism and Local Magnetic Fields. *Phys. Rev. Lett.* **1993**, *70*, 694–697.
- (129) Hong, N. H.; Baria, A.; Sakai, J.; Huong, N. Q. Can Undoped Semiconducting Oxides Be Ferromagnetic? *Phys. Stat. Sol. (c)* **2007**, *4*, 4461–4466.

- (130) Barla, A.; Schmerber, G.; Beaurepaire, E.; Dinia, A.; Bieber, H.; Colis, S.; Scheurer, F.; Kappler, J.; Imperia, P.; Nolting, F.; *et al.* Paramagnetism of the Co Sublattice in Ferromagnetic $Zn_{1-x}Co_xO$ films. *Phys. Rev. B* **2007**, *76*, 125201.
- (131) Hong, N. H.; Sakai, J.; Huong, N. T.; Poirot, N.; Ruyter, A. Role of Defects in Tuning Ferromagnetism in Diluted Magnetic Oxide Thin Films. *Phys. Rev. B* **2005**, *72*, 045336.
- (132) Hong, N. H.; Sakai, J.; Poirot, N.; Brizé, V. Room-Temperature Ferromagnetism Observed in Undoped Semiconducting and Insulating Oxide Thin Films. *Phys. Rev. B* **2006**, *73*, 132404.
- (133) Maca, F.; Kudrnovsky, J.; Drchal, V.; Bouzerar, G. Magnetism without Magnetic Impurities in Oxides ZrO_2 and TiO_2 . *Phil. Mag.* **2008**, *88*, 2755–2764.
- (134) Xu, X.; Xu, C.; Dai, J.; Hu, J.; Li, F.; Zhang, S. Size Dependence of Defect-Induced Room Temperature Ferromagnetism in Undoped ZnO Nanoparticles. *J. Phys. Chem. C* **2012**, *116*, 8813–8818.
- (135) Santara, B.; Giri, P. K.; Imakita, K.; Fujii, M. Evidence of Oxygen Vacancy Induced Room Temperature Ferromagnetism in Solvothermally Synthesized Undoped TiO_2 Nanoribbons. *Nanoscale* **2013**, *5*, 5476–5488.
- (136) Meng, F.; Zhang, C.; Fan, Z.; Gong, J.; Li, A.; Ding, Z.; Tang, H.; Zhang, M.; Wu, G. Hydrothermal Synthesis of Hexagonal CeO_2 Nanosheets and Their Room Temperature Ferromagnetism. *J. Alloys Compd.* **2015**, *647*, 1013–1021.
- (137) Hong, N. H.; Sakai, J.; Brizé, V. Observation of Ferromagnetism at Room Temperature in ZnO Thin Films. *J. Phys. Condens. Matter* **2007**, *19*, 036219.
- (138) Venkatesan, M.; Fitzgerald, C. B.; Coey, J. M. D. Thin Films: Unexpected Magnetism in a Dielectric Oxide. *Nature* **2004**, *430*, 630.
- (139) Schwartz, D. A.; Gamelin, D. R. Reversible 300 K Ferromagnetic Ordering in a Diluted Magnetic Semiconductor. *Adv. Mater.* **2004**, *16*, 2115–2119.
- (140) Zhan, P.; Wang, W.; Liu, C.; Hu, Y.; Li, Z.; Zhang, Z.; Zhang, P.; Wang, B.; Cao, X. Oxygen Vacancy-Induced Ferromagnetism in Un-Doped ZnO Thin Films. *J. Appl. Phys.* **2012**, *111*.
- (141) Kaminski, A.; Das Sarma, S. Polaron Percolation in Diluted Magnetic Semiconductors. *Phys. Rev. Lett.* **2002**, *88*, 247202.

- (142) Bhatt, R. N.; Berciu, M.; Kennett, M. P.; Wan, X. Diluted Magnetic Semiconductors in the Low Carrier Density Regime. *J. Supercond.* **2001**, *15*, 10.
- (143) Farvid, S. S.; Sabergharesou, T.; Hutfluss, L. N.; Hegde, M.; Prouzet, E.; Radovanovic, P. V. Evidence of Charge-Transfer Ferromagnetism in Transparent Diluted Magnetic Oxide Nanocrystals: Switching the Mechanism of Magnetic Interactions. *J. Am. Chem. Soc.* **2014**, *136*, 7669–7679.
- (144) Dietl, T.; Spałek, J. Effect of Thermodynamic Fluctuations of Magnetization on the Bound Magnetic Polaron in Dilute Magnetic Semiconductors. *Phys. Rev. B* **1983**, *28*, 1548–1563.
- (145) Kasuya, T. Stability Condition for Molecular Magnetic Polaron. *Solid State Commun.* **1976**, *18*, 51–53.
- (146) Coey, J. M. D.; Wongsaprom, K.; Alaria, J.; Venkatesan, M. Charge-Transfer Ferromagnetism in Oxide Nanoparticles. *J. Phys. D. Appl. Phys.* **2008**, *41*, 134012.
- (147) Hybler, G. K. Pulsed Laser Deposition. *MRS Bull.* **1992**, *17*, 26–29.
- (148) W. Kern. *Handbook of Semiconductor Wafer Cleaning Technology*; Andrew, William, Norwich, NY, 1993.
- (149) Abràmoff, M. D.; Magalhães, P. J.; Ram, S. J. Image Processing with ImageJ Part II. *Biophotonics Int.* **2005**, *11*, 36–43.
- (150) Goldstein, J. I.; Newbury, D. E.; Echlin, P.; Joy, D. C.; Roming, A.D.J.; Lyman, C. E.; Fiori, C.; LifShin, E. Scanning Electron Microscopy and X-Ray Microanalysis: A text for biologist, Material Scientists and Geologists, 2nd ed., *Plenum Press, New York*, **1992**, p 820.
- (151) Joy, D. C. Scanning He⁺ Ion Beam Microscopy and Metrology. *AIP Conf. Proc.* **2011**, *1395*, 80–84.
- (152) Joy, D. C. Helium Ion Microscopy - Principles and Applications. *Springer*; **2013**.
- (153) Williams, D. B.; Carter, C. B. Transmission Electron Microscopy: A Textbook for Materials Science. *Springer, New York* **1949**.
- (154) L200 Motorised Objective Aperture: Fast and Comfortable Control of the Objective Aperture with the L200 Motorised Objective Aperture.
(http://www.zeiss.com/microscopy/en_de/products/scanning-electron-

microscopes/upgrades/motorised-objective-aperture.html)

- (155) Williams, D. B.; Carter, C. B. Transmission Electron Microscopy: A Textbook for Materials Science. *Springer, New York* **1949**.
- (156) Warren, B. E. X - Ray Diffraction. *Dover Publications, INC., New York*, **1969**.
- (157) Kimura, M. X-Ray Evanescent Diffraction: Application to Metal Surfaces. *Rigaku J.* **1999**, *16*, 25–31.
- (158) Delchar, T. A.; Woodruff, D. P. Modern Techniques of Surface Science. *Cambridge University Press*. **1994**.
- (159) Wanger, C. D.; Riggs, W. M.; Davis, L. E.; Moulder, J. F.; Handbook of X - Ray Photoelectron Spectroscopy, *Physical Electronics Division, Eden Prairie, Minnesota, USA*, **1979**.
- (160) K. Siegbahn, C. Nording, A. Fahlman, R. Nordberg, K. Hamrin, J. Hedman, G. Johansson, T. Bergmark, S.-E. Karlsson, I. Lindgren, B. L. ESCA—Atomic, Molecular and Solid State Structure Studied by Means of Electron Spectroscopy. *Nov. Acta Regiae Soc. Sci. Ups. Revis. Ed. Prep. Almqvist & Wiksells*, **1967**.
- (161) Bard A. J.; Faulkner, L. R. J. Electrochemical Methods : Fundamentals and Applications, 2nd ed. *New York, Wiley*, **2000**.
- (162) Xu, J.; Calaprice, F.; Galbiati, C.; Goretti, A.; Guray, G.; Hohman, T.; Holtz, D.; Ianni, A.; Laubenstein, M.; Loer, B.; *et al.* A Study of the Trace ³⁹Ar Content in Argon from Deep Underground Sources. *Astropart. Phys.* **2015**, *66*, 53–60.
- (163) Barsoukov, E.; Macdonald, J. R. Impedance Spectroscopy. *John Wiley & Sons, Inc.* **2005**.
- (164) Rodrigues, S.; Munichandraiah, N.; Shukla, A. K. Review of State-of-Charge Indication of Batteries by Means of A.C. Impedance Measurements. *J. Power Sources* **2000**, *87*, 12–20.
- (165) Lasia, A. Electrochemical Impedance Spectroscopy and Its Applications, Modern Aspects of Electrochemistry. *Plenum Press, New York* **1999**, *32*, 143–248.
- (166) van der Pauw L. J. A method of measuring specific resistivity and Hall Effect of discs of arbitrary shape, *Philips Res. Rep.* **1958**, *13*, 1-9.
- (167) Amalric Popescu, D.; Herrmann, J.; Ensuque, A.; Bozon-Verduraz, F. Nanosized Tin Dioxide:

- Spectroscopic (UV–VIS, NIR, EPR) and Electrical Conductivity Studies. *Phys. Chem. Chem. Phys.* **2001**, *3*, 2522–2530.
- (168) Clarke, J.; Braginski, A. (Eds.). The SQUID Handbook. Vol. II: Applications of SQUIDS and SQUID Systems; *WILEY-VCH Verlag GmbH & Co. KGaA, Weinheim*, **2006**.
- (169) Ni, M.; Leung, M. K. H.; Leung, D. Y. C.; Sumathy, K. A Review and Recent Developments in Photocatalytic Water-Splitting Using TiO₂ for Hydrogen Production. *Renew. Sustain. Energy Rev.* **2007**, *11*, 401–425.
- (170) Hoang, S.; Guo, S.; Hahn, N. T.; Bard, A. J.; Mullins, C. B. Visible Light Driven Photoelectrochemical Water Oxidation on Nitrogen-Modified TiO₂ Nanowires. *Nano Lett.* **2012**, *12*, 26–32.
- (171) Pu, Y.; Wang, G.; Chang, K.; Ling, Y.; Lin, Y.; Fitzmorris, B. C.; Liu, C.; Lu, X.; Tong, Y.; Zhang, J. Z.; *et al.* Au Nanostructure-Decorated TiO₂ Nanowires Exhibiting Photoactivity across Entire UV-Visible Region for Photoelectrochemical Water Splitting. *Nano Lett.* **2013**, *13*, 3817–3823.
- (172) Hwang, Y. J.; Hahn, C.; Liu, B.; Yang, P. Photoelectrochemical Properties of TiO₂ Nanowire Arrays : A Study of the Dependence on Length and Atomic Layer Deposition Coating. *ACS Nano* **2012**, *6*, 5060–5069.
- (173) Ghicov, A.; Schmuki, P. Self-Ordering Electrochemistry: A Review on Growth and Functionality of TiO₂ Nanotubes and Other Self-Aligned MO(x) Structures. *Chem. Commun.* **2009**, 2791–2808.
- (174) Luo, Z.; Yang, W.; Peng, A.; Zeng, Y.; Yao, J. The Fabrication of TiO₂ Nanorods from TiO₂ Nanoparticles by Organic Protection Assisted Template Method. *Nanotechnology* **2009**, *20*, 345601.
- (175) Riss, A.; Elser, M. J.; Bernardi, J.; Diwald, O. Stability and Photoelectronic Properties of Layered Titanate Nanostructures. *J. Am. Chem. Soc.* **2009**, *131*, 6198–6206.
- (176) Wu, J.; Lo, S.; Song, K.; Vijayan, B. K.; Li, W.; Gray, K. A.; Dravid, V. P. Growth of Rutile TiO₂ Nanorods on Anatase TiO₂ Thin Films on Si-Based Substrates. *J. Mater. Res.* **2011**, *26*, 1646–1652.
- (177) Lau, M.; Dai, L.; Bosnick, K.; Evoy, S. Synthesis and Characterization of TiO_x Nanowires

- Using a Novel Silicon Oxide Support Layer. *Nanotechnology* **2009**, *20*, 025602.
- (178) Wu, J.; Shih, H. C.; Wu, W. Growth of TiO₂ Nanorods by Two-Step Thermal Evaporation. *J. Vac. Sci. Technol. B* **2005**, *23*, 2122.
- (179) Wu, J.; Shih, H. C.; Wu, W. Formation and Photoluminescence of Single-Crystalline Rutile TiO₂ Nanowires Synthesized by Thermal Evaporation. *Nanotechnology* **2006**, *17*, 105–109.
- (180) Chen, C. A.; Chen, Y. M.; Korotcov, A.; Huang, Y. S.; Tsai, D. S.; Tiong, K. K. Growth and Characterization of Well-Aligned Densely-Packed Rutile TiO₂ Nanocrystals on Sapphire Substrates via Metal-Organic Chemical Vapor Deposition. *Nanotechnology* **2008**, *19*, 075611.
- (181) Kolen'ko, Y. V.; Kovnir, K. A.; Gavrillov, A. I.; Garshev, A. V.; Frantti, J.; Lebedev, O. I.; Churagulov, B. R.; Van Tendeloo, G.; Yoshimura, M. Hydrothermal Synthesis and Characterization of Nanorods of Various Titanates and Titanium Dioxide. *J. Phys. Chem. B* **2006**, *110*, 4030–4038.
- (182) Hossain, F. M.; Murch, G. E.; Sheppard, L.; Nowotny, J. The Effect of Defect Disorder on the Electronic Structure of Rutile TiO_{2-x}. *Defect Diffus. Forum* **2006**, *251-252*, 1–12.
- (183) Bazargan, S.; Leung, K. T. Catalyst-Assisted Pulsed Laser Deposition of One-Dimensional Single-Crystalline Nanostructures of Tin(IV) Oxide: Interplay of VS and VLS Growth Mechanisms at Low Temperature. *J. Phys. Chem. C* **2012**, *116*, 5427–5434.
- (184) Sohn, Y.; Pradhan, D.; Radi, A.; Leung, K. T. Interfacial Electronic Structure of Gold Nanoparticles on Si(100): Alloying versus Quantum Size Effects. *Langmuir* **2009**, *25*, 9557–9563.
- (185) Zu, B.; Dai, R.; Pan, Z. W.; Wang, Z. L. Novel Nanostructures of Functional Oxides Synthesized by Thermal Evaporation. *Adv. Funct. Mater.* **2003**, *13*, 9–24.
- (186) Morales, A. M.; Lieber C. M. A Laser Ablation Method for the Synthesis of Crystalline Semiconductor Nanowires. *Science*. **1998**, *279*, 208–211.
- (187) Ross, F. M.; Tersoff, J.; Reuter, M. C. Sawtooth Faceting in Silicon Nanowires. *Phys. Rev. Lett.* **2005**, *95*, 146104.
- (188) Chen, J.; Pan, Y.; Wu, R. Growth Mechanism of Twinned SiC Nanowires Synthesized by a Simple Thermal Evaporation Method. *Phys. E Low-dimensional Syst. Nanostructures* **2010**, *42*, 2335–2340.

- (189) Glushenkov, A. M.; Zhang, H.; Zou, J.; Lu, G. Q.; Chen, Y. Unusual Corrugated Nanowires of Zinc Oxide. *J. Cryst. Growth* **2008**, *310*, 3139–3143.
- (190) Chang, J.; Young, T.; Yang, Y.; Ueng, H.; Chang, T. Silicide Formation of Au Thin Films on (100) Si during Annealing. *Mater. Chem. Phys.* **2004**, *83*, 199–203.
- (191) Miyata, N.; Watanabe, H.; Ichikawa, M. Thermal Decomposition of an Ultrathin Si Oxide Layer around a Si(001)-(2 x 1) Window. *Phys. Rev. Lett.* **2000**, *84*, 1043–1046.
- (192) Watanabe, H.; Fujita, K.; Ichikawa, M. Thermal Decomposition of Ultrathin Oxide Layers on Si(111) Surfaces Mediated by Surface Si Transport. *Appl. Phys. Lett.* **1997**, *70*, 1095.
- (193) Liehr, M.; Dallaporta, H.; Lewis, J. E. Defect Formation in SiO₂/Si(100) by Metal Diffusion and Reaction. *Appl. Phys. Lett.* **1988**, *53*, 589–591.
- (194) Chen, X.; Liu, L.; Liu, Z.; Marcus, M. A.; Wang, W.; Oyler, N. A.; Grass, M. E.; Mao, B.; Glans, P.; Yu, P. Y.; *et al.* Properties of Disorder-Engineered Black Titanium Dioxide Nanoparticles through Hydrogenation. *Sci. Rep.* **2013**, *3*, 1510.
- (195) Thombare, S. V.; Marshall, A. F.; McIntyre, P. C. Kinetics of Germanium Nanowire Growth by the Vapor-Solid-Solid Mechanism with a Ni-Based Catalyst. *APL Mater.* **2013**, *1*, 061101 (1–7).
- (196) Kodambaka, S.; Tersoff, J.; Reuter, M. C.; Ross, F. M. Germanium Nanowire Growth below the Eutectic Temperature. *Science* **2007**, *316*, 729–732.
- (197) Matsuki, Y.; Inamura, T.; Wakashima, K.; Hosoda, H. Effects of Aging on Phase Constitution, Lattice Parameter and Mechanical Properties of Ti-4 mol% Au Near-Eutectoid Alloy. *Mater. Trans.* **2007**, *48*, 385–389.
- (198) Lee, J.; Park, K.; Kim, T.; Choi, H.; Sung, Y. Controlled Growth of High-Quality TiO₂ Nanowires on Sapphire and Silica. *Nanotechnology* **2006**, *17*, 4317–4321.
- (199) Teleki, A.; Pratsinis, S. E. Blue Nano Titania Made in Diffusion Flames. *Phys. Chem. Chem. Phys.* **2009**, *11*, 3742–3747.
- (200) Li, M.; Hebenstreit, W.; Diebold, U.; Tyryshkin, A. M.; Bowman, M. K.; Dunham, G. G.; Henderson, M. A. The Influence of the Bulk Reduction State on the Surface Structure and Morphology of Rutile TiO₂ (110) Single Crystals. *J. Phys. Chem. B* **2000**, *2*, 4944–4950.

- (201) Su, J.; Zou, X.; Chen, J. Self-Modification of Titanium Dioxide Materials by Ti^{3+} And/or Oxygen Vacancies: New Insights into Defect Chemistry of Metal Oxides. *RSC Adv.* **2014**, *4*, 13979–13988.
- (202) Hashimoto, S.; Tanaka, A. Alteration of Ti 2p XPS Spectrum for Titanium Oxide by Low-Energy Ar Ion Bombardment. *Surf. Interface Anal.* **2002**, *34*, 262–265.
- (203) Mizuno, Y.; King, F. K.; Yamauchi, Y.; Homma, T.; Tanaka, A.; Takakuwa, Y.; Momose, T. Temperature Dependence of Oxide Decomposition on Titanium Surfaces in Ultrahigh Vacuum. *J. Vac. Sci. Technol. A* **2002**, *20*, 1716.
- (204) Chiodi, M.; Cavaliere, E.; Kholmanov, I.; de Simone, M.; Sakho, O.; Cepek, C.; Gavioli, L. Nanostructured TiO_x Film on Si Substrate: Room Temperature Formation of $TiSi_x$ Nanoclusters. *J. Nanoparticle Res.* **2010**, *12*, 2645–2653.
- (205) Choi, H.; Kang, M. Hydrogen Production from Methanol/water Decomposition in a Liquid Photosystem Using the Anatase Structure of Cu Loaded TiO_2 . *Int. J. Hydrogen Energy* **2007**, *32*, 3841–3848.
- (206) Kuscer, D.; Kovač, J.; Kosec, M.; Andriesen, R. The Effect of the Valence State of Titanium Ions on the Hydrophilicity of Ceramics in the Titanium–oxygen System. *J. Eur. Ceram. Soc.* **2008**, *28*, 577–584.
- (207) Hwang, Y. J.; Boukai, A.; Yang, P. High Density n-Si/n- TiO_2 Core/Shell Nanowire Arrays with Enhanced Photoactivity. *Nano Lett.*, **2009**, *9(1)*, 410–415.
- (208) Cho, I. S.; Chen, Z.; Forman, A. J.; Kim, D. R.; Rao, P. M.; Jaramillo, T. F.; Zheng, X. Branched TiO_2 Nanorods for Photoelectrochemical Hydrogen Production. *Nano Lett.* **2011**, *11*, 4978–4984.
- (209) Yu, Y.; Yin, X.; Kvit, A.; Wang, X. Evolution of Hollow TiO_2 Nanostructures via the Kirkendall Effect Driven by Cation Exchange with Enhanced Photoelectrochemical Performance. *Nano Lett.* **2014**, *14*, 2528–2535.
- (210) Chen, K.; Feng, X.; Hu, R.; Li, Y.; Xie, K.; Li, Y.; Gu, H. Effect of Ag Nanoparticle Size on the Photoelectrochemical Properties of Ag Decorated TiO_2 Nanotube Arrays. *J. Alloys Compd.* **2013**, *554*, 72–79.
- (211) Cho, I. S.; Logar, M.; Lee, C. H.; Cai, L.; Prinz, F. B.; Zheng, X. Rapid and Controllable

- Flame Reduction of TiO₂ Nanowires for Enhanced Solar Water-Splitting. *Nano Lett.* **2014**, *14*, 24–31.
- (212) Walter, M. G.; Warren, E. L.; McKone, J. R.; Boettcher, S. W.; Mi, Q.; Santori, E. A.; Lewis, N. S. Solar Water Splitting Cells. *Chem. Rev.* **2010**, *110*, 6446–6473.
- (213) Fan, W.; Zhang, Q.; Wang, Y. Semiconductor-Based Nanocomposites for Photocatalytic H₂ Production and CO₂ Conversion. *Phys. Chem. Chem. Phys.* **2013**, *15*, 2632–2649.
- (214) Xu, M.; Da, P.; Wu, H.; Zhao, D.; Zheng, G. Controlled Sn-Doping in TiO₂ Nanowire Photoanodes with Enhanced Photoelectrochemical Conversion. *Nano Lett.* **2012**, *12*, 1503–1508.
- (215) Bazargan, S.; Leung, K. T. Growth of Randomly Oriented Single-Crystalline Tin (IV) Oxide Nanobelts: Control on the Predominant Crystalline Growth Axis. *J. Chem. Phys.* **2013**, *104704*, 1–9.
- (216) Li, L.; Yan, J.; Wang, T.; Zhao, Z.; Zhang, J.; Gong, J.; Guan, N. Sub-10 Nm Rutile Titanium Dioxide Nanoparticles for Efficient Visible-Light-Driven Photocatalytic Hydrogen Production. *Nat. Commun.* **2015**, *6*, 5881 (1–10).
- (217) Liu, Q.; He, J.; Yao, T.; Sun, Z.; Cheng, W.; He, S.; Xie, Y.; Peng, Y.; Cheng, H.; Sun, Y.; *et al.* Aligned Fe₂TiO₅-Containing Nanotube Arrays with Low Onset Potential for Visible-Light Water Oxidation. *Nat. Commun.* **2014**, *5*, 5122 (1–7).
- (218) Cho, I. S.; Lee, C. H.; Feng, Y.; Logar, M.; Rao, P. M.; Cai, L.; Kim, D. R.; Sinclair, R.; Zheng, X. Codoping Titanium Dioxide Nanowires with Tungsten and Carbon for Enhanced Photoelectrochemical Performance. *Nat. Commun.* **2013**, *4*, 1723 (1–10).
- (219) Agrawal, A. A.; Hastings, A. P.; Johnson, M. T. J.; Maron, J. L.; Salminen, J. Future CO₂ Emissions and Climate Change from Existing Energy Infrastructure. *Science*. **2010**, *329*, 1330–1333.
- (220) Hoffert, M. I. Climate Change. Farewell to Fossil Fuels? *Science* **2010**, *329*, 1292–1294.
- (221) Hill, J.; Nelson, E.; Tilman, D.; Polasky, S.; Tiffany, D. Environmental, Economic, and Energetic Costs and Benefits of Biodiesel and Ethanol Biofuels. *Proc. Natl. Acad. Sci. U. S. A.* **2006**, *103*, 11206–11210.
- (222) Lewis, N. S. Toward Cost-Effective Solar Energy Use. *Science*. **2007**, *315*, 798–802.

- (223) Bookbinder, D. C.; Bruce, J. A.; Dominey, R. N.; Lewis, N. S.; Wrighton, M. S. Synthesis and Characterization of a Photosensitive Interface for Hydrogen Generation: Chemically Modified P-Type Semiconducting Silicon Photocathodes. *PNAS* **1980**, *77*, 6280–6284.
- (224) Kay, A.; Cesar, I.; Grätzel, M. New Benchmark for Water Photooxidation by Nanostructured α -Fe₂O₃ Films. *J. Am. Chem. Soc.* **2006**, *128*, 15714–15721.
- (225) Reddy, V. R.; Hwang, D. W.; Lee, J. S. Photocatalytic Water Splitting over ZrO₂ Prepared by Precipitation Method. *Korean J. Chem. Eng.* **2012**, *20*, 1026–1029.
- (226) Khaselev, O.; Turner, J. A. A Monolithic Photovoltaic-Photoelectrochemical Device for Hydrogen Production via Water Splitting. *Science*, **2013**, *280*, 425–427.
- (227) Aharon-Shalom, E.; Heller, A. Efficient p-InP (Rh-H Alloy) and p-InP (Re-H Alloy) Hydrogen Evolving Photocathodes. *J. Electrochem. Soc.* **1982**, *129*, 2865–2866.
- (228) Tang, J.; Durrant, J. R.; Klug, D. R. Mechanism of Photocatalytic Water Splitting in TiO₂. Reaction of Water with Photoholes, Importance of Charge Carrier Dynamics, and Evidence for Four-Hole Chemistry. *J. Am. Chem. Soc.* **2008**, *130*, 13885–13891.
- (229) Linsebigler, A. L.; Linsebigler, A. L.; Yates Jr, J. T.; Lu, G.; Lu, G.; Yates, J. T. Photocatalysis on TiO₂ Surfaces: Principles, Mechanisms, and Selected Results. *Chem. Rev.* **1995**, *95*, 735–758.
- (230) Chen, X.; Chen, X.; Burda, C.; Burda, C. The Electronic Origin of the Visible-Light Absorption Properties of C-, N- and S-Doped TiO₂ Nanomaterials. *J. Am. Chem. Soc.* **2008**, 5018–5019.
- (231) Choi, W.; Termin, A.; Hoffmann, M. R. The Role of Metal Ion Dopants in Quantum-Sized TiO₂: Correlation between Photoreactivity and Charge Carrier Recombination Dynamics. *J. Phys. Chem.* **1994**, *98*, 13669–13679.
- (232) Bae, D.; Pedersen, T.; Seger, B.; Malizia, M.; Kuznetsov, A.; Hansen, O.; Chorkendorff, I.; Vesborg, P. C. K. Back-Illuminated Si Photocathode: A Combined Experimental and Theoretical Study for Photocatalytic Hydrogen Evolution. *Energy Environ. Sci.* **2015**, *8*, 650–660.
- (233) Hou, J.; Yang, C.; Cheng, H.; Jiao, S.; Takeda, O.; Zhu, H. High-Performance p-Cu₂O/n-TaON Heterojunction Nanorod Photoanodes Passivated with an Ultrathin Carbon Sheath for

- Photoelectrochemical Water Splitting. *Energy Environ. Sci.* **2014**, *7*, 3758–3768.
- (234) Kim, J. Y.; Magesh, G.; Youn, D. H.; Jang, J.-W.; Kubota, J.; Domen, K.; Lee, J. S. Single-Crystalline, Wormlike Hematite Photoanodes for Efficient Solar Water Splitting. *Sci. Rep.* **2013**, *3*, 2681.
- (235) Lee, J. Y.; Park, J.; Cho, J. H. Electronic Properties of N- and C-Doped TiO₂. *Appl. Phys. Lett.* **2005**, *87*, 2014–2017.
- (236) Highfield, J. Advances and Recent Trends in Heterogeneous Photo(electro)-Catalysis for Solar Fuels and Chemicals. *Molecules* **2015**, *20*, 6739–6793.
- (237) Massalski, B. T. B.; Okamoto, H.; Abriata, J. P. The Au-Zr (Gold-Zirconium) System. *Springer*, **1985**, *6*, 1328–1330.
- (238) Hisatomi, T.; Kubota, J.; Domen, K. Recent Advances in Semiconductors for Photocatalytic and Photoelectrochemical Water Splitting. *Chem. Soc. Rev.* **2014**, *43*, 7520-7535.
- (239) Ohmi, T. Total Room Temperature Wet Cleaning for Si Substrate Surface. *J. Electrochem. Soc.* **1996**, *143*, 2957–2964.
- (240) Ganduglia-Pirovano, M. V.; Hofmann, A.; Sauer, J. Oxygen Vacancies in Transition Metal and Rare Earth Oxides: Current State of Understanding and Remaining Challenges. *Surf. Sci. Rep.* **2007**, *62*, 219–270.
- (241) Hildebrandt, E.; Kurian, J.; Miller, M. M.; Schroeder, T.; Kleebe, H. J.; Alff, L. Controlled Oxygen Vacancy Induced p-Type Conductivity in HfO_{2-x} Thin Films. *Appl. Phys. Lett.* **2011**, *99*, 4.
- (242) Tsukazaki, A.; Ohtomo, A.; Onuma, T.; Ohtani, M.; Makino, T.; Sumiya, M.; Ohtani, K.; Chichibu, S. F.; Fuke, S.; Segawa, Y.; *et al.* Repeated Temperature Modulation Epitaxy for P-Type Doping and Light-Emitting Diode Based on ZnO. *Nat. Mater.* **2004**, *4*, 42–46.
- (243) Sun, K.; Jing, Y.; Li, C.; Zhang, X.; Aguinaldo, R.; Kargar, A.; Madsen, K.; Banu, K.; Zhou, Y.; Bando, Y.; *et al.* 3D Branched Nanowire Heterojunction Photoelectrodes for High-Efficiency Solar Water Splitting and H₂ Generation. *Nanoscale* **2012**, *4*, 1515–1521.
- (244) Hou, J.; Cheng, H.; Takeda, O.; Zhu, H. Unique 3D Heterojunction Photoanode Design to Harness Charge Transfer for Efficient and Stable Photoelectrochemical Water Splitting. *Energy Environ. Sci.* **2015**, *8*, 1348–1357.

- (245) Oh, I.; Kye, J.; Hwang, S. Enhanced Photoelectrochemical Hydrogen Production from Silicon Nanowire Array Photocathode. *Nano Lett.* **2012**, *12*, 298–302..
- (246) Kim, H.; Monllor-Satoca, D.; Kim, W.; Choi, W. N-Doped TiO₂ Nanotubes Coated with a Thin TaO_xN_y Layer for Photoelectrochemical Water Splitting: Dual Bulk and Surface Modification of Photoanodes. *Energy Environ. Sci.* **2015**, *8*, 247–257..
- (247) Kong, L.; Wang, C.; Zheng, H.; Zhang, X.; Liu, Y. Defect-Induced Yellow Color in Nb-Doped TiO₂ and Its Impact on Visible-Light Photocatalysis. *J. Phys. Chem. C*, **2015**, *119*, 16623–16632.
- (248) Li, W.; Kuc, A.; Walther, C. F. J.; Heine, T. Detailed Atomistic Investigation of Fe-Doped Rutile Phases. *J. Phys. Chem. A* **2015**, *119*, 5742–5748.
- (249) Pinna, N.; Hocheplied, J.; Niederberger, M.; Gregg, M. Chemistry and Physics of Metal Oxide Nanostructures. *Phys. Chem. Chem. Phys.* **2009**, *11*, 3607.
- (250) Hossain, F. M.; Murch, G. E. The Effect of Defect Disorder on the Electronic Structure of Rutile TiO_{2-x}. *Defect and Diffusion Forums* **2006**, *251-252*, 1–12.
- (251) Lottermoser, T.; Lonkai, T.; Amann, U.; Hohlwein, D.; Ihringer, J.; Fiebig, M. Magnetic Phase Control by an Electric Field. *Nature* **2004**, *430*, 541–544..
- (252) Beaulac, R.; Schneider, L.; Archer, P. I.; Bacher, G.; Gamelin, D. R. Light-Induced Spontaneous Magnetization in Doped Colloidal Quantum Dots. *Science* **2009**, *325*, 973–976.
- (253) Fert, A. Origin, Development, and Future of Spintronics (Nobel Lecture). *Angew. Chemie - Int. Ed.* **2008**, *47*, 5956–5967.
- (254) Furdyna, J. K. Diluted Magnetic Semiconductors. *J. Appl. Phys.* **1988**, *64*, R29-R64.
- (255) Lee, J.; Oszwaldowski, R.; Gøthgen, C.; Autić, I. Mapping between Quantum Dot and Quantum Well Lasers: From Conventional to Spin Lasers. *Phys. Rev. B* **2012**, *85*, 1–13.
- (256) Rangaraju, N.; Peters, J. A.; Wessels, B. W. Magnetoamplification in a Bipolar Magnetic Junction Transistor. *Phys. Rev. Lett.* **2010**, *105*, 1–4.
- (257) Žutić, I.; Fabian, J.; Sarma, S. Das. Spintronics: Fundamentals and Applications. *Rev. Mod. Phys.* **2004**, *76*, 323–410.
- (258) Coey, J. M. D.; Venkatesan, M.; Fitzgerald, C. B. Donor Impurity Band Exchange in Dilute

- Ferromagnetic Oxides. *Nat. Mater.* **2005**, *4*, 173–179.
- (259) Philip, J.; Punnoose, A.; Kim, B. I.; Reddy, K. M.; Layne, S.; Holmes, J. O.; Satpati, B.; LeClair, P. R.; Santos, T. S.; Moodera, J. S. Carrier-Controlled Ferromagnetism in Transparent Oxide Semiconductors. *Nat. Mater.* **2006**, *5*, 298–304.
- (260) Bonanni, A.; Dietl, T. A Story of High-Temperature Ferromagnetism in Semiconductors. *Chem. Soc. Rev.* **2010**, *39*, 528–539.
- (261) Jit, S.; Weerasekara, A. B.; Jayasinghe, R. C.; Matsik, S. G.; Perera, A.; Buchanan, M.; Sproule, G. I.; Liu, H. C.; Stintz, A.; Krishna, S.; *et al.* Dopant Migration-Induced Interface Dipole Effect in N-Doped GaAs/AlGaAs Terahertz Detectors. *IEEE Electron Device Lett.* **2008**, *29*, 1090–1093.
- (262) Matsumoto, Y.; Murakami, M.; Shono, T. Room-Temperature Ferromagnetism in Transparent Transition Metal-Doped Titanium Dioxide. *Science*, **2001**, *291*, 854–857.
- (263) Rahman, G.; García-Suárez, V. M.; Hong, S. C. Vacancy-Induced Magnetism in SnO₂: A Density Functional Study. *Phys. Rev. B* **2008**, *78*, 184404.
- (264) Coey, J. M. D.; Chambers, S. A. Oxide Dilute Magnetic Semiconductors—Fact or Fiction? *MRS Bull.* **2008**, *33*, 1053–1058.
- (265) Li, T.; Ong, C. S.; Heng, T. S.; Yi, J. B.; Bao, N. N.; Xue, J. M.; Feng, Y. P.; Ding, J. Surface Ferromagnetism in Hydrogenated-ZnO Film. *Appl. Phys. Lett.* **2011**, *98*, 2009–2012.
- (266) Qi, W.; Nieh, R.; Lee, B. H.; Kang, L.; Jeon, Y.; Lee, J. C. Electrical and Reliability Characteristics of ZrO₂ Deposited Directly on Si for Gate Dielectric Application. *Appl. Phys. Lett.* **2000**, *77*, 3269.
- (267) Mannhart, J.; Schlom, D. G. Semiconductor Physics: The Value of Seeing Nothing. *Nature* **2004**, *430*, 620–621.
- (268) Mannhart, J.; Schlom, D. G. Oxide Interfaces-an Opportunity for Electronics. *Science* **2010**, *327*, 1607–1611.
- (269) Sohn, Y.; Pradhan, D.; Radi, A.; Leung, K. T. Interfacial Electronic Structure of Gold Nanoparticles on Si(100): Alloying versus Quantum Size Effects. *Langmuir* **2009**, *25*, 9557–9563.

- (270) Wagner, R. S.; Ellis, W. C. Vapor-Liquid-Solid Mechanism of Crystal Growth and its application to Silicon. *App Phys. Lett.* **1964**, *4*, 89.
- (271) Ning, S.; Zhan, P.; Xie, Q.; Li, Z.; Zhang, Z. Room-Temperature Ferromagnetism in Undoped ZrO₂ Thin Films. *J. Phys. D. Appl. Phys.* **2013**, *46*, 445004.
- (272) Wang, D. D.; Qi, N.; Jiang, M.; Chen, Z. Q. Defects versus Grain Size Effects on the Ferromagnetism of ZrO₂ Nanocrystals Clarified by Positron Annihilation. *Appl. Phys. Lett.* **2013**, *102*.
- (273) Sundaresan, A.; Bhargavi, R.; Rangarajan, N.; Siddesh, U.; Rao, C. N. R. Ferromagnetism as a Universal Feature of Nanoparticles of the Otherwise Nonmagnetic Oxides. *Phys. Rev. B* **2006**, *74*, 1–4..
- (274) Panigrahy, B.; Aslam, M.; Misra, D. S.; Ghosh, M.; Bahadur, D. Defect-Related Emissions and Magnetization Properties of ZnO Nanorods. *Adv. Funct. Mater.* **2010**, *20*, 1161–1165.
- (275) Foster, A. S.; Sulimov, V. B.; Lopez Gejo, F.; Shluger, A. L.; Nieminen, R. M. Structure and Electrical Levels of Point Defects in Monoclinic Zirconia. *Phys. Rev. B* **2001**, *64*, 224108.
- (276) Xiu, F.; Wang, Y.; Kim, J.; Hong, A.; Tang, J.; Jacob, A. P.; Zou, J.; Wang, K. L. Electric-Field-Controlled Ferromagnetism in High-Curie-Temperature Mn_{0.05}Ge_{0.95} Quantum Dots. *Nat. Mater.* **2010**, *9*, 337–344.
- (277) van der Meulen, M. I.; Petkov, N.; Morris, M. A.; Kazakova, O.; Han, X.; Wang, K. L.; Jacob, A. P.; Holmes, J. D. Single Crystalline Ge_{1-x}Mn_x Nanowires as Building Blocks for Nanoelectronics. *Nano Lett.* **2009**, *9*, 50–56.
- (278) Zippel, J.; Lorenz, M.; Setzer, A.; Wagner, G.; Sobolev, N.; Esquinazi, P.; Grundmann, M. Defect-Induced Ferromagnetism in Undoped and Mn-Doped Zirconia Thin Films. *Phys. Rev. B* **2010**, *82*, 125209.
- (279) Sharma, P.; Gupta, A.; Rao, K. V.; Owens, F. J.; Sharma, R.; Ahuja, R.; Guillen, J. M. O.; Johansson, B.; Gehring, G. A. Ferromagnetism above Room Temperature in Bulk and Transparent Thin Films of Mn-Doped ZnO. *Nat. Mater.* **2003**, *2*, 673–677.
- (280) Wan, W.; Huang, J.; Zhu, L.; Hu, L.; Wen, Z.; Sun, L.; Ye, Z. Defects Induced Ferromagnetism in ZnO Nanowire Arrays Doped with Copper. *CrystEngComm* **2013**, *15*, 7887.

- (281) Patel, S. K. S.; Gajbhiye, N. S. Oxygen Deficiency Induced Ferromagnetism in Cr-Doped TiO₂ Nanorods. *J. Magn. Magn. Mater.* **2013**, *330*, 21–24.
- (282) Patel, S. K. S.; Gajbhiye, N. S. Intrinsic Room-Temperature Ferromagnetism of V-Doped TiO₂ (B) Nanotubes Synthesized by the Hydrothermal Method. *Solid State Commun.* **2011**, *151*, 1500–1503.
- (283) Banerjee, S.; Mandal, M.; Gayathri, N.; Sardar, M. Enhancement of Ferromagnetism upon Thermal Annealing in Pure ZnO. *Appl. Phys. Lett.* **2007**, *91*, 1–4.
- (284) Xing, G.; Wang, D.; Yi, J.; Yang, L.; Gao, M.; He, M.; Yang, J.; Ding, J.; Sum, T. C.; Wu, T. Correlated d⁰ Ferromagnetism and Photoluminescence in Undoped ZnO Nanowires. *Appl. Phys. Lett.* **2010**, *96*, 0–3.
- (285) Potzger, K.; Zhou, S.; Grenzer, J.; Helm, M.; Fassbender, J. An Easy Mechanical Way to Create Ferromagnetic Defective ZnO. *Appl. Phys. Lett.* **2008**, *9*, 182504.
- (286) Ghosh, S.; Khan, G. G.; Mandal, K. Defect-Driven Magnetism in Luminescent n/p-Type Pristine and Gd-Substituted SnO₂ Nanocrystalline Thin Films. *ACS Appl. Mater. Interfaces* **2012**, *4*, 2048–2056.
- (287) Stoneham, A. M. Theory of Defects in Solids. *Clarendon, Oxford* **1975**, chapter 16.
- (288) Chang, L. Te; Wang, C. Y.; Tang, J.; Nie, T.; Jiang, W.; Chu, C. P.; Arafın, S.; He, L.; Afsal, M.; Chen, L.; Wang, K. L. Electric-Field Control of Ferromagnetism in Mn-Doped ZnO Nanowires. *Nano Lett.* **2014**, *14*, 1823–1829.
- (289) Dery, H.; Dalal, P.; Cywiński, L.; Sham, L. J. Spin-Based Logic in Semiconductors for Reconfigurable Large-Scale Circuits. *Nature* **2007**, *447*, 573–576.
- (290) Jansen, R. Spintronics: Solar Spin Devices See the Light. *Nat. Mater.* **2013**, *12*, 779–780.
- (291) Patel, S. K. S.; Dewangan, K.; Gajbhiye, N. S. Synthesis and Room Temperature d⁰ Ferromagnetic Properties of α -MoO₃ Nanofibers. *J. Mater. Sci. Technol.* **2015**, *31*, 453–457.
- (292) Gao, D.; Zhang, Z.; Li, Y.; Xia, B.; Shi, S.; Xue, D. Abnormal Room Temperature Ferromagnetism in CuO–ZnO Heterostructures: Interface Related or Not? *Chem. Commun.* **2015**, *51*, 1151–1153.
- (293) Pal, B.; Dhara, S.; Giri, P. K.; Sarkar, D. Evolution of Room Temperature Ferromagnetism

- with Increasing 1D Growth in Ni-Doped ZnO Nanostructures. *J. Alloys Compd.* **2015**, *647*, 558–565.
- (294) Chuang, P.; Ho, S.; Smith, L. W.; Sfigakis, F.; Pepper, M.; Chen, C.; Fan, J.; Griffiths, J. P.; Farrer, I.; Beere, H. E.; *et al.* All-Electric All-Semiconductor Spin Field-Effect Transistors. *Nat. Nanotechnol.* **2014**, *10*, 35–39.
- (295) Ho, D.; Sun, X.; Sun, S. Monodisperse Magnetic Nanoparticles for Theranostic Applications. *Acc. Chem. Res.* **2011**, *44*, 875–882.
- (296) Ramesh, R.; Spaldin, N. A. Multiferroics: Progress and Prospects in Thin Films. *Nat. Mater.* **2007**, *6*, 21–29.
- (297) Pradel, K. C.; Ding, Y.; Wu, W.; Bando, Y.; Fukata, N.; Wang, Z. L. Optoelectronic Properties of Solution Grown ZnO n-p or p-n Core–Shell Nanowire Arrays. *ACS Appl. Mater. Interfaces* **2016**, *8*, 4287–429.
- (298) Ganjipour, B.; Wallentin, J.; Borgström, M. T.; Samuelson, L.; Thelander, C. Tunnel Field-Effect Transistors Based on InP-GaAs Heterostructure Nanowires. *ACS Nano* **2012**, *6*, 3109–3113.
- (299) Sinova, J.; Žutić, I. New Moves of the Spintronics Tango. *Nat. Mater.* **2012**, *11*, 368–371.